

# Florida State University Libraries

---

Electronic Theses, Treatises and Dissertations

The Graduate School

---

2005

## Mathematical Modeling of Transport and Reaction in Cellular and Tissue Engineering

Pragyansri Pathi



**THE FLORIDA STATE UNIVERSITY  
FAMU-FSU COLLEGE OF ENGINEERING**

**MATHEMATICAL MODELING OF TRANSPORT AND  
REACTION IN CELLULAR AND TISSUE ENGINEERING**

**By**

**Pragyansri Pathi**

**A Dissertation submitted to the  
Department of Chemical and Biomedical Engineering  
in partial fulfillment of the  
requirements for the degree of  
Doctor of Philosophy**

**Degree Awarded:  
Summer Semester, 2005**

**Copyright © 2005  
Pragyansri Pathi  
All Rights Reserved**

The members of the Committee approve the dissertation of Pragyansri Pathi defended on 06-28-2005.

Bruce R. Locke  
Professor Directing Dissertation

Timothy S. Moerland  
Outside Committee Member

Teng Ma  
Committee Member

Kevin Chen  
Committee Member

Approved:

Bruce R. Locke, Chairperson, Department of Chemical and Biomedical Engineering

Ching-Jen Chen, Dean, College of Engineering

The Office of Graduate Studies has verified and approved the above named committee members.

*To*  
*Nana & Mama*

## **ACKNOWLEDGEMENT**

First and foremost, I would like to thank my advisor, Dr Bruce R Locke for giving me this exciting and challenging opportunity. Throughout the last four years, he has been a constant source of guidance, support, insight and inspiration, and has often had more faith in me than I myself! I thank him for his generous time and commitment. Words are not enough to express my deepest sense of gratitude and respect I feel for him.

I appreciate the opportunity for having an exceptional doctoral committee and wish to thank them for their valuable suggestions, and support: Dr Timothy S. Moerland, for sharing his biological expertise on muscle project; Dr Teng Ma, for discussions and experimental support on tissue engineering projects; and, Dr Kevin Chen, for his support and encouragement. Each of them, in their own way, helped make this a valuable learning experience.

This work would not have been complete without the enthusiastic support of my collaborators. I am greatly indebted to Dr Stephen Kinsey and his students at the University of North Carolina, Wilmington. Their experimental results and countless discussions have made the crustacean muscle metabolic modeling part of my research successful. I thank Dr Feng Zhao for all the experimental support and helpful discussions on the tissue engineering model development. I am also thankful to Dr Craig J Galban and Dr Richard Spencer of National Institute of Health for their suggestions on cartilage tissue modeling section in my work. I have to also thank COMSOL Support group for their prompt responses concerning the use of FEMLAB.

I would like to acknowledge the financial support of the Department of Chemical Engineering, FAMU-FSU College of Engineering; Defense Advanced Research Projects Agency (DARPA); and, National Science Foundation (NSF).

I take this opportunity to thank the friends who have made my time here so enjoyable. I have met many fine people during my stay in Tallahassee. My special thanks to Mike, Selma, Warren, and Frank for all the coffee breaks, long beer sessions and the innumerable discussions, that I will never forget. I am grateful to my close friends Jyothy, Srilu and Anu for their support and encouragement. I am also thankful to the incredible staff at the Department of Chemical & Biomedical Engineering.

None of this would be possible without the love and support from my family. The hardest part of graduate school was having to move so far away from all the near and dear ones in my life. I have dedicated this work to my loving parents, Dr S. N. Pathi and Dr Pranati Mishra, for instilling in me a love for learning. They have always pushed me to do my best, and never settle for the second best. Special thanks to my brother, Soumya, and my sister, Bagmisri, for their understanding, endless patience, encouragement, and for always being there when I needed them the most. I cannot thank my grandparents enough; Aja, Bou, Ai and Bapa, for all the love, blessings, and support to pursue my dreams and reach heights. As nana says without Ma's blessings none of this would have been possible...and I know Ma you are always there with all of us!

Finally, I would like to thank my best friend and fiancé, Sasi, for his unflinching love and faith in me over the last few years.

# TABLE OF CONTENTS

LIST OF TABLES.....	x
LIST OF FIGURES.....	xi
<b>ABSTRACT.....</b>	<b>xviii</b>

	<b>Page</b>
<b>1 Introduction</b>	<b>1</b>
<b>PART I : MATHEMATICAL MODELING OF TISSUE GROWTH IN REACTOR SYSTEMS</b>	<b>9</b>
<b>PART I (A) Role of Nutrient Supply and Product Formation on Cell Growth in Bioreactor Design for Tissue Engineering of Hematopoietic Cells</b>	<b>9</b>
<b>2 Background and Literature Review</b>	<b>9</b>
2.1 Introduction	9
2.2 Process of Hematopoiesis	10
2.3 Bone Marrow Microenvironment	11
2.4 HSC Culture	11
2.4.1 Need for culture and potential applications	11
2.4.2 Culture conditions that affect cell expansion	12
2.4.3 System for expansion of hematopoietic cells	17
2.5 Mathematical Modeling	23
2.5.1 Motivation	23
2.5.2 Need for modeling hematopoietic system	24
2.5.3 Available mathematical Models	24
2.5.3.1 Krogh's model	25

	2.5.3.2	Palsson's perfusion bioreactor model	29
	2.5.3.3	Grooved perfusion bioreactor model	33
	2.5.3.4	Population balance model	37
2.6		Introduction to Method of Volume Averaging	41
<b>3</b>		<b>Analysis of oxygen supply on granulocyte progenitor cell growth in 3-dimensional perfusion bioreactor</b>	<b>45</b>
	3.1	Problem Statement	45
	3.2	Model Formulation	46
	3.2.1	Reactor design	46
	3.2.2	Mathematical model	46
	3.2.2.1	Model equations	47
	3.2.2.2	Solution procedure	57
	3.2.2.3	Macroscopic area averaging	57
	3.2.2.4	Fixed oxygen concentration model	58
	3.2.2.5	Well-Mixed bioreactor model	59
	3.3	Results and Discussion	60
	3.4	Conclusions	83
<b>4</b>		<b>Analysis of glucose and oxygen supply and by-product (lactate) concentration on progenitor and mature cells in 3-dimensional well-mixed reactor</b>	<b>85</b>
	4.1	Introduction	85
	4.2	Literature Review	87
	4.2.1	Model factors	87
	4.2.1.1	Effect of glucose supply on cell growth in the 3-dimensional perfusion bioreactor	87
	4.2.1.2	Effect of lactate production on cell growth in the 3-dimensional perfusion bioreactor	89
	4.2.1.3	Multiple cell population	93
	4.2.1.4	Geometry of cell layer in the bioreactor	94
	4.2.1.5	Local 3-dimensional cell geometry	94
	4.2.2	Model equations	96
	4.2.3	Parameter estimation	101
	4.2.4	Preliminary results on Well-Mixed Bioreactor Model	109
	4.3	Conclusions	111
	4.4	Recommendations for Future Work	112
		<b>PART I (B) Effects of Oxygen Transport on 3-dimensional Human Mesenchymal Stem Cell Tissue Development in Perfusion and Static Cultures</b>	<b>114</b>
<b>5</b>	5.1	Problem Statement	114
	5.2	Reactor Designs	115
	5.3	Experimental Data	116



5.4	Mathematical Model Development	116
5.4.1	Model equations perfusion reactor (Unit 1)	118
5.4.2	Model equations static culture (Unit 2)	119
5.4.3	Parameter estimation	121
5.4.4	Solution procedure	123
5.5	Results and Discussion	124
5.6	Conclusions	129
 <b>PART I (C) Analysis of Cartilage Tissue Growth and Extracellular Matrix Formation <i>Ex Vivo</i> in Hollow Fiber Bioreactor</b>		<b>130</b>
<b>6</b>	6.1 Introduction	130
	6.2 Methodology	134
	6.2.1 Experimental Data	134
	6.2.2 Model Formulation	134
	6.2.2.1 Outline	134
	6.2.2.2 Model equations	137
	6.2.3 Note on parameters	156
	6.2.4 Sensitivity analysis formulation	157
	6.2.5 Solution procedure	157
	6.3 Results and Discussion	158
	6.4 Conclusions	178
 <b>PART II METABOLIC MODELING OF MUSCLE METABOLISM</b>		<b>179</b>
<b>7</b>	7.1 Introduction	179
	7.2 Current Modeling Objectives	181
	7.3 Model Formulation	185
	7.3.1 Model schematic	185
	7.3.2 Model reactions	187
	7.3.3 Model equations	192
	7.3.4 Parameter estimation	195
	7.3.5 Solution procedure	197
	7.4 Results	197
	7.5 Discussion	204
	7.6 Future Recommendation	210
<b>8</b>	<b>Summary</b>	<b>213</b>
 <b>Appendix A: List of Parameters Used in Chapter 3</b>		<b>219</b>
 <b>Appendix B: List of Parameters Used in Chapter 4</b>		<b>221</b>

<b>Appendix C: List of Parameters Used in Chapter 5</b>	<b>225</b>
<b>Appendix D: Experimental Data (Potter <i>et al.</i>, 1998) Used for Model Validation in Chapter 6</b>	<b>227</b>
<b>Appendix E: List of parameters Used for Model Development in Chapter 6</b>	<b>228</b>
<b>Appendix F: Computation of Average Radii of Free Space for Water Diffusion in <i>ex vivo</i> Cartilage Culture in HFBR</b>	<b>231</b>
<b>Appendix G: List of Parameters Used in Chapter 7</b>	<b>233</b>
<b>Appendix H: Permission from John Wiley &amp; Sons, Inc.</b>	<b>235</b>
<b>References</b>	<b>236</b>
<b>Bibliographical Sketch</b>	<b>250</b>

## LIST OF TABLES

<b><u>Table</u></b>	<b><u>Description</u></b>	<b><u>Page</u></b>
2. 1	Bioreactors most frequently used for the culture of hematopoietic stem cells (HSCs) (Cabrita <i>et al.</i> , 2003)	23
4. 1	Experimental results of cell numbers from Yan <i>et al.</i> , 2001	102
4. 2	Experimental result of lactate concentration from Yan <i>et al.</i> , 2001	103

## LIST OF FIGURES

<u>Figure</u>	<u>Description</u>	<u>Page</u>
2. 1	Structure of the Hematopoietic system. All cell types above the dotted line are found in the BM and all the cells below (the mature blood cells) are found in the circulating PB	12
2. 2	Bioreactors more frequently used for the culture of hematopoietic stem cells: (a) perfusion chamber; (b) grooved surface of perfused chamber; (c) stirred tank; (d) air-lift fixed bed; and (e) fixed bed or fluidized bed bioreactor (Cabrita <i>et al.</i> , 2003)	22
2.3	Graphical representation of the Kroghian model (Chow <i>et al.</i> , 2001 a)	26
2. 4	Two-dimensional schematic diagram of a radial flow perfusion bioreactor	30
2. 5	Model of a flat bed perfusion bioreactor system with a series of grooves to retain cells in the presence of constant perfusion. This is a closed system with no headspace. Medium flows in the $z$ direction across the chamber. $y'$ and $z'$ represent the local co-ordinate system in a cavity (Horner <i>et al.</i> , 1998)	34
2. 6	Three models of specialization (Nielsen <i>et al.</i> , 1998)	39
2. 7	Graphical representation of heterogeneous tissue slice (method of volume averaging)	42
3. 1	Schematic of perfusion bioreactor model (Florida State University)	47
3. 2	Non-dimensional oxygen concentration (in color) varying in space at nearly 15 days ( $13 \cdot 10^5$ s) in the perfusion bioreactor. Parameters: $T=0.6$ cm; $l=0.06$ cm; $res\_time=1$ hr; $F=4.17 \cdot 10^{-3}$ cm <sup>3</sup> /s; $v_{avg}=2.8 \cdot 10^{-3}$ cm/s	62
3. 3	Macroscopically averaged oxygen consumption by metabolism ( $\langle mm \rangle$ ) and for cell growth ( $\langle growth\_o \rangle$ ) at various times. Parameters: $T=0.6$ cm; $l=0.06$ cm; $res\_time = 1$ hr; $F=4.17 \cdot 10^{-3}$ cm <sup>3</sup> /s; $v_{avg}=2.8 \cdot 10^{-3}$ cm/s	63

3.4 a	Spatial variation in non-dimensional oxygen concentration in the cell layer at nearly 15 days ( $13 \cdot 10^5$ s)	64
3.4 b	Simulated growth in the cell layer at nearly 15 days ( $13 \cdot 10^5$ s)	64
3.5	Macroscopically averaged flux of oxygen through the FEP membrane and through flow variation with time. Parameters $T=0.6$ cm; $l=0.06$ cm; $res\_time=1$ hr; $F=4.17 \cdot 10^{-3}$ cm <sup>3</sup> /s; $v_{avg}=2.8 \cdot 10^{-3}$ cm/s	65
3.6 a	Simulated macroscopically averaged oxygen concentrations in the cell layer (matrix) and the liquid layer for varying liquid layer heights ( $T$ ) at different times. Parameters $T=0.6 - 0.3$ cm; $l=0.06$ cm; $res\_time = 1$ hr; $F=2.08 \cdot 10^{-3}$ cm <sup>3</sup> /s- $4.17 \cdot 10^{-3}$ cm <sup>3</sup> /s; $v_{avg} = 2.8 \cdot 10^{-3}$ cm/s	67
3.6 b	Spatially averaged cell growth for various liquid layer heights at different time. Parameters $T=0.6 - 0.3$ cm; $l=0.06$ cm; $res\_time = 1$ hr; $F=2.08 \cdot 10^{-3}$ cm <sup>3</sup> /s- $4.17 \cdot 10^{-3}$ cm <sup>3</sup> /s; $v_{avg} = 2.8 \cdot 10^{-3}$ cm/s	68
3.6 c	Simulated fluxes through the membrane with time. Parameters: $T=0.6 - 0.3$ cm; $l=0.06$ cm; $res\_time=1$ hr; $F=2.08 \cdot 10^{-3}$ cm <sup>3</sup> /s- $4.17 \cdot 10^{-3}$ cm <sup>3</sup> /s; $v_{avg} = 2.8 \cdot 10^{-3}$ cm/s	69
3.7 a	Simulated average oxygen concentration and averaged cell volume fraction in the cell layer of the bioreactor with time. Parameters $T=0.6$ cm; $l=0.06$ cm; $res\_time = 0$ hr- $2$ hr; $F=0$ cm <sup>3</sup> /s- $8.33 \cdot 10^{-3}$ cm <sup>3</sup> /s; $v_{avg} = 2.8 \cdot 10^{-3}$ cm/s	70
3.7 b	Spatial variation in cell volume fraction in the cell layer at nearly 15 days ( $13 \cdot 10^5$ s) for different residence times and correspondingly different flow rates ( $F$ )	71
3.8 a	The effect of different modes of oxygen supply on the averaged oxygen concentration in the cell layer and the cell volume fraction. Parameters: $T=0.3$ cm; $l=0.06$ cm; $res\_time=1$ hr; $c_{gas\ chamber}=1$ ; $c_{in\_flow}=1$ ; $F= 2.083 \cdot 10^{-3}$ cm <sup>3</sup> /s; $v_{avg} = 2.8 \cdot 10^{-3}$ cm/s	72
3.8 b	The effect of different modes of oxygen supply on the averaged oxygen concentration in the cell layer and the cell volume fraction. Parameters: $T=0.4$ cm; $l=0.06$ cm; $res\_time=1$ hr; $c_{gas\ chamber}=1$ ; $c_{in\_flow}=1$ ; $F= 2.8 \cdot 10^{-3}$ cm <sup>3</sup> /s; $v_{avg} = 2.8 \cdot 10^{-3}$ cm/s	73
3.8 c	The effect of different modes of oxygen supply on the averaged oxygen concentration in the cell layer and the cell volume fraction. Parameters: $T=0.6$ cm; $l=0.06$ cm; $res\_time=1$ hr; $c_{gas\ chamber}=1$ ; $c_{in\_flow}=1$ ; $F= 4.17 \cdot 10^{-3}$ cm <sup>3</sup> /s; $v_{avg} = 2.8 \cdot 10^{-3}$ cm/s	74
3.9 a	Oxygen concentration variation with time in a mixed bioreactor under different oxygen supply conditions with different membrane permeability, $km$ and medium flow rates ( $Perm=1.343 \cdot 10^{-4}$ cm/s known value of permeability of the FEP membrane, $F=4.17 \cdot 10^{-3}$ cm <sup>3</sup> /s)	78

3. 9 b	Cell volume fraction variation with time in a mixed bioreactor under different oxygen supply conditions with different membrane permeability, $km$ and medium flow rates ( $Perm=1.343*10^{-4}$ cm/s, $F=4.17*10^{-3}$ cm <sup>3</sup> /s)	79
3.10 a	Simulation of average oxygen concentration in the cell layer for various modes of oxygen supply with time. Parameters: $T=0.6$ cm; $l=0.06$ cm; $res\_time = 1$ hr; $F= 4.17*10^{-3}$ cm <sup>3</sup> /s; $v_{avg} = 2.8*10^{-3}$ cm/s	80
3. 10 b	Effect of mode of oxygen supply on cell volume fraction of granulocyte progenitors at different times. Parameters: $T=0.6$ cm; $l=0.06$ cm; $res\_time = 1$ hr; $F= 4.17*10^{-3}$ cm <sup>3</sup> /s; $v_{avg} = 2.8*10^{-3}$ cm/s	81
4. 1	Schematic of a proposed grooved matrix (cell layer) of the bioreactor (Florida State University)	94
4. 2	Schematic of cell proliferation and differentiation process	97
4.3	Bioreactor schematic showing continuous flow of oxygen	97
4.4 a	Increase in progenitor cells (group 1) and post-progenitor cells (group 2) over culture time in 3-dimensional batch culture. Modeling results (solid line) compared to available experimental data (dots) from Yan <i>et al.</i> , 2001 shown in Table 4.1	104
4.4 b	Lactate concentration in 3-dimensional batch culture	105
4.4 c	Fold increase in Lactate concentration in 3-dimensional batch culture. Modeling results (solid line) compared to available experimental data (dots) from Yan <i>et al.</i> , 2001 shown in Table 4.2	105
4.4 d	Glucose concentration in 3-dimensional batch culture	106
4. 4 e	Oxygen in 3-dimensional batch culture	106
4.5 a	Increase in progenitor cells (group 1) and post-progenitor cells (group 2) over culture time in 3-dimensional batch culture using new kinetic expression for anaerobic metabolism shown in equation 4.15. Modeling results (solid line) compared to available experimental data (dots) from Yan <i>et al.</i> , 2001 shown in Table 4.1.	108
4. 5 b	Fold increase in lactate concentration in 3-dimensional batch culture using new kinetic expression for anaerobic metabolism shown in equation 4.15. Modeling results (solid line) compared to available experimental data (dots) from Yan <i>et al.</i> , 2001 shown in Table 4.2	108
4.6 a	Increase in progenitor cells (group 1) and post-progenitor cells (group 2) over culture time in 3-dimensional well-mixed perfusion bioreactor system. Model parameters used are discussed in Appendix B.	109
4.6 b	Lactate concentrations in 3-dimensional well-mixed perfusion bioreactor system. Model parameters used are discussed in Appendix B.	110

4.6 c	Glucose concentrations in 3-dimensional well-mixed perfusion bioreactor system. Model parameters used are discussed in Appendix B.	110
4.6 d	Oxygen concentrations in 3-dimensional well-mixed perfusion bioreactor system. Model parameters used are discussed in Appendix B. Oxygen concentration increases to a non-dimensional value of one and reaches a steady state.	111
5.1	Schematic of the Culture units (a) Perfusion Reactor (Unit 1) (b) Static Culture (Unit 2)	117
5.2	Growth kinetics of hMSCs under (a) static and (b) perfusion conditions. Cell density is expressed in cells/ml.	122
5.3	Experimental results of the specific oxygen consumption rate (open diamond) throughout the culture period and polynomial fit for model development (solid line)	123
5.4 a	Mathematical simulation of the spatio-temporal variation of oxygen concentration in the cell layer of the perfusion bioreactor Unit 1	125
5.4 b	Mathematical simulation of the spatio-temporal variation of oxygen concentration in the bulk liquid layer of the perfusion reactor Unit 1	126
5.4 c	Mathematical simulation of the spatio-temporal variation of oxygen concentration in the cell layer and bulk liquid layer in static culture Unit 2	127
5.5	Average non-dimensional oxygen concentration variations in cell layer with time for static and perfusion culture units	127
6.1	Schematic of the reactor showing the idealized single hollow fiber with cells growing radially from the outer walls of the hollow fiber	136
6.2	Schematic of the averaging volume showing the cell phase and details of the extracellular matrix.	138
6.3	Model-data comparison for the growth of cells ( $\varepsilon_c = V_c/V$ ) with time (Experimental error bars obtained using error percentage of 5%)	160
6.4	Model-data comparison for total Collagen mass (g) in the reactor with time (Experimental error bars obtained using error percentage of 5%)	160
6.5	Model-data comparison for total GAG mass (g) in the reactor variation with time (Experimental error bars obtained using error percentage of 5%)	161
6.6	Model-data comparison for total number of cells in the reactor (around all 6 fibers), $[n_c]$ with time (Experimental error bars obtained using error percentage of 5%)	161
6.7	Non-dimensional nutrient concentration ( $\mu$ ) variation with time	162
6.8 a	Effective diffusion coefficient of oxygen ( $D_{eff}$ ) in the reactor	165

6. 8 b	Effective diffusion coefficient of water ( $D_{eff}^w$ ) in the reactor	166
6. 9	Model-data comparison for normalized diffusion coefficient of water in cartilage construct in HFBR ( $appD_{eff} = D_{eff}^w/Dl$ ) where $D_{eff}^w$ is the effective diffusion coefficient of water in cartilage tissue, $Dl$ is the diffusion coefficient of water in cartilage free constructs (Experimental error bars obtained using error percentage of 5%)	166
6. 10	Model-data comparison for effective relaxation constant [ $Tl_{eff}$ ] variation with time (Experimental error bars obtained using error percentage of 5%)	167
6.11 a	Validity test for the quasi-steady state assumption (Equation 6.14 a)	167
6. 11 b	Validity test of Equation 6.14 b showing that the nutrient consumption rate is small relative to diffusion during the 4 weeks of culture	168
6.12 a	Normalized Sensitivity of Collagen volume fraction with varying model parameters as a function of time; sensitivity highest to collagen production parameters	170
6.12 b	Normalized Sensitivity of GAG volume fraction with varying model parameters as a function of time; sensitivity highest to GAG production parameter	170
6.12 c	Normalized Sensitivity of cell number with varying model parameters as a function of time; sensitivity highest to cell proliferation and cell growth parameters	171
6.12 d	Normalized Sensitivity of cell volume fraction with varying model parameters as a function of time; sensitivity highest to cell growth and proliferation parameters	171
6.12 e	Normalized Sensitivity of nutrient concentration with varying model parameters as a function of time; sensitivity highest to cell proliferation, first order oxygen consumption rate and oxygen binding parameters	172
6.12 f	Normalized Sensitivity of effective oxygen diffusion coefficient in the reactor with varying model parameters as a function of time; sensitivity highest to oxygen GAG binding coefficient and the GAG production rate	172
6.12 g	Normalized Sensitivity of water diffusion coefficient in the reactor with varying model parameters as a function of time; sensitivity highest to water GAG binding coefficient and GAG production rate coefficient	173
6. 12 h	Normalized Sensitivity of NMR effective relaxation coefficient in the reactor with varying model parameters as a function of time; sensitivity highest to water GAG binding coefficient, GAG production rate coefficient, cell growth and proliferation parameters	173
6.13 a	Cartilage tissue growth over time obtained by the use of modified Contois function with respect to nutrient concentration and no dependence on cell number (as shown by the equation in case 1). Model results are shown	174



	by solid line and experimental results in dots.	
6.13 b	Cartilage tissue growth over time obtained by the use of modified Contois function with respect to nutrient concentration and 1 <sup>st</sup> order dependence on cell number (as shown by the equation in case 2).	174
6.13 c	Cartilage tissue growth over time obtained by the use of modified Contois function with respect to nutrient concentration and 3 <sup>rd</sup> order dependence on cell number (as shown by the equation in case 3).	175
6.13 d	Cartilage tissue growth over time obtained by the use of modified Contois function with respect to nutrient concentration and 1 <sup>st</sup> order inverse (inhibitory) dependence on cell number (as shown by the equation in case 4).	175
6.13 e	Cartilage tissue growth over time obtained by the use of modified Contois function with respect to nutrient concentration and no dependence on cell number (as shown by the equation in case 5).	176
6.13 f	Cartilage tissue growth over time obtained by the use of modified Contois function with respect to nutrient concentration and 1 <sup>st</sup> order dependence on cell number (as shown by the equation in case 6).	176
6.13 g	Cartilage tissue growth over time obtained by the use of modified Contois function with respect to nutrient concentration and 2 <sup>nd</sup> order dependence on cell number (as shown by the equation in case 7).	177
7. 1	(A) Cross-sectional view of a muscle fiber cell. Packs of myofibrils, mitochondria, Sarcoplasmic Reticulum and the cell membrane or Sarcolemma also shown. (B) One-dimensional schematic of the intra-mitochondrial spacing as used for model development.	186
7. 2	One-dimensional schematic of the intra-mitochondrial spacing as used for model development showing the various reactions occurring in the myofibrillar region (bulk) and in the mitochondria (surface). Arginine Kinase (AK) mediates ATP-equivalent flux in Crustacean muscle. (A) Reactions and diffusion distance in small white fibers of juvenile crabs (B) Reaction and diffusion distances over hundreds of microns in large white fibers of adult crab. Anaerobic glycogenolysis is believed to occur following contraction in large fibers, presumably to speed up phases of the recovery process. [Johnson <i>et al.</i> , 2004]	190
7. 3	Relative changes in AP and Pi concentrations in small (filled symbols) and large (open symbols) light levator fibers during a contraction-recovery cycle. [ $N \geq 5$ for every point]. (Experimental results from Dr Kinsey's Laboratory, University of North Carolina, Wilmington)	199
7. 4	Model output for small light levator fibers using parameters in Appendix G assuming a uniform distribution of mitochondria. The temporally- and spatially-resolved concentrations of AP, Pi, ATP and ADP during a	200

- contraction-recovery cycle are shown (Arg is not shown, but its concentration changes in reciprocal fashion to that of AP). [ $V_{mmito} = 1.9e-17$  mmoles/micron<sup>2</sup>.s: 5 Hz frequency with 50% duty, 7s Stimulation, *Mesh points*: 120 pts, *Time Step*: 0:0.1:7, 8:1:99, 100:100:8000s]
7. 5 Model output for large light levator fibers using parameters in Appendix G assuming only subsarcolemmal mitochondria. The temporally- and spatially-resolved concentrations of AP, Pi, ATP and ADP during a contraction-recovery cycle are shown (Arg is not shown, but its concentration changes in reciprocal fashion to that of AP). Arrows indicate the mild spatial gradients seen in the concentration 3-dimensional profiles. [ $V_{mmito} = 1.67*10^{-15}$  mmoles/micron<sup>2</sup>.s: 5 Hz frequency with 50% duty, 7s Stimulation, *Mesh points*: 120 pts, *Time Step* – 0:0.1:7, 8:1:99, 100:100:8000s] 201
7. 6 Measured AP recovery (symbols) compared to the volume averaged model of AP recovery (solid line) in small (top) and large (bottom) fibers. The measured AP data has been normalized to a resting concentration of 34.3 mM to coincide with that of the model. In the model, the myosin ATPase was activated long enough to cause a decrease in AP that was comparable to the measured data. The dotted line indicates the resting concentration. 202
7. 7 The effect of increasing the rate of mitochondrial ATP production in large fibers on the temporal and spatial profiles of AP (left panels) and ATP (right panels) concentration. All parameters are the same as in Figure 7.5, except that the  $V_{mmito}$  has been increased over the value used in Figure 7.5 by 2-fold (A), 10-fold and (B), and 100-fold (C). [ $V_{mmito} = 1.67*10^{-15}$  mmoles/micron<sup>2</sup>.s: 5 Hz frequency with 50% duty, 7s Stimulation, *Mesh points*: 120 pts, *Time Step* – 0:0.1:7, 8:1:99, 100:100:8000s] 205
7. 8 Model output for dark levator fibers using parameters in Appendix G. The temporally- and spatially-resolved concentrations of AP, Pi, ATP and ADP during a contraction-recovery cycle are shown (Arg is not shown, but its concentration changes in reciprocal fashion to that of AP). Mild spatial gradients are seen in the concentration 3-dimensional profiles. [ $V_{mmito} = 1.67*10^{-15}$  mmoles/micron<sup>2</sup>.s: 1 Hz frequency with 50% duty, 30s Stimulation, *Mesh points*: 120 pts, *Time Step* - 0:0.01:30, 31:1:99, 100:50:600s] 206

## **ABSTRACT**

Tissue engineering is a rapidly developing field seeking to solve biomedical problems which have a wide-range of clinical applications. Bioreactor cultures have been shown to be essential for improving the functional properties of the tissue engineered constructs. However, the major obstacle to-date for the generation of functional tissues in these reactors for wide-spread clinical use is the limited understanding of the regulatory role of specific physicochemical culture parameters on tissue development. Not only is the cellular environment within and around the constructs ill defined, but the complex cellular responses to this environment are also not fully understood. In this context, computational methods can serve as a valuable tool to facilitate better understanding of the underlying mechanisms governing physical, chemical, and biological processes in a 3-dimensional culture environment. These methods can also be used to correlate the cell and tissue behavior to changes in global biochemical bioreactor inputs.

These concepts are illustrated in the present work by three distinct tissue engineering applications – hematopoietic cell expansion in a perfusion bioreactor, human mesenchymal stem cell expansion in perfusion and static culture units, and cartilage tissue formation in hollow fiber bioreactors. Material balances with mass transport and chemical reaction of nutrient consumption and product formation are coupled with cell growth, differentiation and extracellular matrix formation in 3-dimensional constructs to determine the effects of transport limitations on cell behavior. The method of volume averaging is used for the determination of the effective diffusion and reaction terms in the species continuity equations in terms of local geometry and spatial restrictions in these multiphase systems. The volume averaged equations

are thereafter solved over the macroscopic dimensions of the reactor to assess system performance. This study has the potential to improve tissue engineered functional constructs.

These tissue engineering model development applications considered the cellular processes in terms of net kinetic expressions linked to changes in macroscopic environmental parameters. In order to understand and incorporate a complete model framework an understanding of processes at the cellular level is also essential. To do so, in the second major part of this project, the muscle cell was chosen for study of metabolic processes in terms of production, transport, conversion and utilization of metabolite species. It is known that in a muscle cell many cellular compartments, chemical species, enzymes, biochemical reactions, metabolic pathways, and control mechanisms interact with each other simultaneously to maintain homeostasis of the most important energy delivering metabolite, ATP. A reaction-diffusion model of phosphorous metabolites involved in various metabolic pathways in the muscle was shown to provide a suitable framework for the study of diffusion, reaction, and metabolic organization. This metabolic study is intended to understand the interactions between metabolism and cell structure. The current study is a first step towards an overall goal of setting up a rationale for cellular design for attaining a desired cell function.

# CHAPTER 1

## INTRODUCTION

*“From an engineering perspective the human body is one of the most interesting and challenging “systems” to study and describe.”*

- David Hawkins, PhD  
“Biomechanics of musculoskeletal tissues”, University of California

Biological systems are inherently complex due to the presence of many reacting chemical species in multiphase environments. The art of mathematical modeling is to unravel this complexity by identifying the key features of a given system. This is done by deriving equations based on the fundamental principles of conservation of mass, energy, and momentum, which govern system behavior. Using various mathematical techniques and computer simulations, these equations can be solved over a wide range of physiological parameter values, thereby generating predictions that can be tested in the laboratory (Wastney, 1998; Green, 2003). The focus of the present research is to develop these types of theoretical models which, when integrated with experimental results in a mutually iterative framework, can quantitatively explain the underlying mechanisms governing physical, chemical, and biological processes. These models would help to estimate parameters and variables that cannot be measured directly by experiments, to test proposed hypotheses and previously observed relationships, to address the experimental design issues, and to develop increasing insight and understanding of the system itself, thereby opening up new avenues for research.

Tissue engineering is an exciting new field that uses an engineering approach to solve biological problems with clinical significance. In the past decade, tissue engineering has emerged as a viable alternative to solve the problem of organ and tissue shortage. Tissue engineering aims to develop biological substitutes that can restore, maintain, or improve tissue function (Skalak and Fox, 1991). The engineered tissue, or construct, usually consists of 3-dimensional polymer scaffolds containing living cells in an environment with desired structure and functionality. The constructs are cultured in bioreactors designed for specific purposes that provide the chemical and mechanical environments well suited for cell proliferation and differentiation.

*‘Tissue engineering: mathematical models are helping to take tissue engineering from concept to reality’* (McArthur *et al.*, 2005). The focus of my work is to develop mathematical models for cell growth and overall tissue formation in cell culture reactors in order to build a quantitative platform to analyze and integrate the information on events occurring at the cellular level to their macroscopic environment. In general, this work attempts to develop predictive tools, which would link the cell population response to the external environment using the fundamental principles of transport phenomena and cell biology. These concepts are illustrated in the present work by three distinct tissue engineering applications – hematopoietic cell expansion in perfusion bioreactor, human mesenchymal stem cell expansion in different kinds of culture units, and cartilage tissue formation in hollow fiber bioreactors; and also in the cellular metabolic modeling of the muscle metabolism intended to understand the interactions between metabolism and cell structure.

The first three chapters (Chapter 2, 3, 4) of the thesis focus on my work on large scale *ex vivo* expansion of lymphohematopoietic cells in bioreactors. Hematopoiesis is the process of formation and development of blood cells. In the body these hematopoietic cells (HCs) grow and differentiate in the 3-dimensional bone marrow (BM) microenvironment made up of various stromal cells, extracellular matrix (ECM) proteins, and an array of soluble and ECM-bound growth factors (Mantalaris *et al.*, 1998; Li *et al.*, 2001). *Ex vivo* expansion of these cells in order to reconstitute a functioning bone marrow is a rapidly developing area and has broad range of biomedical applications (Cabrita *et al.*, 2003; Palsson *et al.*, 1993).

Traditional static culture systems such as T-flasks and gas permeable bags (Damas *et al.*, 1999) have been widely used for expanding HCs since the pioneering work of Dexter (Cabrita *et al.*, 2003). However, these culture systems are inherently 2-dimensional and therefore are unable to replicate the in-vivo BM microenvironment. The 2-dimensional culture does not promote proper cell-cell interactions and cell-ECM interactions, thus leading to lower cell growth (Nielsen *et al.*, 1988; Li *et al.*, 2001; Wang and Wu, 1992). For long term production of these cells, 3-dimensional culture systems incorporated within various bioreactors have been studied (Horner *et al.*, 1998; Cabrita *et al.*, 2003; Koller *et al.*, 1993 a; Hevehan *et al.*, 2000; Collins *et al.*, 1998; Mantalaris *et al.*, 1998; Wang and Wu, 1992). For example, static culture systems have been replaced extensively with spinner flask bioreactor or perfusion systems to provide for better control of the culture environment. These topics are discussed in detail in Chapter 2.

The most important factors necessary for control of cell growth in bioreactor systems include pH, nutrient (dissolved oxygen, glucose) concentrations, and metabolic byproduct (lactate) concentration (Koller *et al.*, 1993(a, b, c); Oh *et al.*, 1994; Schwartz *et al.*, 1991; Koller *et al.*, 1992). The effects of dissolved oxygen tension, lactate production, and pH have been extensively studied for these cell types. However, there are very few studies that report on the effect of glucose concentration on HC growth. In addition hematopoietic cultures, unlike any other cell culture system, are very complex, due to the presence of multiple cell types co-existing in culture, each with different rates of proliferation and differentiation and metabolic requirements. Therefore, macroscopic changes observed in culture systems experimentally are cumulative responses for all hematopoietic cell types existing in the culture. These different cell types and the other important factors affecting the expansion of the former are carefully outlined in Chapter 2 of the thesis.

The present work also deals with a novel 3-dimensional perfusion bench top bioreactor system developed in Dr Teng Ma's lab at Florida State University (Zhao *et al.*, 2005). The bioreactor system is being used for lymphohematopoietic cell ex vivo expansion. One of the objectives of the work reported in the present dissertation is to develop mathematical models to quantify the immune lineage cell growth characteristics and macroscopic parameter changes over an extended period of time in and around the 3-dimensional matrix of the bioreactor. The model is also

intended to provide a proper understanding of the physical parameters that govern cell growth leading to the production of specific cell types in the reactor, which in turn, will help in achieving the long term goal of scaling up the bench-top bioreactor system for clinical applications.

Although there are a number of parameters as discussed that affect HC growth and the co-existence of multiple cell types in reactor systems, as a first approach, the model discussed in Chapter 3 of this dissertation deals with the growth of a single cell type, the granulocyte progenitor cell, and one nutrient, oxygen, in this 3-dimensional perfusion bioreactor unit (Pathi *et al.*, 2005). These cells were chosen because they occupy the major fraction of the BM compartment (Chow *et al.*, 2001) and are the fastest growing HCs. They have the highest metabolic rate of oxygen consumption in the BM, and thus they provide a limiting case to assess the depletion of oxygen by cell growth and metabolism. This study can also be used to determine an upper limit to oxygen limitations in these culture systems. Moreover, these cells mature into neutrophils, which have a limited life span of only 48 hours, thereby forming the first line of defense against microbial invasion (Hevehan *et al.*, 2000), and hence *ex vivo* large scale production of this cell type is required.

Various mathematical models have been developed using the population balance approach to account for HC self-renewal, cellular differentiation into mature cells, and cell death (Nielsen *et al.*, 1988; Silva *et al.*, 2003; Hevehan *et al.*, 2000; Abkowitz *et al.*, 2000; Peng *et al.*, 1996). Models of spatial distribution of HCs in the bone marrow hematopoietic compartment have also been developed (Chow *et al.*, 2001). However, these developed models are discrete, and they do not account for cell growth dependence on culture parameters such as oxygen tension. The dynamic model proposed in Chapter 3 is intended to provide quantitative estimates of the oxygen consumption for granulocyte progenitor cell growth and metabolism thus relating macroscopic changes to cellular events using basic physiological principles. Molar balances describing oxygen consumption and cell growth are solved using the volume averaging approach (Whitaker, 1999). The method of volume averaging has been extensively used to study transport and reaction in multiphase systems for various chemical engineering problems (Carbonell and Whitaker, 1984). This method allows for the determination of the effective diffusion and



reaction terms in the molar balances in terms of local geometry and spatial restrictions. This model is extended in Chapter 4 by the addition of material balances accounting for the effects of other nutrients such as glucose and by-product formation such as lactate on multiple cell types coexisting in cultures. These computed macroscopic parameters and cell densities in the bioreactor are used to assess the key bioreactor design parameters and to optimize the overall reactor performance.

The second major application of mathematical model in tissue engineering is demonstrated in the expansion of human mesenchymal stem cells (hMSCs) in various culture units. Experimental data on hMSC growth-kinetics and spatial growth patterns, metabolism, and oxygen consumption in various culture devices - static and perfusion units have been studied (Grayson *et al.*, 2004; Zhao *et al.*, 2005 (a), (b)) to elucidate the effects of perfusion culture on cell growth and tissue development. Convective oxygen transport was found to be important for enabling and sustaining high cell growth rates, high cell density, and uniform growth pattern. In order to reemphasize the significance of flow quantitatively in terms of oxygen delivery on hMSC development, a dynamic mathematical model describing oxygen distribution in the static and perfusion culture units is developed in the present dissertation. The model is based on the principles of mass transport and reaction and provides estimates of the spatio-temporal oxygen concentration profiles in the two units, which is difficult to measure experimentally. The objective of this part of the work, however, is not to develop an *a priori* predictive model but to use the developed model results on spatial oxygen concentrations along with the available experimental data to help understand the role of oxygen transport on cell behavior (growth and metabolism) in different culture units. The model and the results are given in detail in Chapter 5 of this dissertation.

The third major application of mathematical modeling in tissue engineering demonstrated in this dissertation is in the area of the engineering of functional cartilage tissue substitutes. *In vivo*, in mammals, cartilage is primarily found in the skeleton. It is present in small amounts in certain viscera, e.g. in parts of the respiratory tract. Much of the skeletal cartilage is replaced by bone in adults but some persists throughout life as articular, costal and nasal cartilage, for example. The focus of the present study is articular cartilage - a thin layer of connective tissue located within

joints at the end of bones (Buckwalter *et al.*, 1997). This tissue is made up of relatively few cartilage cells called chondrocytes, present in an extensively hydrated extracellular matrix (ECM) made up of collagens and proteoglycans. Degeneration of this articular cartilage in the body is seen to occur during osteoarthritis and joint injury. The limited capacity of the cartilage tissue to respond to mechanical injury with a reparative process has motivated the incorporation of cell-based repair approaches after articular cartilage lesions (Raimondi *et al.*, 2002). Tissue engineering approaches can be thus used to design an *in vitro* cartilage tissue system to resemble the *in vivo* system structurally and functionally. These *in vitro* systems can be used as functional substitutes and also be used for systematic study of the process of chondrogenesis.

Cartilage tissue have been grown successfully in tissue culture bioreactors starting from chondrocyte cells, either attached to biodegradable polymeric scaffolds in mixed flasks and rotating wall bioreactors (Freed and Vunja-Novakovic, 2000b; Vunjak-Novakovic *et al.*, 1999) or in the absence of scaffolds in hollow fiber bioreactors (Petersen *et al.*, 1997; Potter *et al.*, 1998; Ellis *et al.*, 2001). The morphology, composition and mechanical properties of these constructs are strongly influenced by the microenvironment of the cell. Experimental studies have shown mass transfer limited nutrients and/or oxygen supply in these cartilage culture systems which are believed to govern the cell metabolic rates and tissue growth characteristics (Vunjak-Novakovi *et al.*, 1996; Obradovic *et al.*, 1999). Thus, there have been several studies dealing with development of functional cartilage constructs from chondrocyte cells seeded in 2-dimensional T-flasks to 3-dimensional bioreactors in order to understand and optimize cartilage tissue characteristics *in vitro*. To understand, and compile the large amounts of experimental data and to further use this data for the rational design of tissue constructs a mechanistic approach needs to be developed.

Additionally, to reach a stage of clinical applicability a definite need arises for improved control over the functional properties and composition of the developed cartilage tissue engineered constructs in culture units. Mathematical models can help to provide a better understanding of the complex interplay among the array of factors that control the functional tissue development (Sengers *et al.*, 2004). Models can be used to predict the spatio-temporal variations of the concentration of many components involved affect construct composition, formation of new

tissue mass (cell and ECM) and the microenvironment around the cartilage cell. The model developed in the present dissertation relates the kinetics of *in vitro* tissue formation to events occurring at the cellular and molecular levels, and may potentially allow for enhanced design through development of control strategies and may assist in engineered tissue optimization (Williams *et al.*, 2002).

Spencer and coworkers (Petersen *et al.*, 1997; Potter *et al.*, 1998, 2000; Ellis *et al.*, 2001) have developed an *in vitro* 3-dimensional cartilage tissue model in a hollow fiber bioreactor (HFBR) which permits a wide range of interventions and in which both biochemical and noninvasive nuclear magnetic resonance spectroscopy and imaging studies (MRI, EPR Oxygen Mapping) were performed (Potter *et al.*, 2000). HFBRs provide a more realistic diffusion barrier between cells and nutrient supply and permit interaction between chondrocytes and their secreted ECM. Like other 3-dimensional culture systems they support the chondrocyte phenotype and prevent its dedifferentiation into fibroblasts (Ellis *et al.*, 2001).

The present study develops a mathematical model to study the cartilage tissue formation in this hollow fiber bioreactor unit (Potter *et al.*, 1998). In this unit, cells are not grown in constructs (compared to the study by Langer's group). The cells are injected into the extracapillary space of the reactor. They attach themselves onto the outer surface of the hollow fiber tubes or capillaries. These cells then proliferate radially outwards in the space available. The moving boundary approach (Galban and Locke, 1997) coupled with the method of volume averaging (Whitaker, 1999) is utilized in the present work to simulate the experimental cell growth patterns, as well as to account for transport and reaction in the reactor by determination of effective diffusion and reaction terms for tissue formation in terms of local geometry and spatial restrictions. The model was used to determine the tissue parameters and NMR measurable parameters for comparison with available experimental results. The detailed modeling approach is outlined in Chapter 6 of the dissertation. This study would advance our understanding of the factors that affect cell growth and ECM production *in vitro* in bioreactors. The model will help in the development of optimal operational strategies for growing engineered cartilage in these bioreactors. Further, the model would enable understanding and rationalization of vast amount of available experimental results on this system, and provide suggestions for improved

experimental design by identifying the key parameter measurements that need to be made. This work indirectly would help in monitoring and controlling the development of the tissue engineered construct in the bioreactor.

The above models provide quantitative understanding of the effects of macroscopic changes on cellular characteristics, such as growth, metabolism and ECM production. As mentioned, this is accomplished by proposing kinetic functions relating the cellular changes to changes in the microenvironment around the cell. However, understanding at the cellular level is incomplete. As a next step towards the development of structured models, the understanding of metabolism at the cellular level is studied in the work reported in Chapter 7 of this dissertation. This is important from the perspective of cellular engineering to enhance our understanding of the role of metabolism on cellular design. The cell type used for this study is a muscle cell or a myofiber. This cell type was chosen because of its definite structure and the large range of metabolic rates observed due to change in physiological state of the animal (rest to exercise and vice versa). Moreover, these cells have conserved cell structure from organism to organism. In addition, extensive available literature on energy metabolism in muscle is an excellent opportunity to develop quantitative, predictive, and testable model of cellular function across a wide range of spatial and temporal boundaries.

Developing a quantitative understanding of cellular metabolism by studying the production, transport, conversion and utilization of energy carriers, facilitated via metabolic pathways is performed using reaction-diffusion models. The transport and reaction dynamics of phosphorous metabolites involved in various metabolic pathways in the muscle are modeled using species continuity equations. This understanding of muscle energetics is used to study supply verses demand of metabolites in various muscle fiber types. Further this understanding of the interactions between metabolism and cell structure is used in setting up a rationale for cellular design for attaining the desired functions.

## CHAPTER 2

# ROLE OF NUTRIENT SUPPLY AND PRODUCT FORMATION ON CELL GROWTH IN BIOREACTOR DESIGN FOR TISSUE ENGINEERING OF HEMATOPOIETIC CELLS

### Background and Literature Review

#### 2.1. Introduction

Every day the human body produces billions of red blood cells, white blood cells, and platelets to replace the blood cells lost due to normal turnover processes such as death, or due to illness or trauma. A variety of homeostatic mechanisms allow blood cell production to respond quickly to stresses such as bleeding or to infection and allow return to normalcy when the stresses are resolved. This highly orchestrated process is called hematopoiesis (Smith, 2003). Thus hematopoiesis refers to the process of formation and development of blood cells to maintain homeostasis (Wang *et al.*, 1995).

Hematopoiesis *in vivo* takes place primarily in the bone marrow. The bone marrow is made up of a vascular and an extra-vascular compartment. The vascular compartment as the name indicates is supplied by a nutrient artery, which branches into central longitudinal arteries, which in turn send out radial branches that eventually open into the sinuses. These sinuses converge into a central vein which carries the blood out of the bone marrow into the general circulation.

Hematopoiesis takes place in the extra-vascular compartment called the hematopoietic compartment. The extra-vascular compartment consists of stroma made up of reticular connective tissue and a parenchyma of developing blood cells, plasma cell, macrophages and fat cells. Hematopoiesis also occurs in spleen and liver during early stages of development of embryo.

## **2.2. Process of Hematopoiesis**

The commonly accepted theory on the process of hematopoiesis is called the monophyletic theory. This theory states that there exists a single type of stem cell which gives rise to all the different mature blood cells in the body. This stem cell is called the pluripotential (pluripotent) stem cell or also called as hematopoietic stem cell (HSC). Most of these types of cells are found within the bone marrow (BM) at typically very low percentages (typically 0.01-0.05%). They are also found in the circulating peripheral blood (PB), the umbilical cord blood (UCB) and the fetal liver at even lower percentages (typically 0.001%) (Cabrita *et al.*, 2003).

All the HSCs are not identical. Experimental studies reveal that these HSC can be divided into three types: long-term self-renewing HSCs (LT-HSCs), short-term self-renewing HSCs (ST-HSCs) and not self-renewing multipotent progenitors (MPPs) (Cabrita *et al.*, 2003). It is thought that the LT-HSCs self-renew throughout the lifespan of the organism. They maintain hematopoiesis by differentiating into ST-HSCs and then to MPPs. The self renewal capabilities of ST-HSCs and MPPs are only for short duration. These MPPs differentiate again into lineage-committed progenitor cells, which as their name suggests give rise to blood cells of specific lineages. These two specific hematopoietic lineages are called lymphoid lineage and myeloid lineage. The lymphoid lineages consist of T-cell and B-cell lineages. The myeloid lineages include the erythroid (production of erythrocytes or red blood cells), granulocytic (production of neutrophils, infection fighting cells), macrophagic (production of macrophages, cells with general regulatory and immune functions), and megakaryocytic (production of platelets, blood clotting component) lineages. The schematic of this process is shown in Figure 2.1.

## **2.3. Bone Marrow Microenvironment**

The regulation of HSC self-renewal/multilineage differentiation is dependent upon the intimate contact with the bone marrow microenvironment. As discussed already the hematopoietic compartment, which makes up the microenvironment for these cell types, consists of the so-called stromal cells (macrophages, adipocytes, endothelial cells and fibroblasts) and components of the extracellular matrix (ECM). The proliferation and maturation of highly primitive HSC and also the mature lineage committed progenitor cells are influenced by the myriad of growth factors expressed on the surface of and/or secreted by the stromal cells. It is presumed that these growth factors are able to create a suitable microenvironment that plays an important role by binding to specific receptors on the cell membrane of target cells and activating the current messenger pathways.

## **2.4. HSC Culture**

### **2.4.1. Need for Culture and potential applications**

Large-scale hematopoietic cultures could provide several types of important mature blood cells like the granulocytes, platelets, and red blood cells. About 12 million units of RBCs are transfused in the United States every year, the majority of them during elective surgery, and the rest in acute situations. About 4 million units of platelets are transfused every year into patients who have difficulty exhibiting normal blood clotting. Mature granulocytes are transfused to patients with weaker immune system, such as during chemotherapy and during the healing of the burn wounds. The availability of donors is a traditional problem, and coupled with that the short life of blood cells, blood-type incompatibility and some contamination of blood makes the current supply of blood unstable and is not able to meet the major changes in demand by patients (Koller *et al.*, 1993).

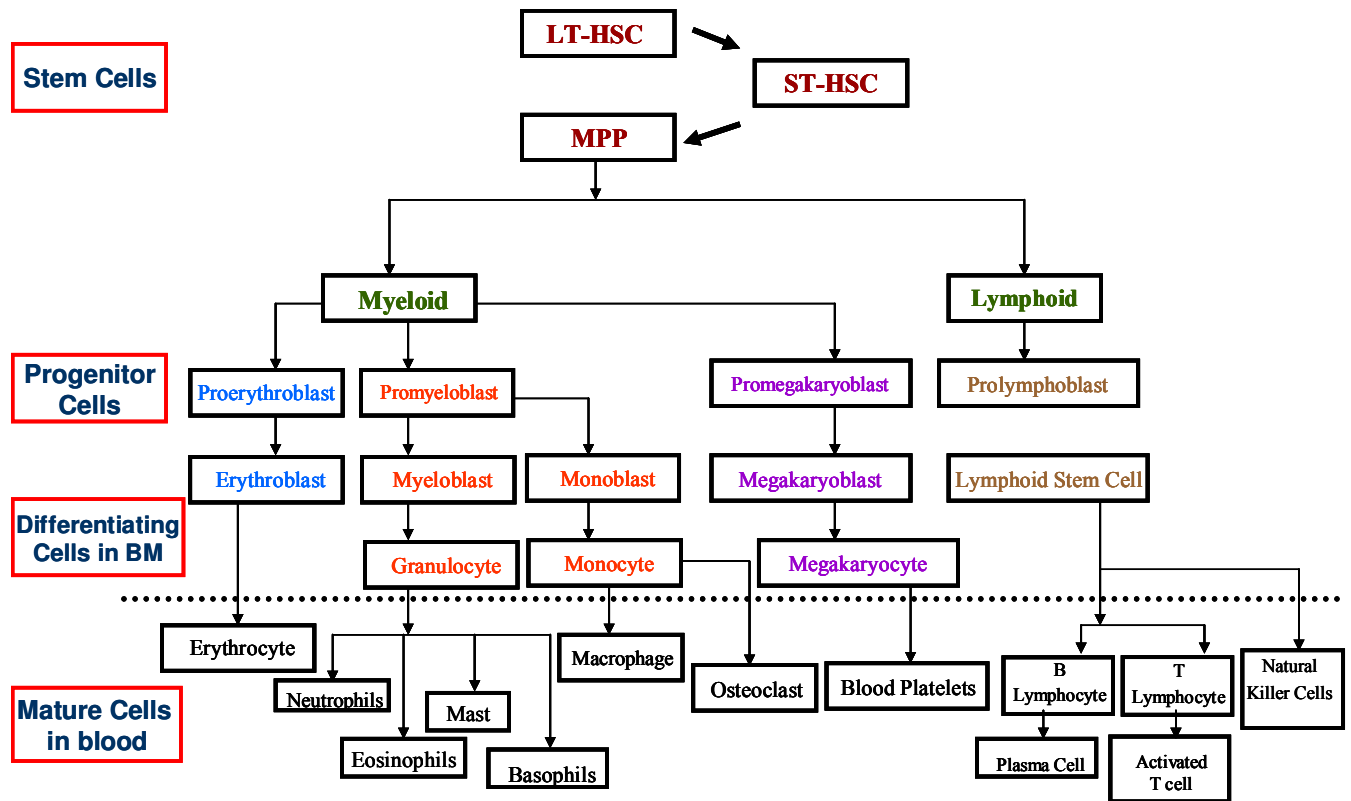


Figure 2. 1 Structure of the Hematopoietic system. All cell types above the dotted line are found in the BM and all the cells below (the mature blood cells) are found in the circulating PB (Cabrita *et al.*, 2003; Web design by Stephen Traub, American Society of Health-System Pharmacists, Inc.)

Hence over the past few years, there has been an increased interest in the development of clinical-scale culture systems for *ex vivo* expansion of hematopoietic cells. These *ex vivo* expanded hematopoietic cells can be used for transplantations following chemotherapy, tumor purging, and gene therapy.

#### 2.4.2. Culture conditions that affect expansion

Choosing optimal culture parameters for the *ex vivo* expansion of hematopoietic cells is a major challenge. This is because of complex kinetics of various cell types in different stages of lineage, their transient nature, and complex dependence upon the culture parameters. The various culture parameters which have been reviewed in the literature for this system include



growth factors, stroma, perfusion or static conditions, serum, dissolved oxygen concentration, pH, inoculum density and the engineered surfaces for cell growth.

### ***Stroma***

Stromal cells consist of the adventitial reticular cells, endothelial cells, adipocytes, and macrophages. These cells support hematopoiesis by synthesizing the ECM and by the production of growth factors. It has been reported that cultures containing a stromal layer or stroma-derived factors have greater longevity and progenitor cell expansion in comparison to cultures without stroma. However, there are a number of complications involved in using a stromal layer. The quantification of the composition of this stromal layer is very complex and so will be the quantification of its effects on various cell processes. Additionally, harvest of the stroma containing cultures is labor-intensive and requires enzymatic treatment. The benefits of stromal cells can always be replaced by defined factors, by frequent medium exchanges, and by the addition of a sufficient amount of growth factors.

### ***Serum/Serum free medium***

The first hematopoietic cultures were performed using serum-containing media. This media provides nutrition, protects the cells from shear stresses within the reactor, and also is believed to influence the transduction of mechanical forces that affect surface receptors. However, the addition of serum to a culture medium leads to an undefined composition and brings uncontrolled variability, complicating the use of cells for clinical purposes. Hence, in order to avoid complications of in vitro cultures, serum free medium is preferred. It has been shown that by addition of multiple cytokines excellent expansion of highly purified HSCs can be obtained (Cabrita *et al.*, 2003).

### ***pH***

HSC cultures might experience a pH variation of up to 0.5 pH units unless pH is controlled. This pH variation is largely due to cellular metabolism which leads to the production of by product lactate (Nielsen, *et al.*, 1999). Many studies have shown that medium acidification causes

growth inhibition (McAdams, *et al.*, 1996). The pH range of 7.2-7.4 supports the survival and differentiation of granulocyte-macrophage. Outside of this range, the differentiation is eliminated, especially at acidic pH.

In an erythroid lineage it is observed that the rate and extent of differentiation increases between pH of 7.1 to 7.6 (McAdams, *et al.*, 1996). At pH less than 7.1, erythroid progenitors are still present and viable, but their differentiation is inhibited. Similarly, the pH range 7.35 - 7.40 promotes differentiation and maturation of Mk cells whereas a lower pH (~ 7.1) extends the expansion of primitive Mk progenitor cells (Cabrita *et al.*, 2003). Therefore, pH is shown to be an important factor for hematopoietic cultures and needs to be suitably controlled to facilitate cell expansion, differentiation, maturation and apoptosis.

### ***Oxygen Tension***

Oxygen tension is an important determinant of proliferation and differentiation of hematopoietic cells. Reduced Oxygen tension ( $pO_2 = 38$  mm Hg, 5%  $O_2$ ) enhances the production of erythroid, megakaryocytic, and granulocytic-monocytic progenitors in vitro (Laluppa, 1998, Chow *et al.*, 2001). However, the formation of mature erythrocytes, mature granulocytes and megakaryocytes (Mks) is extensive under a  $pO_2$  value close to 152 mm Hg (20%  $O_2$ ). Thus, the progenitor cells of most lineages proliferate more rapidly under reduced oxygen tension, which is in regions that are farthest from the supply sources in the BM (the sinus). In contrast, the mature cells of these lineages appear extensively under the higher oxygen tension that occurs in regions close to the sinus or oxygen supply source.

The improved growth of progenitor cells under reduced oxygen tension is in part due to the increased responsiveness of hematopoietic cells to various growth factors. For example, under low oxygen levels CFU-E and BFU-E exhibit increased sensitivity to EPO (Erythropoietin), and macrophage progenitors show increased sensitivity to M-CSF (Macrophage colony stimulating factor). Accessory cells also show different responses to varying oxygen tensions in their production of growth factors. Moreover, oxygen toxicity also plays an important role in the decreased colony formation at high oxygen concentration. Studies performed have shown that in

the presence of lineage specific factors, different oxygen tensions preferentially enhance expansion of one hematopoietic cell lineage (Laluppa, 1998, Chow *et al.*, 2001). Hence the choice of oxygen tension will help to determine the lineage and maturity of cells present in culture.

BM oxygen tensions between 10 and 50 mmHg (indicating that saturation in *ex vivo* conditions by gases containing approximately 5% oxygen) is sufficient to provide an environment similar to the *in vivo* BM microenvironment. Studies have shown that formation of hematopoietic cell colonies in colony assay cultures is enhanced under reduced oxygen conditions resulting in both larger and more numerous colonies. Further studies have extended these findings to long-term hematopoietic cultures (LTHC), both with and without the addition of exogenous cytokines (Koller *et al.*, 1993).

The role of oxygen is very complicated because the oxygen availability in a culture depends on cell density, culture configuration and gas-phase oxygen tension in high cell density bioreactors. A lower oxygen tension may benefit progenitors in the early stage of culture. However, as the cell number increases the oxygen demand will increase and cultures may become oxygen limited. Hence, it is important to replenish the oxygen by either increasing the gas-phase oxygen tensions, the agitation rate, or the perfusion rates, depending upon the culture device (McAdams, *et al.*, 1996). There is also evidence to suggest that stem cells can survive under hypoxic conditions better than more mature progenitor cells. Therefore, the choice of oxygen tension significantly influences the type of cells produced in culture and, together with the choice of cytokine combinations, provides a significant means by which the lineage of the cells produced in the culture can be controlled (McAdams, *et al.*, 1996).

### ***Cell seeding density***

Cell inoculum density affects the total cell and progenitor expansion as well as the percentage of progenitor cells in the culture. In general, experiments have shown, lower cell seeding densities lead to greater total cell expansion and greater depletion of colony forming cells. High density cultures have greater total cell and CFC numbers but lower total cell expansion ratios in

comparison to low density cultures. The positive impact of increasing the rate of medium exchange has been shown to be larger in high density cultures. A greater maintenance of CFCs at high densities has also been seen in bioreactor cultures (McAdams, *et al.*, 1996).

The cell seeding density has been found to affect culture performance for BM MNC, and PB MNC as well as for CD34<sup>+</sup> cell culture systems. Lower density cultures expand total cells preferentially over CFC. In contrast, higher density cultures expand CFC considerably but without larger expansion of the total cells. Thus, it can be understood that a high density culture maintains progenitors and long-term culture-initiating cells (LTC-IC) better than a low inoculum density culture that induces differentiation. Culture systems that can maintain higher number of progenitor cells are desirable. Hence a perfusion system (discussed in the next section) that can maintain pH and oxygen tension in desirable levels in high density cultures is what is necessary (Laluppa, 1998, Chow *et al.*, 2001).

### ***Feeding/Perfusion***

Perfusion and the rate of medium exchange are important culture variables. Hematopoiesis in BM takes place under homeostatic conditions, which in vitro can be achieved under frequent or continuous (perfusion) feeding. The in vivo perfusion rate of plasma through the BM is approximately 0.1 ml/cc of marrow per minute (Laluppa, 1998, Chow *et al.*, 2001). High-density bioreactor systems with higher cell densities may require correspondingly higher perfusion rates. In contrast, the standard feeding protocol for hematopoietic LTHC cells is a weakly exchange of 50%-100% of the medium rather than the daily rate (Koller *et al.*, 1993).

### ***Hematopoietic growth factors***

Colony-stimulating factors (CSF) and interleukins (IL) are the primary regulators of the growth and differentiation of hematopoietic cells. The exact combination of the two growth factors for optimal expansion of hematopoietic stem cells, progenitor cells and mature cells are still unknown. Cytokines such as erythropoietin (EPO), thrombopoietin (TPO), and granulocyte-colony stimulating factor (G-CSF) are 'lineage specific' and support proliferation and maturation of committed progenitors. IL-3, granulocyte macrophage-CSF (GM-CSF) are intermediate

acting ‘lineage non-specific’ factors and support proliferation of multipotential progenitors. Other factors such as IL-6, G-CSF, IL-11, and stem cell factor (SCF), when associated with IL-3 bring primitive, quiescent progenitors into the cell cycle and increase proliferation. Growth factors like EPO, IL-3, GM-CSF, G-CSF, and SCF are considered to be survival factors because they suppress apoptosis in cells at various stages in the hematopoietic lineage.

These regulators are added depending on the kind of cells being cultured and the desired lineage. For example a combination of IL-6, G-CSF, GM-CSF are used for the expansion of more mature cells and progenitors of the neutrophil lineage (Laluppa, 1998). The proliferation and maturation of Mks requires the addition of TPO. However, the growth factor combination for maintenance and expansion of primitive progenitors (LTC-IC) is still not well defined. A combination of growth factors that would bring about proliferation of progenitor cells, prevent their differentiation and apoptosis are desired (Laluppa, 1998, Chow *et al.*, 2001).

### ***Local geometry***

Local geometry can influence the function of cells in culture. A 2-dimensional flat surface provided by standard tissue culture plastic is non-physiological, and is probably undesirable for retaining normal physiological function over extended periods of time (Koller *et al.*, 1993). A 3-dimensional tissue culture might provide a similar microenvironment to the *in vivo* environment and result in long-term multilineage production of hematopoietic cells. This topic will be further discussed in the section dealing with culture devices.

### **2.4.3 System for expansion of hematopoietic cells**

BM cells have traditionally been cultured on flat, two-dimensional surface of tissue culture dishes. Dexter *et al.*, 1977 were the first to develop a long term murine hematopoietic (bone marrow) culture system, which primarily produced granulocytes. The key features of this system were the establishment of the stromal layer during the first few weeks of the culture followed by progenitor cells expanding into colonies in the next few weeks. Since then investigators began using static culture systems such as well plates, T-flasks and gas permeable blood bags for

expanding hematopoietic cells. These systems, however, suffer, severe limitations including the following:

- (a) lack of mixing resulting in critical gradients for dissolved oxygen (low solubility) and nutrients (such as cytokines and metabolites); hence heterogeneity,
- (b) lack of control options for dissolved oxygen concentration and pH,
- (c) lack of support for frequent feeding,
- (d) productivity limited by the number of cells that can be supported by a given surface area,
- (e) cumbersome for large scale applications, because of the need for more flasks, bags or dishes,
- (f) low process reproducibility, and
- (g) increased risk of contamination due to repeated handling required to feed cultures or to obtain data on culture performance.

These limitations restrict the usefulness of static systems to relatively low density cultures with low total cell requirements.

The use of bioreactor systems is an alternative approach to standard flask culture systems *in vitro*. Advanced bioreactors are necessary when a large number of cells are required, accessory cells are used and high cell density is desired. These systems may also have the potential to become automated. They are closed systems which thereby decrease the space and labor requirements, reduce contamination, and facilitate continuous automated medium exchange. They can be well monitored and optimally controlled, and thus can be used to develop an understanding of the influence of various input parameters in the culture system on the hematopoietic cell expansion and commitment. The most important bioreactors used so far for the expansion of hematopoietic cells include: perfusion chambers, stirred reactors, fluidized bed reactors, fixed (packed bed) reactors, airlift reactors and hollow fiber reactors.

### ***Perfusion chambers***

Palsson and collaborators (Schwartz *et al.*, 1991; Palsson *et al.*, 1993) have developed a perfusion culture system based on flat small-scale cell culture chambers with an attached stromal layer to retain inoculated cells. The design of such a reactor is driven by the fact that more

frequent medium exchanges and the supply of soluble growth factors increased the total cell production and progenitor maintenance in the culture. Radial flow type chambers are used in order to provide a uniform environment (because of the absence of walls parallel to the flow path and hence no slow-flowing regions). The bioreactor schematic is shown in Figure 2.2 (a).

These cultures have achieved approximately 20-fold expansion of CFU-GM, 2-7-fold expansion of primitive LTC-IC as these reactor systems could maintain better-defined culture parameters, such as pH, and dissolved oxygen concentration by continuously supplying cells with nutrients and removing metabolic byproducts. Clinical trials have been initiated using a prototype of a perfusion system developed by the University of Michigan and Aastrom Bioscience. The cell production system (CPS) operates as a fully automated, closed system with pre-sterilized, disposable reactor cassettes and automated sterile cell recovery.

It was found out that *ex vivo* expansion of these cells (from PB, UCB, BM-MNC) for clinical applications would be simplified by using a long-termed hematopoietic culture without an attached stroma. Hence the perfusion bioreactor was modified to a grooved flat bed perfusion system by the addition of grooves perpendicular to the flow direction at the bottom of the chamber (Horner *et al.*, 1998). The schematic of the grooved perfusion flat bed bioreactor is shown in Figure 2.2 (b). The grooves retain cells in the bioreactor in the presence of continuous perfusion. They also reduce mechanical stresses on the cells by isolating them from the primary flow. The simple design also provides the ease for harvesting cells at the end of the culture period; in direct contrast to hollow fiber bioreactors (to be discussed later). Moreover, the growth environment in this chamber is reproducible and has well defined, substantial advantages for automation. Table 2.1 lists the various cells that have been grown using these bioreactors.

### ***Stirred bioreactors***

Stirred bioreactors are easy to operate: allow sampling, monitoring and control of culture conditions. They provide a homogeneous environment for cell growth because mixing overcomes the diffusion limitations of static cultures. Most common operating modes of stirred

bioreactors are batch, fed-batch and perfusion mode (retention of cells by means of internal/external filtration modules). The schematic of the bioreactor is shown in Figure 2.2 (c). Although these reactors are simple to operate, readily scalable and provide relatively homogeneous environment, it was not certain how well they can support the accessory cells unless a microcarrier was added or the cells were encapsulated. Moreover HCs are relatively sensitive to shear and hence agitation due to mixing in this reactor might affect cell growth (thought to affect the surface marker expression, including cytokine receptors).

### ***Packed and fluidized bed reactors***

Packed bed bioreactors (Figure 2.2 (e)) are designed to provide 3-dimensional scaffolding for cell attachment and culture. In these systems an initial attachment-dependent stromal cell culture is started on the bed particles whereupon the HSCs can be co-cultivated (Wang *et al.*, 1995; Mantalaris *et al.*, 1998). The bioreactors are operated in small volumes (approximately 500 ml working volume). The screening and optimization of the culture conditions were effectively performed in a miniaturized loop reactor containing a fixed bed of collagen microcarriers with a working volume of 1 ml, which can be placed in conventional tissue culture plates. In the case of fluidized bioreactors the carrier movement inhibited the addition of HSCs to stromal cells.

### ***Other reactor types***

‘Hollow fiber’ and ‘air-lift’ (Figure 2.2 (d)) reactors were also used to culture HCs. They did not provide considerable cell expansion (Sardoni and Wu, 1993). The poor performance of the hollow fiber bioreactor was due to the difficulty of harvesting cells from the reactor. The culture environment in such a bioreactor is highly spatially non-homogeneous, which creates large concentration gradients of critical nutrients, e.g., oxygen, and pH. Gradients of pH and oxygen could result in the production of different cell types in different sections of the reactor. Process monitoring could be problematic in such a reactor since the cells cannot be easily sampled or observed during the culture. In addition, limited recovery of cells from this type of reactor has been reported. ‘Rotating vessel bioreactors’, a new low shear bioreactor that would be able to reproduce some of the *in vivo* characteristics related to HC growth, differentiation, maturation and death are yet to be implemented for culturing these cells.



Bioreactor systems are advantageous because they have the potential to become automated. They are closed systems thereby decreasing space and labor requirements and contamination and also facilitating compliance with regulatory requirements. A uniform culture environment and a simple design are the primary advantages of stirred systems. However, hematopoietic cells being shear sensitive possess a major disadvantage in using stirred systems. Flat bed perfusion systems would provide a low shear environment, a proper supply of nutrients maintaining the various culture conditions and culture cells more effectively over all the bioreactor system. However, being 2-dimensional they still do not provide proper cell-cell and cell-matrix interactions for optimal cell growth. Hence, it is critical to design a similar system but with 3-dimensional microstructure.

Further studies need to be conducted in order to determine the sensitivity of a particular hematopoietic lineage to various culture parameters discussed above. This includes analysis of the effects of such factors as oxygen and lactate concentrations, pH, shear forces, and other conditions to determine how closely they should be controlled in the bioreactor system in order to replicate the *in vivo* bone marrow microenvironment.

The field of hematopoietic stem and progenitor cell expansion has progressed rapidly since the first Dexter cultures were performed in the mid-1970s. Within these few years progress has been especially rapid in the identification of suitable microenvironment for large scale cell expansion. This includes the utilization of 3-dimensional matrices and novel bioreactor systems that help in maintaining high levels of nutrient concentration and facilitating byproduct removal. The potential for *ex vivo* expansion is manifest, as clinicians have already begun to utilize *ex vivo* expanded hematopoietic cells for transplantation and gene therapy. Clinically the potential for *ex vivo* expansion are promising, however, still many factors need to be considered before the process can be a clinical routine. My research deals with the development of mathematical models for these novel 3-dimensional culture systems for optimally desired *ex vivo* expansion of these cells. This will advance research on mathematical modeling for this system.

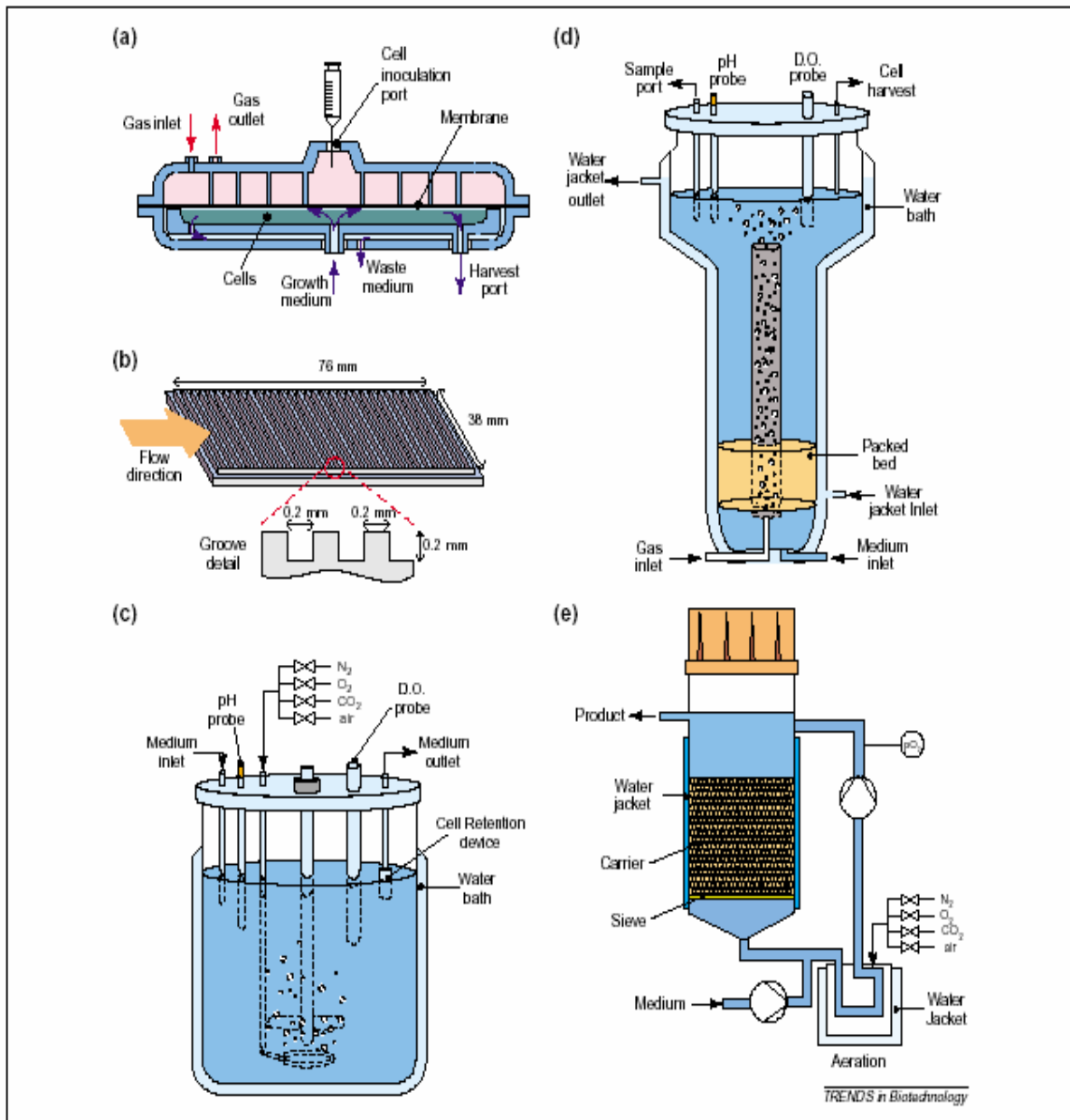


Figure 2. 2 Bioreactors more frequently used for the culture of hematopoietic stem cells: (a) perfusion chamber; (b) grooved surface of perfused chamber; (c) stirred tank; (d) air-lift fixed bed; and (e) fixed bed or fluidized bed bioreactor (Cabrita *et al.*, 2003)

**Table 2. 1 Bioreactors most frequently used for the culture of hematopoietic stem cells (HSCs)  
(Cabrita *et al.*, 2003)**

<b>Bioreactor Type</b>	<b>Culture mode</b>	<b>Progenitor cell expansion<sup>a</sup></b>
Perfusion chamber	Small scale perfusion chamber (3 ml)	3-fold LTC-IC
	Large scale perfusion chamber (30 ml)	7.5-fold LTC-IC
Stirred tank	Grooves perpendicular to the direction of flow	LTC-IC maintenance
	Batch suspension culture in controlled bioreactor (working volume 120 ml)	6-fold hematopoietic progenitors
	Batch suspension culture in spinner flask (total volume 250 ml) with periodical cytokine addition	2.6-fold BFU-E
	Batch suspension culture in controlled bioreactor (working volume 550 ml)	8-fold CFU
	Batch culture with microcarriers in spinner flask (total volume 250 ml) with periodical cytokine addition	1.8-fold BFU-E
	Batch suspension culture in spinner flask (working volume 20 ml) with periodical medium replacement	7-fold LTC-IC
	Batch culture of microencapsulated cells in spinner flask (working volume 50 ml with 12–13 ml of capsules) with daily exchange of 10 ml of medium	11-fold BFU-E
	Fluidized bed	173 working volume. Bed of gelatine-modified open porous glass carriers (32 ml)
Fixed (packed) bed	173 ml working volume. Bed of gelatine-modified open porous glass carriers (20 ml)	7-fold CFU-GM
	28 ml working volume. Bed of macroporous collagen microcarriers (10 ml)	114-fold CFU-GM
	1 ml working volume. Bed of macroporous collagen microcarriers	N/A
Airlift	Batch suspension culture in spinner flask (total volume 250 ml) with periodical cytokine addition	0.8-fold BFU-E
Hollow Fiber	Medium from a 250 ml reservoir was passed into the hollow fiber cartridge (1.0 sq ft fiber surface area, 10 000 MW cutoff)	No expansion

## 2.5 Mathematical Modeling

### 2.5.1 Motivation

Implementing a successful 3-dimensional bioreactor system for either clinical study or basic-study requires a reliable transport-reaction model. Such a model would allow for the estimation of operational limits of a given bioreactor design for a particular cell culture application by ensuring that the cells are grown under non-limiting culture conditions. The model would also allow for the selection of suitable design characteristics and/or operational variables to achieve a desirable level of one or more culture parameters, such as dissolved oxygen, pH, and nutrient or byproduct concentrations. This would directly affect the growth of that cell in that culture

system. Hence, the growth of the cell in the bioreactor system may be effectively manipulated by the use of mathematical models (Horner *et al.*, 1998).

### **2.5.2 Need for modeling of hematopoietic system**

As discussed in the introduction *in vivo* hematopoiesis process occurs in the bone marrow (BM). Compared with all other tissues in the body the bone marrow has been extensively studied. Bone marrow cultures have significant applications to clinical practice and to basic scientific studies of tissue structure-function relationships (Koller and Palsson, 1993). Therefore, hematopoiesis is a logical candidate system for the initial development of mathematical models of *ex vivo* function.

Section 2.4.3 described the importance of 3-dimensional bioreactor systems for *ex vivo* expansion of hematopoiesis in order to reconstitute a functioning BM. Evaluating the kinetics in these hematopoietic culture systems is complicated by the distribution of cells of multiple lineages over different stages of differentiation. Thus, an observed response (experimentally) is an integral response from several cell populations of cells. Models are developed to predict the different kinetic parameters of various HC types that are experimentally difficult to determine. For example, the developed models can be used to obtain the cell growth of early progenitors (present in low frequencies in culture), as their content and distribution cannot be identified even by flow cytometry (Yang *et al.*, 2000). The concentration of various nutrients and products in the matrix that are important in determining and manipulating cell growth can be studied. This information obtained from the model can be further used in the optimization of *ex vivo* cultures.

### **2.5.3 Available Mathematical Models**

Various mathematical models have been reported in literature describing the hematopoiesis process *in vivo* in the BM and *ex vivo* in the culture systems. A few of the most important models are briefly reviewed below.

### 2.5.3.1 Krogh's Model

Krogh's model (Krogh, 1918) approximates a tissue as a cylinder and has been extensively used in the modeling of oxygen transfer through different types of tissues, including the skeletal muscle, myocardium, brain, lung, and the skin.

Chow and coworkers (Chow *et al.*, 2001 a) have used this Krogh's modeling approach to estimate the oxygen partial pressure ( $pO_2$ ) (or concentration distribution) in the bone marrow hematopoietic compartment (BMHC). The model simulates the cellular arrangement of various cell types depending on the oxygen consumption. A tissue cylinder consisting of various cell types with the bone marrow sinus at the center is constructed. The following assumptions are made to simplify the mathematical formulation:

1. steady state oxygen transfer,
2. oxygen molecules are assumed not to bind to any carriers or preferentially adsorb on certain parts of the cells,
3. sinuses are assumed to be straight and parallel for a length sufficient to establish equilibrium between the sinus and hematopoietic tissue,
4. oxygen consumption and resistance to oxygen diffusion of the sinusoidal wall are insignificant, and
5. extra-vascular tissue in BMHC is composed of only one cell type (i.e., a homogeneous Kroghian model).

The oxygen transport and utilization can be mathematically described as:

$$K\nabla^2 P = Q(P) \tag{2.1}$$

where  $K$  is the effective oxygen permeability (mol/cm/s/mm Hg),  $P$  is the oxygen partial pressure  $pO_2$  (mm Hg), and  $Q(P)$  is the volumetric oxygen consumption rate (mol/cm<sup>3</sup>/s). The effective oxygen permeability is the product of the oxygen diffusivity ( $D$ , cm<sup>2</sup>/s) and the oxygen

solubility coefficient ( $\alpha$ , mol/cm<sup>3</sup>/mm Hg).  $Q$  is the ratio of the specific oxygen uptake rate ( $q_{O_2}$ , mol/cell/h) and the specific cell volume ( $V$ , cm<sup>3</sup>/cell).

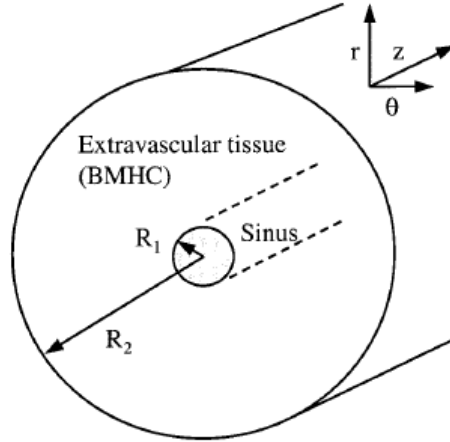


Figure 2. 3 Graphical representation of the Kroghian model (Chow *et al.*, 2001 a)

Assuming  $P$  in the extra-vascular tissue depends only on the radial position ( $R$ ) relative to sinus, equation 2.1 describing the oxygen continuity reduces to,

$$\frac{1}{r} \left[ \frac{d}{dr} \left( r \frac{dP}{dr} \right) \right] = \frac{Q(P)}{K} \quad (2.2)$$

The  $P$  at the sinus wall ( $R_1$ ) in Figure 2.3 equals the saturation oxygen tension ( $P_s$ ) and the oxygen flux is zero at the boundary wall of the cylinder at  $R_2$  (symmetry boundary condition).

$$P = P_s \quad \text{when } r = R_1 \quad (\text{at the sinus wall})$$

$$\frac{dP}{dr} = 0 \quad \text{when } r = R_2 \quad (\text{at the outer boundary of the tissue cylinder}) \quad (2.3)$$

Dimensionless forms of the oxygen continuity equation 2.2 and the boundary conditions (equation 2.3) are given as,

$$\frac{1}{r^*} \frac{d}{dr^*} \left( r^* \frac{dP^*}{dr^*} \right) = \frac{Q(P)}{K} \frac{R_2^2}{P_s} \quad (2.4)$$

$$P^* = 1 \quad \text{when} \quad r^* = \beta \quad (\text{at the sinus wall})$$

$$\frac{dP^*}{dr^*} = 0 \quad \text{when} \quad r^* = 1 \quad (\text{at the boundary of the tissue cylinder}) \quad (2.5)$$

where  $r^* = r/R_2$ ,  $P^* = P/P_s$  and  $\beta = r/R_2 = R_1/R_2$ .

The volumetric oxygen consumption rate  $Q(P)$  is written either as a zero order kinetics, a first order oxygen uptake kinetics, or as a saturation-type (Michaelis-Menten) kinetics,

Zero order:  $Q(P) = Q_{\max}$ , where  $Q_{\max}$  is the maximal oxygen uptake rate

First order:  $Q(P) = k \cdot Q_{\max} \cdot P$ , where  $k$  is first-order rate constant

Michaelis-Menten:  $Q(P) = \frac{Q_{\max} P}{K_M + P}$ , where  $K_M$  is the oxygen affinity constant (2.6)

The expression for the non-dimensional oxygen partial pressure is calculated using the zero order kinetics as,

$$P^* = 1 + \phi^2 \left[ \frac{r^{*2} - \beta^2}{4} + \frac{1}{2} \ln \left( \frac{\beta}{r^*} \right) \right] \quad (2.7)$$

Equation 2.7 was solved for different cell types (assuming one cell type in the extra-vascular space at a time) and oxygen partial pressures were obtained along the tissue (BMHC). The model is more effectively used to determine the radius at which each type of cell is located. The model showed that progenitor cells are found to be located farther away from the sinus whereas the mature cells are located closer to the sinus.

Chow *et al.*, 2001 (Part II) modified their homogeneous Kroghian model in order to incorporate the presence of multiple cell types in the BMHC. The three different approaches used are described below.

1. In order to evaluate the effects of heterogeneity in cellular properties on the  $pO_2$  distribution in BMHC the extra vascular tissue was divided into multiple cell layers with different metabolic and transport characteristics (multi-layer model) surrounding a sinus (oxygen source) called the 'Multi-layer Kroghian model'. Different layers were made up of different cells – from early progenitors to the mature cells – of the same lineage or different lineages. The simulated results of the typical  $pO_2$  distribution of a composite tissue (multi-layer model) shows that the metabolically active cells should be located further away from the sinus, as that would cause a lower  $pO_2$  levels in their proximity.
2. The homogeneous Krogh model was modified to a 2-dimensional model by adding another spatial dimension to describe the complicated cellular architecture in which cells are arranged in clusters. Large hematopoietic cell types (Megakaryocytes or Adipocytes) closely resemble cells in cluster. These cells are considered as the secondary cell type. The granulocytes occupy most of the BMHC and are defined as the primary cell type. The primary cell type is assumed to occupy the extra vascular tissue space as shown in Figure 2.3. The secondary cell types are chosen to be located either close to the sinus or further away from the sinus. The  $pO_2$  profiles in this model are asymmetric because of localized variations in cell types.
3. Further on, in order to simulate the  $pO_2$  distributions in colony type cellular arrangements, such as in erythroblastic islets, granulocytic loci, and lymphocytic nodules, the multi-layer model is modified by placing the sinus outside the colonies. The results show that the macrophage at the center of the islet is a metabolically active cell and



experiences the lowest  $pO_2$  values, while the mature erythrocytes (with low metabolic activity) are located at the outer periphery and against the sinus wall, which is region of highest  $pO_2$  value (close to supply).

The above three models provided us with a simplified picture of the  $pO_2$  distribution in a heterogeneous cell-type situation. The simulation results can be used to eliminate the cellular architectures that are physiologically unrealistic. The 2-dimensional model can be used to account for the asymmetry in cellular arrangements that might not be arranged as in the multi-layer model. Finally, the modified cylinder model in which the sinus is located in the outer periphery is used to describe cells that grow in colony like structures such as the erythroblastic islets, granulocytic loci, to name a few.

In these Krogh's models (Part I and Part II) the importance of the oxygen partial pressures on the growth of specific cell types was determined. The models were used to determine the oxygen partial pressure distribution *in vivo*, in the bone marrow, and in systems with cell distributions similar to that in the bone marrow tissue. These models were used to obtain the metabolic functions and parameters describing the oxygen consumption *in vivo* of different cell types for analysis in the *ex vivo* bioreactor model. The model results showed the growth of mature cells at regions of higher oxygen tension and early progenitors at regions of lower oxygen tension in BMHC. These results indicate a similar spatial distribution in the bioreactor *ex vivo*. Moreover, the dimensions of different cell types in the BM and diffusivity of oxygen in cellular media is also obtained from the information provided in this study.

#### ***2.5.3.2 Palsson's Perfusion Bioreactor Model***

Palsson and collaborators were the first group to develop perfusion bioreactors to grow HCs (discussed in section 2.4.3). In hematopoietic bioreactors, as discussed, oxygen plays an important role in a variety of physiological processes such as cell attachment, spreading, cell growth and differentiation. HCs experience growth inhibition and even toxicity at high oxygen concentrations, and anoxia at low oxygen concentrations. Hence, maintaining an optimal oxygen concentration range near the cell surface is important in attaining a successful culture. However,

measurement of the local oxygen concentration near the cells is difficult; hence a mathematical analysis is needed to estimate the local oxygen concentration.

Peng and Palsson (1996) have developed a mathematical model of oxygen delivery to the cells in a perfusion bioreactor. The schematic of the bioreactor is shown in Figure 2.4. The growth medium with oxygen (concentration,  $C_{in}$ ) is pumped with a peristaltic pump and flows parallel to the lower plate (i.e., the bottom of the bioreactor) with a fully developed laminar velocity profile  $u(x)$ . Oxygen in the gas phase permeates through the membrane into the liquid layer and diffuses across into the cell bed. The oxygen concentration at the liquid side of the membrane is assumed to be at saturation  $C^*$ . The cell bed is located at the bottom of the reactor. Cells consume oxygen and the uptake rate is described by Michaelis-Menten kinetics (similar to that explained by the Kroghian model). The local oxygen concentration is computed based on the design parameters: oxygen partial pressure, medium depth ( $h$ ), and cell inoculum density.

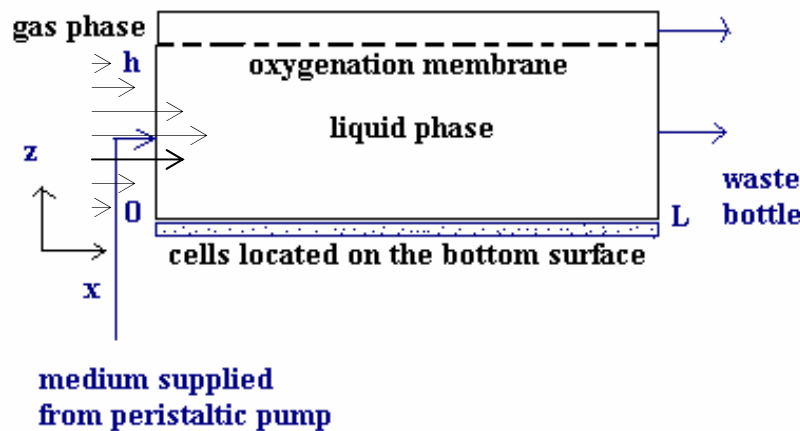


Figure 2. 4 Two-dimensional schematic diagram of a radial flow perfusion bioreactor

A mathematical model describing this process is developed with the following assumptions:

1. Medium flow rate is slow corresponding to a transit time of 1.33 days. The diffusional response time is nearly 1 hr. Therefore, the ratio of the diffusional time to transit time is much smaller than unity, hence the effects of fluid flow can be neglected in the liquid phase,

2. pseudo-steady state analysis is used since the rate of diffusion is much faster than the growth rate of cells (cell doubling time is nearly 24-48 hour),
3. cells are uniformly distributed at the lower boundary of the liquid layer i.e. in cell layer.

Oxygen mass balance in the reactor is dominated by diffusion and is described as,

$$D \frac{\partial^2 C}{\partial x^2} = 0 \tag{2.8}$$

The oxygen is at saturation at the membrane surface (i.e. @  $x=h$ ) and the oxygen flux at the cell surface (i.e. @  $x=0$ ) is the uptake rate by the cells for their metabolic and growth needs. So boundary conditions are written as,

$$\begin{aligned} C &= C^* & \text{at } x &= h \\ D \frac{\partial C}{\partial x} &= N_o & \text{at } x &= 0 \end{aligned} \tag{2.9}$$

The pseudo-steady state and Michaelis-Menten uptake rate kinetics for oxygen consumption by cells is given as,

$$N_o = \frac{q \cdot X \cdot C_o}{K_m + C_o} \tag{2.10}$$

where  $C_o$  is the oxygen concentration at the bottom surface, i.e. the local oxygen concentration experienced by the cells,  $q$  is the specific oxygen uptake rate of the cells,  $K_m$  is Michaelis-Menten constant (1-5% of  $C^*$ ) and  $X$  is the cell density. Upon solving the equation 2.8 with the boundary conditions (equation 2.9) the oxygen concentration profile is given by,

$$C_o^2 + (K_m - C^* + qXh/D)C_o - C^*K_m = 0 \quad (2.11)$$

Non-dimensionalizing the oxygen concentration relative to saturation we get,

$$\sigma_o^2 + (\kappa + \phi - 1) \cdot \sigma_o - \kappa = 0$$

where

$$\kappa = K_m / C^* = 0.01 - 0.05$$

$$\phi = qXh / DC^* = \frac{h^2 / D}{hC^* / qX} = \frac{t_{diffusion}}{t_{uptake}} \quad (2.12)$$

The parameter  $\phi$  measures the ratio of the time constants for oxygen diffusion to oxygen uptake (i.e. reaction). The numerical estimation of  $\phi$  suggests that at the earlier time of the culture the value is less than unity as the oxygen diffusion is fast and hence sufficient oxygen reaches the cell bed. With time the cell density changes and hence the time for oxygen uptake becomes faster and hence the value of  $\phi$  becomes much higher than unity and by the end of the culture oxygen delivery is limited to the cells. Therefore, the most important aspect of this bioreactor design is to maintain the value of  $\phi$  small, by manipulating the liquid layer height, the cell density and the gas phase oxygen concentration.

This model is a simple way of quantitatively determining the oxygen concentration in the liquid layer and explaining the various parameters that need to be manipulated for optimizing the design and performance of the perfusion hematopoietic bioreactor. This model is definitely a first step towards describing ways of bioreactor optimization by manipulating the supply vs. consumption rate.

However, this model has the following major drawbacks which need to be improved.

1. In this model the calculations are made at fixed values of cell density. In reality in cultures the cell densities are related to the local oxygen concentration and vary in space and time in cultures.
2. This model accounts for total oxygen consumption rate. Oxygen is consumed for metabolism and for growth (two distinct processes). In order to understand the oxygen dependence on cell growth separate functions describing oxygen consumption for metabolism and oxygen consumption for growth need to be developed.
3. The model assumes diffusion to be the most important mode of oxygen delivery rather than oxygen delivery by convective transport. Hence the model does not take into account variations of oxygen concentration in three dimensions. However, for higher liquid layer heights (greater than 3 mm), hydrodynamic flow would be required along with supply from headspace oxygen chambers, to avoid oxygen limitations in the bioreactor. Then it would be necessary to model spatial variation in the oxygen concentration in the liquid layer.
4. This model does not have a separate cell layer made up of the matrix and cells and hence need not account for the oxygen concentration and cell density spatial variation in the cell layer, which exists in *ex vivo* experiments.
5. The model accounts for the overall cell growth rate. However, hematopoietic cultures are different from other cell cultures. As discussed in section 2.2 multiple cell types coexist and cells along different lineages grow, differentiate, mature and die. It is essential to consider the dynamic distribution of various cell types along different lineages in these culture systems. A population modeling approach (described in section below) need to be coupled to these established transport models.

### ***2.5.3.3 Grooved Perfusion Bioreactor Model***

Grooved perfusion bioreactors have been shown to overcome some of the mass transfer limitations present in other cultures, and these reactors retain cells (subjected to constant perfusion in the bioreactor) under reduced mechanical stresses by isolating them from primary

flow. The bioreactor schematic is shown in Figure 2.5. An advection-diffusion model was developed by Horner *et al.*, 1998 to describe 2-dimensional version of this bioreactor system.

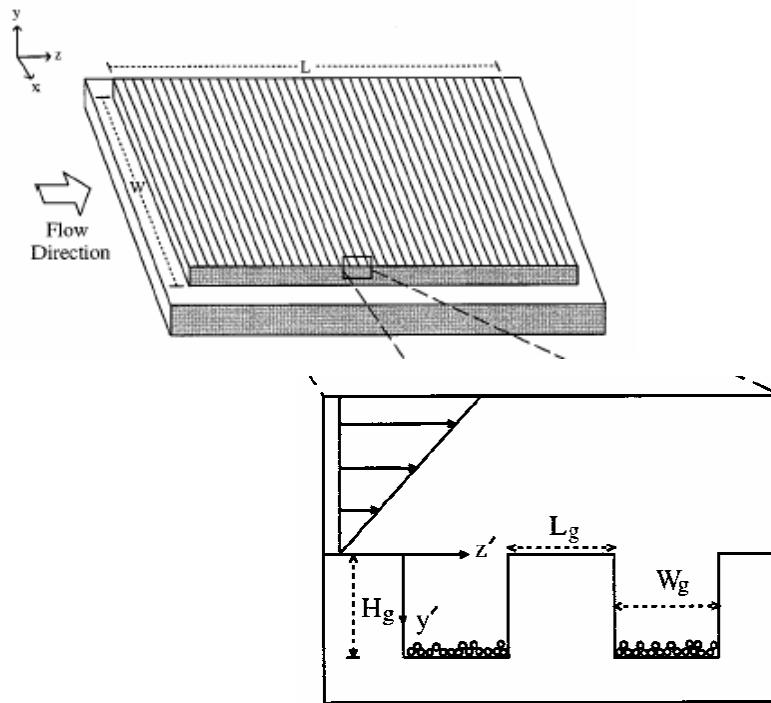


**Figure 2.5 Model of a flat bed perfusion bioreactor system with a series of grooves to retain cells in the presence of constant perfusion. This is a closed system with no headspace. Medium flows in the  $z$  direction across the chamber.  $y'$  and  $z'$  represent the local co-ordinate system in a cavity (Horner *et al.*, 1998)**

The model considers oxygen consumption and lactate production by HCs. The model assumptions include:

1. flow is steady state,
2. mass transfer of model solutes (oxygen and lactate) are given by a pseudo-steady approach,
3. average cell doubling time ( $\sim 1$ day) is long compared to the time required for establishment of steady state of model solutes.

The Navier-Stokes equation and species continuity equation are used to describe the flow in the perfusion chamber and the molar balance for each solute, respectively. The solute balance is coupled to the flow balance (hydrodynamics) in the dilute solution limit.

$$\rho \left( \frac{\partial u}{\partial t} + u \cdot \nabla u \right) = -\nabla P + \mu \nabla^2 u$$

reduced to,

$$\rho \left( v_y \frac{\partial v_y}{\partial y} + v_z \frac{\partial v_y}{\partial z} \right) = -\frac{\partial P}{\partial y} + \mu \cdot \left( \frac{\partial^2 v_y}{\partial y^2} + \frac{\partial^2 v_y}{\partial z^2} \right)$$

$$\rho \left( v_y \frac{\partial v_z}{\partial y} + v_z \frac{\partial v_z}{\partial z} \right) = -\frac{\partial P}{\partial z} + \mu \cdot \left( \frac{\partial^2 v_z}{\partial y^2} + \frac{\partial^2 v_z}{\partial z^2} \right)$$

(2.13)

$$\frac{\partial C}{\partial t} - (D \cdot \nabla^2 C - u \cdot \nabla u) = 0$$

reduced to,

$$v_y \frac{\partial C_i}{\partial y} + v_z \frac{\partial C_i}{\partial z} = -D_{i,med} \left( \frac{\partial^2 C_i}{\partial y^2} + \frac{\partial^2 C_i}{\partial z^2} \right)$$

(2.14)

where  $i$  denotes solutes oxygen and lactate. Heterogeneous zero order reaction boundary conditions were applied at the bottom of each groove and the no slip conditions at the reactor walls and is given as,

$$-D \frac{\partial C}{\partial y} \Big|_{y' = -H_g} = r_{\max} = \frac{q_i \cdot N|_{time}}{(WL/2)}$$

$$-D \frac{\partial C}{\partial y} \Big|_{y' = +H_g} = 0 \quad (\text{no flux condition})$$

(2.15)

The magnitude of the effective reaction rate of solutes ( $i$ ) is obtained by multiplying the specific reaction rate of the solute ( $i$ ) to the total cell number and then dividing by the surface area for reaction. The time period of culture is divided into three phases early, middle and late, and the cell numbers for these phases are obtained from literature. Computational fluid dynamics (CFD) code (FIDAP) was used to solve these equations. The velocity field and solute concentration distribution in the grooved chamber is obtained.

The model showed that the hematopoietic cultures were neither oxygen-limited nor lactate-inhibited. High (20%) oxygen feed concentration for flow rates greater than 1.0 ml/min the late cultures with  $20 \times 10^6$  cells were not oxygen limited. However, for lower oxygen feed (5%) concentration, the culture may become oxygen limited during the late phase of the culture. The model study suggests that the perfusion rate may be started from 0.5 ml/min and increased up to 2.5 ml/min. This would decrease the amount of media needed to be recycled. During the early phase of the culture medium should be fed at 2.5 ml/min and in equilibrium with low (5%) oxygen feed concentration, favoring progenitor growth. Later in the culture the oxygen feed should be increased (20%) to promote progenitor cell differentiation. Similar observations were also made from calculations with the model developed and shown in Chapter 3 of this proposal. This model also did not show an increase in lactate concentration above the inhibitory level (<20mM). However, in culture the cell numbers may increase to levels greater than the fixed number of cells assumed in the model during the late phase of the culture and this in turn would increase the lactate concentration in the grooves above the inhibitory range, inhibiting further cell growth in the grooves.

This model has similar drawbacks as those discussed for the Palsson's perfusion bioreactor model. However, this model provides an approximation of averaged nutrient and product concentrations for a desired cell growth in a grooved perfusion bioreactor. The addition of grooves as shown in the model provides good cell retention for very high medium flows (20 ml/min). Thus, modification of bioreactor geometry can be used to effectively manipulate cell growth, by controlling the delivery of nutrients and removal of products. Future work needs to consider the improvements of this model because of its significance for HC growth.



#### **2.5.3.4 Population balance model**

The population balance method is a discrete modeling approach that incorporates the (pseudo-) stochastic and deterministic elements of the hematopoietic process. A number of models in the literature have used this modeling approach to incorporate the dynamic variation of the various cell types in hematopoietic cultures (Nielsen *et al.*, 1998; Silva *et al.*, 2003; Hevehan *et al.*, 2000; Abkowitz *et al.*, 2000; Peng *et al.*, 1996, Williams *et al.*, 2002). The model developed by Nielsen *et al.*, 1998 using similarity of the hematopoietic system to chemical engineering reactors is explained as a basic study for a clear understanding of this approach.

Hematopoiesis is described using chemical engineering metaphors of tanks and tubular reactors. This kinetic model describes five processes: (1) differentiation (2) growth (3) death (4) phase transition from cycling to quiescent phase (5) phase transition from quiescent cells to cycling cells. Modeling these processes of cell expansion and differentiation from the early stem cells to mature blood cells is complex as the molecular and regulatory mechanisms governing these processes are still largely unknown.

#### **Differentiation process**

Two types of patterns can macroscopically describe the cell differentiation process: discrete and continuum patterns. Stem cells exist in discrete states in which they grow without losing their stem cell potential. They lose this state through an apparently stochastic and discrete process of commitment. The apparent stochastic nature of stem cells may be due to a set of complex deterministic mechanisms and hence the process is termed as pseudo-stochastic. In contrast to stem cells the lineage committed cells follow a continuous, deterministic differentiation pattern. In between the two, the specialization process can be considered as discrete or continuum.

These two types of differentiation are modeled using the similarities of the process to tank and tubular reactors. Discrete differentiation of stem cells has the features of a tank reactor; the elements do not have any history. The probability of a particular cell/molecule leaving the compartment/tank is independent of how long it has been therein. The commitment /exit of the cell/molecule is governed by a stochastic process. Similarly the continuum differentiation

process of lineage committed cells shares the features of a tubular reactor: the elements have a history. The ‘axial dimension of a tubular reactor’ is in ‘a cell compartment’ the measure of the extent of differentiation and the ‘flow rate’ is equivalent to the ‘rate of differentiation’. The reactions in these reacting compartments are those of cell growth (auto catalytic), cell death (degradation) and phase transition. The three distinct stages of differentiation include: stem cell commitment, specialization and expansion and maturation discussed in detail below.

### ***Stage 1: Stem cell commitment***

It is not exactly clear as to how the body balances the stem cell self-renewal versus commitment which leads to differentiation to maintain homeostasis in the body. Mathematically, this process can be explained by a multi-component discrete model using the self-renewal probability ( $p$ ), i.e., the probability that a newborn daughter cell will remain as a stem cell. The two-phases or populations are defined as active ( $S$ ) and quiescent ( $S_o$ ), the cycle time as  $T_s$ , exit rate as the specific rate of commitment  $\lambda$ , the two reaction rates as – the specific growth rate,  $\mu$ , and the specific death rate,  $\delta$ , and the two transition rates as the specific rate of quiescent-to-active transition,  $\alpha$ , and the specific rate of active-to-quiescent transition,  $\beta$ .

$$\frac{dS}{dt} = p \cdot \frac{S}{T_s} - (1-p) \cdot \frac{S}{T_s} = (2p-1) \frac{S}{T_s}$$

$$\frac{dS}{dt} = \alpha \cdot S_o + (\mu - \delta - \lambda - \beta) \cdot S$$

$$\frac{dS_o}{dt} = \beta \cdot S - \alpha \cdot S_o$$

(2.16)

The growth rate ( $\mu$ ) and the commitment rate ( $\lambda$ ) are independent parameters as the model is discrete. The model does not account for any spatial variation or dependence on environmental factors.

### ***Stage 2: Specialization***

There is no well-established mechanism of specialization and hence it is difficult to propose a model for the specialization process. The model specialization process has a temporal extension,

which causes cell number expansion, distributes the cells among the different branches of hematopoiesis, and allows for quiescence. There are three possible models that can be used to describe this process as shown in Figure 2.6.

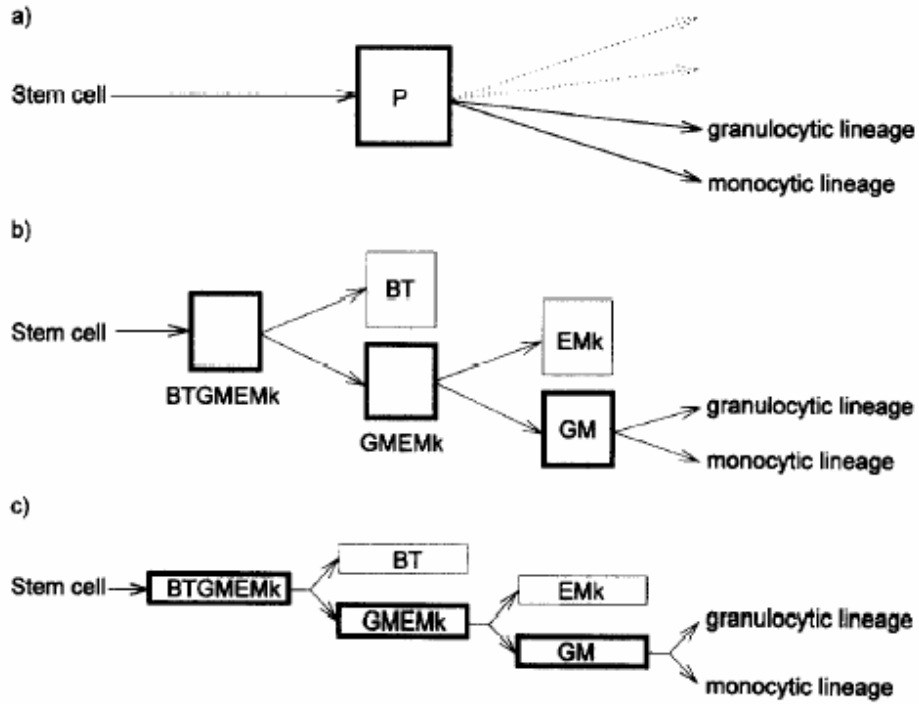


Figure 2. 6 Three models of specialization (Nielsen *et al.*, 1998)

The simplest model is a single tank reactor (Figure 2.6 a) with outlets to all branches of hematopoiesis. Let  $P$  and  $P_o$  be the numbers of pluripotent progenitors in the cycle and in quiescence, respectively, then population balance yields,

$$\frac{dP}{dt} = \lambda \cdot S + \alpha \cdot P_o + (\mu - \delta - \beta - \sum \lambda_i) \cdot P$$

$$\frac{dP_o}{dt} = \beta \cdot P - \alpha \cdot P_o$$

(2.17)

where  $\lambda_i$ 's represent the rate of commitment into different branches in the tree.

The second model (Figure 2.6 b) is a little more extensive and considers several tanks in series and parallel. The myeloid branch of hematopoiesis, for example, could be described with separate tanks for pluripotent cells, erythroid-megakaryocytic bipotent, and granulocytic-monocytic bipotent cells.

The third model (Figure 2.6 c) describing the specialization process is still more extensive. The lineage commitment can occur through a series of asymmetric divisions; the committed stem cell divides into a lymphoid and myeloid progenitor, and then each of these progenitors subdivides into different distinct lineages. This fully deterministic model is best described by a series of tubular reactors with each reactor representing a single division cycle. In this case the doubling of cell number will occur at one upstream and two downstream reactors. For example as cells leave the granulocytic-monocytic (GM) reactor cell division causes the flux to double so that the flux into either the granulocytic (G) or monocytic (M) pipe equals the flux leaving the GM reactor.

### ***Stage 3: Expansion and maturation***

Following the stage of specialization/lineage commitment, expansion of cells occurs through a number of cell divisions. This process almost goes hand in hand with the differentiation process (at least during the later stages of differentiation, when cells are in the mature stage). The kinetic model for the process is written as,

$$\frac{\partial n}{\partial t} = -\frac{\partial(v \cdot n)}{\partial \tau} + \alpha \cdot n_o + (\mu - \delta - \beta) \cdot n \quad (2.18)$$

where  $n(t, \tau)$  is the distributed density population at time  $t$  and at a differentiation stage  $\tau$  ( $\tau = 0$  corresponds to the specific lineage cell entering the expansion and maturation phase and  $\tau = 1$  corresponds to the mature cells that join the blood stream) and  $v(t, \tau)$  represents the rate of cell differentiation. The number of cells in the quiescent stage are given as  $n_o(t, \tau)$ . The cycling between the quiescent and active cell populations is given as

$$\frac{\partial n_o}{\partial t} = \beta \cdot n - \alpha \cdot n_o \tag{2.19}$$

The kinetic model equations 2.16-219 are simultaneously solved to obtain the cell numbers of different cell types at different stages of differentiation. However to be noted here, the model is discrete, not continuous, hence it does not account for the continuous process of cell growth, differentiation, expansion, maturation, and cell death. Moreover, the model does not incorporate the effects of the cell growth environment, which typically plays a major role in the process of hematopoiesis. These models have been applied for erythropoietic and granulopoietic processes. For example, in the erythropoietic process the model can predict the total cell number along the differentiation lineage and the total number of mature blood cells (RBCs). Using these data it has been determined that TGF- $\beta$ 1 (differentiation promoting cytokine) accelerated differentiation throughout the pathway rather than at a particular stage in the pathway.

## 2.6 Introduction to method of volume averaging

The method of volume averaging first developed by Whitaker (1967) is a technique used to analyze transport and reaction in multiphase systems. Species continuity equations (mass balances) describing transport and reaction of every species in particular phases in multiphase systems can be spatially smoothed to obtain equations that are valid everywhere. Thus, in other words, the volume averaging approach allows for a single reacting species for example in a two-phase system, to be represented by a single averaged continuity equation. These equations are called volume averaged equations (Whitaker, 1999). This method is explained by means of an example below.

Oxygen transport in respiring tissue can be studied using the method of volume averaging. Figure 2.7 illustrates the system of analysis. The first step is to select an averaging volume ‘ $V$ ’ as shown in Figure 2.7. The averaging volume is large in comparison to the cell volume, however, much smaller than the total system volume. This volume is representative of the whole

system. The system under consideration is made up of two distinct phases, the cell phase ( $\gamma$ ) and the fluid phase ( $\beta$ ). The volume of the cell phase ( $V_\gamma$ ) and fluid phase ( $V_\beta$ ) change with time (increase in cell number) however, the total averaging volume ( $V$ ) remains the same (Galban, 1999).

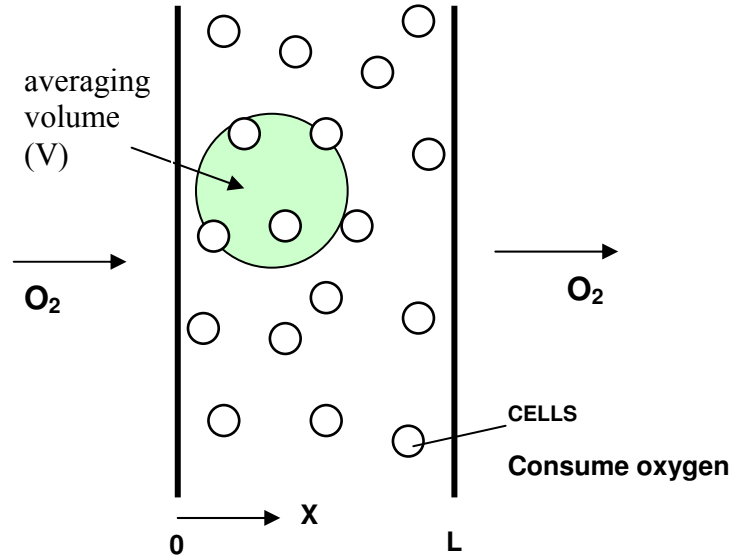


**Figure 2. 7 Graphical representation of heterogeneous tissue slice (method of volume averaging)**

The cells in the averaging volume ( $V$ ) consume oxygen as well as grow. Consumption occurs only in the cell phase. Species continuity equations describing the transport-reaction of oxygen by cells in the cell phase and transport in the fluid phase of the averaging volume are written. These describe the local point oxygen concentrations in the averaging volume cell phase ( $C_\gamma$ ) and fluid phase ( $C_\beta$ ). A similar material balance for cell growth in the cell phase is also written. The equations are averaged in the volume  $V$ . A single averaged species continuity equation for the oxygen concentration in the two phase system is obtained using the principle of local mass equilibrium described below. The equilibrium weighted concentration is written as,

$$\{C\} \equiv \frac{1}{V} \int_V C \cdot dV = \frac{1}{K_{eq}} \cdot \varepsilon_\gamma \cdot \langle C_\gamma \rangle^\gamma + \varepsilon_\beta \cdot \langle C_\beta \rangle^\beta \quad (2.20)$$

along with the macroscopic spatial deviation concentrations given by,

$$\begin{aligned} \hat{C}_\gamma &= \langle C_\gamma \rangle^\gamma - K_{eq} \cdot \{C\} \\ \hat{C}_\beta &= \langle C_\beta \rangle^\beta - \{C\} \end{aligned} \quad (2.21)$$

and the local spatial deviation in concentration is given by Gray's decomposition

$$\begin{aligned} \tilde{C}_\gamma &= C_\gamma - \langle C_\gamma \rangle^\gamma \\ \tilde{C}_\beta &= C_\beta - \langle C_\beta \rangle^\beta \end{aligned} \quad (2.22)$$

where  $\varepsilon_i$  is the  $i^{\text{th}}$  volume fraction ( $V_i/V$ ),  $\langle C_i \rangle^i$  is the intrinsic phase average concentration and  $K_{eq}$  is the equilibrium coefficient. Equation 2.22 is based on the fact that the macroscopic spatial deviations in concentration in  $\beta$  and  $\gamma$  phase given as  $\hat{C}_i$  is zero when the system is in equilibrium. The averaged species continuity equations in both the phases are now reduced to a single equation expressed in terms of both the volume averaged concentration and the local and macroscopic spatial deviation concentrations. Similar equations are also used in the derivation of the cell growth equations.

The final step in this approach is to obtain a differential equation for the local spatial deviations  $\tilde{C}_\beta$  and  $\tilde{C}_\gamma$ . This is called the 'closure problem'. Thus, this closure problem would provide a

solution for the local spatial deviation concentration in terms of geometry of the averaged system. Thus, an effective diffusion coefficient and an effective rate coefficient are derived which are functions of cell volume fraction. The macroscopic spatial deviation concentration can be assumed to be very small in comparison to the local spatial deviation concentration. These equations coupled to the single averaged species continuity equation would give the species (oxygen/cells) variation in the entire volume (Ochoa, 1986; Galban, 1999; Whitaker, 1999).

In this study we have used this established approach for the analysis of transport process in multiphase systems. Details of the implications are discussed for the various systems in Chapters 3, 4, 5, 6 and 7.



## CHAPTER 3

### **ROLE OF NUTRIENT SUPPLY AND PRODUCT FORMATION ON CELL GROWTH IN BIOREACTOR DESIGN FOR TISSUE ENGINEERING OF HEMATOPOIETIC CELLS**

#### **Analysis of oxygen supply on granulocyte progenitor cell growth in 3-dimensional perfusion bioreactor**

*(Pathi et al., 2005 a; Reproduced with permission from John Wiley & Sons, Inc.)*

#### **3.1 Problem Statement**

In the present study, a dynamic mathematical model of the growth of granulocyte progenitors in the hematopoietic process is developed based on the principles of diffusion and chemical reaction. This model simulates granulocyte progenitor cell growth and oxygen consumption in a three-dimensional (3-D) perfusion bioreactor system. Molar balances describing oxygen consumption and cell growth are developed using the volume averaging approach (Whitaker, 1999). Spatial variations of oxygen concentration and granulocyte progenitor cell density are obtained in the bioreactor in order to assess the roles of convection and diffusion on oxygen supply and cell growth. The model provides quantitative estimates of the oxygen consumption for growth and for metabolism, and information on oxygen consumption and cell growth are further used to estimate the roles of key bioreactor design parameters, including flow rates and liquid depth, and to optimize the reactor performance.

## **3.2 Model Formulation**

### **3.2.1 Reactor Design**

Analysis of granulocyte progenitor cell proliferation is conducted for a 3-dimensional perfusion bioreactor system developed in Dr Teng Ma's lab at Florida State University. The bioreactor is a rectangular block with 10 cm length, 2.5 cm width, and 13.2 mm thick. This bioreactor has a polyethylene terephthalate (PET) porous matrix (1.2 mm thick) sandwiched between two perfusion chambers made of polycarbonate (PC). A gas permeable FEP (fluorocarbon film) membrane is attached on the outer sides along the length of the perfusion chambers as shown in Figure 3.1. The bioreactor is placed in an incubator with a fixed oxygen supply. Cells grow in the matrix and form the cell layer of the bioreactor. Medium supplying nutrients to cells in the cell layer flows through the perfusion chambers above and below the cell layer (labeled bulk liquid layers). Oxygen diffuses into the reactor through the FEP membranes into the bulk liquid layers.

The modes of mass transport are convection, diffusion, and inter-phase mass transport across the gas permeable membranes. In the bulk liquid layer oxygen is subject to both convective and diffusive transport, whereas in the cell layer oxygen is carried only by diffusive transport. The absence of flow in the cell layer prevents flow restrictions on cell growth by, for example, shear forces. Furthermore, the absence of flow in this region promotes adhesion of the cells to the matrix surface. Oxygen can be supplied by convection through either a once through mode or by recirculation of the bulk liquid layer medium as well as through inter-phase mass transport across the FEP membrane from the incubator.

### **3.2.2 Mathematical model**

A mathematical model is developed for this reactor to quantitatively describe the oxygen concentration variations in space and time. The model describes the effect of oxygen supply on the growth of cells. This model is also used to assess various configurations for the design of the bioreactor by quantifying the relative contributions of the diffusive oxygen supply through the

FEP membrane and convective oxygen supply through flow in the reactor and hence can be used to determine the most important mode of supply.

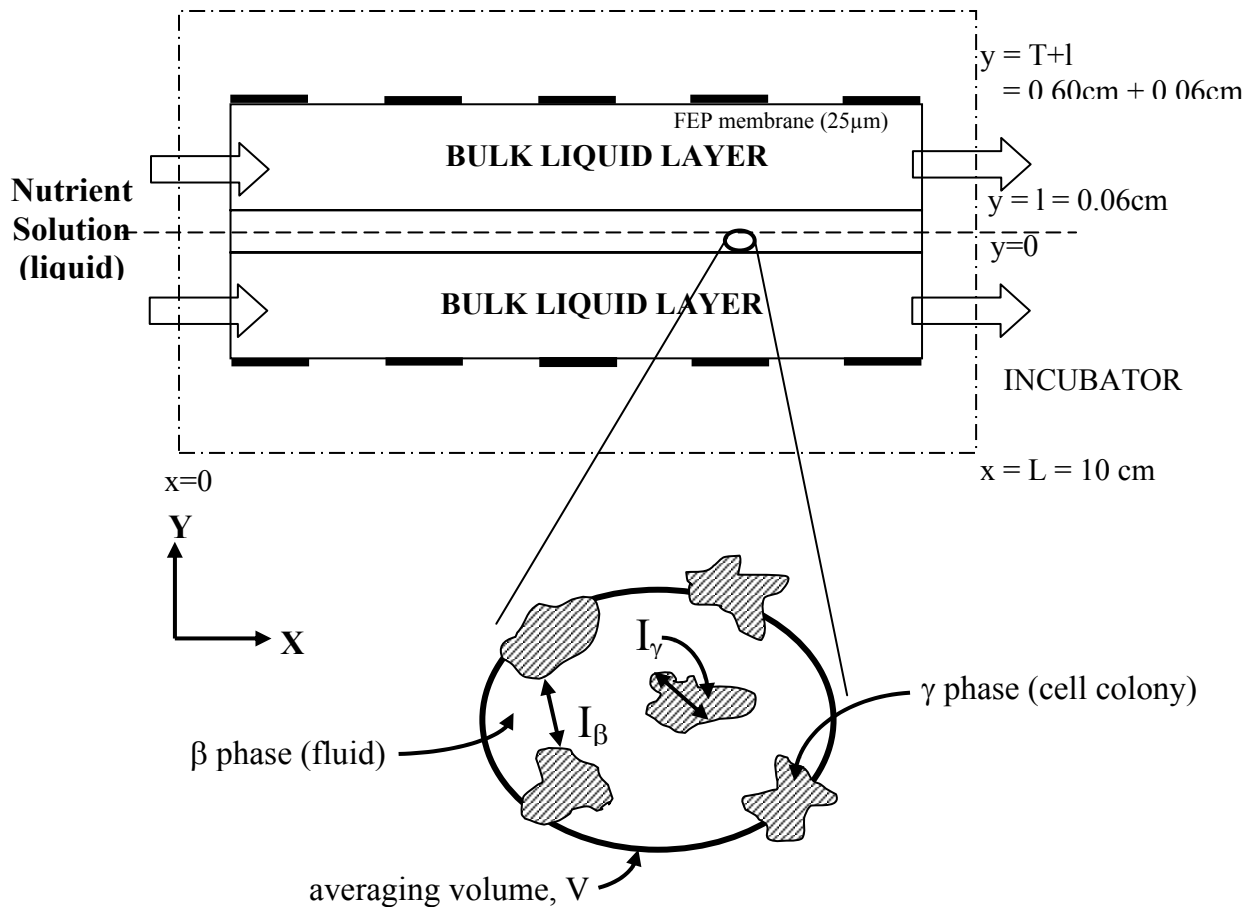


Figure 3. 1 Schematic of perfusion bioreactor model (Florida State University)

### 3.2.2.1 Model equations

For the development of the model one half of the reactor is considered because of symmetry. Species continuity equations describing the spatial and temporal variations of oxygen concentration and cell number are written for both the bulk liquid layer and the cell layer. The method of volume averaging is used to develop a single species continuity equation for the

multiphase cell layer made up of cells and medium solution (Wood *et al.*, 2000; Wood *et al.*, 2002; Whitaker, 1999; Galban and Locke, 1999). Volume averaging allows representation of the local 3-dimensional structure in the porous matrix where the cells are growing. The primary factor in the present model affected by this 3-dimensional structure is the effective diffusion coefficient. It can be noted that the overall reactor model is solved in two dimensions since the width of the reactor is much larger than the depth and thus variations in the width are neglected.

### **Bulk liquid layer**

The bulk liquid consists of the nutrient medium solution containing dissolved oxygen. Transport of oxygen takes place by diffusion and convective flow in this layer. There are no cells in this layer, hence there are no reaction terms describing oxygen consumption. The molar species continuity equation describing the oxygen concentration variation in space and time is given as

$$\frac{\partial c}{\partial t} = (\nabla D_{\beta} \cdot \nabla c) - \underline{v} \cdot \nabla c \quad (3.1)$$

where  $c$  is the non-dimensionless oxygen concentration in the bulk liquid layer\*,  $D_{\beta}$  is the oxygen diffusion coefficient in the liquid,  $\underline{v}$  is the velocity vector of the fluid flow. The one-dimensional flow is oriented along the reactor length (x-direction) and is assumed to be laminar (Re=0.17). The velocity profile is thus

$$v_x = \frac{6 \cdot v_{avg}}{T^2} * \left[ (T + 2 \cdot l) y - (y \cdot y) - (l^2 + T \cdot l) \right] \quad (3.2)$$

where  $v_{avg}$  is the average velocity of medium flow in the perfusion chamber (bulk liquid layer),  $y$  is the direction perpendicular to the direction of flow,  $l$  is half the height of the matrix (cell layer) and  $T$  is the height of the liquid layer in the bioreactor.

---

\* The oxygen concentration terms are non-dimensionalized by dividing the oxygen concentration at any point in space and time with the dissolved oxygen concentration in equilibrium with air (20% oxygen).

### **Cell layer**

The cell layer is a two phase region made up of cells and the liquid nutrient medium. The cell phase is indicated as the  $\gamma$  phase and the nutrient or liquid phase is indicated as the  $\beta$  phase. As discussed above the method of volume averaging is used to formulate the material balances for this multi-phase transport problem. Equations valid in a particular phase are written and spatially smoothed to produce equations that are valid everywhere in the reactor (Whitaker, 1999).

In this method a small representative volume termed the averaging volume ( $V$ ) is selected. Figure 3.1 shows a schematic of the averaging volume. Cell growth is expressed in terms of the cell volume fraction ( $\varepsilon_\gamma$ ), i.e., the volume occupied by cells in the averaging volume,  $V_\gamma$ , relative to the total averaging volume  $V$  in the cell layer. The sum of the volume fractions of the cell phase and the fluid phase in the averaging volume is one.

$$1 = \varepsilon_\gamma + \varepsilon_\beta \tag{3.3}$$

Molar balances describing the oxygen concentration and cell growth in the cell phase and nutrient phase (in the averaging volume) are described below.

### ***Nutrient balance***

Oxygen is assumed to be the rate limiting nutrient since it plays an important role in granulocyte progenitor expansion and also because other much more soluble nutrients such as glucose are assumed to be present in excess. The molar species continuity equations for oxygen include diffusive transport and consumption in the cell layer and are written for the  $\beta$  (liquid) and  $\gamma$  (cell) phases as,

$$\frac{\partial C_\beta}{\partial t} = \nabla \cdot D_\beta \nabla C_\beta \quad \text{in } V_\beta \tag{3.4 a}$$

$$\frac{\partial C_\gamma}{\partial t} = \nabla \cdot D_\gamma \nabla C_\gamma - k_m - k_g \quad \text{in } V_\gamma \quad (3.4 \text{ b})$$

where  $C_\beta$  and  $C_\gamma$  are the oxygen concentrations in the fluid phase ( $\beta$ ) and cell phase ( $\gamma$ ), respectively;  $D_\beta$  and  $D_\gamma$  are the oxygen diffusivities in  $\beta$  and  $\gamma$  phases, respectively;  $k_m$  and  $k_g$  are the oxygen consumption rates by these cells for metabolism and for growth, respectively.

The cells consume oxygen both for metabolic requirements (Hevehan *et al.*, 2000) as well as for growth. The metabolic oxygen consumption by cells is suggested in previous literature (Collins *et al.*, 1998; Chow *et al.*, 2001) to be best described by a Michaelis-Menten kinetics,

$$k_m = \frac{Q_{mm} \cdot C_\gamma}{K_m + C_\gamma} \quad (3.5)$$

where  $Q_{mm}$  and  $K_m$  are the metabolic rate parameters. The parameters used in the present study were obtained from the literature and are listed in Appendix A. The growth rate is given by an inhibitory kinetic form, and the oxygen consumption for growth is written as,

$$k_g = \frac{1}{Y} \bullet \frac{kk \cdot C_\gamma}{K1 + \frac{C_\gamma}{K_I} + C_\gamma^2} \quad (3.6)$$

where  $Y$  is the yield coefficient given as the ratio of the mass of cells to the mass of oxygen consumed and  $kk$ ,  $K1$ ,  $K_I$  are the growth rate parameters. The reason for the use of this type of kinetic function is described in detail later in the text.

The material balances equations. 3.4 (a) and 3.4 (b) describe the variation of oxygen concentration in the cell phase and in the fluid phase of  $V$  and are generally applicable at any spatial position in the appropriate phase in  $V$ . In order to develop a locally averaged equation to describe the concentration fields in the cell layer of the reactor, these equations are averaged spatially to obtain volume-averaged equations. The principle of local mass equilibrium is used to obtain a single averaged species continuity equation for the oxygen concentration variation in  $V$  (Whitaker, 1999; Ochoa, 1988; Galban and Locke, 1999). Thus, using the kinetic expressions for oxygen consumption described in equations 3.5 and 3.6, the single averaged species continuity equation is written as,

$$\frac{\partial C}{\partial t} = \nabla D_{eff} \nabla C - \frac{Q_{mm} \cdot K_{eq} \cdot \varepsilon_{\gamma} \cdot C}{K_m + K_{eq} \cdot C} - \frac{1}{Y} \cdot \frac{kk \cdot C \cdot \varepsilon_{\gamma}}{K_1 + \frac{C}{K_I} + C^2} \quad (3.7)$$

where  $C$  is the volume-averaged dimensional oxygen concentration and  $D_{eff}$  is the effective diffusion coefficient.

The averaged equation 3.7 is obtained assuming the following length scale constraints in the averaging volume (Galban and Locke, 1999; Carbonell and Whitaker, 1984; Wood *et al.*, 1994; Wood *et al.*, 2002),

$$\frac{l_{\gamma}}{R} \gg \frac{R}{l} \quad or \quad \frac{l_{\beta}}{R} \gg \frac{R}{l} \quad (3.8)$$

where  $l_{\beta}$  and  $l_{\gamma}$  are the distances across the respective phase (fluid and cell respectively) within averaging volume ( $V$ ),  $R$  is the radius of averaging volume, and  $l$  is the height of the bioreactor cell layer or the matrix. At least one of these constraints must be valid for changes in cell volume fraction over time. The initial length scale for the cell phase ( $l_{\gamma}$ ) is nearly 10  $\mu\text{m}$  while the initial length scale for the liquid phase is approximately 50  $\mu\text{m}$ . As the cell density increases

the magnitude of  $l_\beta$  decreases and  $l_\gamma$  increases. The ratio  $R/l$  is constant and approximately 0.083, where  $R$  is 50  $\mu\text{m}$  and  $l$  is 0.06 cm. Although  $l_\beta$  and  $l_\gamma$  may vary with time the condition in equation 3.8 will typically hold since the size of the reactor is much larger than the averaging volume. The averaging volume ( $V$ ) remains constant keeping  $R$  much less than  $l$ , but the volumes of cell and liquid phase in the volume  $V$  changes with time. This is expressed as,

$$V = V_\beta(t) + V_\gamma(t) \quad (3.9)$$

where the volume of the cell phase ( $V_\gamma$ ) and volume of the liquid phase ( $V_\beta$ ) are functions of time while the total averaging volume is not (Galban and Locke, 1999).

The effective diffusion coefficient and effective rate coefficient for oxygen consumption for metabolism and growth are determined as functions of the cell volume fraction and oxygen concentrations. In principle, the effective diffusion coefficient can be determined as a function of the volume fraction from solution of a closure problem posed over a well defined unit cell (Whitaker, 1999). For complex unit cell geometry numerical solutions are required, however a number of analytical solutions are available for isotropic media with simple geometry (see Locke, 2001 for review). In the present study an analytical expression for the effective diffusion coefficient of an isotropic two dimensional two phase medium defined by a square unit cell (Ochoa, 1988) containing circular particles is used. Although this relationship is derived for two dimensional media, the effective transport coefficients for 2-dimensional media are very similar to those for 3-dimensional media for isotropic systems that do not exhibit percolation limits (Trinh *et al*, 2000). This relationship accounts for the diffusion in the non-cellular (liquid)  $\beta$  phase and the cellular  $\gamma$  phase as well as the mass transport across the two phases. This effective diffusion coefficient is written as,

$$D_{eff} = \frac{D_\beta}{(\varepsilon_\gamma \cdot K_{eq} + \varepsilon_\beta)} * \left[ \frac{2k - (k-1)\varepsilon_\beta + \varepsilon_\beta \varepsilon_\gamma^{-1/2} \alpha}{2 + (k-1)\varepsilon_\beta + (2 - \varepsilon_\beta) \varepsilon_\gamma^{-1/2} \alpha} \right] \quad (3.10)$$



where  $k = (K_{eq} D_\gamma/D_\beta)$  is the ratio of the diffusion coefficient in the cell phase over that in the void phase (here the liquid phase) and  $\alpha = (D_\gamma/L P)$  is the ratio of the cell phase diffusion coefficient over the mass transfer coefficient at the cell-liquid inter-phase in the averaging volume.  $P$  represents the mass transfer coefficient at the cell membranes, i.e. at  $A_{\beta\gamma}$ , and  $K_{eq}$  is the equilibrium coefficient for oxygen between  $\beta$  and the  $\gamma$  phases of the averaging volume. For cellular transport of very permeable solutes such as oxygen it can be assumed that at local mass equilibrium the solute concentrations across the cell membrane are equal and hence the parameter  $K_{eq}$  is equal to one (Wood *et al.*, 2000). The effective diffusion coefficient can also be described in other ways, e.g., Chang's unit-cell solution, Maxwell's solution, or other functions depending upon the geometry of the system considered (Galban and Locke, 1999; Wood *et al.*, 2000; Wood *et al.*, 2002). Calculations with the present model (not presented here) showed that the model results are not highly sensitive to the functional form of the diffusion coefficient since diffusive restrictions of oxygen in the cellular region are not very large. For analysis of larger solutes that would have larger restrictions to diffusion in the cellular phase further consideration of the local 3-dimensional geometry and solution of the closure problem in such systems is needed.

The volume averaged oxygen species continuity equation 3.7 is non-dimensionalized,

$$\frac{\partial c}{\partial t} = \nabla D_{eff} \nabla c - \frac{Q_m \cdot K_{eq} \cdot \varepsilon_\gamma \cdot c}{(K_m / C_o) + K_{eq} \cdot c} - \frac{1}{Y} \bullet \frac{p \cdot c \cdot \varepsilon_\gamma}{q + r \cdot c + c^2} \quad (3.11)$$

where the non-dimensional oxygen concentration,  $c = C/C_o$ ,  $C_o$  is the dissolved oxygen concentration in equilibrium with the saturated oxygen concentration in air (20%) and  $p$  ( $=kk/C_o$ ),  $q$  ( $=Kl/C_o^2$ ) and  $r$  ( $=1/(Kl \cdot C_o)$ ) are the non-dimensional growth parameters. The oxygen consumption rates by metabolism and growth, i.e., the second and third terms on the right hand side in the above expression, are denoted as *mm* and *growth\_o*, respectively.

### Cell balance

The conservation of cell mass is given by,

$$\frac{\partial m(t)}{\partial t} = \frac{\partial}{\partial t} \int_{V_\gamma(t)} \rho_\gamma dV = \int_{V_\gamma(t)} R_\gamma dV \quad (3.12)$$

where  $m(t)$  is the cell mass,  $\rho_\gamma$  is the specific cell density,  $V_\gamma$  the volume occupied by the cells and  $R_\gamma$  is the rate of cell growth. The above equation is based on the assumptions that the cell phase is made up of only cells (i.e., the granulocyte progenitors), that the diffusivity of cells in the cell phase is negligible, and that the specific cell density in the cell phase is uniform.

The integral in the above equation is evaluated over an arbitrary volume  $V_\gamma$  within the averaging volume  $V$  to give

$$\frac{d\varepsilon_\gamma}{dt} = \frac{1}{\rho_\gamma V} \int_{V_\gamma} R_\gamma dV^* \quad (3.13)$$

It has been reported in the literature that very low oxygen concentration retards the growth of these cells and very high concentration may be inhibitory or even toxic (Hevehan *et al.*, 2000). An oxygen concentration of 5% in the gaseous phase equilibrated with the medium is optimal for progenitor cell growth (Hevehan *et al.*, 2000). Hence substrate inhibition kinetics can be used to describe the growth kinetics of these cells and this is represented by

$$R_\gamma = \frac{kk \cdot C_\gamma}{K1 + \frac{C_\gamma}{K_I} + C_\gamma^2} \quad (3.14)$$

---

\* Mass transport of cells (by diffusion) is not included in the model, however it can be noted that future work may consider the effects of cell migration by diffusion or chemotaxis.

where  $k_k$ ,  $K_I$  and  $K_I$  are the kinetic parameters. The values for these parameters were determined using the experimental results of Hevehan *et al.* (2000). Oxygen consumption for cell growth in equation 3.11 was obtained by multiplying a suitable yield coefficient to the above expression. The cell material balance can be rewritten by substituting equation 3.14 in equation 3.13, and further integrating and non-dimensionalizing to give,

$$\frac{\partial \varepsilon_\gamma}{\partial t} = \frac{p \cdot c \cdot \varepsilon_\gamma}{q + r \cdot c + c \cdot c} \quad (3.15)$$

where  $c$  is the dimensionless oxygen concentration,  $p$ ,  $q$ , and  $r$  are the non-dimensional rate parameters. The growth rate on the right hand side of equation 3.15 is denoted as *growth*. The growth function is first order with respect to the cell volume fraction and the parameters are determined to give maximal cell growth in regions where the oxygen concentration is the liquid phase concentration that is in equilibrium with a 5% gas phase concentration.

### ***Boundary conditions***

Oxygen flux at the upper boundary of the bulk liquid layer with the membrane is represented by the rate of mass transfer of oxygen from the incubator (saturated with oxygen in equilibrium with concentration  $c_o$ ) through the FEP membrane (with permeability,  $Perm$ ) into the bulk liquid. This boundary condition is written as,

$$-D_\beta \frac{\partial c}{\partial y} = Perm \cdot (c_o - c) \quad \forall x = [0, L] \quad y = l + T \quad (3.16 a)$$

The Danckwerts boundary conditions, extensively applied to convection-diffusion problems in chemical reactors, includes a flux balance at the inlet of the reactor coupled with a zero diffusive gradient condition at the end of the reactor (Danckwerts, 1953). These conditions are given by

$$v \cdot c_{in} = v \cdot c - D_{\beta} \frac{\partial c}{\partial x} \quad \forall y = [l, l+T] \quad x = 0 \quad (3.16 \text{ b})$$

$$D_{\beta} \frac{\partial c}{\partial x} = 0 \quad \forall y = [l, l+T] \quad x = L \quad (3.16 \text{ c})$$

where  $c_{in}$  is the dissolved oxygen concentration being delivered by flow at the inlet. The oxygen concentration  $c_{in}$  is equal to 20 % gas phase oxygen in equilibrium with the liquid phase.

The equal flux condition exists at the interface of the cell layer and the liquid layer, and it is given as,

$$-D_{\beta} \nabla c \Big|_{\text{liquidlayer}} = -D_{eff} \nabla c \Big|_{\text{celllayer}} \quad (3.16 \text{ d})$$

It is assumed that there is no flux of oxygen along the external boundaries of the cell layer with the solid walls of the reactor. Hence,

$$\nabla D_{eff} c = 0 \quad \forall y = [0, l] \quad x = 0 \quad (3.16 \text{ e})$$

$$\nabla D_{eff} c = 0 \quad \forall y = [0, l] \quad x = L \quad (3.16 \text{ f})$$

$$\nabla D_{eff} c = 0 \quad \forall x = [0, L] \quad y = 0 \quad (3.16 \text{ g})$$

### 3.2.2.2 Solution procedure

The equations describing variations in oxygen concentration in the fluid layer (equation 2.1) and in the cell region (equation 2.11) and the cell volume fraction in the cell region (equation 2.15) in space and time are solved simultaneously coupled with the appropriate boundary conditions. A MATLAB (version 6.5, The Mathworks, Inc.) based FEMLAB (version 2.3, COMSOL) program utilizing a finite element method was used to numerically solve the system of partial differential equations. The model is run from the initial state until the time point where the oxygen concentration is depleted to zero at any position in the reactor. Since the model does not account for inhibitory factors on cell growth such as natural cell death, the cell growth can also increase without bound. Thus, an additional limit is when the cell volume fraction approaches 1.0.

### 3.2.2.3 Macroscopic area averaging

The locally averaged oxygen concentrations and cell volume fractions obtained using the FEMLAB software can be further averaged over the entire domains, i.e., the cell layer and the liquid layer, and these averages are referred to as macroscopic averages. One reason to compute these averages is to condense a large amount of model output, in terms of time and 2-dimensional spatial variations, into output containing only time variation. Thus, macroscopic area averaging is performed to obtain the area averaged oxygen concentration  $\langle c \rangle$ , cell volume fraction  $\langle \varepsilon_v \rangle$ , oxygen consumption rates ( $\langle mm \rangle$ ,  $\langle growth\_o \rangle$ ) and growth rate ( $\langle growth \rangle$ ) in the bulk liquid layer and cell layer separately. For example the area averaged oxygen concentration is obtained as,

$$\langle c \rangle = \frac{\iint c \cdot dx \cdot dy}{\iint_A dx \cdot dy} \quad (3.17)$$

The variation of the oxygen concentration and granulocyte progenitor cell volume fraction from their macroscopic average values at various points in the cell layer of the bioreactor are computed as,

$$c\_std = \left( \sum_{all\ points} [c_i - \langle c \rangle]^2 \right)^{\frac{1}{2}} \quad (3.18)$$

where  $c_i$  is the non-dimensional oxygen concentration at a location  $i$  in the cell layer of the reactor and  $\langle c \rangle$  is the macroscopically averaged oxygen concentration.

#### 3.2.2.4 Fixed Oxygen Concentration Model

In order to assess the results from the finite element solution and to obtain a putative maximum cell growth rate, a simplified model neglecting all transport limitations can be considered. Since maximum cell growth occurs in a well mixed reactor when the oxygen concentration is at a value in equilibrium with 5% oxygen in the gas phase, the cell material balance can be solved with constant oxygen concentration,  $c_{5\%}$ ,

$$\frac{d\varepsilon_\gamma}{dt} = \frac{p \cdot c_{5\%} \cdot \varepsilon_\gamma}{q + r \cdot c_{5\%} + c_{5\%}^2} \quad (3.19 a)$$

The solution of this expression is denoted as  $\varepsilon_{max}$  and is a simple exponential function given by,

$$\varepsilon_{max} = \varepsilon_o \cdot e^{\frac{p \cdot c_{5\%}}{q + r \cdot c_{5\%} + c_{5\%}^2} \cdot t} \quad (3.19 b)$$

### 3.2.2.5 Well-Mixed bioreactor model

Another limit to the full spatial distribution model can be formed by assuming that the cell layer and the fluid domain as well mixed compartments. This limit removes the spatial variation of the oxygen concentrations in the cell and bulk liquid layers and the cell volume fraction in the cell layer of the bioreactor while retaining the effects of nutrient mass transfer supply. Oxygen is delivered to the reactor both by mass transfer through the membrane and by hydrodynamic flow at the entrances and exits of the bulk liquid layer of the bioreactor. Hence, the molar balances describing variation of the oxygen concentration in the cell layer (1) and bulk liquid layer (2) and cell volume fraction are written as,

$$\begin{aligned}
 V_1 \frac{dc_1}{dt} &= Fc_{in} - Fc_1 + k_{m1}A(c_o - c_1) - k_{m2}A(c_1 - c_2) && \text{bulk liquid layer} \\
 V_2 \frac{dc_2}{dt} &= -V_2 \cdot \frac{Q_m \cdot K_{eq} \cdot c_2 \cdot \varepsilon_\gamma}{K_m/c_o + \varepsilon_\gamma \cdot c_2} - V_2 \cdot \frac{1}{Y} \cdot \frac{p \cdot c_2 \cdot \varepsilon_\gamma}{q + r \cdot c_2 + c_2^2} + Ak_{m2}(c_1 - c_2) && \text{cell layer} \\
 \frac{d\varepsilon_\gamma}{dt} &= \frac{p \cdot c_2 \cdot \varepsilon_\gamma}{q + r \cdot c_2 + c_2^2} && \text{cell layer}
 \end{aligned}
 \tag{3.20}$$

where  $V_1$  and  $V_2$  are the volumes of the cell and bulk liquid layers, respectively,  $F$  is the medium flow rate,  $A$  is the area for mass transfer between the two layers,  $c_{in}$  and  $c_o$  are the inlet dissolved oxygen concentration through flow and through the FEP membrane in saturation with gas phase oxygen concentration, respectively, and  $k_{m1}$  and  $k_{m2}$  are the mass transfer coefficients for transport across the membrane to the bulk liquid layer and across the bulk liquid layer to the cell layer, respectively. The rate of mass transfer across the membrane is determined by the membrane permeability. Mass transfer in the presence of convective flow in the bulk liquid layer,  $k_{m2}$  is dominated by the flow field and for laminar flow is written as (Middleman, 1998),

$$k_{m2} = 1.165 \cdot D_\beta^{2/3} \cdot \left( \frac{\langle v \rangle}{L \cdot T} \right)^{1/3}
 \tag{3.21}$$

In principle, these equations can be obtained by averaging the material balances in equations 3.1, 3.11, 3.15 and 3.16 that includes the spatial variation terms.

### 3.3 Results and Discussion

The spatial variation of the dimensionless oxygen concentration at approximately 15 days in the reactor is shown in Figure 3.2. The dimensionless oxygen concentration represents the fractional liquid-phase oxygen saturation as mentioned earlier. The color represents the variation in oxygen concentration in space, i.e., along the reactor length (varying from 0 cm to 10 cm) and the reactor thickness (varying from 0 cm to 0.66 cm). The oxygen concentration of the inlet flowing liquid and the oxygen concentration in the incubator are set to values in equilibrium with 20% gas phase oxygen (which corresponds to the non-dimensional value 1). The residence time for flow is 1 hr, and the flow rate is computed as the ratio of the volume of the liquid layer and the residence time of flow. The gradients in oxygen concentration seen in the bulk liquid layer arise from mass transfer and flow coupled to reaction, i.e., consumption by cells in the cell layer, that consume oxygen at a rate faster than it can be supplied. The oxygen concentration in the cell layer is severely depleted by this time because of consumption by the cells (see also discussion of Figure 3.4(a) below).

As discussed previously, the granulocyte progenitors in the cell layer consume oxygen for their growth and metabolic needs. The consumption rates are functions of the oxygen concentration and the amount of cells present at any time in space as shown in equation 3.11. In order to obtain the total oxygen consumption rate for growth and the oxygen consumption rate for metabolism in the cell layer at any time the rates are macroscopically averaged in the cell layer (as given by equation 3.17) and are denoted as  $\langle growth\_o \rangle$  and  $\langle mm \rangle$ , respectively. The variations in the macroscopically area-averaged consumption rates with time are shown in Figure 3.3. It can be seen that the oxygen consumption rates increase with time over a large time span because of the formation of cells. However, when the oxygen concentration reaches very low values where there is little available oxygen for consumption, the metabolic consumption rate levels off. If the model is run for longer time, as the oxygen concentrations deplete to zero the



rate of metabolism will also decrease to zero. The figure also shows that the metabolic oxygen consumption rate is nearly three orders of magnitude higher than the rate of oxygen consumption for cell growth. This result is consistent with the fact that an individual cell spends much more time in metabolism than in growth.

The variation of cell volume fraction in space (along with the corresponding expanded view of the oxygen concentration in the cell layer) at approximately 15 days in the reactor is shown in Figure 3.4 (for all the same parameters as in Figures 3.2 and 3.3). The maximum cell volume fraction reached is around 0.63 (Figure 3.4(b)) and this corresponds to a cell density of  $2.25 \cdot 10^8$  cells/ml ( $cell\ density = \frac{\epsilon_v}{V_g}$ ). The figure shows that the concentration of progenitor cells is

higher in the region closer to the center of the matrix and nearer to the source of convective supply. This peak value in cell density is a result of the time course of the process whereby cells seeded in the deep interior do not obtain enough oxygen for high growth rates while cells on the periphery are exposed to more inhibitory oxygen levels. The oxygen concentration in the cell layer at this time is almost completely depleted as seen in Figure 3.4(a). This result partially resembles the *in vivo* state where the progenitors are found in the niches (with a relatively lower oxygen concentration around 5%) farther away from the sinus (higher value of oxygen concentration around 10%) and is essentially due to the inhibitory nature of the kinetics describing cell growth.

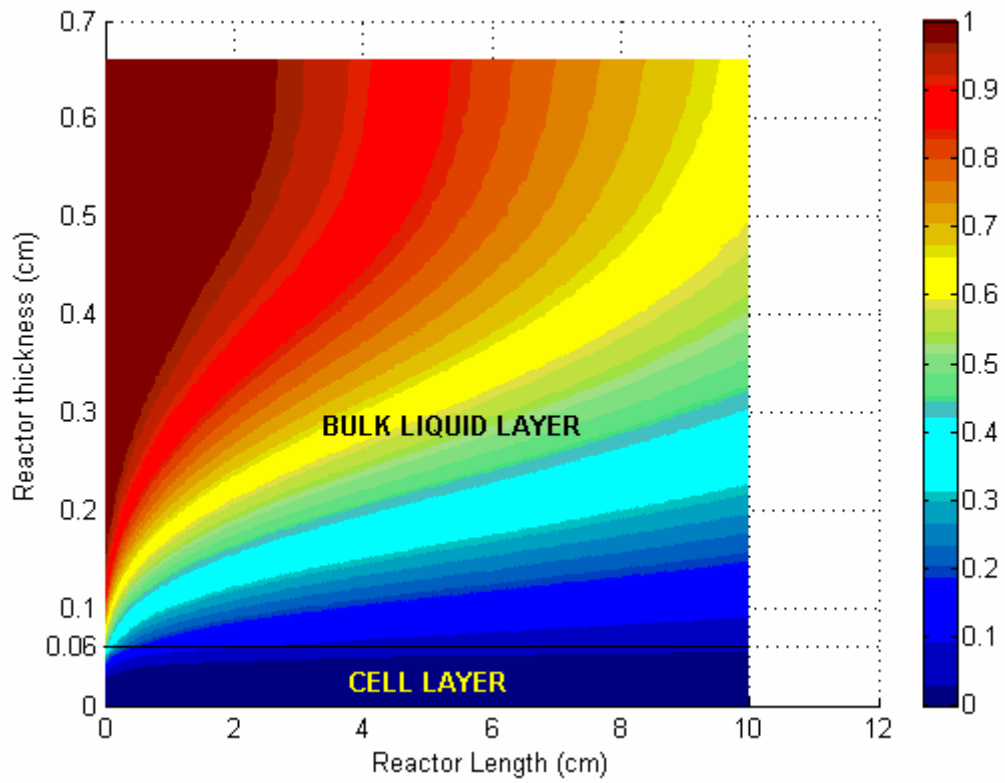


Figure 3. 2 Non-dimensional oxygen concentration (in color) varying in space at nearly 15 days ( $13 \cdot 10^5$  s) in the perfusion bioreactor. Parameters:  $T=0.6$  cm;  $l=0.06$ cm;  $res\_time = 1$ hr;  $F=4.17 \cdot 10^{-3}$  cm<sup>3</sup>/s;  $v_{avg} = 2.8 \cdot 10^{-3}$  cm/s

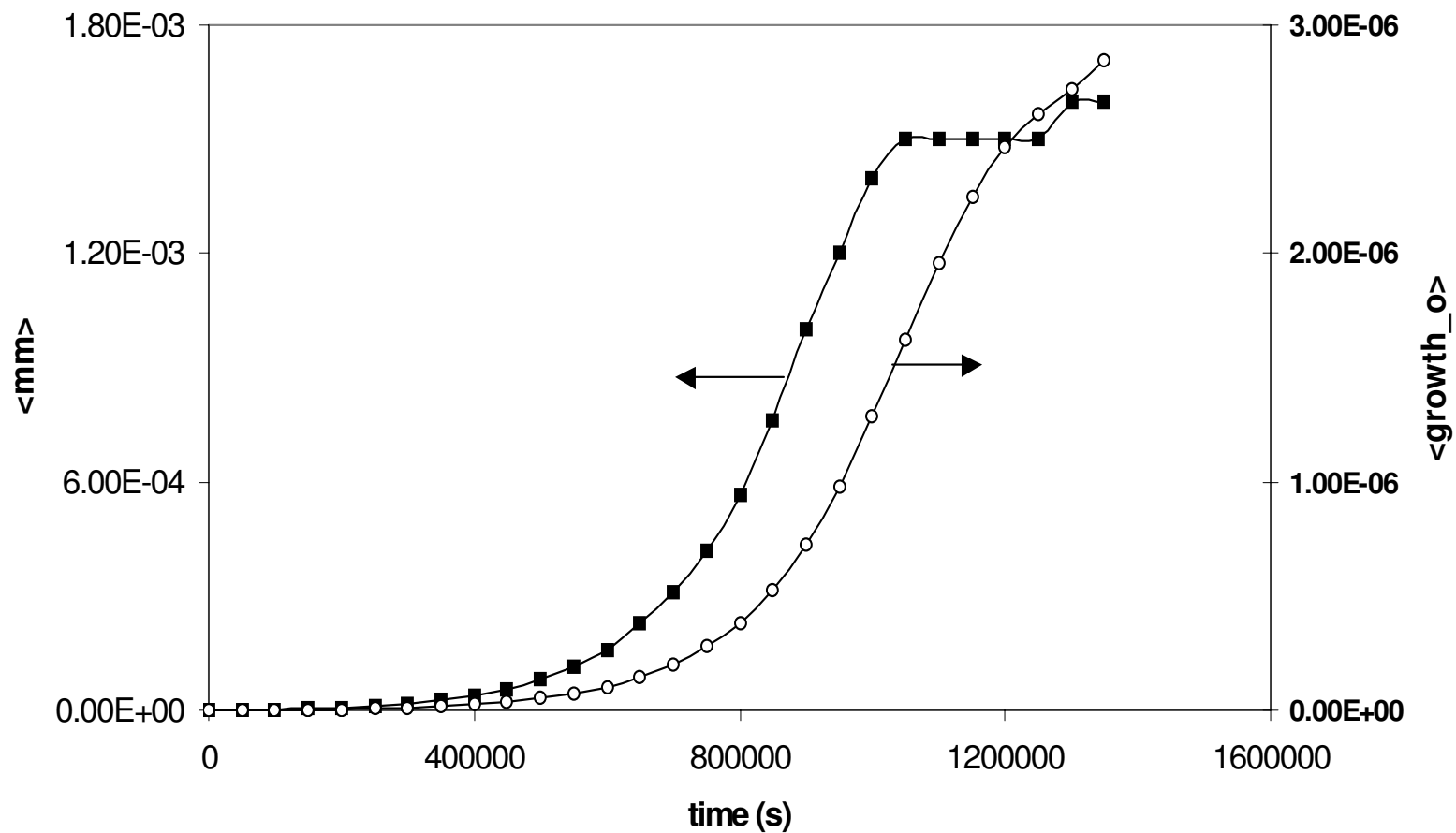
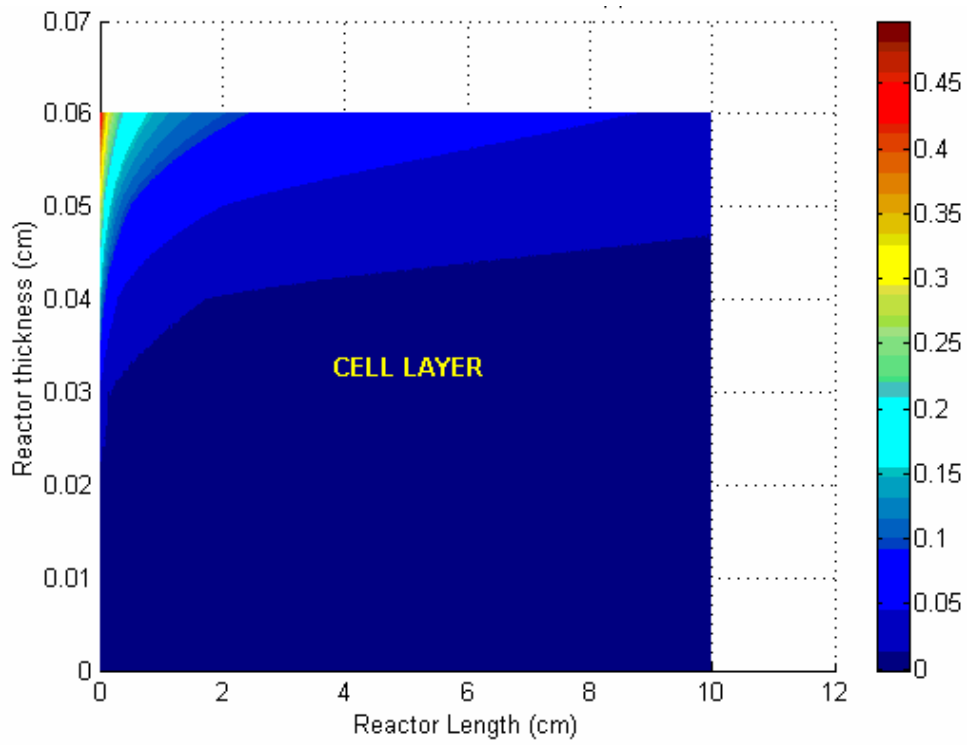
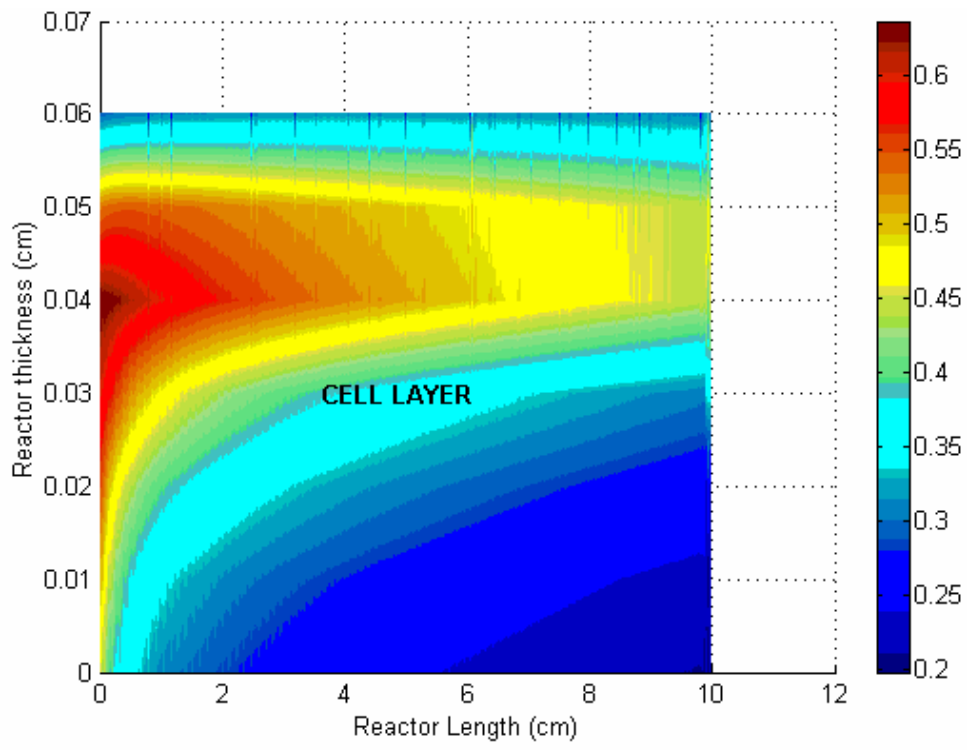


Figure 3.3 Macroscopically averaged oxygen consumption by metabolism (<mm>) and for cell growth (<growth\_o>) at various times. Parameters:  $T=0.6$  cm;  $l=0.06$ cm;  $res\_time = 1$ hr;  $F=4.17 \cdot 10^{-3}$  cm<sup>3</sup>/s;  $v_{avg} = 2.8 \cdot 10^{-3}$  cm/s



**Figure 3.4 a** Spatial variation in non-dimensional oxygen concentration in the cell layer at nearly 15 days ( $13 \cdot 10^5$  s)



**Figure 3.4 b** Simulated growth in the cell layer at nearly 15 days ( $13 \cdot 10^5$  s)

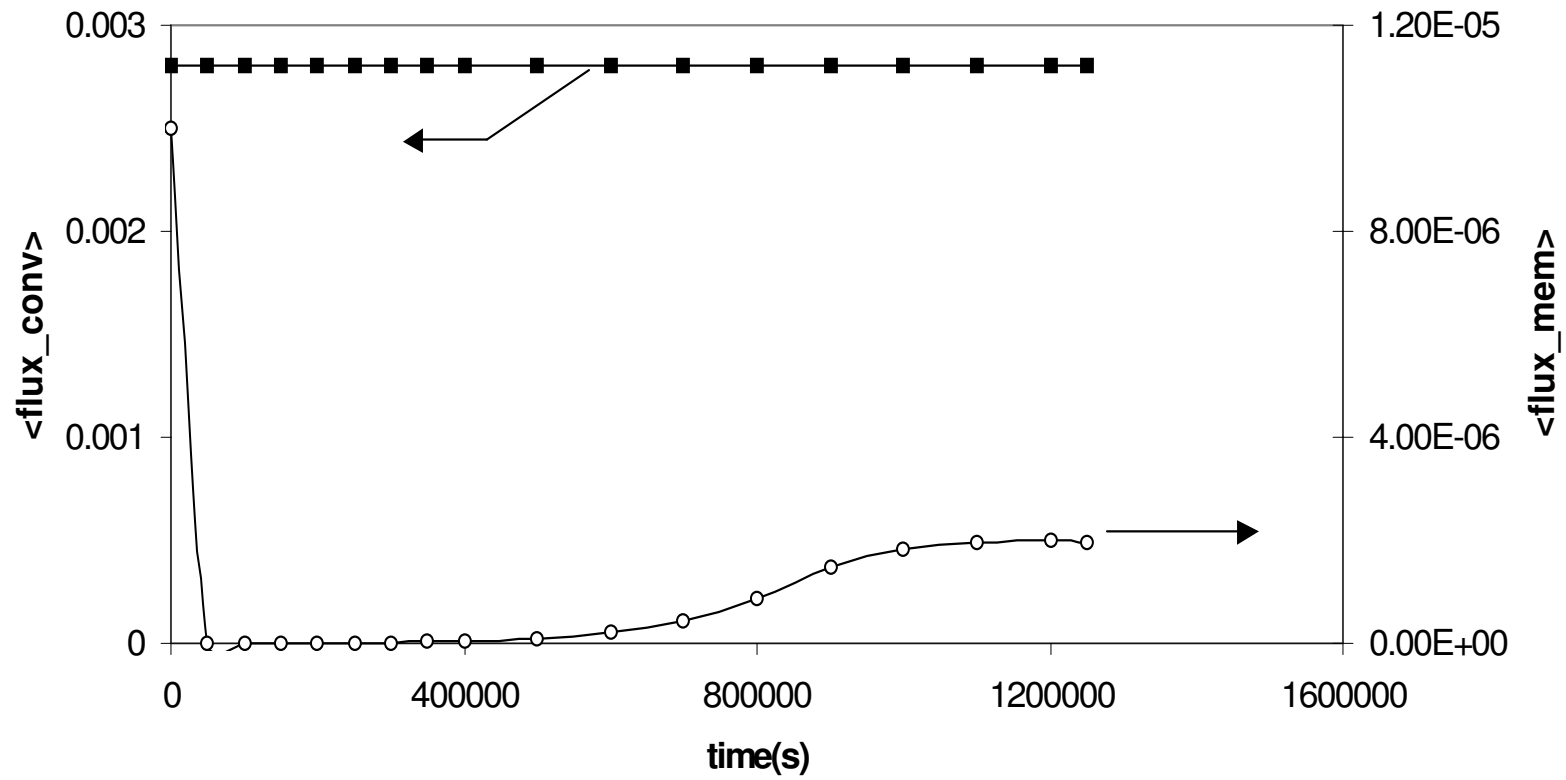


Figure 3. 5 Macroscopically averaged flux of oxygen through the FEP membrane and through flow variation with time. Parameters  $T=0.6$  cm;  $l=0.06$ cm;  $res\_time = 1$ hr;  $F=4.17 \cdot 10^{-3}$  cm<sup>3</sup>/s;  $v_{avg} = 2.8 \cdot 10^{-3}$  cm/s

The perfusion bioreactor has two sources of oxygen: one by diffusion through the FEP membrane from the incubator filled with oxygen saturated air (20% Oxygen) and the other by convective flow with the entering media containing dissolved oxygen in equilibrium with saturated air (20% Oxygen). The variations of the averaged fluxes of oxygen through these two sources with time are plotted in Figure 3.5 (again for same parameters as in the previous figures). It can be seen that the influx of oxygen by convective transport ( $\langle flux_{conv} \rangle$ ) is constant, as expected, and is much higher than by diffusive transport through the membrane ( $\langle flux_{mem} \rangle$ ). As the cell number increases with time the oxygen demand also increases leading to a larger oxygen concentration gradients between the bulk liquid and incubator oxygen level, thus increasing the supply of oxygen by diffusion across the membrane. However, membrane restrictions to oxygen transport remain very high for all times, hence the values of average flux through the membrane,  $\langle flux_{mem} \rangle$  are always considerably smaller than the convective flux.

### **Design parameters**

The model is also used to assess the effects of the liquid layer height, the residence time of the fluid flow, and the various modes of oxygen supply. The objective is to determine how these system parameters affect the spatial and temporal variations of cell density and oxygen concentration in the bioreactor.

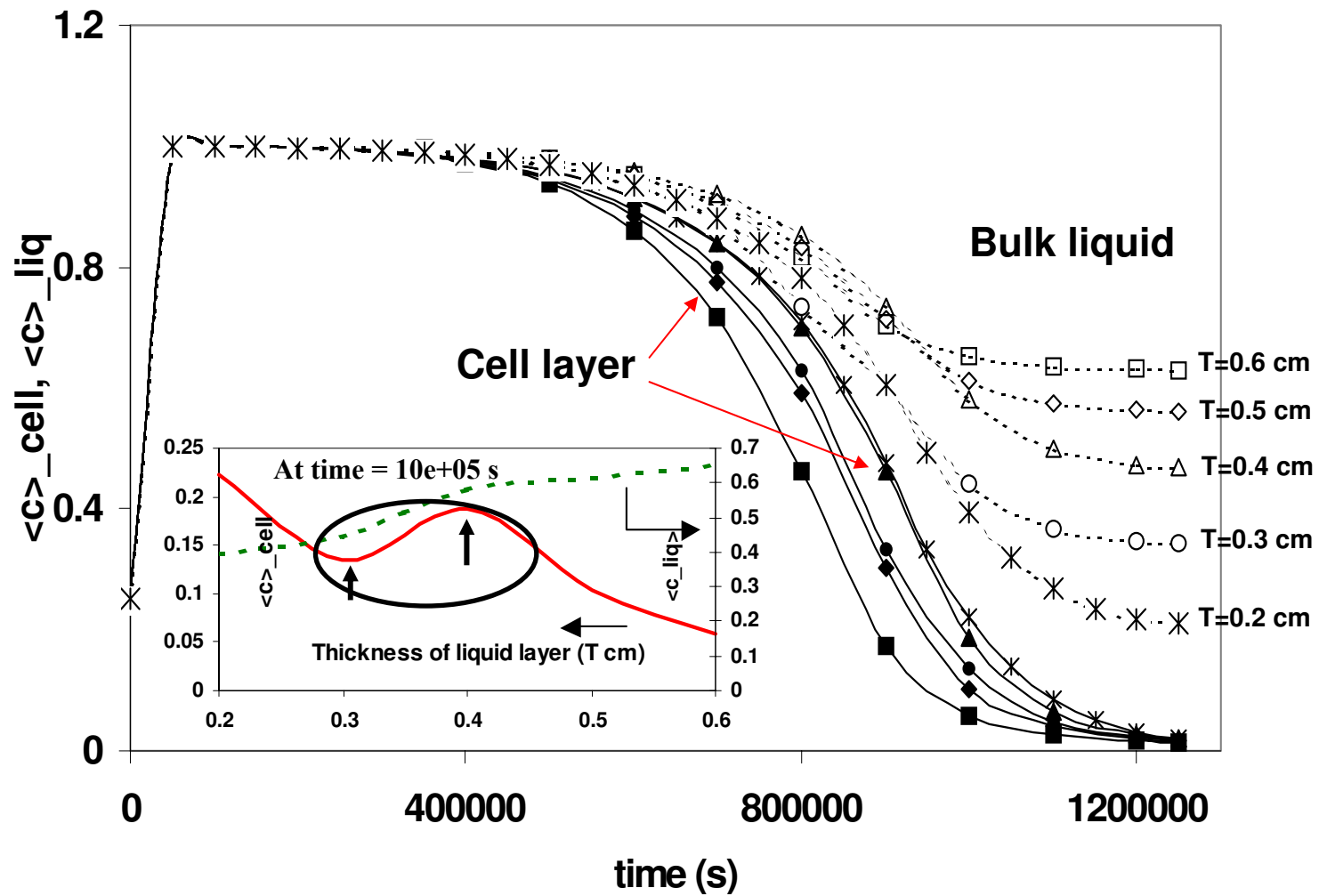


Figure 3.6 a Simulated macroscopically averaged oxygen concentrations in the cell layer (matrix) and the liquid layer for varying liquid layer heights ( $T$ ) at different times. Parameters  $T=0.6$ – $0.3$  cm;  $l=0.06$ cm;  $res\_time = 1$ hr;  $F=2.08 \cdot 10^{-3}$  cm<sup>3</sup>/s–  $4.17 \cdot 10^{-3}$  cm<sup>3</sup>/s;  $v_{avg} = 2.8 \cdot 10^{-3}$  cm/s

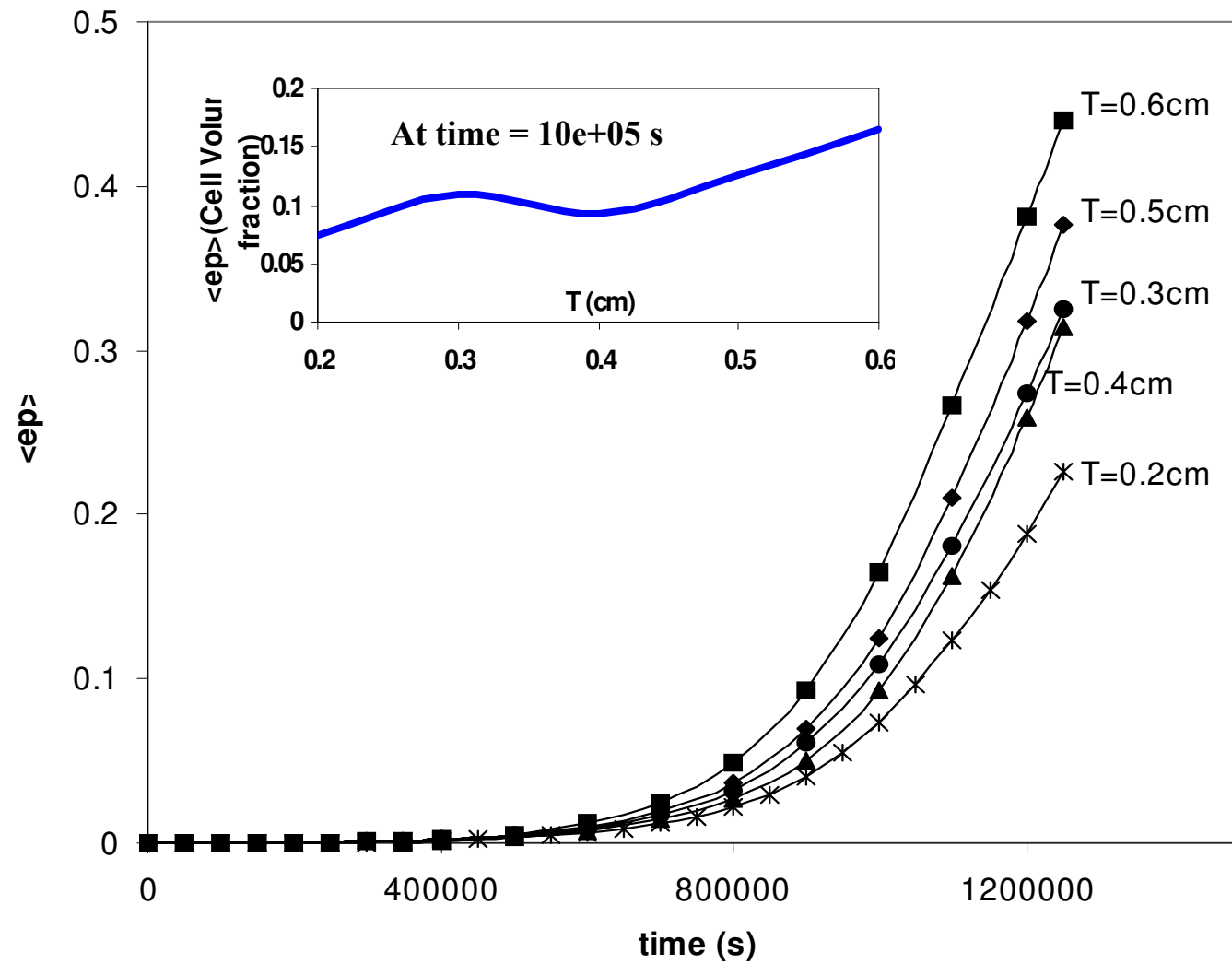


Figure 3.6 b Spatially averaged cell growth for various liquid layer heights at different time. Parameters  $T=0.6-0.3$  cm;  $l=0.06$ cm;  $res\_time = 1$ hr;  $F=2.08$   
 $\ast 10^{-3}$  cm<sup>3</sup>/s-  $4.17 \ast 10^{-3}$  cm<sup>3</sup>/s;  $v_{avg} = 2.8 \ast 10^{-3}$  cm/s



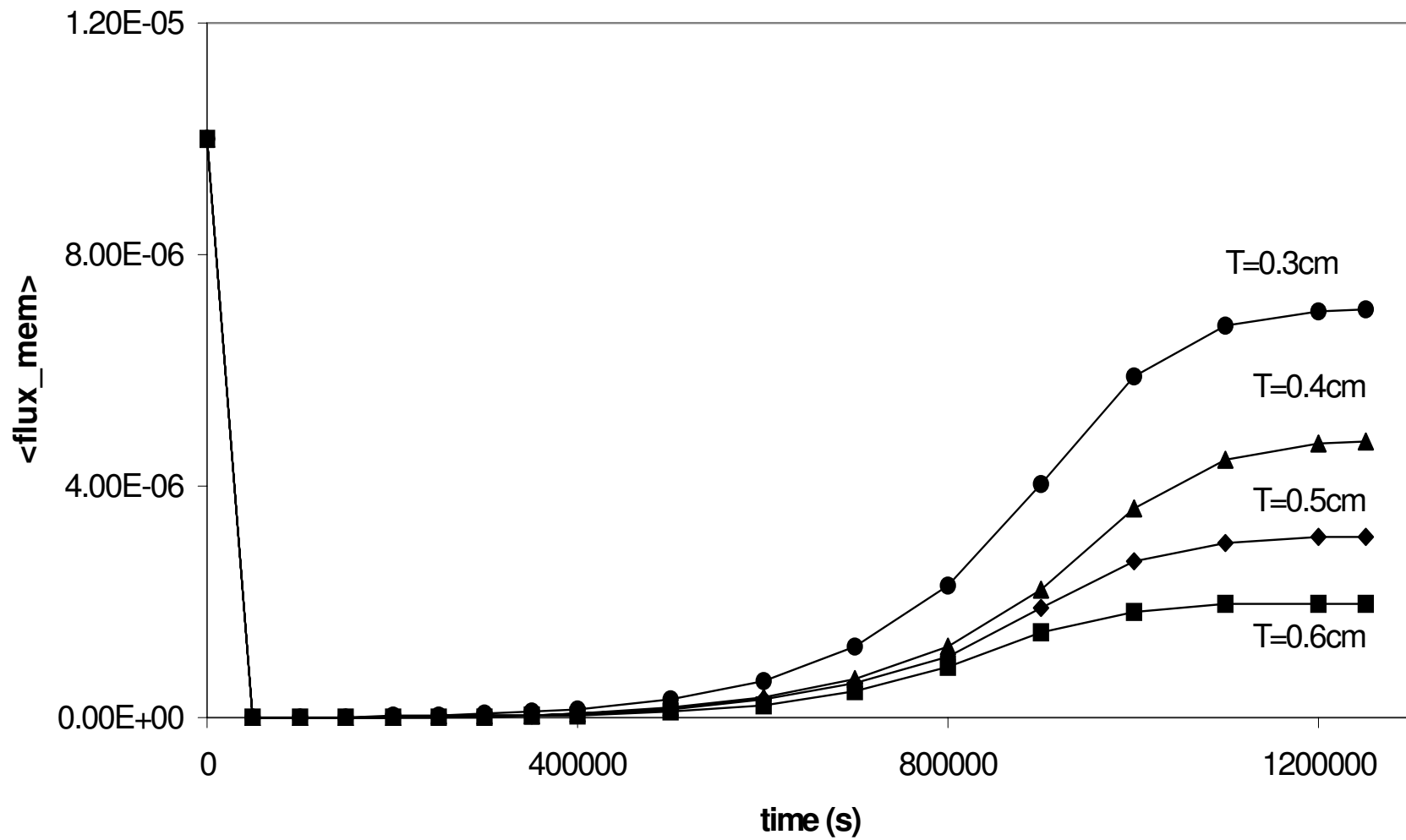


Figure 3. 6 c Simulated fluxes through the membrane with time. Parameters:  $T=0.6-0.3$  cm;  $l=0.06$ cm;  $res\_time = 1$ hr;  $F=2.08 \cdot 10^{-3}$  cm<sup>3</sup>/s-  $4.17 \cdot 10^{-3}$  cm<sup>3</sup>/s;  $v_{avg} = 2.8 \cdot 10^{-3}$  cm/s

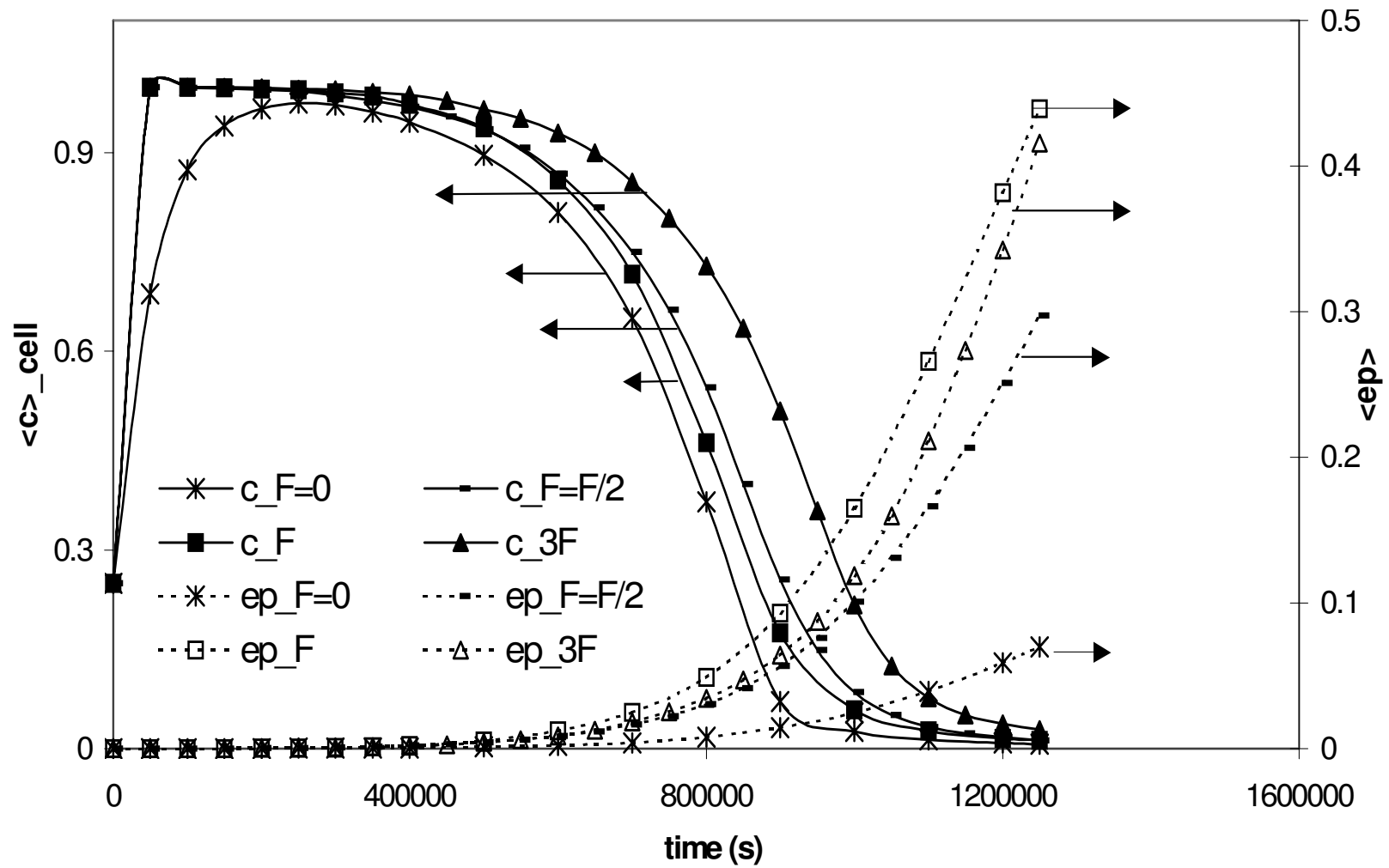


Figure 3.7 a Simulated average oxygen concentration and averaged cell volume fraction in the cell layer of the bioreactor with time. Parameters  $T=0.6$  cm;  $l=0.06$ cm;  $res\_time = 0\text{hr}-2\text{hr}$ ;  $F=0$  cm<sup>3</sup>/s-  $8.33 \times 10^{-3}$  cm<sup>3</sup>/s;  $v_{avg} = 2.8 \times 10^{-3}$  cm/s

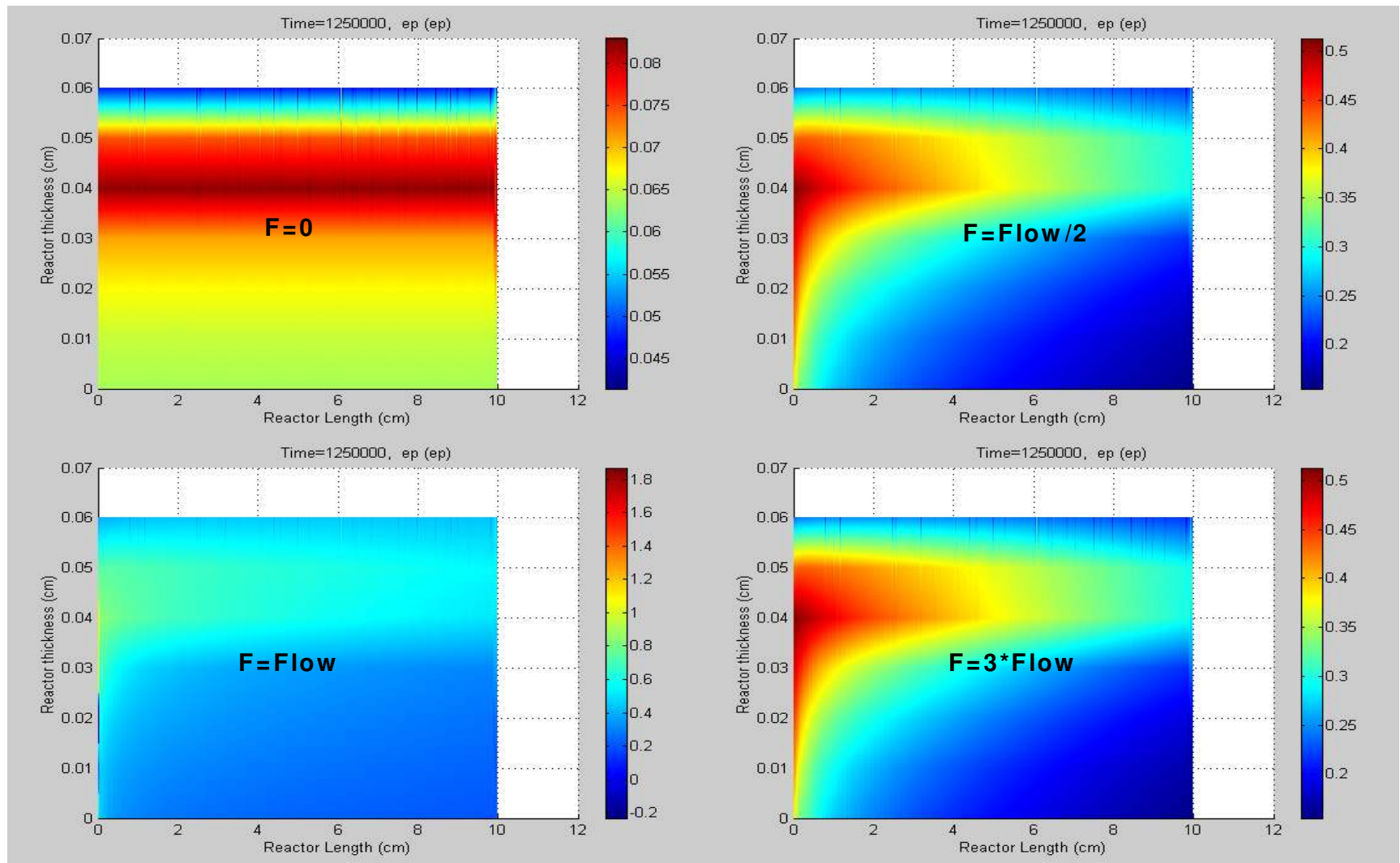


Figure 3. 7 b Spatial variation in cell volume fraction in the cell layer at nearly 15 days ( $13 \cdot 10^5$  s) for different residence times and correspondingly different flow rates (F)

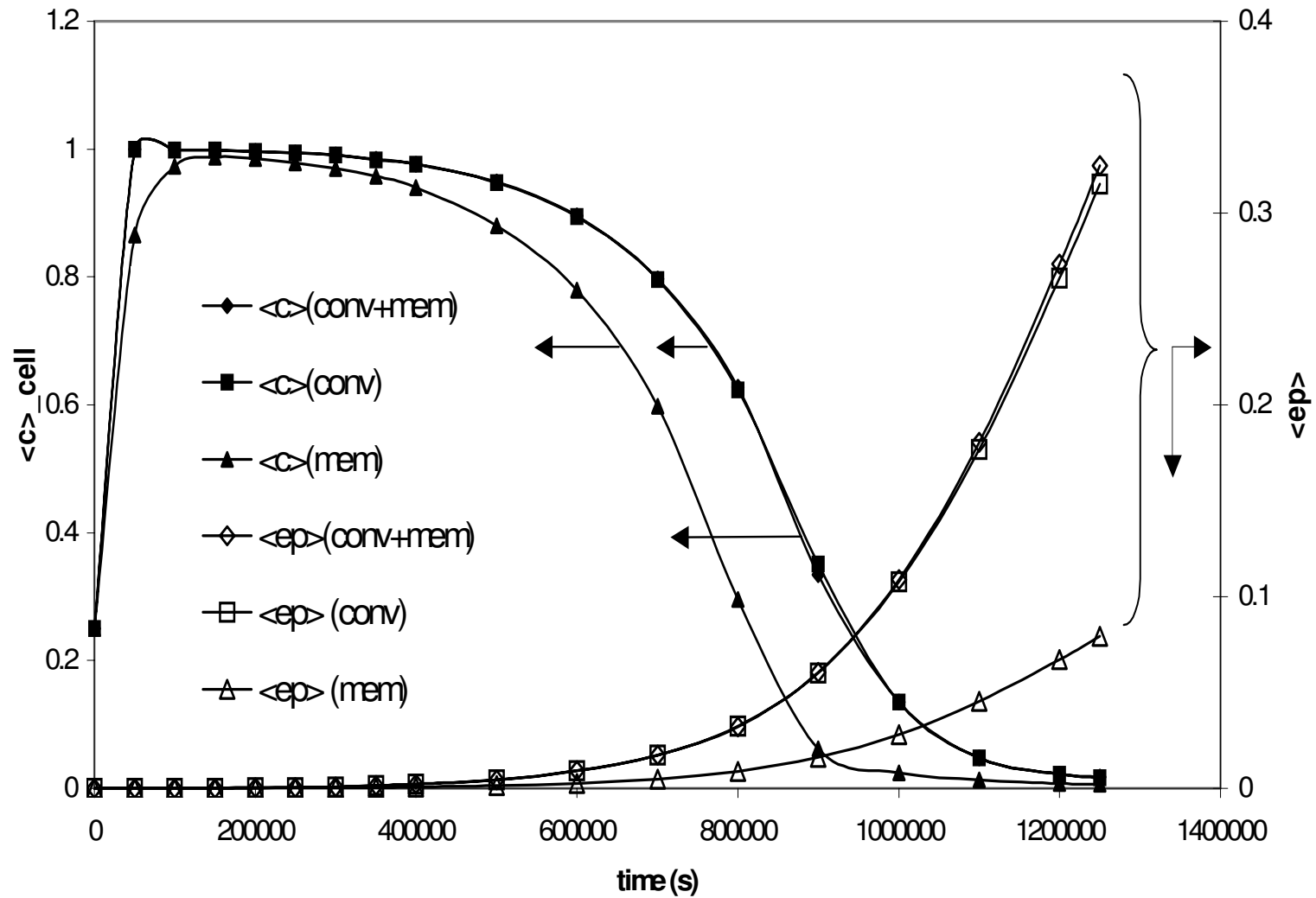


Figure 3.8 a The effect of different modes of oxygen supply on the averaged oxygen concentration in the cell layer and the cell volume fraction. Parameters:  $T=0.3$  cm;  $l=0.06$ cm;  $res\_time = 1$ hr;  $c_{\text{gas chamber}} = 1$ ;  $c_{\text{in\_flow}} = 1$ ;  $F=2.083 \cdot 10^{-3}$  cm<sup>3</sup>/s;  $v_{\text{avg}} = 2.8 \cdot 10^{-3}$  cm/s

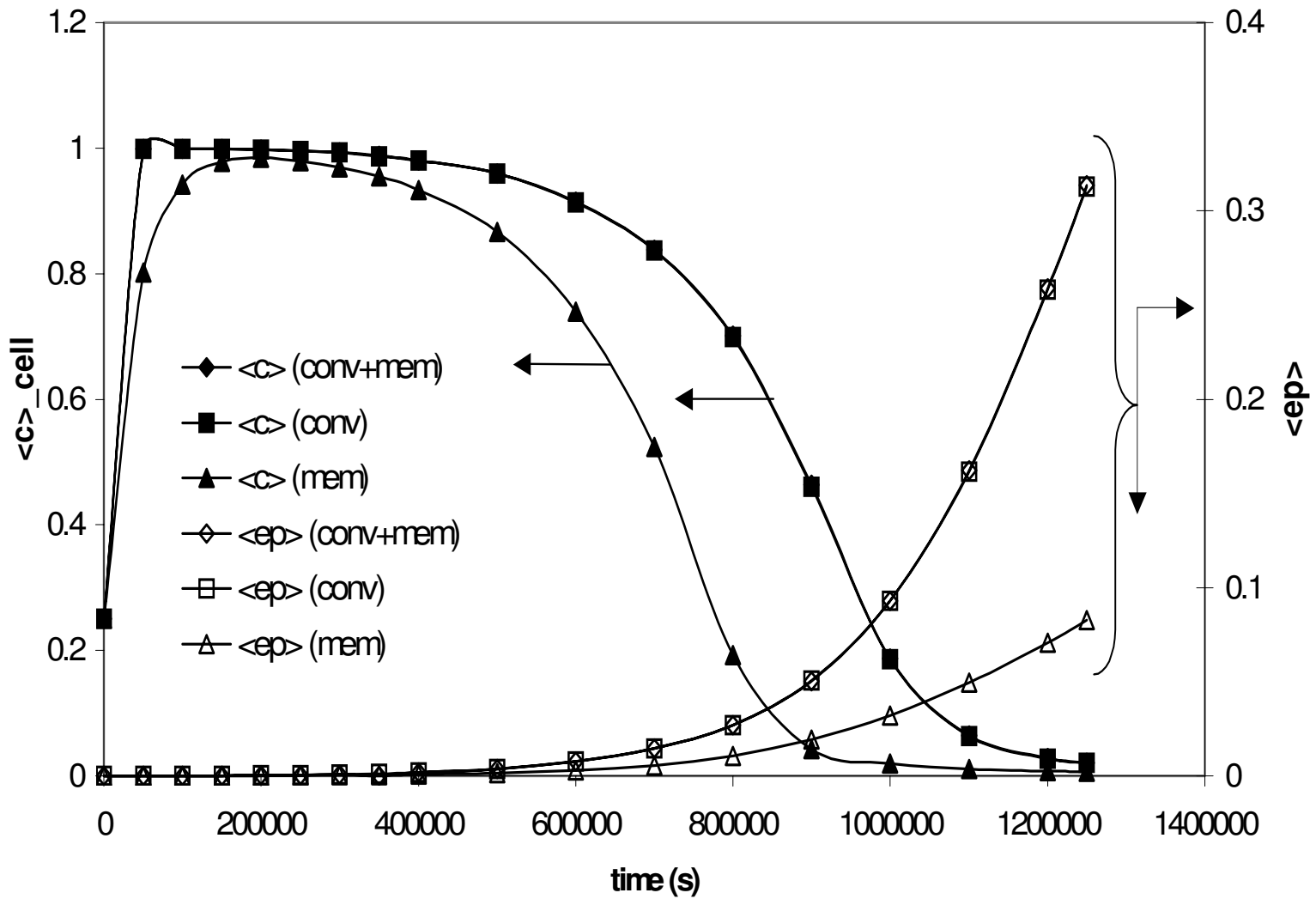


Figure 3.8 b The effect of different modes of oxygen supply on the averaged oxygen concentration in the cell layer and the cell volume fraction. Parameters:  $T=0.4$  cm;  $l=0.06$ cm;  $res\_time = 1$ hr;  $c_{\text{gas chamber}} = 1$ ;  $c_{\text{in\_flow}} = 1$ ;  $F=2.8 \cdot 10^{-3}$  cm<sup>3</sup>/s;  $v_{\text{avg}} = 2.8 \cdot 10^{-3}$  cm/s

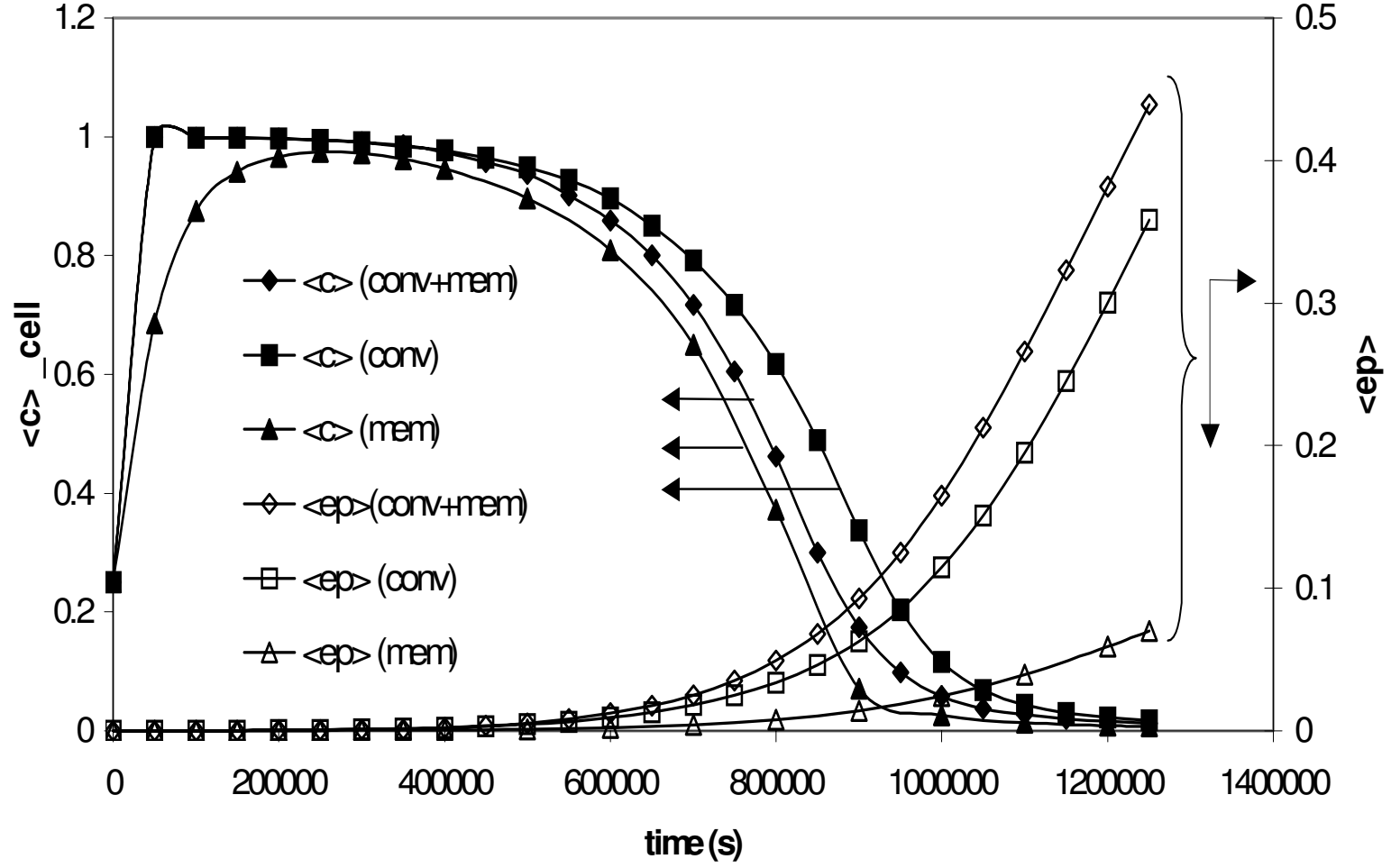


Figure 3. 8 c The effect of different modes of oxygen supply on the averaged oxygen concentration in the cell layer and the cell volume fraction. Parameters:  $T=0.6$  cm;  $l=0.06$ cm;  $res\_time = 1$ hr;  $c_{gas\ chamber} = 1$ ;  $c_{in\_flow} = 1$ ;  $F= 4.17 \cdot 10^{-3}$  cm<sup>3</sup>/s;  $v_{avg} = 2.8 \cdot 10^{-3}$  cm/s

### ***Liquid layer height***

Figure 3.6(a) shows the effect of varying the liquid layer height on the macroscopically area-averaged oxygen concentrations in the cell and bulk liquid layers. The average oxygen concentrations in the bulk liquid layer are higher for larger liquid layer heights since the bulk molar flow rate is larger at a fixed residence time. At long times the oxygen concentrations in the bulk liquid appear to level off indicating limitations in metabolic consumption. In general since there is more available oxygen, the oxygen consumption rates are higher for larger liquid layer heights thus leading to larger depletion of oxygen in the cell layer and thus the figure also shows lower oxygen concentration in the cell layer at larger liquid layer thickness. However, the oxygen profiles in the cell layer are not monotonic functions of the bulk liquid layer height as indicated by similar rates of decrease for the 0.5 and 0.3 cm and the 0.4 and 0.2 cm. These trends are partially reflected in the cell density profiles (Figure 3.6(b)) whereby growth is highest for 0.6 cm and lowest for 0.2 cm, but the growth of cells is slightly larger for 0.3 cm than for 0.4 cm. Similar results were also seen when the flow is changed to plug flow (results not shown here). These non-monotonic variations might be attributed to the convective flow coupled to the non-linear growth characteristics. It can be noted that calculations with the well mixed model did not lead to such variation in the oxygen profile with bulk liquid layer height (results not shown). There was a monotonic decrease in oxygen concentration in the cell layer with various liquid layer heights and a monotonic increase in cell growth with higher supply of oxygen by convective flow.

The oxygen supply by diffusion through the FEP membrane is also affected by increases in bulk liquid layer heights. As seen in Figure 3.6(c) the oxygen delivery by diffusive supply through the membrane is larger in the case of smaller bulk liquid layer heights in comparison to larger bulk liquid layers. However, the magnitude of oxygen delivery by diffusion is much smaller compared to that of flow, and thus this larger supply is still not as significant at the smaller bulk liquid layer heights.

### ***Residence time***

The residence time of the flow is a measure of the contact time for the flowing fluid, i.e., the rate at which oxygen is supplied to the cells through convection. Longer residence times imply the flow is slow and that there would be large oxygen depletion in the regions of the reactor farther away

from the supply end in comparison to the cell regions closer to the inlet. Thus, longer residence times lead to regions of very low oxygen concentration and might lead to formation of dead zones.

Figure 3.7(a) shows the averaged oxygen concentrations and cell volume fractions in the cell layer of the reactor at different residence times. Variation of residence time with a constant liquid layer height of 0.6 cm changes the medium flow rate, and hence the average velocity at which oxygen is transported by convection through the reactor. A residence time of 1 hr corresponds to a flow rate  $F$ . The oxygen concentration in the cell layer is seen to deplete much faster (Figure 3.7b) in the case where there is no flow ( $F = 0$ ), i.e., oxygen is delivered only through the FEP membrane. Correspondingly, the growth rate of cells is much slower due to these transport limitations and the maximum cell volume fraction reached is less than 0.1 (Figure 3.7a). However, upon introducing flow more oxygen is delivered to the cell layer by convective flow and hence the growth rate increases for flows of  $F/2$  and  $F$ . However, at flow rates of  $3F$  the growth rate as shown in Figure 3.7(a) is less than that for  $F$ . It is likely that the higher oxygen concentrations (Figure 3.7b) occurring at this higher flow rate lead to inhibitory kinetics thus decreasing the growth rate. Thus, there exists an optimal flow rate that leads to maximum cell growth due to transport limitations at low flow and kinetic inhibitions at high flow. Similar effects were also seen for the case in which oxygen was supplied by plug flow with the same average velocity rather than by laminar flow (result not shown here).

### ***Mode of oxygen supply***

It is already shown above that convection clearly enhances the cell growth, as compared to cell growth that occurs when diffusion is the only mode of supply. In order to further consider this factor, analysis is conducted to compare cases with convection alone, diffusion alone, and combinations of convection and diffusion. These comparisons are important because perfusion bioreactors are generally more complex and difficult to set up and operate than reactors that only utilize diffusive supply. Therefore a quantitative analysis of the role of convection on oxygen supply is needed to determine when flow is necessary. The present model can be used to quantitatively determine the relative contribution of oxygen supply through flow in comparison to diffusive supply through the FEP membrane. Thus, the model can be used to determine if diffusive



transport of oxygen through the FEP membrane can meet the demands of the cells or if convective flow needs to be added in the bioreactor design.

Figures 3.8(a), 3.8(b) and 3.8(c) show that for three different liquid layer heights the oxygen delivered to the cell layer by diffusion through the membrane is less effective in maintaining cell growth for longer periods of time than would be possible with the addition of convective flow. The membrane restrictions are so large that the amount of oxygen delivered to the cell layer in the case of both membrane transport and hydrodynamic flow and the case of only oxygen delivered by convective flow are seen to be similar by model calculations. In addition, the cell volume fractions in the cell layers are similar for these two cases. Thus for these levels of oxygen consumption the membrane would appear to be superfluous, however it may still be useful to incorporate such a backup mechanism for oxygen supply in case of problems with the fluid pumps.

Figure 3.9 summarizes results for the cell density and oxygen concentration for a number of cases. For example, increasing the concentration of oxygen in the incubator and the oxygen concentration in the supply by flow to values in equilibrium with 100% oxygen gas causes the oxygen concentration in the cell layer to take a longer time to deplete in comparison to supply at 20%. In addition, convection and membrane transport at 100% supply maintains the oxygen concentration at higher values for longer periods of time than all other cases. However, the higher oxygen concentrations for this 100% supply lead to kinetic inhibition for longer times, thus reducing the growth rate (Figure 3.9b). The cell volume fraction achieved upon complete depletion of oxygen (at some position in the reactor) for the 100% supply is lower than the case with 20% supply as shown in Figure 3.9(b). Further the convective diffusive supply at 100% has a lower rate of cell growth than the membrane supply alone and the convection supply alone. This confirms the effect that the higher oxygen concentrations in the 100% range lead to slower cell growth.

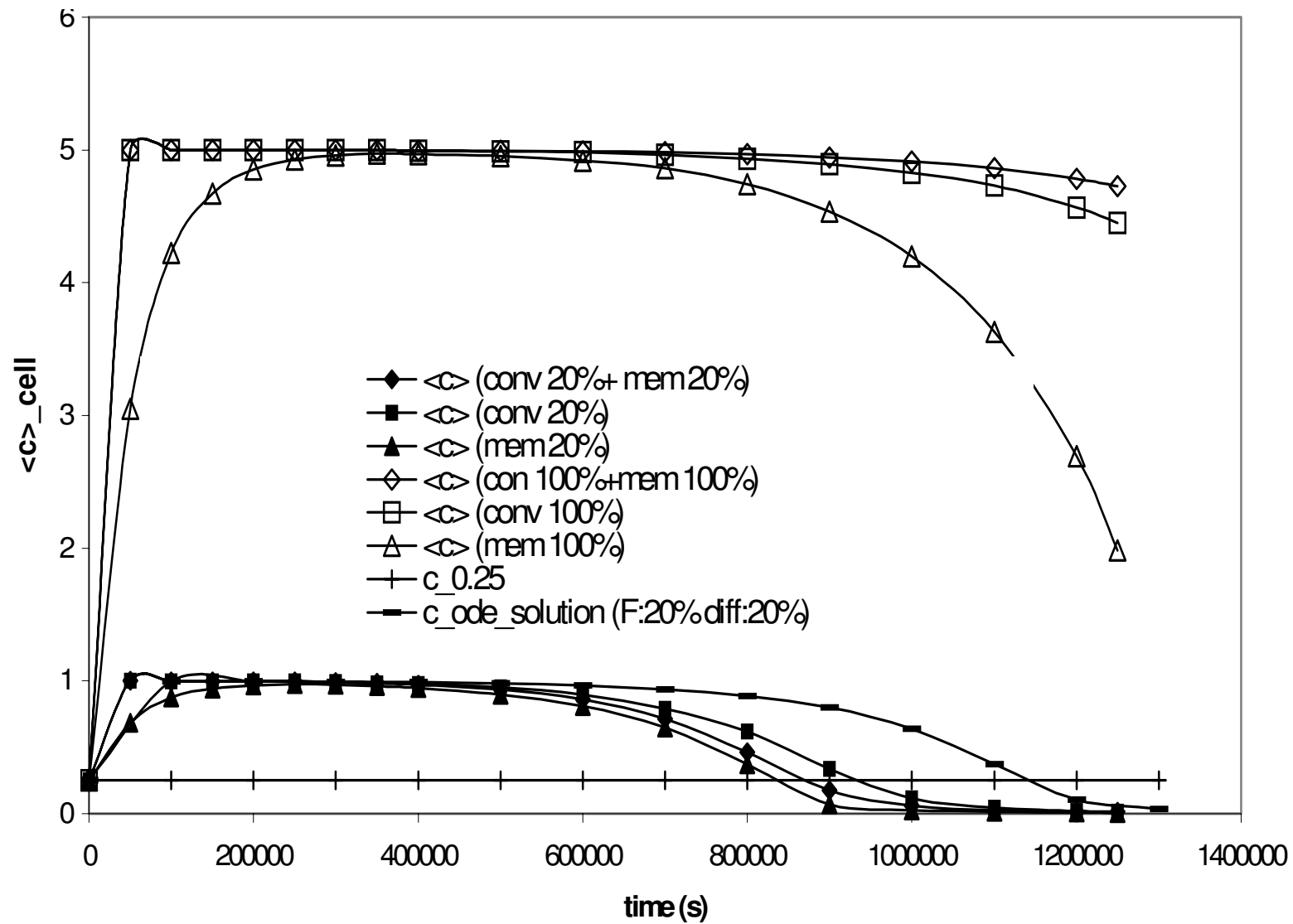


Figure 3.9 a Oxygen concentration variation with time in a mixed bioreactor under different oxygen supply conditions with different membrane permeability,  $k_m$  and medium flow rates (Perm= $1.343 \times 10^{-4}$  cm/s known value of permeability of the FEP membrane,  $F=4.17 \times 10^{-3}$  cm<sup>3</sup>/s)

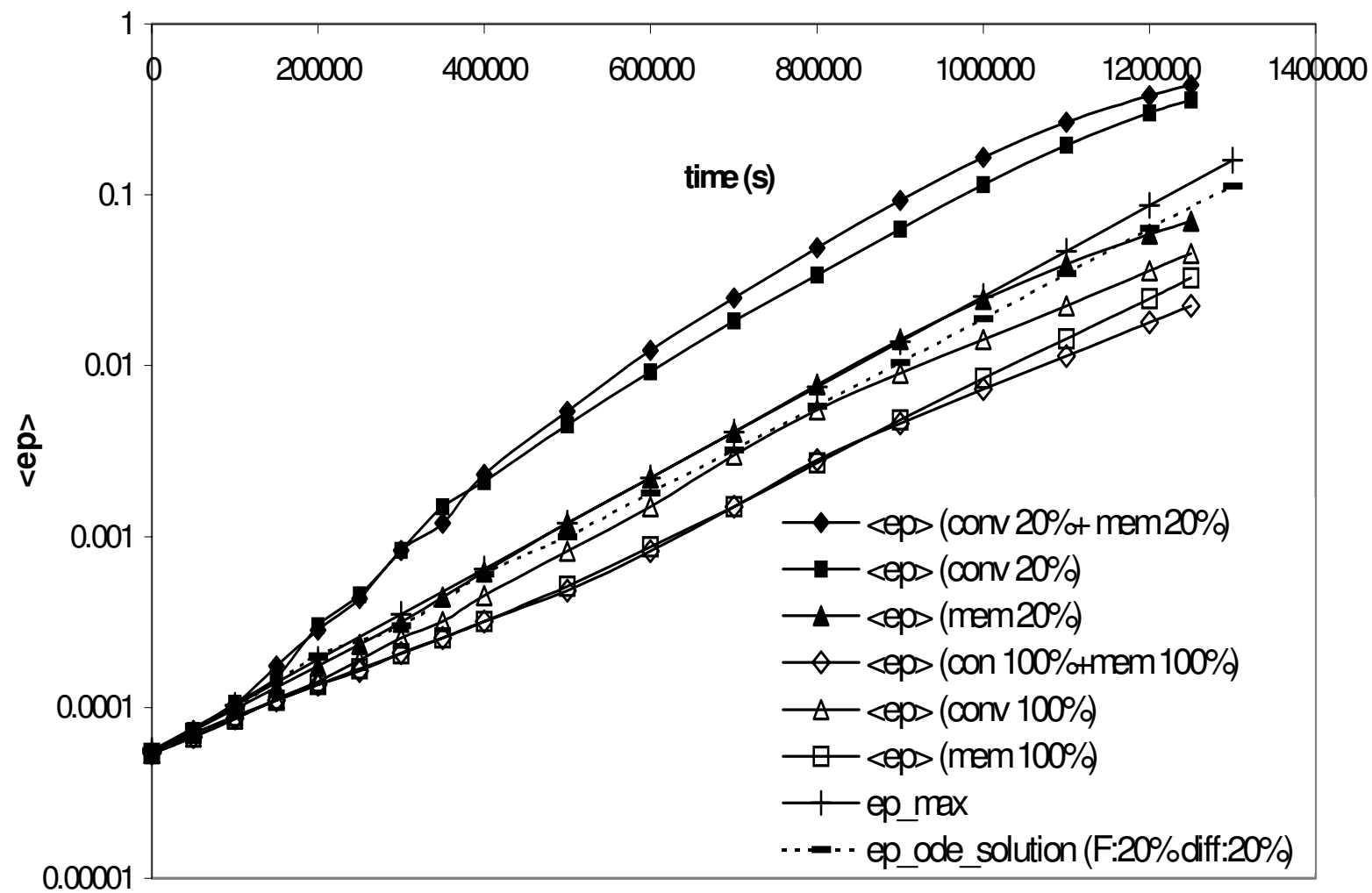
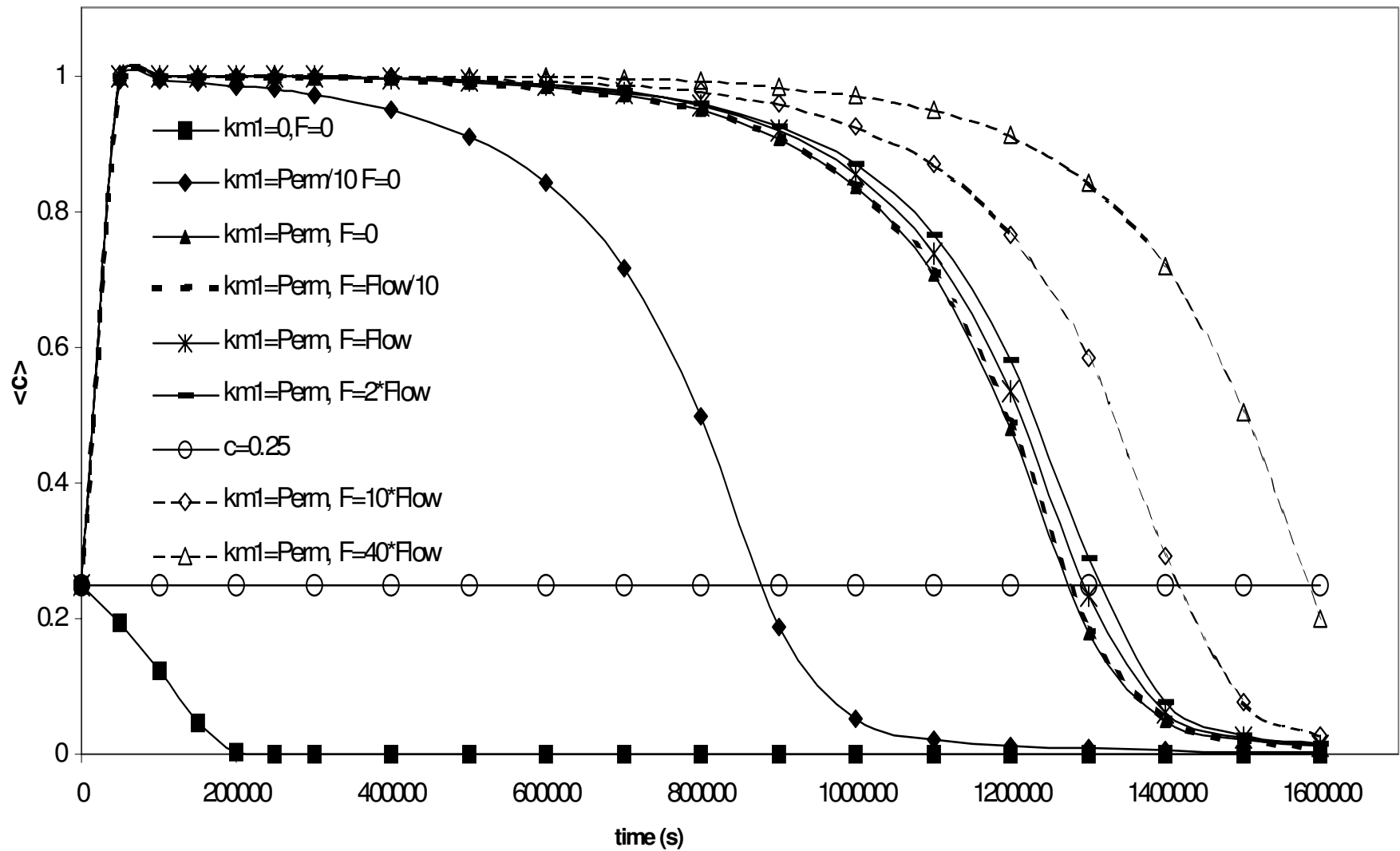


Figure 3. 9 b Cell volume fraction variation with time in a mixed bioreactor under different oxygen supply conditions with different membrane permeability,  $km$  and medium flow rates ( $Perm=1.343 \cdot 10^{-4}$  cm/s,  $F=4.17 \cdot 10^{-3}$  cm<sup>3</sup>/s)



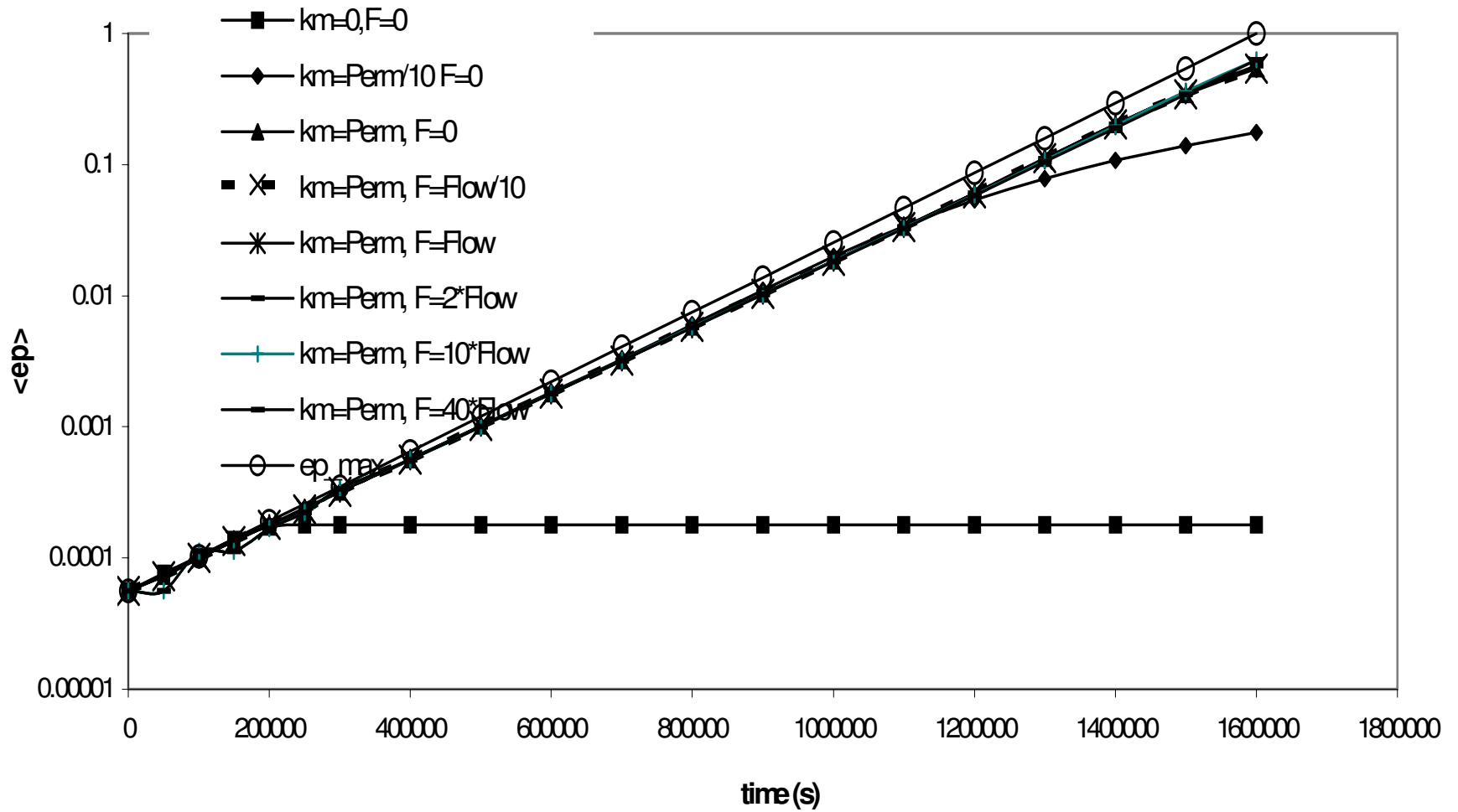


Figure 3. 10 b Effect of mode of oxygen supply on cell volume fraction of granulocyte progenitors at different times. Parameters:  $T=0.6$  cm;  $l=0.06$ cm;  $res\_time = 1$ hr;  $F= 4.17 \cdot 10^{-3}$  cm<sup>3</sup>/s;  $v_{avg} = 2.8 \cdot 10^{-3}$  cm/s

The case of a well-mixed tank reactor for 20% supply at similar flow rates was analyzed using equation 3.20. In this case, the cell growth rate is higher than all cases for 100% supply but lower than most of the other cases for 20% supply. The mixed reactor gave cell growth similar to the membrane-only supply at 20%, however the growth was significantly lower than the convective and convective-diffusive supplies at 20%. Mixing clearly decreases performance of the flow reactor, as expected, but only slightly affects performance of the diffusion only.

Also shown in Figure 3.9 are the results for the putative maximum growth rate ( $\mu_{max}$ ) whereby the oxygen concentration is set at concentration in equilibrium with 5% gas phase oxygen throughout the reactor (Fixed oxygen concentration model). The kinetics for the cell growth are developed from experimental results that show that these cell have maximum growth rates at an oxygen concentration around 5%. Oxygen concentrations higher and lower to this value inhibit cell growth. Equation 3.19 was used to determine the cell volume fraction changes with time for a uniform oxygen concentration in the cell layer of 5%. The growth rate at this putative maximum is higher than the cases for 100% supply and for the mixed reactor and membrane-only supply at 100%. However, surprisingly as shown in Figure 3.9(b) the cell growth is faster for the cases of oxygen supply at 20% by flow and membrane transport and by flow alone than the putative maximum growth case.

It is possible that this effect can be due to either the amount of nutrient delivery or to the spatial distribution of the delivery. To address this issue, the mixed bioreactor case is solved for different oxygen supply rates. Supply in the mixed reactor case was varied by changing the flow rates ('Flow' corresponding to flow rate for 0.6 cm liquid layer height and residence time of 1 hr, i.e.  $4.17 \cdot 10^{-3}$  cm/s) and by changing mass transfer rates across the membrane (the membrane permeability,  $k_m$ ). It is seen clearly in Figure 3.10(a) and 3.10(b) that either by increasing the oxygen supply by flow to 40 times the value 'Flow' or increasing the membrane permeability the growth rates is still below the expected putative maximum growth rate. Hence the higher growth rates for the cases seen in Figure 3.9 (b) cannot be obtained simply by increasing supply rates and must be attributed to the spatial distribution of oxygen in the bulk liquid layer and the cell layer of the bioreactor.

The results shown in Figure 3.9(b) clearly indicate that optimal cell growth can be attained by operating the reactor with convective-diffusive supply at 20% concentration for nearly 15 days ( $12.5 \times 10^5$  s). However, by that time the oxygen concentration is severely depleted. In order to maintain high cell growth for a longer time, it is thus necessary to increase the gas phase supply to 100% and add convective flow at 100% gradually. Thus, the model results suggest that an increase in feed oxygen concentration should begin at approximately  $10^5$  s and should gradually rise to maintain the highest rates of cell growth.

### **3.4 Conclusions**

The present study models a three-dimensional perfusion bioreactor system seeded with granulocyte progenitors. The method of volume averaging is used to formulate the material balances for the cells and nutrients in the porous matrix containing the progenitor cells. The model is used to compute the variation in oxygen concentration with space and time in the matrix as well as the bulk liquid region. The results of the model illustrate the effects of oxygen mass transfer restrictions in the matrix due to cell growth. This model includes the dependence of cell growth on the oxygen concentration. The derived effective diffusivities and effective rate expressions used for solving the effect of oxygen delivery to the cells account for local 3-dimensional geometry. However, the volume averaged expressions do not include the effect of the local 3-dimensional cell-cell interactions and ECM environment, an important factor in the 3-dimensional structure that affects cell proliferation. Future experimental and theoretical work shall consider these aspects.

The model is used to analyze the various design parameters of the reactor. Cells consume much larger amounts of oxygen for metabolism compared to cell growth. Hence, a larger supply of oxygen with an optimal reactor design is necessary to improve the productivity of the reactor. The model shows the effects of liquid layer height and residence time, as well as the roles of the mode of oxygen supply. Variation of the liquid layer height between 0.3 cm and 0.6 cm affected the rates of oxygen supply by hydrodynamic flow and membrane delivery. However, the delivery of oxygen by hydrodynamic flow always exceeds that by membrane transport, thus

leading to larger growth rates at higher liquid layer heights. Lower residence times, i.e. higher flow rates, supplied larger amounts of oxygen to the cell layer of the bioreactor. Larger amounts of the oxygen were then available for cell growth and metabolic consumption, which produced larger number of progenitor cells. However, an optimal growth rate at a specific flow rate was found whereby at lower flows the growth was transport limited by oxygen supply and at higher flows the growth was limited by kinetic inhibition. The spatial pattern of delivery by convection was also found to play a significant role increasing the rate of cell growth. The model results clearly indicate that variation of the oxygen concentration in the inlet feed with time may lead to enhanced granulocyte progenitor cell growth in the 3-dimensional perfusion bioreactor.

This model can be further extended to include the effects of glucose consumption and the effects of lactate production (Patel *et al.*, 2000). Cell loss because of flow and product inhibition may occur and needs to be included in future studies. Moreover, in order to model a bioreactor used for growing hematopoietic cultures it will also be necessary to incorporate the presence of multiple cell populations, starting from the progenitor cells to the mature cells of all lineages (Cabrita *et al.*, 2003; Nielsen *et al.*, 1988; Silva *et al.*, 2003; Hevehan *et al.*, 2000). Our preliminary work on including these parameters in the model is discussed in detail in Chapter 4.



## **CHAPTER 4**

### **ROLE OF NUTRIENT SUPPLY AND PRODUCT FORMATION ON CELL GROWTH IN BIOREACTOR DESIGN FOR TISSUE ENGINEERING OF HEMATOPOIETIC CELLS**

#### **Analysis of glucose and oxygen supply and by-product (lactate) concentration on progenitor and mature cells in 3-dimensional well- mixed reactor**

#### **4.1 Introduction**

In Chapter 2 we discussed the complicated process of hematopoiesis (cell proliferation, differentiation, and maturation), the need for ex vivo hematopoietic cell expansion, the various factors that affect hematopoietic cell expansion in cultures, and also the different culture devices that are being used for this process. The necessity for higher cell production and more progenitor expansion led researchers from simple Dexter hematopoietic (bone marrow) cultures to various complicated bioreactors (spinner flasks, perfusion bioreactors) by maintaining systems at ‘better-defined’ culture conditions (pH, dissolved oxygen, other metabolic reactants and products).

The reactor designed at Florida State University, as discussed in Chapter 3, is a continuous perfusion bioreactor with cells growing on 3-dimensional PET matrices. The bioreactor is chosen so that the reactor is maintained at the so-called ‘better-defined’ culture conditions with

cells continuously bathing with nutrients and flow removing the byproducts. The reactor provides a 3-dimensional growth environment for cells, close to the microenvironment *in vivo* and results in long-term multilineage production of hematopoietic cells. The hydrodynamic flow in the bulk liquid layer allows cells to settle in the matrix and grow. However, some cells will fall and be carried away by the flowing fluid. Moreover, by isolating the cells from the primary flow they can be protected from the mechanical stress exerted by the flow.

Chapter 2 discussed the various continuous and discrete mathematical models developed for describing hematopoietic process in bone marrow and in culture devices in literature. The Krogh's model of the bone marrow is indicative of the distribution of the various progenitor and mature cell types in the bone marrow and their location relative to the sinus. Oxygen was found to be one of the most important parameters that controlled this cell distribution in the bone marrow compartment. Efforts were also made to develop mathematical models to describe physicochemical behavior of cells in '*in vitro*' culture devices (discussed in Chapter 2.5.3). This can be done by a careful selection of suitable design characteristics and operational variables to achieve a desirable level of one or more culture parameters (dissolved oxygen, pH, and nutrient or byproduct concentrations) that directly affect the growth.

The importance of oxygen on hematopoietic cells led to the development of the dynamic mathematical model explained in Chapter 3. The reactor as mentioned has a distinct cell layer comprising of the PET matrix where the cells grow, squeezed in between two flow chambers, which make up the bulk liquid layer of the reactor. The granulocyte progenitor cells are shown to become oxygen-limited in the cell layer although there is a large supply from the bulk liquid above. This mathematical model was the first of its kind to describe the spatio-temporal changes in cells coupled to transport of nutrient (oxygen) delivery in *ex vivo* hematopoietic cultures. Thus, the mathematical model determines the immune lineage cell growth characteristics (granulocyte progenitors) in the 3-dimensional matrix of the bioreactor and quantitatively describes progenitor cell production and substrate consumption (oxygen) over an extended period of time. Material balances on cells are coupled to the nutrient (oxygen) balances in 3-dimensional matrices to determine the effects of transport limitations on cell growth. This model has flexibility to be extended to cell types other than hematopoietic cells based on the availability

of growth kinetics for that cell type of interest. However, future work on understanding the other important parameters is necessary in order to improve the modeling of 3-dimensional hematopoietic bioreactor system. To address this issue, the current chapter develops models that build upon the model developed in Chapter 3, by incorporating other important environmental factors (other than oxygen), accounting for the co-existence of multiple cell population, understanding the effects of various cell-cells, cell-ECM interactions, and addressing the effects of using of different matrix geometries.

## **4.2 Literature Review**

### **4.2.1 Model Factors**

The most important factors that have been addressed extensively in literature and discusses here in the model perspective include are the metabolic parameters - glucose consumption and lactate production by hematopoietic cells; multiple cell populations in culture systems, and the effects of a different cell microenvironment in terms of geometry of the reactor.

#### ***4.2.1.1 Effect of glucose supply on cell growth in the 3-dimensional perfusion bioreactor***

Glucose is the most commonly used carbohydrate energy source for cells and it is normally included in culture at concentrations between 5 and 25 mM. Few studies have been conducted to determine the glucose consumption rate and to assess its effect on hematopoietic cell metabolism and growth. This is because experiments reported (Collins *et al.*, 1997; Patel *et. al.*, 2000) have shown that cell cultures inoculated at low cell densities in spinner flask cultures have shown a wide scatter in glucose data. The error in the glucose assay was approximately the same order of magnitude as the amount of glucose consumed. Experimental studies in the perfusion bioreactor in Dr Ma's lab and modeled in our current study (Chapter 3) have shown similar scatter in data during the early culture phase, however the scatter stabilizes late during the culture. Therefore, the effect of glucose on hematopoietic cell growth in culture should be studied for two reasons. Glucose is one of the most important nutrients for cell metabolism and growth and is also one of

the sources of lactate production observed in hematopoietic cultures. Moreover, glucose concentration can be measured in real time in the culture, thus enabling comparison of model results to experimental data.

Glucose is consumed in cultures both aerobically and anaerobically. In oxidative or aerobic metabolism glucose and oxygen produce carbon dioxide, water, and energy in the form of ATP through the well known Krebs cycle. Anaerobic metabolism, which takes place in the absence of oxygen, involves the formation of lactate from glucose by glycolysis.

Collins *et al.*, 1997 examined the specific glucose consumption rate for hematopoietic cultures carried out in spinner flasks. The glucose consumption increased from day zero until a maximum was attained, and then decreased until it reached a minimum value maintained until the end of the culture. A similar increase and decrease in the fraction of colony forming cells (CFCs) in this culture system was also seen. This shows that rapidly proliferating cells (CFCs) have much greater metabolic demand. These cells consume glucose for metabolism, and, thus manipulating glucose concentration in *ex vivo* cultures can help in manipulating desired cell growth. The specific glucose consumption rate at day 'n' was computed by Collins and coworkers as a time weighted average given as,

$$q_{glu,n} = \frac{\Delta t_b \left( \frac{-\Delta G_a}{(CD_{LM,a})(\Delta t_a)} \right) + \Delta t_a \left( \frac{-\Delta G_b}{(CD_{LM,b})(\Delta t_b)} \right)}{\Delta t_a + \Delta t_b} \quad (4.1)$$

The effect of glucose as a substrate (or nutrient) along with oxygen on the growth of different cell types is explored by adding a glucose mass balance to the model developed in Chapter 3. Suitable glucose consumption rates for metabolism and cell growth were obtained from the literature. Details on the model development are discussed in section 4. 2.2.

#### ***4.2.1.2 Effect of lactate production on cell growth in the 3-dimensional perfusion bioreactor***

Lactate is a metabolic product of glycolysis and is largely derived from glucose although glutamine may also contribute to the accumulation of lactate. Studies have shown that the cell proliferation ceases – in hematopoietic cultures of varying cell densities – when the lactate concentration approaches 20 mM (Patel et. al., 2000). Hence the effect of lactate on hematopoietic cell growth has been extensively studied and reported in the literature.

Collins *et al.*, 1997 observed a strong correlation between the specific lactate production rate ( $q_{lac}$ ) and the percentage of CFCs – with a close correspondence between maxima in  $q_{lac}$  and % CFC and a low value for  $q_{lac}$  after the CFCs are depleted for cultures of cord blood (CB) mononuclear cells (MNC), peripheral blood (PB) MNC. Hence as for glucose, an understanding of the lactate production would help in increased expansion of the CFC (early progenitor cells) in cultures. It was also shown that this difference in the  $q_{lac}$  can be used to group cells along a lineage into two distinct groups - progenitors and post-progenitor cell types. This information is used to develop a two cell population model which will be discussed in detail in section 4.2.2.

Further analysis by the same group (Collins et. al., 1998) for different feeding protocols also showed that there was a maximum in  $q_{lac}$  near the maximum in %CFC. However, for some feeding protocols there was a secondary increase in  $q_{lac}$  that exceeded the initial peak value although the specific oxygen consumption rate  $q_{O_2}$  did not show a significant secondary peak. Thus, this showed that *post-progenitors are highly glycolytic and do not have high oxidative metabolic activity*. The ratio of the specific lactate production rate to specific oxygen consumption rate ( $Y_{lac,ox}$ ) for the cells in this stirred bioreactor culture varied with time, increasing with increase in post-progenitor cells further showing utilization of glycolysis by post-progenitor cells for energy production.

Two distinct models were proposed to model lactate concentration in culture units (Collins *et al.*, 1997, 1998; Yang *et al.*, 2000)-

##### **a) Linear Chemometric or Two Population Model**

Based upon the experimental observation of the linear correlation between the specific lactate production rate ( $q_{lac}$ ) and the percentage of colony forming cells (%CFCs) Collins *et al.* 1997

established a ‘Linear Chemometric model’ relating the lactate production rate to the percentage of the CFC production,

$$q_l(t) = \frac{\%CFC}{100} \cdot \alpha + \left(1 - \frac{\%CFC}{100}\right) \cdot \beta \quad (4.2)$$

where  $\alpha$  and  $\beta$  are the model parameters for the two population model (CFC or progenitor cells and other post-progenitor cells). The model groups all the different progenitor cells as CFCs and remaining cells as post-progenitor cells assuming that cells belonging to each of these separate groups have the same lactate production rate. This is correct as a first approximation due to unavailability of quantitative experimental data on rate constants for individual cell types. However in culture, different progenitor cells and post-progenitor cells have a different lactate production rate that also varies with the culture conditions.

## **b) Modified Linear Chemometric Model**

### ***Multi-population Model***

Yang *et al.*, 2000 extended the two population model of Collins and co-workers by grouping all cell types of granulomonocytic lineage into six distinct cell types (groups) with different growth rates, cell density and metabolite consumption/formation rates.

$$q_s(t) = \sum_{j=1}^p x_j(t) \beta_{s,j} \quad (4.3)$$

where  $x_j(t)$  and  $\beta_{s,j}$  are the respective cell fraction and specific metabolic rate of cell type j, and p (=6) is the number of cell types (groups) considered. The model assumes that the specific metabolic rates for each cell type are constant at any culture time and any cell composition. However, for hematopoietic cultures the metabolic activities depend on culture conditions, such as pH, availability of nutrients (dissolved oxygen, glucose), amino acids and cytokines.

However, theoretically, through regular feeding and saturation the concentration of these substances can be always kept nearly in the desirable range.

***Growth Rate Influence Model***

The linear model ignores the effect of growth rate and hence the specific lactate production can be also calculated as,

$$q_{Specific} = -\left(\frac{\mu}{Y_{X/S}} + m_S\right) \quad \text{Pirt (1965)}$$

$$q_{Specific} = a_S \mu + b_S \quad \text{Ludeking and Piret (1962)}$$

(4.4)

These models have been extensively used in describing microbial metabolite uptake and formation rates, respectively, where  $Y_{X,S}$  is the yield coefficient,  $m_S$  is the maintenance rate,  $a_S$  the growth associated product formation coefficient, and  $b_S$  is the non-growth associated product formation rate. This model is supported by experimental data showing a tendency for higher lactate production rate with increasing growth rate in cultures.

***Combination of Multi- population Model and Growth Rate Influence Model***

The growth rate influence can be added to the linear model described in equation 4.3,

$$q_s(t) = \sum_{j=1}^p x_j(t) (\alpha_{S,j} \cdot \mu_j(t) + \beta_{S,j})$$

(4.5)

The cellular overcrowding ('crowding effect') especially observed in two-dimensional cultures (2-dimensional) and also observed in spinner flask cultures (Collins *et al.*, 1998) was found to decrease the metabolic activity of the cells. This can be further incorporated in equation 4.4 by

assuming that the cell density and other factors (growth rate and cell types) affect cell metabolism independently.

$$q_s(t) = \sum_{j=1}^p x_j(t) \left( \alpha_{s,j} \cdot \mu_j(t) + \beta_{s,j} \right) \frac{K_{s,j}}{K_{s,j} + C_X(t)} \quad (4.6)$$

Thus, the total metabolic activity is made up of two parts. The first part describes the metabolic activity at very low ('zero') cell density, while the second part represents the dependence of the maximum metabolic activity on cell density.

These developed models could be used to establish accurate relationship between the specific lactate production rate and the cell density of various cell types in the granulomonocytic lineage. After model parameters are determined by comparing the model output of lactate concentration with the available experimental results for the system, the model can be used to get an estimate of the percentage of the cell types in culture for a known lactate concentration. This would further help in calculating the harvest time for different cell types in culture to obtain a desired cell density than using the uniform harvest time for all cell types. The model development section outlined below incorporates these already proposed approaches for lactate production kinetic rates to the overall model.

Experiments in the perfusion bioreactor with hematopoietic mononuclear cells (at FSU) have not shown an increase in lactate concentration beyond the inhibitory range for the culture conditions used in the model. However, it is necessary to examine the effects of lactate for a better understanding of the sensitivity to the toxic metabolite (lactate) accumulation on the growth of different hematopoietic cell types. This understanding would further add to the long range goal of optimization and control of the developed bioreactor.



#### ***4.2.1.3 Multiple cell population***

As described in Chapter 2, hematopoietic cultures are made up of multiple cell types starting from the stem cells, to progenitor cells, to lineage committed cells and mature cells with different growth rates and metabolite consumption and production rates. Hence a complete mathematical model to describe such a culture needs to consider multiple cell types. Use of specific cytokines helps to produce cells of certain lineages only, thus streamlining the model to a three compartment model as described in Chapter 2.5.3.4. Each compartment involves the production of different cell types by processes of proliferation, differentiation, and maturation. The models discussed in Chapter 2 with multiple-population are discrete models and does not account for the effects of environmental changes on cell growth of different cell types. These models do not describe the growth rate in culture, nor do they account for mass transfer restrictions and its effects on cell growth.

There are no continuous mathematical models that have accounted for the effect of changes in the environmental condition, for example oxygen tension, glucose or lactate concentrations on the changing hematopoietic cell population (cell growth, cell differentiation and cell maturation) in *ex vivo* 3-dimensional cultures. The model developed in Chapter 3 of this work using a single population model (granulocyte progenitor cells) has shown the importance of a continuous change in oxygen tension with time and in space and its effects on cell growth in perfusion 3-dimensional bioreactor. The importance of oxygen tension distribution has also been shown *in vivo* in the bone marrow (Chow *et al.*, 2001).

As a next step towards improvement of the current models we intend to add the effects of nutrient supply (oxygen and glucose) and metabolite product (lactate) removal in the 3-dimensional perfusion bioreactor by diffusion and convection. As a first step this model incorporates the coexistence of only two distinct cell types the ‘progenitor cells’ and the ‘post-progenitor cells’ as discussed above.

#### 4.2.1.4 Geometry of the cell layer in bioreactor

Several groups have studied the effect of changes in the geometry of the bioreactor cell layer on the cell growth, differentiation, and maturation. One such proposed modification in the geometry is shown in Figure 4.1. The addition of grooves in the matrix, i.e., the cell layer of the bioreactor is believed to provide an enhanced supply of nutrients (oxygen and glucose) and removal of byproduct (lactate) by increasing the surface area for mass transfer (Horner *et al.*, 1998). These grooves will deliver oxygen locally to all regions in the cell layer, which would lead to uniform cell growth in the entire cell layer. The modeling of such a reactor would be used to quantitatively estimate the importance of grooved perfusion reactor units in terms of enhanced cell growth.

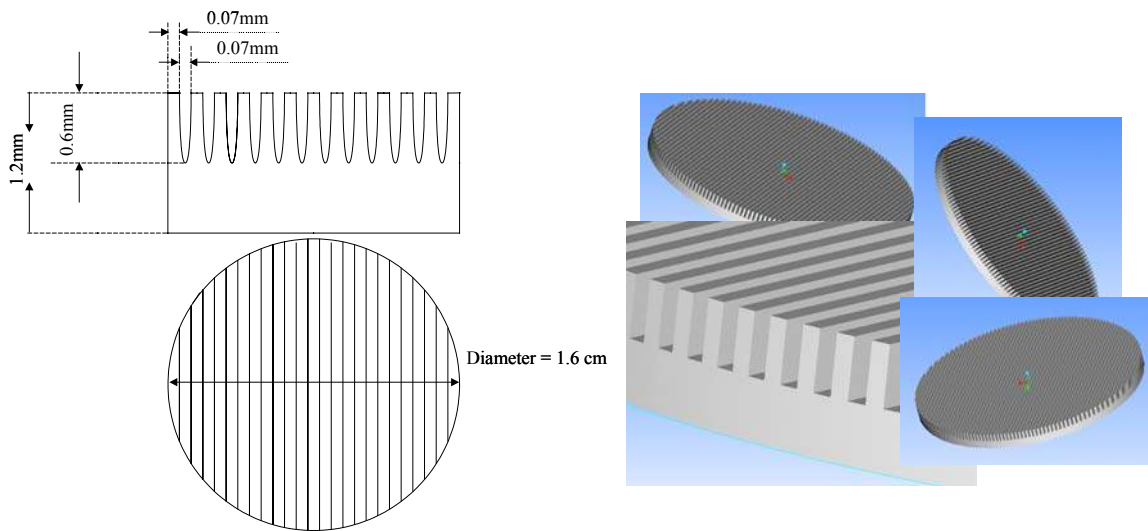


Figure 4. 1 Schematic of a proposed grooved matrix (cell layer) of the bioreactor (Florida State University)

#### 4.2.1.5 Local 3-dimensional cell geometry

The dynamic mathematical model developed in Chapter 3 for studying the growth of granulocyte progenitor cells in the hematopoietic process in the 3-dimensional perfusion bioreactor uses an

analytical expression for the effective diffusion coefficient of an isotropic two dimensional two phase medium defined by a square unit cell (Ochoa, 1988) containing spherical particles. This relationship accounts for the diffusion in the non-cellular  $\beta$  phase and the cellular  $\gamma$  phase as well as the mass transport across the two phases. This macroscopic viewing of the process can be used for analysis of low molecular weight solutes in 3-dimensional environment. However, for analysis of solutes that have larger restrictions (glucose and lactate) to diffusion in the cellular phase further consideration of the local 3-dimensional geometry and solution of the closure problem in such systems are needed.

Moreover, Chang's unit cell approach can be transformed from the original cubic unit cell (used in the model in Chapter 3) with the spherical  $\gamma$  phase to a spherical unit cell with similar  $\gamma$  phase particles (Ochoa, 1988). The effective diffusivity is then given as,

$$D_{eff} = \frac{D_{\beta}}{(\varepsilon_{\gamma} \cdot K_{eq} + \varepsilon_{\beta})} * \left[ \frac{3k - 2 \cdot (k - 1) \cdot \varepsilon_{\beta} + 4\varepsilon_{\beta} \alpha_{\gamma} \varepsilon_{\gamma}^{-1/3}}{3 + (k - 1)\varepsilon_{\beta} + 2 \cdot \alpha_{\gamma} \cdot (3 - \varepsilon_{\beta}) \varepsilon_{\gamma}^{-1/3}} \right] \quad (4.7)$$

In order to address the local 3-dimensional cell geometry 3-dimensional cell-cells interactions, the effects of cellular overcrowding and environmental factors needs to be addressed. Analysis of these factors requires more extensive evaluation of the volume averaging formalism. The current work utilizes effective diffusion coefficients based on specific 'unit cells'. In the full 3-dimensional culture, the three dimensional nature of the local environment may affect more than the effective diffusion coefficient as accounted for in the present work. To fully deal with these issues we may need to take more creative approaches such as incorporating the cellular automata or other simulations of cell growth in local regions and coupling those to the macroscopic models based on volume averaging. The approach as to which other models need to be incorporated (for studying hematopoietic cell growth and the changes in their local cell environment) with the macroscopic volume averaging approach has not been worked out for this tissue engineering application. This is primarily because even if the model was developed there

is not sufficient quantitative experimental data available in literature or work in Dr Ma's lab to validate the model for the current system under study.

To be noted here, however, Chapter 6 of this dissertation outlines a step-by-step procedure to approach the effects of 3-dimensional local geometry that incorporates local cell-cell interactions along with the overall macroscopic variation in mass transport of various reacting species for cartilage growth in a hollow fiber bioreactor. The model can be extended for this system, however, unlike the cartilage tissue which is made up of a single type of cells (chondrocytes) this system is made up of a number of different cell types where obtaining the growth, metabolic, and extracellular matrix synthesis rates for each cell type is not that simple.

## **4.2.2 Model Equations**

### ***Outline***

The next step towards improvement of the current model discussed in Chapter 3 is to incorporate the metabolic nutrients – oxygen and glucose; metabolic by-product – lactate and the presence of more than one cell type in the perfusion reactor. The model developed has two cell types the 'progenitor cells (cell type 1)' and the 'post-progenitor cells (cell type 2)'. The schematic of this process is shown in Figure 4.2

### ***Well-Mixed Model***

Species continuity balances describing the variation in oxygen, glucose and lactate concentrations are written in the cell and bulk liquid layer of the bioreactor (shown in Figure 4.3). The cell volume fractions of cell type 1 (progenitor cells) and cell type 2 (post progenitor cells) are written in the cell layer.

The modeling approach similar to that described for well-mixed compartments in Chapter 3 (section 3.2.2.5) is used. The spatial variations of metabolic species concentrations in the cell and bulk liquid layers and the cell volume fractions in the cell layer of the bioreactor are removed while retaining the effects of nutrient mass transfer supply.

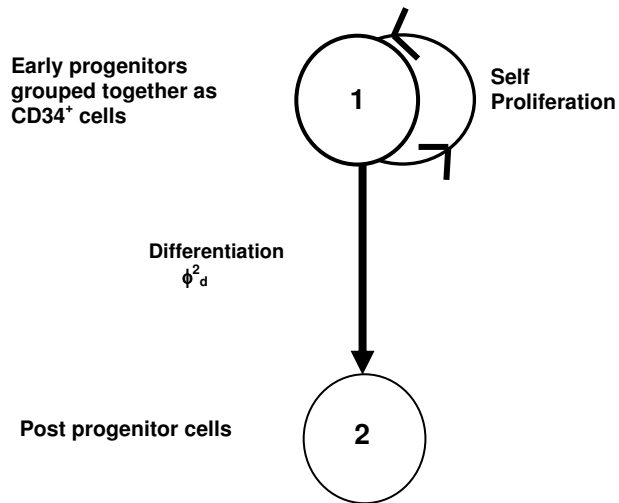


Figure 4. 2 Schematic of cell proliferation and differentiation process

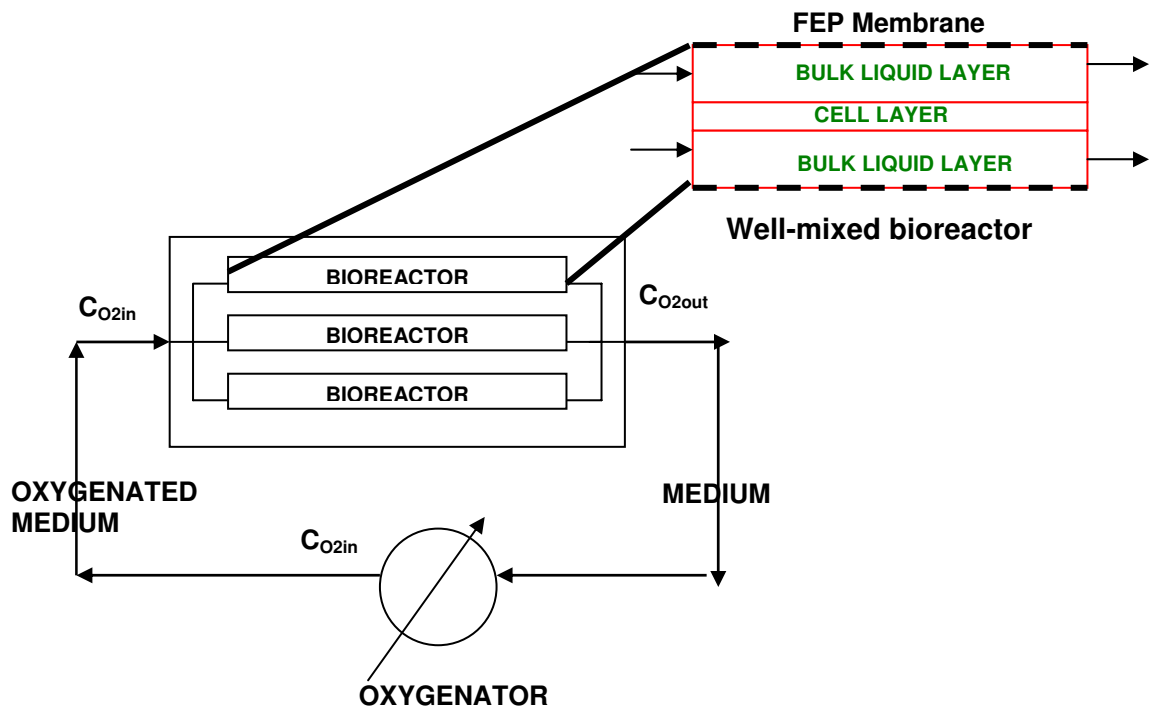


Figure 4. 3 Bioreactor Schematic showing continuous flow of oxygen

Oxygen is delivered to the reactor by mass transfer through the membrane and also by hydrodynamic flow at the entrances and exits of the bulk liquid layer of the bioreactor (shown in Figure 4.3). Glucose and lactate transport through the reactor occurs by convective flow and diffusive transport. The delivery of oxygen is continuous while lactate and glucose are replaced at specific time intervals. Thus, the reactor is continuous with oxygen supply but batch with respect to glucose supply and lactate removal. The conditions used with respect to the time interval of media exchange and concentration of oxygen are similar to the experimental system being modeled.

### **Liquid Layer**

Molar balances of oxygen, glucose and lactate concentrations are written as,

$$\frac{dC_{O_2}^l}{dt} = \frac{F}{V_l} \cdot (C_{O_2}^{in} - C_{O_2}^l) + \frac{k_{mem} \cdot A}{V_l} \cdot (C_{O_2}^g - C_{O_2}^l) - \frac{km_o \cdot A}{V_l} \cdot (C_{O_2}^l - C_{O_2}^c)$$

$$\frac{dC_{glu}^l}{dt} = -\frac{km_g \cdot A}{V_l} \cdot (C_{glu}^l - C_{glu}^c)$$

$$\frac{dC_{lac}^l}{dt} = +\frac{km_{lac} \cdot A}{V_l} \cdot (C_{lac}^l - C_{lac}^c)$$

(4.8)

where  $C_{O_2}^l$ ,  $C_{glu}^l$ , and  $C_{lac}^l$  are the averaged oxygen, glucose and lactate concentrations respectively in the bulk liquid layer of the bioreactor;  $C_{O_2}^c$ ,  $C_{glu}^c$ , and  $C_{lac}^c$  are the averaged oxygen, glucose and lactate concentrations respectively in the cell layer of the bioreactor.  $km_o$ ,  $km_{glu}$ ,  $km_{lac}$  are the mass transfer coefficients for transport of oxygen, glucose and lactate across the bulk liquid layer to the cell layer respectively; and  $k_{mem}$  is the oxygen mass transfer coefficient for transport across the membrane to the bulk liquid layer.  $F$  is the medium flow rate,  $A$  is the area for mass transfer between the two layers, and  $V_l$  is the volume of the liquid layer.  $C_{O_2}^{in}$  and  $C_{O_2}^g$  are the inlet dissolved oxygen concentration through flow and through the FEP membrane in saturation with gas phase oxygen concentration, respectively.

### Cell Layer

Molar balances on oxygen, glucose and lactate concentrations are written as,

$$\begin{aligned} \frac{dC_{O_2}^c}{dt} &= + \frac{A \cdot km_{O_2}}{V_c} \cdot (C_{O_2}^l - C_{O_2}^c) - mm_a \cdot (\varepsilon_{\gamma 1} + \varepsilon_{\gamma 2}) - \frac{1}{Y_{cell/O_2}} \cdot growth_o \\ \frac{dC_{glu}^c}{dt} &= + \frac{A \cdot km_{glu}}{V_c} \cdot (C_{glu}^l - C_{glu}^c) - [Y_{glu/O_2} \cdot mm_a] - mm_{an} - \frac{1}{Y_{cell/glu}} \cdot growth_glu \\ \frac{dC_{lac}^c}{dt} &= + \frac{A \cdot km_{lac}}{V_c} \cdot (C_{lac}^l - C_{lac}^c) + \frac{1}{Y_{cell/lac}} \cdot mm_{an} \end{aligned} \quad (4.9)$$

where  $Y_{cell/O_2}$ ,  $Y_{glu/O_2}$ ,  $Y_{glu/lac}$ ,  $Y_{cell/lac}$ ,  $Y_{cell/glu}$  are the yield coefficients. These are discussed in detail in Appendix B.

Oxygen and glucose consumption by aerobic metabolism ( $mm_a$ ) are given by Michaelis-Menten kinetics (Chow *et al.*, 2001). Glucose is also consumed for anaerobic metabolism. As mentioned in section 4.2.1.1 and 4.2.1.2 the rates of glucose consumption and lactate production are directly proportional to the percentage of proliferating cells, a linear dependence with cell growth rate is proposed for anaerobic ( $mm_{an}$ ) metabolism

$$\begin{aligned} mm_a &= \frac{Q_m \cdot C_{O_2}^c}{\left(\frac{K_m}{C_o}\right) + C_{O_2}^c} \\ mm_{an} &= \frac{Y_{glu/lac}}{Y_{cell/lac}} \cdot \mu = \frac{1}{Y_{cell/glu}} \cdot \mu \cdot \varepsilon_{\gamma 1} \end{aligned} \quad (4.10)$$

where  $Q_m$  and  $K_m$  are the Michaelis-Menten parameters;  $\mu$  is the specific growth rate of progenitor cells (cell group 1) and  $\varepsilon_{\gamma 1}$  is the cell volume fraction of this cell type in an averaging

volume. As mentioned before cell volume fraction is defined as the ratio of volume occupied by the cells to the total volume of the selected averaging volume. The specific growth rate of progenitor cells ( $\mu$ ) depends on glucose, oxygen, lactate concentrations and is discussed in more detail below.

Oxygen consumption for cell growth ( $growth\_o$ ) is described by inhibition kinetics as discussed in Chapter 3. Glucose consumption for growth ( $growth\_glu$ ) is given as a Michaelis-Menten function.

$$\begin{aligned}
 growth\_o &= \frac{(kk/C_o) \cdot C_{O_2}^c}{\frac{K_1}{C_o^2} + \frac{C_{O_2}^c}{(K_I \cdot C_o)} + C_{O_2}^{2c}} \\
 growth\_glu &= \frac{k_{glu} \cdot C_{glu}^c}{\frac{K_{glu}}{C_{glu}^o} + C_{glu}^c}
 \end{aligned} \tag{4.11}$$

The cell growth of cell type 1, i.e. the progenitor cells in the cell layer, is written as a function of oxygen, glucose and lactate concentrations. The dependence of growth rate of cell group 1 on glucose and lactate concentration is given by competitive product inhibition kinetics as used by Truskey and coworkers (1990) for HuT-78 cell line. Differentiation of cell type 1 at a rate  $\phi_d^2$  gives rise to the post progenitor cells or cell type 2. The species balances for varying cell volume fractions of cells in the culture is written as,

$$\begin{aligned}
 \frac{d\varepsilon_{\gamma 1}}{dt} &= + f(growth\_o, growth\_glu, inhib\_lac) \\
 &= \left[ \varepsilon_{\gamma 1} \cdot \frac{\mu_m \cdot C_{glu}^c}{\frac{K_s}{C_{glu}^o} \cdot (1 + K_P \cdot C_{lac}^o \cdot C_{lac}^c) + C_{glu}^c} \cdot \frac{(kk/C_o) \cdot C_{O_2}^c}{\frac{K_1}{C_o^2} + \frac{C_{O_2}^c}{(K_I \cdot C_o)} + C_{O_2}^{2c}} \right] - \phi_d^2 \cdot \varepsilon_{\gamma 1} = \varepsilon_{\gamma 1} \cdot \mu - \phi_d^2 \cdot \varepsilon_{\gamma 1} \\
 \frac{d\varepsilon_{\gamma 2}}{dt} &= \phi_d^2 \cdot \varepsilon_{\gamma 1}
 \end{aligned} \tag{4.12}$$



### 4.2.3 Parameter Estimation

The parameters for the model can be obtained by comparing experimental data performed by using a cytokine, directing cells to differentiate along a particular lineage and fitting the model to the total number of early progenitor cells started off with and the total number of mature cells formed. Moreover, on-line measurements of glucose and oxygen consumption and lactate production obtained experimentally in 3-dimensional batch culture units are used to fit the model bulk liquid layer glucose, oxygen and lactate concentrations.

In order to obtain the metabolic and growth parameters, the model equations for species concentrations are reduced for a tissue culture flask system (2-dimensional). This is done to compare with the experimental data of Yan *et al.*, 2001. In the experimental set-up the HCs were grown in 3-dimensional non-woven PET matrices (diameter = 1.4 cm; thickness = 1mm) and placed in 24 culture plates. 2 ml of long-term culture medium was added to each of the plates. Twice weekly medium exchange was performed with 1 ml replaced every week. The cells were cultured for 7-10 weeks.

The model equations of only the liquid layer (equation 4.8) has to be changed to incorporate no-flow conditions for this culture system and are given as,

$$\begin{aligned}C_{O_2}^l &= C_{O_2}^g \\ \frac{dC_{glu}^l}{dt} &= -\frac{km_g \cdot A}{V_l} \cdot (C_{glu}^l - C_{glu}^c) \\ \frac{dC_{lac}^l}{dt} &= +\frac{km_{lac} \cdot A}{V_l} \cdot (C_{lac}^l - C_{lac}^c)\end{aligned}\tag{4.13}$$

Oxygen in this system is not supplied by convective transport by medium flow or by diffusive transport through any membranes. Diffusion of oxygen occurs from the outside gas phase to the bulk liquid layer and then to the cell layer. Assuming that the gradient across the bulk liquid

layer can be neglected due to frequent medium exchanges, the oxygen concentration can be assumed to be constant in the liquid layer and is the same as the 21% gas phase oxygen concentration in equilibrium with liquid. Glucose and lactate concentration change in the liquid layer due to removal from the liquid layer and byproduct addition to the liquid layer of the reactor.

The model equations in the cell layer (equation 4.9) and in the bulk liquid layer (equation 4.13) along with metabolic and growth kinetics (equation 4.10 – 4.12) for the 3-dimensional batch culture were solved in MATLAB, to obtain the time-varying changes in the cell numbers of cell group 1 and group 2, and metabolic species i.e. glucose, lactate and oxygen concentrations. These model results are compared with available experimental results on cell numbers and lactate metabolism (Yan *et al.*, 2001). Yan and coworkers have reported the total cell number and number of progenitor (CD34+) cells in their work. The experimental results are shown below in Table 4.1.

**Table 4. 1 Experimental results of cell numbers from Yan *et al.*, 2001**

Time (weeks)	% CD34+ cells	CD34+ cell number (Cell Type 1)	Total cell no.	Total – CD34+ cell number (Cell Type 2)
0	69.4	$0.35 \times 10^5$	$0.504 \times 10^5$	$0.154 \times 10^5$
3	12.4	$1.89 \times 10^5$	$1.524 \times 10^6$	$1.335 \times 10^6$
5	10.1	$2.46 \times 10^5$	$2.436 \times 10^6$	$2.1896 \times 10^6$
7	7.7	$2.39 \times 10^5$	$3.104 \times 10^6$	$2.865 \times 10^6$

The experimental results on the specific lactate production rate in the liquid medium as a function of time were available for this system. The trapezoidal rule of integration under a given area was used to compute the lactate concentration at specific intervals of time (as shown in Table 4.2). The lactate fold increase is computed comparing the lactate concentration at all time points compared to the initial lactate concentration in the media added to the tissue culture plates.

**Table 4. 2 Experimental result of lactate concentration from Yan *et al.*, 2001**

<b>Time (days)</b>	<b>Sp. Lac Prod. Rate (mg/l/h)</b>	<b>[Lactate] mol/cm<sup>3</sup></b>	<b>Lactate fold increase</b>
0	0.25	$2.360 \times 10^{-8}$	
10	0.7	$5.970 \times 10^{-8}$	2.53
15	0.8	$1.014 \times 10^{-7}$	4.30
20	2.25	$1.860 \times 10^{-7}$	7.88
25	4.9	$3.850 \times 10^{-7}$	16.31
30	6.4	$6.990 \times 10^{-7}$	29.62
35	6.95	$1.153 \times 10^{-6}$	48.86
40	6.95	$1.540 \times 10^{-6}$	65.25

To be noted here, the model reduction, allows for comparison with available on-line measurements of metabolites and cell numbers, in order to obtain the unknown metabolic and growth parameters for this cell type under consideration. Modeling results for cell numbers in cell group 1 and group 2 are plotted in Figure 4.4 (a). The model appears to follow the experimental results very well. Figure 4.4 (b) shows the lactate concentrations varying with time of culture. 50% liquid media is exchanged twice weekly which can be seen as a decrease in lactate concentration every 3.5 days in the culture. The drop in lactate concentration in the cell layer is due to lactate transport to the bulk liquid layer, which as seen in equation 4.14 is driven by a concentration difference between the cell and liquid layer. Medium exchange lowers the lactate concentration accumulation in the bulk liquid layer, and allows for more flux of lactate into the liquid layer. This can be seen as a decrease followed by an increase in lactate concentration in the cell layer, similar to that of liquid layer. The rate of lactate concentration increase is smaller during the initial few weeks which is the time corresponding to the formation of aerobic progenitor cells. However, the lactate concentration reaches a much higher steady state and rate of lactate consumption after every media exchange due to formation of post-progenitor cells. The lactate concentrations in Figure 4.4 (b) are averaged to compute the lactate fold increase as shown in Figure 4.4(c). These results are compared to the experimental data as shown in Table 4.2.

Figure 4.4 (d) shows changes in non-dimensional glucose concentration in the cell layer and the liquid layer in this 3-dimensional culture system. With every media exchange the glucose concentration in the bulk liquid layer increased, thereby increasing the supply to the cell layer. However over the culture time of 69 days the rate of decrease in glucose concentration increases with time even with frequent feeding because of increase in cell number. The drop in non-dimensional oxygen concentration in the cell layer is only by 20% because of the high end supply in the liquid layer maintaining uniformly maximum oxygen concentration in this layer (shown in Figure 4.4(e)).

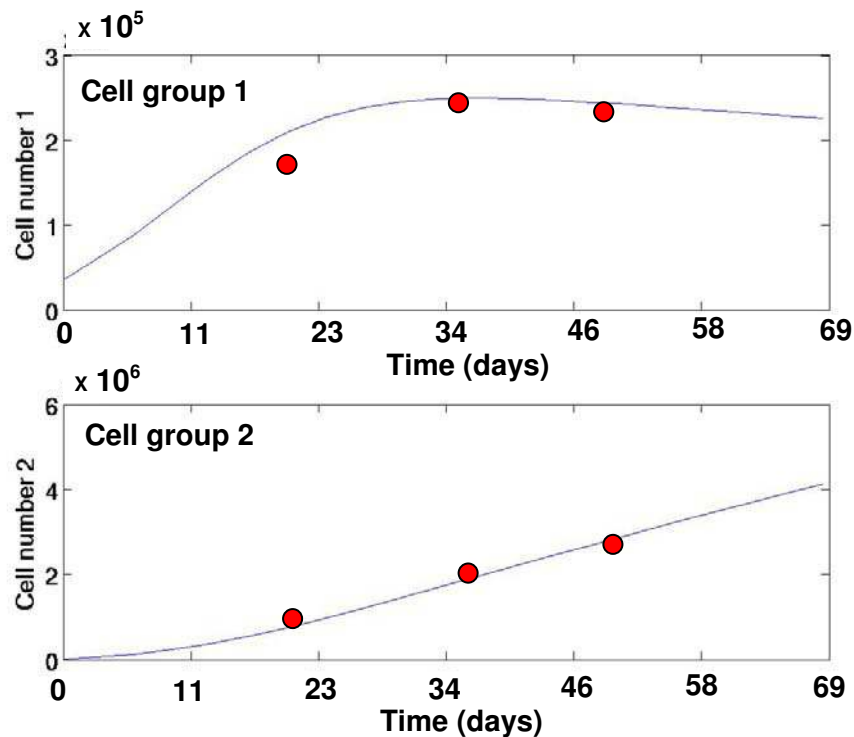


Figure 4.4 a Increase in progenitor cells (group 1) and post-progenitor cells (group 2) over culture time in 3-dimensional batch culture. Modeling results (solid line) compared to available experimental data (dots) from Yan *et al.*, 2001 shown in Table 4.1

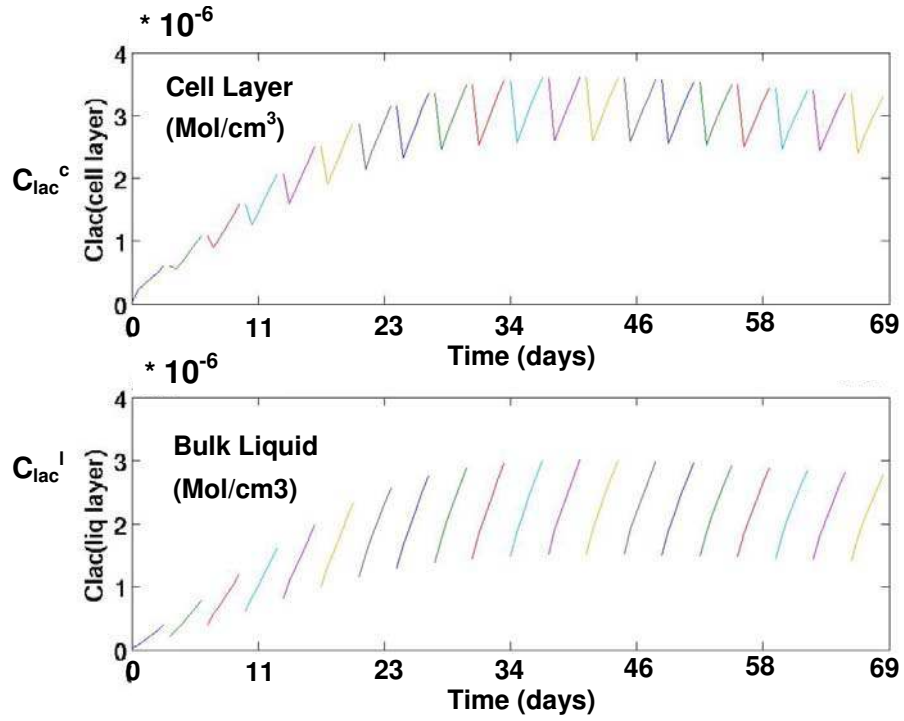


Figure 4.4 b Lactate concentration in 3-dimensional batch culture

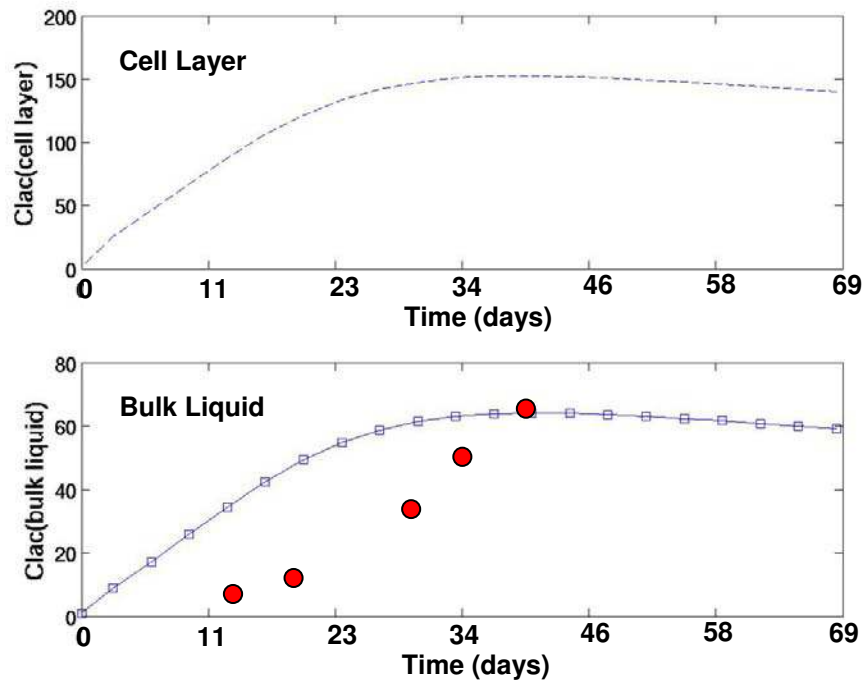


Figure 4.4 c Fold increase in Lactate concentration in 3-dimensional batch culture. Modeling results (solid line) compared to available experimental data (dots) from Yan *et al.*, 2001 shown in Table 4.2

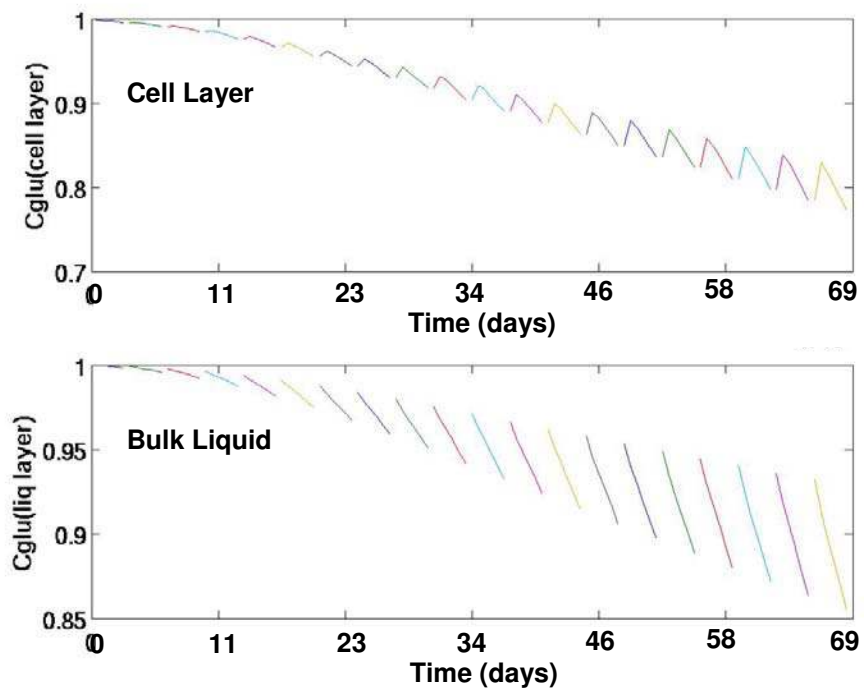


Figure 4.4 d Glucose concentration in 3-dimensional batch culture

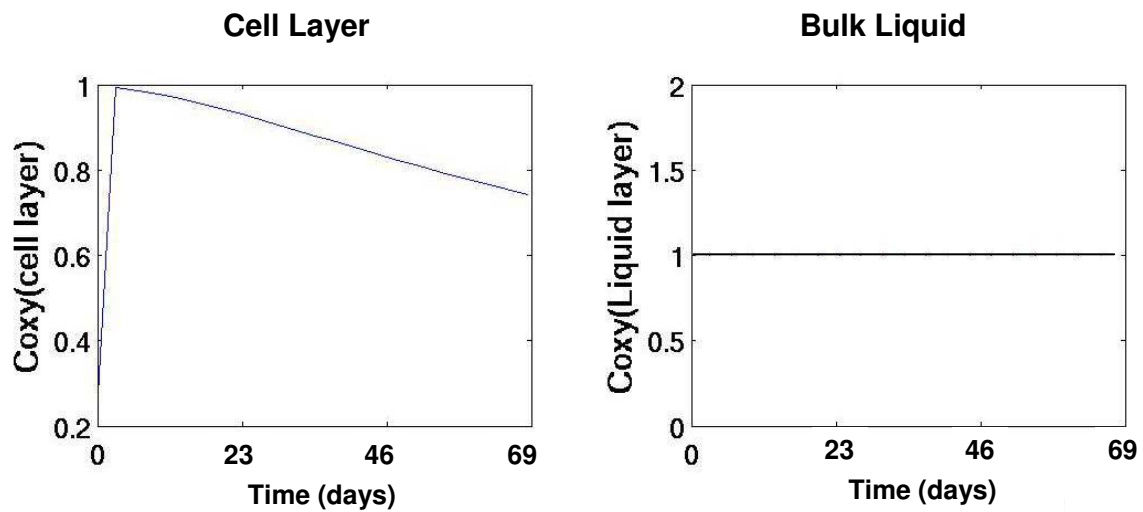


Figure 4. 4 e Oxygen in 3-dimensional batch culture

This model did not seem to fit the lactate kinetics well as seen in Figure 4.4 (c). This is possibly because the above model establishes a direct correlation of lactate production with the growth of progenitor cells. However, as mentioned in section 4.2.1.2, it is the post-progenitor cells i.e. non-CD34+ cells are the cells that are really anaerobic, and a major contributor to lactate produced in cultures. Therefore, the kinetic expression for the anaerobic lactate production rate in equation 4.10 was modified as given by the ‘linear chemometric model’,

$$\begin{aligned}
 mm_{an} &= \alpha \cdot (\text{cell no.}_1) + \beta \cdot (\text{cell no.}_2) \\
 &= \alpha \cdot (\text{cell no.}_1) + \beta \cdot (\text{Tot cell} - \text{cell no.}_1)
 \end{aligned}
 \tag{4.14}$$

The lactate production rates for cell group 2 ( $\beta$ ) was set to be higher than the lactate production coefficient of cell type 1 ( $\alpha$ ) as described above. The new model results on number of cells of each group and the lactate fold increase are shown in Figure 4.5 (a) and 4.5 (b). The change in the expression of rate of anaerobic metabolism expression is able to obtain model results on lactate fold increase similar to the experimental results available (Figure 4.5 (b)). During the early weeks of culture the number of cells of group 1 or progenitor cells is high as seen in Figure 4.5 (a). However, by the process of differentiation in culture the number of progenitor cells drops giving rise to post-progenitor cells or cells of group 2. This new formulated model is also better able to handle the experimental results in terms of cell numbers of various cell groups.

These estimated specific metabolic and growth parameter values are enlisted in Appendix B. So now these values and the functional forms of glucose, lactate, and oxygen metabolism for these types of cells can be used to compute the cell kinetics and nutrient-byproduct concentrations in the bioreactor system discussed in Chapter 4.2.2.

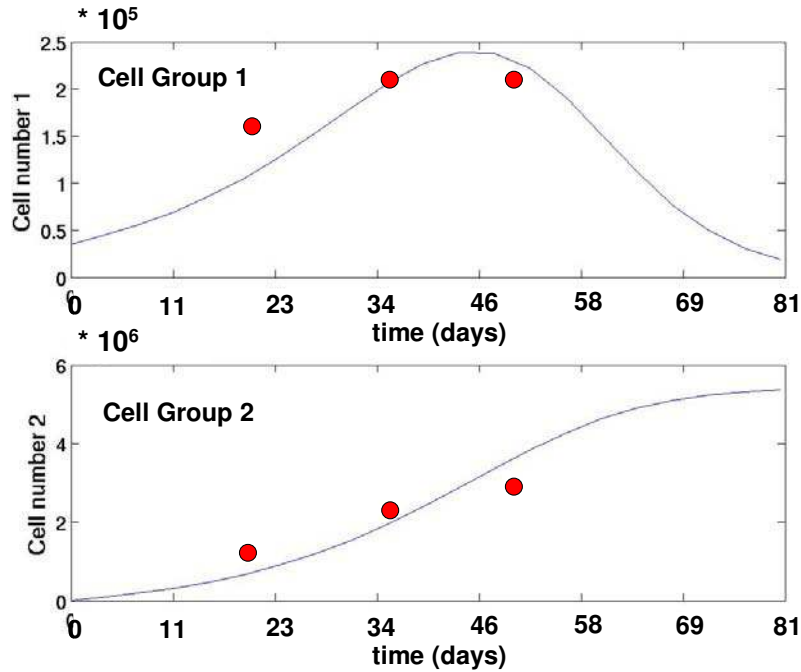


Figure 4.5 a Increase in progenitor cells (group 1) and post-progenitor cells (group 2) over culture time in 3-dimensional batch culture using new kinetic expression for anaerobic metabolism shown in equation 4.15. Modeling results (solid line) compared to available experimental data (dots) from Yan *et al.*, 2001 shown in Table 4.1.

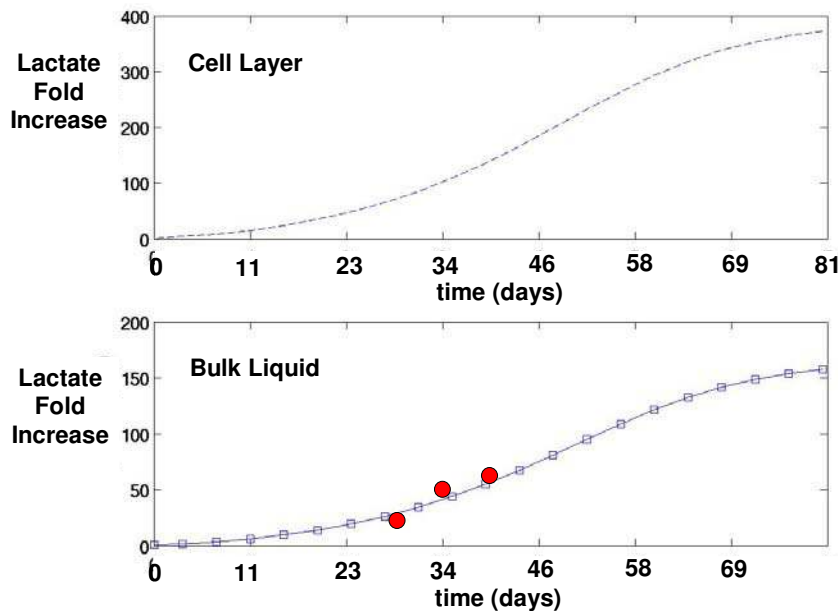


Figure 4.5 b Fold increase in lactate concentration in 3-dimensional batch culture using new kinetic expression for anaerobic metabolism shown in equation 4.15. Modeling results (solid line) compared to available experimental data (dots) from Yan *et al.*, 2001 shown in Table 4.2



#### 4.2.4 Preliminary results on Well-Mixed Bioreactor Model

Once the rate parameters are obtained by model-experimental fit for the current cell type in 3-dimensional batch reactor systems, these numbers are used to predict the cell growth and metabolic characteristics for the well-mixed reactor. The growth of progenitor cells (Group 1) and post progenitor cells in the reactor are shown in Figure 4.6 (a). The model predicts an increase in cells of both group 1 and group 2 throughout the entire time of culture. The maximum progenitor cell number and post progenitor cell number reached are  $\sim 6 \times 10^4$  cells and  $\sim 1 \times 10^6$  cells by the end of  $\sim 70$  day.

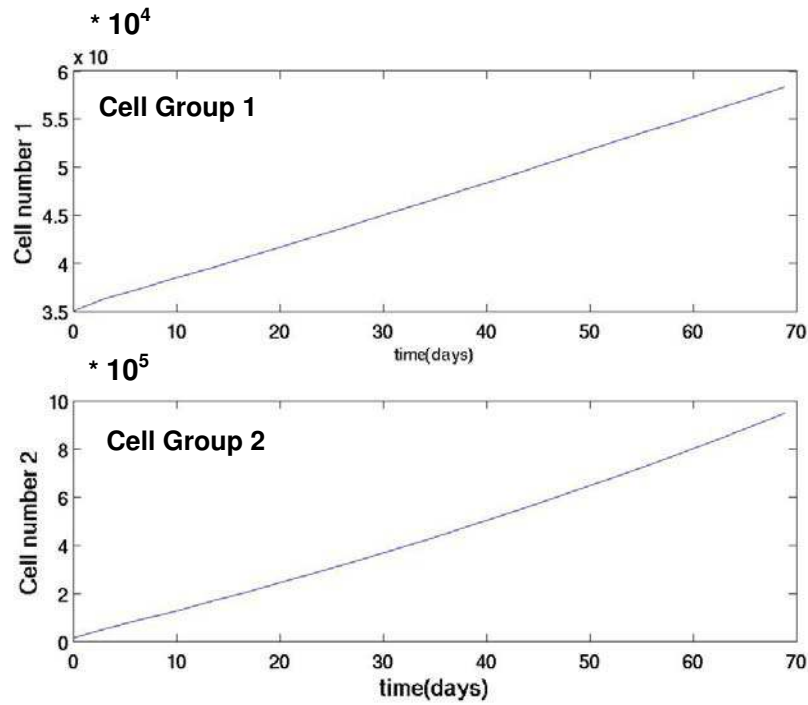


Figure 4.6 a Increase in progenitor cells (group 1) and post-progenitor cells (group 2) over culture time in 3-dimensional well-mixed perfusion bioreactor system. Model parameters used are discussed in Appendix B.

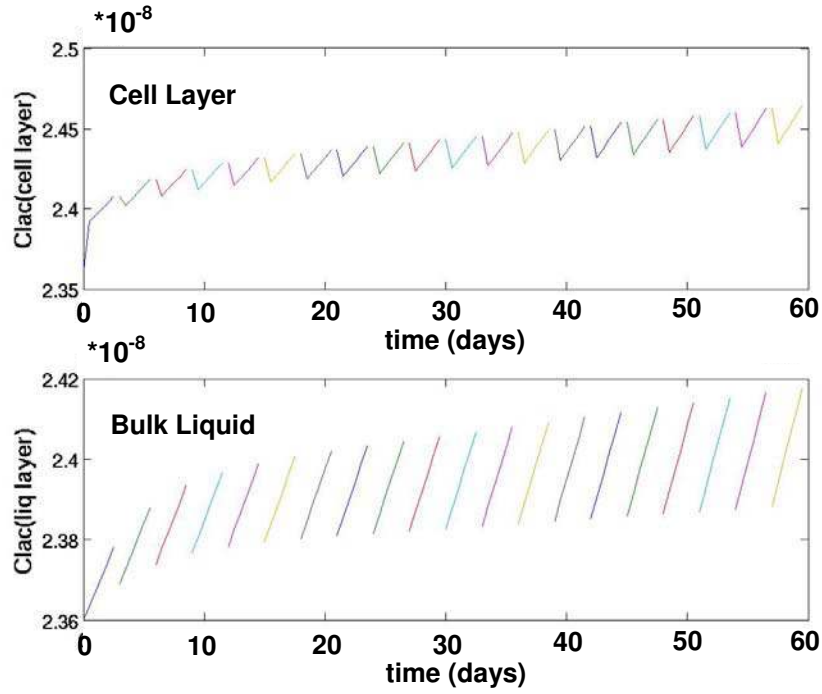


Figure 4.6 b Lactate concentrations in 3-dimensional well-mixed perfusion bioreactor system. Model parameters used are discussed in Appendix B.

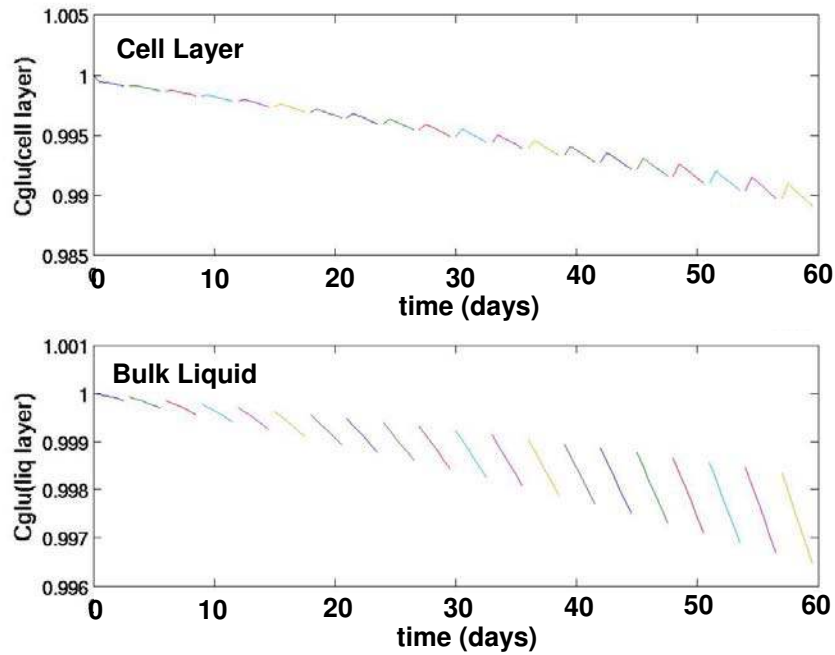
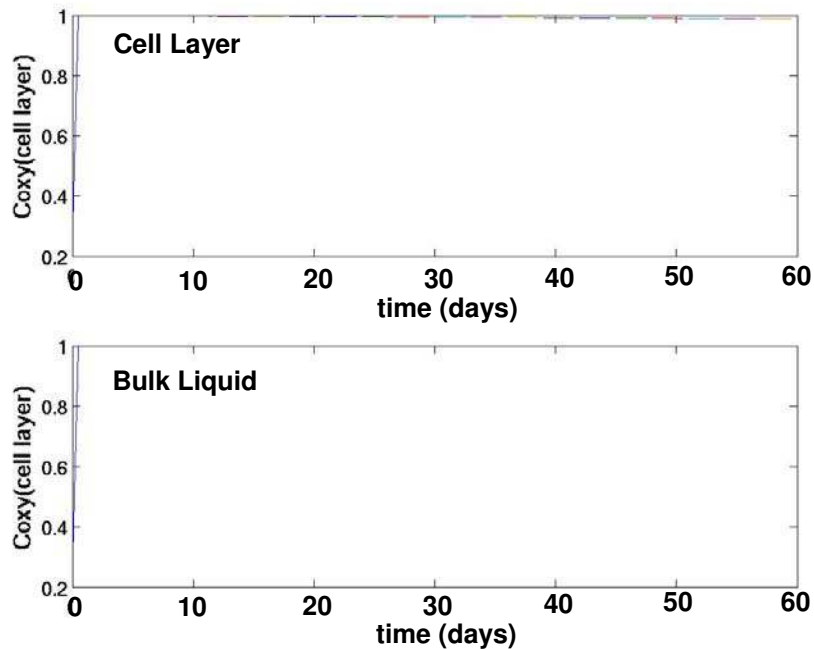


Figure 4.6 c Glucose concentrations in 3-dimensional well-mixed perfusion bioreactor system. Model parameters used are discussed in Appendix B.



**Figure 4. 6 d Oxygen concentrations in 3-dimensional well-mixed perfusion bioreactor system. Model parameters used are discussed in Appendix B. Oxygen concentration increases to a non-dimensional value of one and reaches a steady state**

The supply of glucose and removal of lactate by frequent medium flow reduces the drop in glucose concentration and rise in lactate concentration in the cell and liquid layers of the bioreactor as compared to batch culture. This is shown in Figure 4.6(b) and 4.6(c). Moreover, continuous supply of oxygen by medium flow and diffusive transport through the FEP membrane keeps the oxygen concentration in the bulk liquid layer high and prevents drop of concentration in the cell layer. The variations in oxygen concentration in the cell and bulk liquid layer of the reactor are shown in Figure 4.6(d).

### 4.3 Conclusions

Summarizing, this chapter discusses the need for quantitative estimation of other environmental factors along with oxygen, such as metabolite glucose and by-product lactate concentration in order to improve the model developed in Chapter 3. The idea of co-existence of more than one cell type in culture is incorporated by the use of a simple two cell-group model. The cell types

are separated on the basis of large differences in their metabolic lactate production rates. Experimental data for 3-dimensional batch culture (tissue-flask) system is utilized for obtaining the rate parameters for the CD34+ or the progenitor cells (cell group 1) and the mature or post-progenitor cells (cell group 2) by model-experimental data fit. Once a suitable list of parameters is obtained, these numbers are utilized for predicting cell growth, glucose and oxygen consumption, and lactate production in the bioreactor system. The model developed here is for a well-mixed reactor system. This is done by spatially averaging the concentration of metabolites and cells in the cell layer and the bulk liquid layer of the perfusion reactor unit discussed in chapter 3. The current study shows that the reactor system can sustain larger cell growth rates, by maintaining the glucose and oxygen concentration high enough and by efficient removal of lactate.

#### **4.4 Recommendations for Future Work**

This model can be extended by improving the well-mixed reactor model by incorporating the effects of mass transport due to flow and computing the spatial distribution of nutrients and products. This could be done by adding glucose, lactate, and cell growth balances for the progenitor and post-progenitor cell types to the full spatial variation model presented in Chapter 3. The mathematical model results of glucose, oxygen and lactate concentrations in the bulk liquid layer can be compared to experimental results obtained from the experiment on the 3-dimensional perfusion bioreactor from Dr Ma's lab. The effects of rates of nutrients (oxygen and glucose) delivery and byproduct (lactate) removal and their spatial distributions in the cell layer on cell growth can be studied. Initial calculation of the model would incorporate two cell types as developed above. However, in further studies glucose consumption and lactate production by multiple cells in the same lineage and in different lineages need to be studied. This understanding would add to the long-range goal of optimization and control of the developed bioreactor. Despite the large potential contribution, numerical models involving multiple cell types and their kinetic and metabolic behavior in culture systems will only be useful when properly validated. This requires a large amount of systematic experimental data with respect to the same or similar reference systems. Hence, suitable experimental strategies should be

developed to obtain this information. The model is a good way of suggesting new experimental designs by making it easy for the experimenter to know the parameters to be accurately determined.

The growth and kinetic parameters for the perfusion unit can then be obtained by fitting model to available experimental data for this system. This model could then be used to obtain variable variations in terms of design, flow, and media used for the 3-dimensional perfusion bioreactor model (FSU). Moreover, the effects of 3-dimensional cell-cell interactions and the formation of extracellular matrix (ECM) leading to cell-ECM interactions on cell behavior as discussed in Chapter 4.2.1.5 need to be studied. The study could incorporate model developments for different matrix geometries, to improve upon cell growth in the reactor unit. One such matrix type is suggested in Chapter 4.2.1.4 of the text. This model when complete would closely replicate the *ex vivo* environment in cultures more effectively. This robust model can be used in the estimation of different cell numbers and in the long run for designing appropriate conditions for the formation of the cell types of interest.

## CHAPTER 5

### **EFFECTS OF OXYGEN TRANSPORT ON 3-DIMENSIONAL HUMAN MESENCHYMAL STEM CELL TISSUE DEVELOPMENT IN PERFUSION AND STATIC CULTURES**

*(Reproduced in part with permission from Biotechnology Progress, in press Zhao et al., 2005.  
Unpublished work copyright [2005] American Chemical Society.)*

#### **5.1 Problem Statement**

Human Mesenchymal Stem Cell's (hMSC's) potential applications for treating wide range of diseases including osteogenesis imperfecta (Horwitz *et al.*, 1999, Prockop, 1997), stroke (Chen *et al.*, 2004, Chen *et al.*, 2003), and heart failure (Orlic *et al.*, 2001) have made it necessary to obtain high yields of these cells *in vitro* in suitable culture devices. Experimental data on hMSC growth-kinetics and spatial growth patterns, metabolism, and oxygen consumption in various hMSC culture devices such as static and perfusion units have been studied (Zhao *et al.*, 2005 (a,b)) to elucidate the effects of perfusion culture on cell growth and tissue development. The modular perfusion system similar to the unit discussed in Chapter 3 was used to measure growth kinetics, metabolism, and oxygen consumption experimentally in Dr Ma's lab (Florida State University). Convective oxygen transport was found to be important for enabling and sustaining high cell growth rates, high cell density, and uniform growth pattern. In order to reemphasize the significance of flow quantitatively in terms of oxygen delivery on hMSC development, a dynamic mathematical model describing oxygen distribution in the static and perfusion culture units is developed. The model is based on the principles of mass transport and reaction and

provides estimates of the spatio-temporal oxygen concentration profiles in the two units, which is difficult to be measured experimentally. The objective here is not to develop an *a priori* predictive model but to use the developed model along with the available experimental data and understand the role of oxygen transport on cell behavior (growth and metabolism) in these different culture units.

## 5.2 Reactor Designs

### Perfusion reactor design (Unit 1)

Unit 1 represents the 3-dimensional perfusion chamber as shown as a schematic in Figure 5.1(a). The dimensions of this perfusion unit are similar to the one discussed in Chapter 3. hMSCs are grown in the 3-dimensional matrix and form what is termed the ‘cell layer’ of the chamber. This cell layer is assumed to be a rectangle for modeling simplicities and also because the accuracy of calculation does not need the exact dimensions of circular constructs used for experiments (Zhao *et al.*, 2005 (a)). Medium supplying nutrients to cells in the cell layer flows through the perfusion chambers above and below the matrix and is termed the ‘bulk liquid layer’.

As mentioned earlier oxygen transport to the bulk liquid layer is by convective and diffusive transport. Nutrients are supplied by convection through either a once through mode or by recirculation of the bulk liquid layer medium. Diffusion of oxygen from the incubator occurs through the gas permeable, FEP membrane into the perfusion chambers. In the cell layer oxygen is delivered by diffusive transport only. Convective oxygen supply in the construct is not proposed because the matrix is assumed to be incompressible and the two perfusion chambers above and below the matrix are identical with respect to flow and resistances. Moreover, the absence of flow in the cell layer prevents flow restrictions on cell growth by shear or other mechanical forces and promotes adhesion of the cells to the matrix surface.

### Static culture design (Unit 2)

In order to study the effects of flow on tissue development the same 3-dimensional PET matrix is placed in a tissue culture plate as is used in a static culture unit. Unit 2 (Figure 5.1b) is used to

model this static culture system. The unit used for the model is a similar rectangular block 10 cm length, 2.5 cm width, and 13.2 mm thick as the flow unit. The 3-dimensional PET porous matrix (1.2 mm thick) is placed on the bottom of the reactor and forms the ‘cell layer’. Medium supplying nutrients (oxygen) above the matrix forms the ‘bulk liquid layer’. The mode of oxygen supply to the cells in the cell layer is only by diffusion through the stagnant liquid layer above the construct. Transport of oxygen in the cell layer is also by diffusion only, again to avoid the effects of shear and to allow cell adhesion to the matrix. In addition to the absence of convection in the bulk liquid layer of Unit 2, the surface area for oxygen transport to the construct is also reduced to one half of that in the perfusion bioreactor (Unit 1), reducing the amount of oxygen delivered to meet cell demands.

### **5.3 Experimental Data**

Cell numbers in the PET matrices in static and perfusion culture units were determined by DNA assays. The cell density was computed by dividing the cell number and matrix volume and is shown as open triangles in Figure 5.2 (a), (b). Oxygen tension was measured through sampling ports located at the inlets and outlets of the perfusion chambers. Oxygen consumption is computed by the difference between the measured oxygen tensions at the two ports. The specific oxygen consumption rate in the perfusion reactor was obtained by dividing this oxygen consumption in the perfusion chambers by the cell numbers at that time point and the residence time of the nutrient media (Zhao *et al.*, 2005 b).

### **5.4 Mathematical Model Development**

Mathematical models for oxygen transport and reaction are modeled in perfusion and static culture units to assess the importance of perfusion flow on cell proliferation and metabolism.



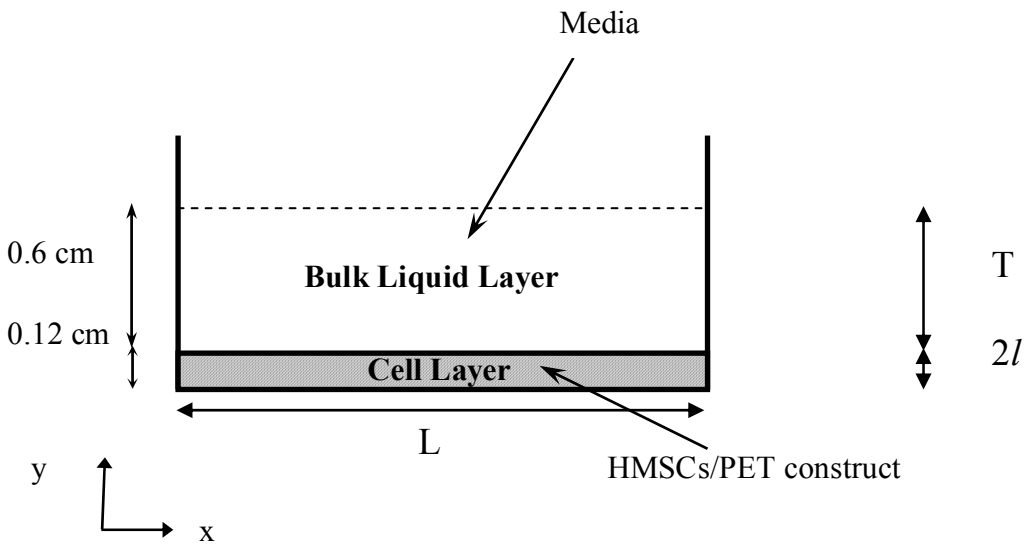
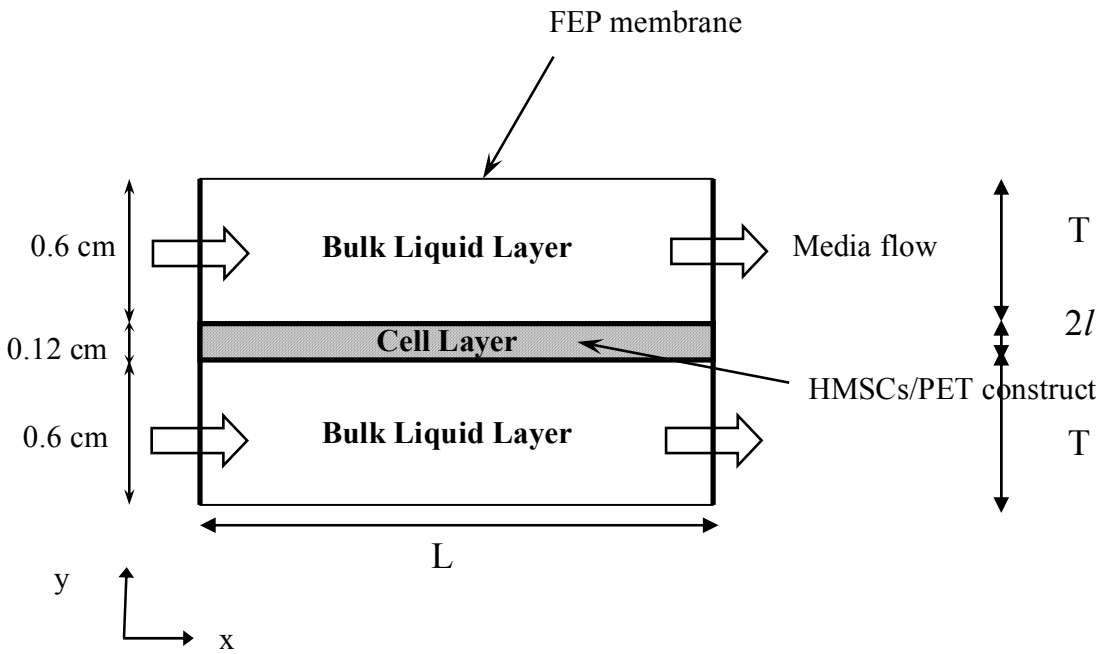


Figure 5. 1 Schematic of the Culture units (a) Perfusion Reactor (Unit 1) (b) Static Culture (Unit 2)

### 5.4.1 Model Equations Perfusion Reactor (Unit 1)

For the model development of Unit 1, only half of the reactor needed to be considered because of symmetry. Species continuity equations describing the spatial and temporal variations of oxygen concentration were written for both the bulk liquid layer and the cell layer. The method of volume averaging was used to develop a single species continuity equation for the multiphase cell layer made up of cells and medium solution (Pathi *et al.*, 2005; Galban *et al.*, 1999; Whitaker *et al.*, 1999). It can be noted that the overall reactor model was solved in two dimensions (length and depth) since variation over the width are small compared to the length and depth. Similar formulation of the model and boundary conditions as described in chapter 3 was considered for this reactor unit (equations 3.16).

$$\begin{aligned} \frac{\partial c_l}{\partial t} &= (\nabla D_\beta \cdot \nabla c_l) - v_x \cdot \nabla c_l && \text{Bulk Liquid Layer} \\ \frac{\partial c_c}{\partial t} &= \nabla D_{eff} \nabla c_c - \frac{Q_m \cdot K_{eq} \cdot \varepsilon_\gamma \cdot c_c}{(K_m / C_o) + K_{eq} \cdot c_c \cdot \varepsilon_\gamma} && \text{Cell Layer} \end{aligned} \tag{5.1}$$

where  $c_c$  and  $c_l$  are non-dimensional oxygen concentration in the cell layer and bulk liquid layer<sup>1</sup>;  $\varepsilon_\gamma$  is the cell volume fraction;  $v_x$  is the velocity profile;  $D_\beta$  is the oxygen diffusion coefficient of oxygen in the bulk liquid layer;  $D_{eff}$  is the effective diffusion coefficient;  $K_{eq}$  is the equilibrium coefficient of oxygen between the cell and the nutrient phases of the averaging volume. The effective diffusion coefficient accounts for the diffusion in the cellular and the nutrient (non-cellular) phase as well as the mass transport between the two phases in the cell layer (Pathi *et al.*, 2005; Ochoa *et al.*, 1988; Galban *et al.*, 1999 a,b; Whitaker *et al.*, 1999). The one-dimensional flow is oriented along the reactor length (x-direction) and is assumed to be laminar ( $Re = 0.28$ ) corresponding to flow rate of 0.1 mL/min). The reaction rate kinetic function describing the overall oxygen consumption (for metabolic and growth processes) is assumed to follow

---

<sup>1</sup> The oxygen concentration terms are non-dimensionalized by dividing the oxygen concentration at all point in space and time with the dissolved oxygen concentration in equilibrium with air ( $C_o=20\%$  oxygen or 152 mmHg or  $2.10 \cdot 10^{-7}$  mol/cm<sup>3</sup>).

Michaelis-Menten kinetics (Chow *et al.*, 2001 a, b).  $Q_m$  and  $K_m$  are Michaelis-Menten parameters.

Cell growth in the model is expressed in terms of the cell volume fraction ( $\varepsilon_\gamma$ ). The cell volume fraction is defined as the fraction of volume occupied by cells in the averaging volume,  $V_\gamma$ , relative to the total averaging volume  $V$  in the cell layer of the culture units. The cell mass balance in the cell layer of the perfusion reactor is written assuming exponential homogeneous growth and neglecting effects of oxygen on cell growth and occurrence of cell death and is given as,

$$\varepsilon_\gamma = \varepsilon_{\gamma 0} e^{m \cdot t} \quad (5.2)$$

where  $\varepsilon_{\gamma 0}$  is the initial cell volume fraction (computed from initial cell density) and  $m$  is the cell growth rate.

#### 5.4.2 Model Equations Static Culture (Unit 2)

For the static culture unit there is no convective flow either in the bulk liquid layer or in the cell layer. The effective area of supply of oxygen is reduced to one half as the supply is only at the upper boundary of the construct. Similar to the perfusion Unit 1 material balances describing the oxygen transport and reaction are written in the bulk liquid layer and cell layer for this unit. The continuity equation describing oxygen concentration variation due to diffusion in the bulk liquid layer and cell layer is written as,

$$\begin{aligned} \frac{\partial c}{\partial t} &= \nabla D_\beta \cdot \nabla c && \text{Bulk Liquid Layer} \\ \frac{\partial c}{\partial t} &= \nabla D_{eff} \nabla c - \frac{Q_m \cdot K_{eq} \cdot \varepsilon_\gamma \cdot c}{(K_m / C_o) + K_{eq} \cdot c \cdot \varepsilon_\gamma} && \text{Cell Layer} \end{aligned} \quad (5.3)$$

*Boundary conditions*

Oxygen concentration at the upper boundary of the bulk liquid layer is in equilibrium with 21% oxygen concentration in gas phase ( $C_{atm}$ ). This boundary condition is written as,

$$c = C_{atm} \quad \forall x = [0, L] \quad y = 2l + T \quad (5.4 \text{ a})$$

The equal flux condition exists at the interface of the cell layer and the liquid layer, and it is given as,

$$-D_{\beta} \nabla c \Big|_{liquidlayer} = -D_{eff} \nabla c \Big|_{celllayer} \quad (5.4 \text{ b})$$

As for the perfusion unit it is assumed that there is no flux of oxygen along the external boundaries of the cell layer with the solid walls of the reactor. Hence,

$$\nabla D_{eff} c = 0 \quad \forall y = [0, 2l] \quad x = 0 \quad (5.4 \text{ c})$$

$$\nabla D_{eff} c = 0 \quad \forall y = [0, 2l] \quad x = L \quad (5.4 \text{ d})$$

$$\nabla D_{eff} c = 0 \quad \forall x = [0, L] \quad y = 0 \quad (5.4 \text{ e})$$

As in perfusion unit the dependence of cell mass on cell volume fraction for the static culture unit is also written by assuming exponential homogeneous growth and neglecting effects of oxygen on cell growth and occurrence of cell death as,

$$\varepsilon_{\gamma} = \varepsilon_{\gamma 0} e^{m \cdot t} \quad (5.5)$$

where  $\varepsilon_{\gamma 0}$  is the initial cell volume fraction (computed from initial cell density information for this reference system) and  $m$  is the cell growth rate.

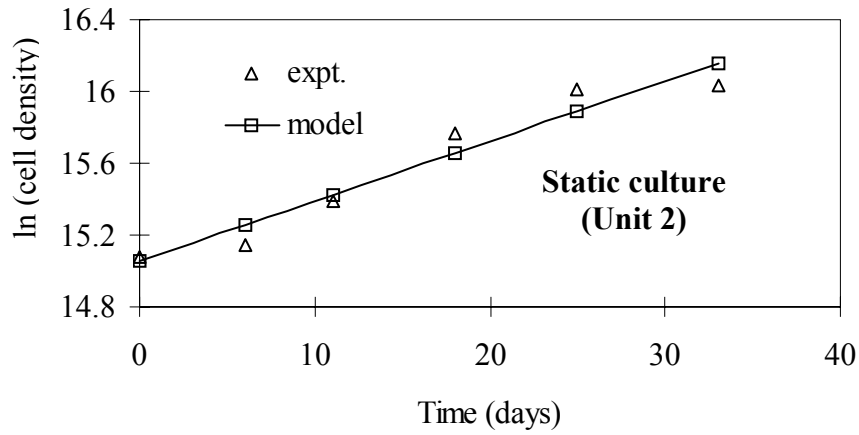
### 5.4.3 Parameter Estimation

#### *Metabolic parameters:*

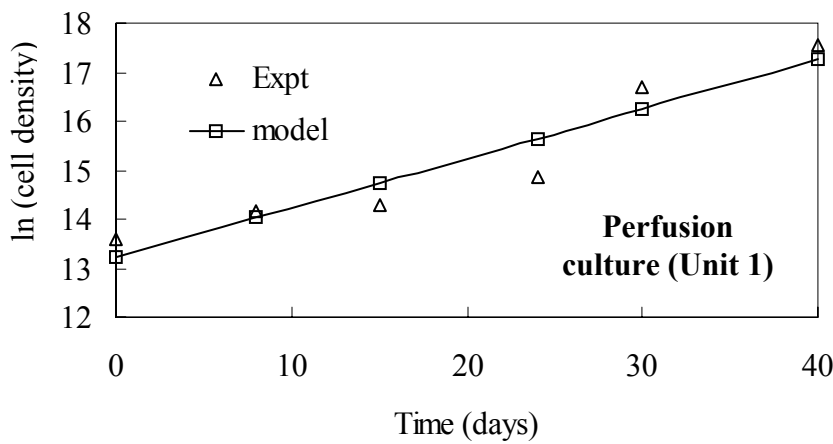
The specific oxygen consumption rate,  $Q_m$  for perfusion unit (Unit 1) is directly determined from experimental data using a second order polynomial equation fit (Figure 5.3). The cell growths in static and perfusion culture units are seen to be similar for the first 24 days of culture. Hence  $Q_m$  for the static culture unit is obtained by averaging the specific oxygen consumption of the first three experimental data points obtained for the perfusion unit (Figure 5.3).  $K_m$  value for hMSCs have been reported in literature to be in the similar range as that of other human cells i.e.  $\sim 1.5 - 7.6$  mm Hg of the saturation oxygen tension (Chow *et al.*, 2001 a, b; Peng *et al.*, 1996 a). So for our model a  $K_m$  value of  $0.05 \cdot C_o$  (7.6 mm Hg) is chosen for oxygen consumption in the static and perfusion units.

#### *Cell growth parameters*

The cell growth rate for hMSCs in perfusion and static culture units are determined by statistical methods only during the growth phase. Linear least square regression analysis is used to obtain the best-fit curve as shown in Figure 5.2 (e-Handbook of Statistical Methods). The exponential growth rate coefficient  $m$  is calculated to be  $1.177 \times 10^{-6} \text{ s}^{-1}$  and  $3.875 \times 10^{-7} \text{ s}^{-1}$  for perfusion reactor (Unit 1) and static culture (Unit 2) respectively. Using the value of this computed growth coefficient and known initial cell density for the respective units in equation 5.2 and 5.5 cell growth function for the perfusion unit (Unit 1) and static culture unit (Unit 2) are generated. Appendix C lists down all the model parameter values.



(a)



(b)

**Figure 5. 2 Growth kinetics of hMSCs under (a) static and (b) perfusion conditions. Cell density is expressed in cells/ml.**

### 5.4.4 Solution Procedure

Linear least square regression analysis was used to obtain the best-fit curves for computing growth rate coefficients. The equations describing variations in oxygen concentration in the bulk liquid layer and in the cell layer (equation 5.1) and the cell growth (equation 5.2) in space and time were solved simultaneously coupled with the appropriate boundary conditions (equation 3.16 detailed in Chapter 3) and growth parameters for perfusion culture (Unit 1). Similarly for the static culture (Unit 2), species continuity balances equation 5.3 coupled with specific growth kinetics (equation 5.5) were solved using the boundary conditions stated in equation 5.4. A MATLAB (version 6.5, The Mathworks, Inc.) based FEMLAB (version 2.3, COMSOL) program utilizing a finite element method was used to numerically solve the system of partial differential equations. The oxygen concentration in both units at the initial time is set to be  $C_{atm}$  (oxygen concentration in equilibrium with 21% oxygen in gas phase). The local oxygen concentrations obtained are macroscopically averaged to obtain the area averaged oxygen concentration as a function of time (area averaging approach discussed in detail in Chapter 3).

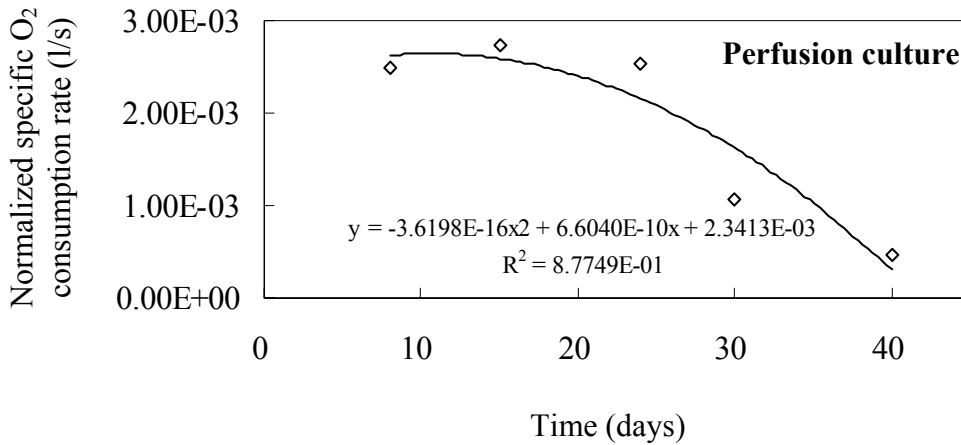


Figure 5. 3 Experimental results of the specific oxygen consumption rate (open diamond) throughout the culture period and polynomial fit for model development (solid line)

## 5.5 Results and Discussion

HMSCs modeled to be grown in similar 3-dimensional PET constructs placed under different flow conditions, i.e. static (or no-flow) vs. perfusion (or flow), are believed to have different cell growth and metabolic oxygen needs. Mathematical models can provide a better understanding of the complex interplay between the spatial and temporal oxygen concentration distribution in the reactors and its role in functional tissue development. Therefore, the oxygen profiles in the perfusion and static culture units are simulated and compared.

The spatial and temporal variations of oxygen concentration in the cell layer and bulk liquid layer of the perfusion reactor (Unit 1) are shown in Figure 5.4(a) and 5.4(b), respectively. The color represents the oxygen concentration variation in space, along the reactor length (from 0 – 10 cm) and thickness (from 0 – 0.66 cm). The oxygen concentration of the inlet flowing liquid was set to values in equilibrium with 21% gas phase oxygen (which corresponds to the non-dimensional value 1.05). The oxygen concentration decreased along with reactor depth and flow direction. The gradients in the liquid layer (Figure 5.4b) are believed to arise from mass transfer and flow coupled with reaction, i.e., consumption by cells in the cell layer, that consume oxygen at a faster rate than it can be supplied. Figure 5.4(a) shows the oxygen concentration variation in time and space for the flow Unit 1 in the cell layer. As the cells in the matrix (or the cell layer) grow exponentially, the highest oxygen consumption is to be expected at the later periods of time. However, during these times the specific oxygen consumption rate of these cells decreases considerably (as obtained from experimental data shown in Figure 5.3), thus decreasing the total rate of oxygen consumption. This decrease in specific oxygen consumption rate and the large supply of oxygen by convective flow leads to an increase in the oxygen concentration around day 35.



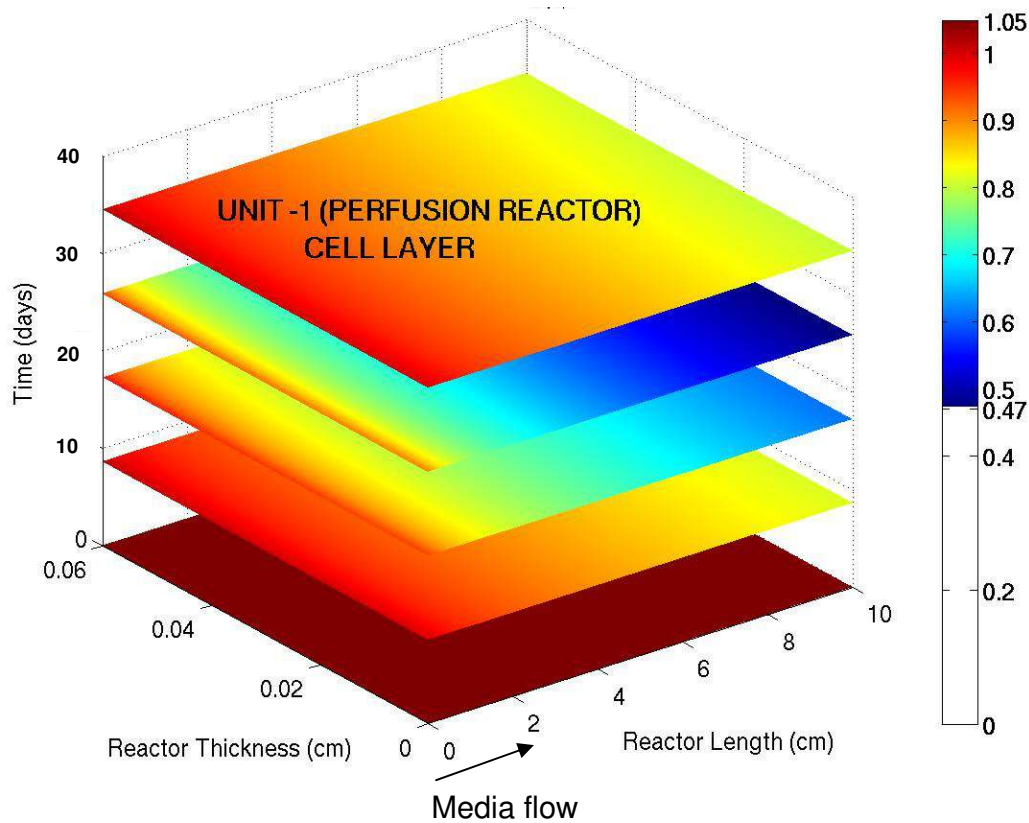


**Figure 5.4 a Mathematical simulation of the spatio-temporal variation of oxygen concentration in the cell layer of the perfusion bioreactor Unit 1**

For static culture (Unit 2), the calculated growth rate from the experimental data (Figure 5.2b) and oxygen consumption parameters as described in the parameter estimation section are used to determine the oxygen concentration distribution. Oxygen concentration profiles in the bulk liquid layer and the cell layer are obtained as a function of space and time for the no-flow Unit 2 (Figure 5.4c). Compared with perfusion culture, this unit has a more uniform oxygen concentration distribution in space but a faster depletion during the whole culture time period. The larger depletion of oxygen in static culture (drops to non-dimensional value of 0.19) compared to the perfusion bioreactor (drops to a non-dimensional value of 0.47), is attributed to the mode of oxygen supply, the surface area for oxygen supply, different cell growth kinetics and, the physiological differences in specific oxygen consumption in the two units.

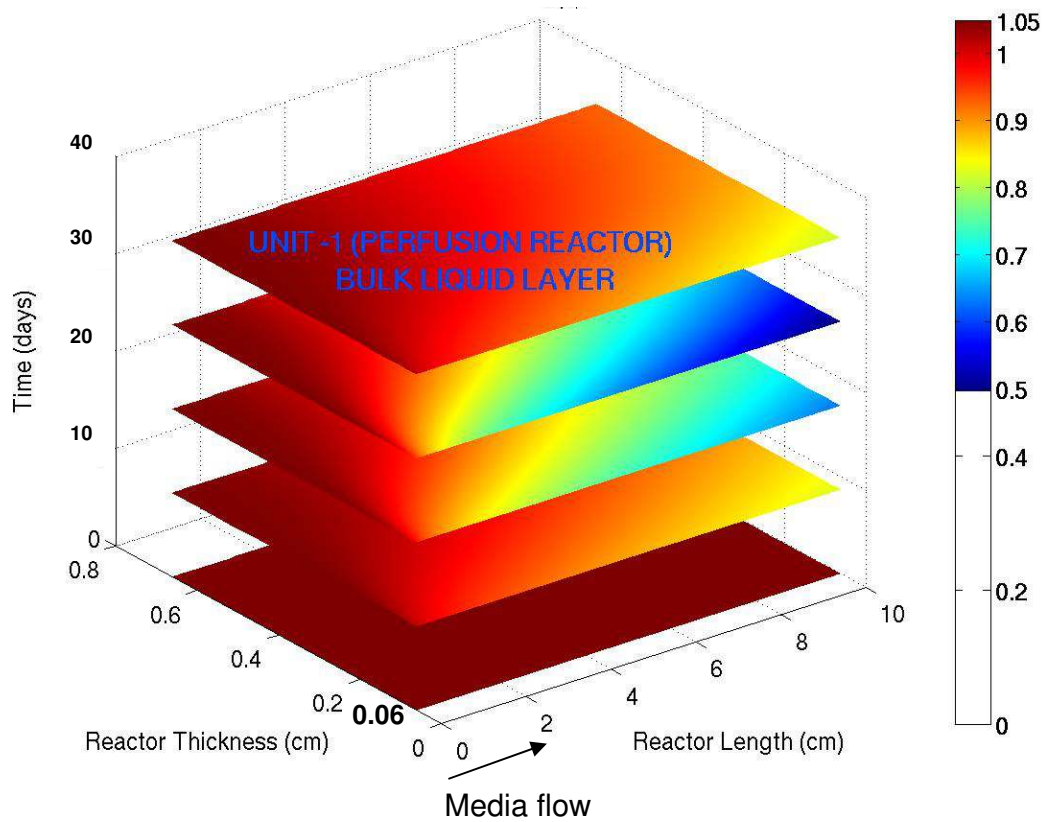


**Figure 5.4 b Mathematical simulation of the spatio-temporal variation of oxygen concentration in the bulk liquid layer of the perfusion reactor Unit 1**

The 2-dimensional concentration profiles in the cell layer of the static (Figure 5.4 c) and perfusion (Figure 5.4 a) units are spatially averaged to obtain the macroscopically averaged oxygen concentration variation in time. As also seen in the spatial-temporal plots the averaged result shows that oxygen concentration gradually decreased in the cell constructs or the cell layer both in static and perfusion units (Figure 5.5). However, the predicted depletion rate of oxygen in the static culture unit is approximately double that of the perfusion unit, confirming that the presence of flow in liquid layer prevents the depletion of oxygen in the cell layer of the bioreactor throughout the course of the culture. The increase of averaged oxygen level in both bulk media and cell constructs of the perfusion unit after 35 days are attributed to the decreased specific oxygen consumption rate and higher cell densities.

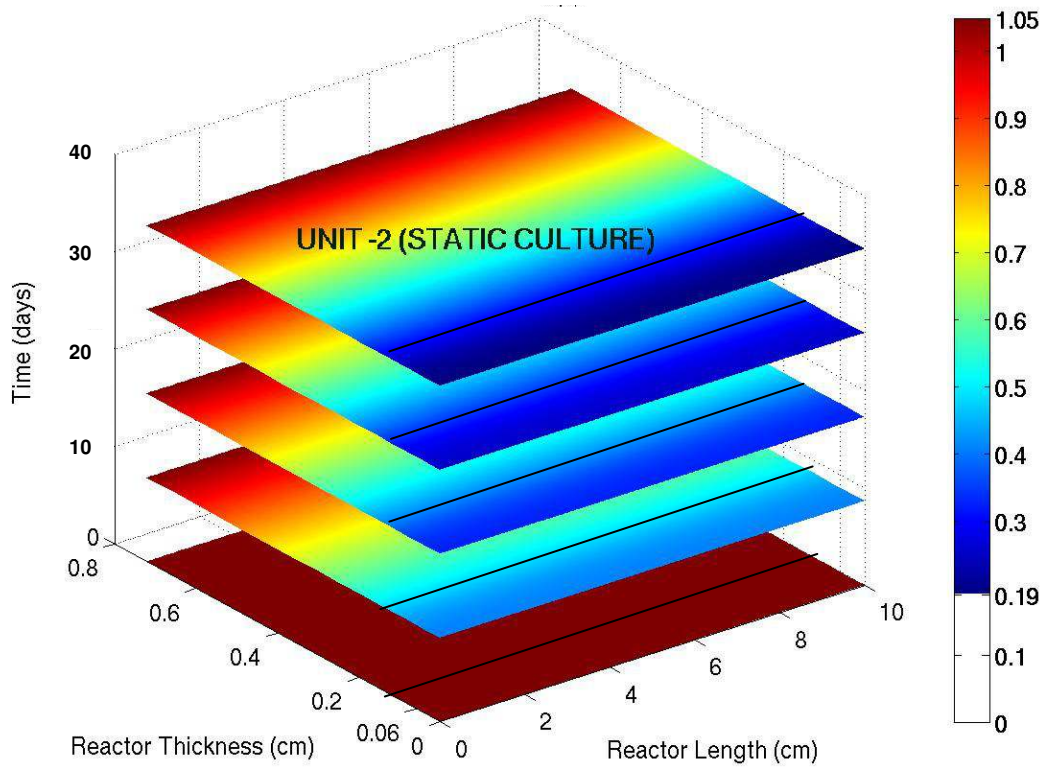


Figure 5. 4 c Mathematical simulation of the spatio-temporal variation of oxygen concentration in the cell layer and bulk liquid layer in static culture Unit 2

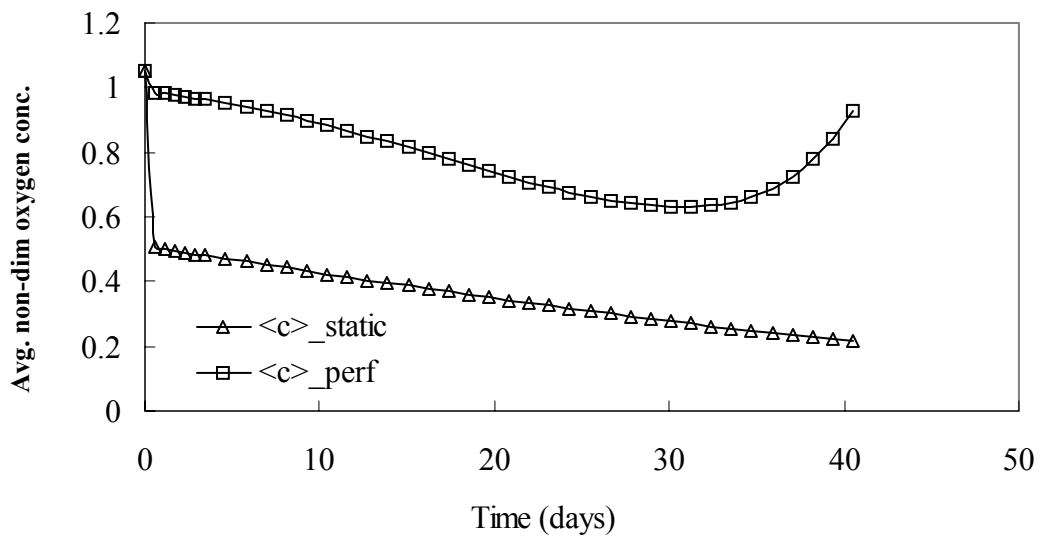


Figure 5. 5 Average non-dimensional oxygen concentration variations in cell layer with time for static and perfusion culture units

Oxygen tension has been mentioned to be one of the various environmental factors that influence cellular events leading to the construct formation, including cell attachment and spreading (Mitchell *et al.*, 2004, Rotem *et al.*, 1994), proliferation (Mitchell *et al.*, 2004, Duggan *et al.*, 2004), migration (Annabi *et al.*, 2003), secretion of ECM (Chen *et al.*, 2003, Gebb *et al.*, 2003), and differentiation (Cipolleschi *et al.*, 1993, Terai *et al.*, 2002). Experimental results using BrdU staining in Dr Ma's lab have shown different cell proliferation patterns under static culture on either sides of the PET construct (Zhao *et al.*, 2005 b); with higher proliferating cells on the upper surface of the construct exposed to higher oxygen and nutrient supply. On the other hand for constructs grown in the perfusion condition there was no difference in the growth patterns at the two surfaces of the constructs (Zhao *et al.*, 2005 b).

In the perfusion bioreactor (Unit 1) the results from modeling indicate that there exists an oxygen gradient in the constructs at high cell densities. The lowest level of oxygen tension in the construct was maintained above 0.47 (~ 9.4 % gas phase oxygen) throughout the culture period even at the highest cell densities. However, to be noted in static culture (Unit 2) the lowest non-dimensional oxygen level in the cell layer decreased from nearly 0.5 (~ 10 % gas phase oxygen) in the initial phase (around 10 days) of the culture period to nearly 0.19 (~ 3.8 % gas phase oxygen) at end of the culture period (around 40 days). Experimental studies have shown that the effects of oxygen tension on cell proliferation and ECM secretion are significant only when the oxygen tension is lower than 40 mmHg (Jiang *et al.*, 1996), which corresponds to the dimensionless oxygen tension of 0.26 (~ 5.3 % gas phase oxygen) in this study. Therefore, it is reasoned that the oxygen level in the constructs of the perfusion bioreactor system (Unit 1) is maintained above the level that could lead to the significant cellular physiological changes, whereas oxygen distribution might limit the cell growth and metabolism of the constructs in static culture (Unit 2). The non-uniform growth patterns in the static culture are again attributed to the oxygen and nutrient transfer limitations. These results demonstrate the significant role of perfusion in sustaining the development of engineered tissue constructs.

It is important to note, however, that oxygen tension may not be the only factor that influences cell spatial growth pattern in these different culture units. In addition to oxygen, diffusion also limits other nutrients delivery and waste removal in the static culture that possibly hinders cell

growth in this unit. Moreover, the medium flow and shear stress also influence cell proliferation in the perfusion bioreactor (Li *et al.*, 2004) and the expression of various hMSC differentiation markers (Li *et al.*, 2004; Meinel *et al.*, 2004; Park *et al.*, 2004). While the flow rate of 0.1 ml/min ( $Re = 0.28$ ) used in this study is sufficiently low compared to these studied ( $Re \sim 50$ ), further investigation under different flow rate is necessary to independently elucidate the effects of shear stress on cell growth.

## 5.6 Conclusions

High cell density and construct uniformity are important parameters for *in vitro* 3-dimensional tissue development which require sufficient nutrient delivery. In this study, we modeled the oxygen profiles of the 3-dimensional constructs grown under static and perfusion conditions, and evaluated the effects of the culture environment on construct development. Within the construct, some degree of empiricism and approximation is utilized to determine an estimate of oxygen concentration. The results show that the 3-dimensional constructs grown in static cultures developed significant oxygen gradients and have the tendency to give rise to spatially non-uniform and inconsistent construct development. The perfusion system provides the cells a controlled environment with enhanced nutrient transport by maintaining a much higher oxygen concentrations that sustains a high proliferation rate and high cell density. Experimental results on the cell spatial developmental patterns between the cells grown in static culture as opposed to perfusion culture could possibly be attributed to the spatial variations in oxygen concentration in the 3-dimensional constructs within the flow and no-flow units. Our study demonstrates the need to use perfusion bioreactor systems to support engineered tissue construct development.

## CHAPTER 6

### **ANALYSIS OF CARTILAGE TISSUE GROWTH AND EXTRACELLULAR MATRIX FORMATION *EX VIVO* IN HOLLOW FIBER BIOREACTOR**

*(Submitted July 2005 to Biotechnology and Bioengineering)*

#### **6.1 Introduction**

Articular cartilage is a thin layer of connective tissue located within joints at the end of bones (Buckwalter *et al.*, 1997). It is made up of relatively few cartilage cells called chondrocytes present in an extensively hydrated extracellular matrix (ECM), composed primarily of collagens and proteoglycans. The proteoglycan molecules exhibit a tendency to swell and provide the tissue with resistance to compression. The collagen network in the cartilage provides the tissue with integrity and mechanical strength during tensile and shear loading (Dimico *et al.*, 2003). The chondrocyte cells though few in number do fulfill a very essential function of ensuring that the composition of the cartilage matrix (or ECM) remains constant. The synthesis of ECM alters the microenvironment around the cells. *In vivo* or *in vitro* it is clearly seen that cells and ECM are mutually interdependent; chondrocyte activity is necessary for matrix synthesis; in turn matrix controls the environment of cells (Wilkins *et al.*, 2000).

Degeneration of articular cartilage occurs during osteoarthritis and joint injury. The limited capacity of cartilage to respond to mechanical injury with a reparative process has motivated the incorporation of cell-based repair approaches to articular cartilage lesions (Raimondi *et al.*,

2002). Tissue engineering approaches are extensively being employed to produce replacement cartilage, which closely resembles healthy native cartilage both structurally and functionally. These neocartilage samples, commonly designed as plugs, are manufactured within *in vitro* bioreactor systems, which can further be used for systematic studies of the process of chondrogenesis. Current bioreactor technologies – spinner flasks, rotating vessels, perfusion reactor, hollow fiber reactors, and cylindrical bioreactors – provide a uniform and quantifiable growth environment (Temenoff *et al.*, 2000; Williams *et al.*, 2002). Enhanced growth observed in these bioreactor systems is partly due to increased efficiency in nutrient transport as compared to static culture systems. Efficient oxygen delivery in mixed flasks and rotating vessels resulted in aerobic conditions, which is shown to favor rapid tissue formation (Vunjak-Novakovi *et al.*, 1996; Obradovic *et al.*, 1999). It is seen that the morphology, composition, and mechanical properties of the developed tissue constructs are strongly influenced by the microenvironment of the cells.

Although these bioreactor systems deliver large amounts of nutrients to cells and provide a better biochemical and mechanical environment to support chondrogenesis in comparison to static culture units, there exist spatial and temporal gradients in nutrient concentrations that would directly affect the growth of cartilage tissue. For suitable scale-up for clinical applicability to produce cartilage constructs with desired composition and functional properties a better understanding of the processes occurring in the reactor is necessary. Mathematical models can be used to parametrically relate the kinetics of *in vitro* tissue formation to events occurring at cell and molecular levels, and can also be utilized to investigate various designs and operating conditions for enhancing bioreactor performance. This could be done by quantifying the nutrient transport and consumption processes for various tissue functionalities. Understanding of the transport and reaction processes of various metabolites would enhance our understanding of the complex interplay among the array of known factors that control the functional tissue development (Sengers *et al.*, 2004). The model can be used to predict the spatio-temporal variations in construct composition, with regard to new tissue mass (cell and ECM) and the microenvironment around the cartilage cell. Further, the mathematical model can also be used to compile and understand the vast amounts of experimental data available for cartilage growth in

2-dimensional flasks and 3-dimensional bioreactors and can be utilized for suggesting rational designs for tissue constructs.

Various models have been developed to simulate chondrogenesis in tissue culture systems. Galban and Locke (1999 b) used volume averaging methods, first developed by Whitaker, 1967, to study growth kinetics, diffusion, mass transfer restrictions, and spatial variations of cell mass within polymer matrix. The model results were compared to the experimental data of Freed *et al.*, 1994b for chondrocyte growth in petri-dishes. They refined their model (Galban and Locke, 1999 a) by introducing effects of nutrient concentration and product inhibition and cell death in expression for cell growth kinetics. However, in their study they observed that two component models including cells and substrate are not sufficient to describe the range of behavior observed in the experiments and a more wide range of cell and tissue specific parameters need to be incorporated. Computational fluid dynamics (CFD) models to quantify momentum and mass transport under conditions of tissue growth in cylindrical bioreactors have also been developed (Williams *et al.*, 2002). CFD models are used to calculate flow-fields, shear stresses, and oxygen profiles around non-porous constructs simulating cartilage development in concentric cylinder bioreactors.

Several other models have been developed to describe the role of oxygen on GAG synthesis and distribution in cellular constructs in rotating bioreactors (Obradovic *et al.*, 2000, Pisu *et al.*, 2003). These models account for the spatio-temporal changes in oxygen concentration due to diffusion and consumption for chondrocyte metabolism and matrix synthesis. GAG deposition is described by product inhibition kinetics with respect to GAG formation and a first order dependence with respect to oxygen concentrations. Cell density variations in time and space are described using mass structured population balances. The simulated GAG concentrations were compared with available experimental data as a function of space. Several other time varying models describing ECM synthesis (accumulation of both GAG and collagen) and the degradation of polymeric scaffold for constant cell mass have been formulated for engineered cartilage construct (Wilson *et al.*, 2002). Malda *et al.*, 2004 have improved upon the work of Obradovic and coworkers by correlating pseudo-steady state simulated oxygen concentration variations in the construct with their experimentally measured local oxygen concentrations. However, all



these models suffer from the inherent drawback of not accounting for suitable mass transport of nutrients that is directly affected by the increase in cell mass by growth and differentiation, as well as ECM production. The above models also do not incorporate the effects of the restricted diffusion of nutrients on the chondrocyte activity.

The present study develops a mathematical model of cartilage tissue formation in the hollow fiber bioreactor (HFBR) unit developed by Spencer's group (Petersen *et al.*, 1997; Potter *et al.*, 1998; Ellis *et al.*, 2001). As seen in this unit, cells were not grown in constructs (compared to the study by Langer's group). The cells were injected into the extracapillary space between the hollow fiber tubes in the reactor. Thereafter these cells attach themselves onto the outer surface of the hollow fiber tubes or capillaries. These cells then proliferate radially outwards in the space available. The moving boundary approach (Galban and Locke, 1997) coupled with the method of volume averaging (Whitaker, 1967) is proposed to simulate the experimental radial cell proliferation pattern, as well as account for transport and reaction processes in the reactor by determination of effective diffusion and reaction terms for tissue formation in terms of local geometry and spatial restrictions. The model computes the tissue and NMR measurable parameters for comparison with available experimental results.

This study is intended to enhance our understanding of various factors that affect cell growth and ECM production *in vitro* in bioreactors. The model would enable a further rationalization of experimental results providing suggestions for improved experimental design and identifying the key cell and tissue parameter measurements need to be made during cell cultures. Understanding the responses of chondrocyte cells in terms of growth, differentiation, and ECM production with respect to changes in the environment in the reactor would help in development of optimal operational strategies in these reactors. Indirectly, the model would improve our understanding of ways to monitor and control the development of the tissue engineered constructs *in vitro* in bioreactors.

## 6.2 Methodology

### 6.2.1 Experimental Data

Spencer's group at NIH have used HFBR units for production and development of 3-dimensional hyaline cartilage from isolated chondrocytes (Petersen *et al.*, 1997; Potter *et al.*, 1998; Ellis *et al.*, 2001). The unique feature of their methodology is the use of NMR to monitor tissue development. This technique evaluates the over-all- tissue formation in the reactor without disrupting the sample. The NMR measurable parameters are correlated to the chemical characteristics of the tissue (cartilage tissue growth, metabolism and ECM composition); opening up a new field in tissue engineering.

The NMR measurable parameters include water diffusion coefficient, relaxation parameters (T1, longitudinal spin-lattice relaxation time constant and T2, transverse spin-spin relaxation time constant), and magnetization transfer and proton densities. Measurement of the water diffusion coefficient ( $D_{eff}^w$ ) and T1 relaxation constant ( $T1_{eff}$ ) gives information on the obstruction to the motion of water in the tissue due to tissue formation. This can be due to an increase in cell mass or increase in ECM mass produced by the cells over the culture time. Magnetization transfer (MT) measures the degree of interaction between the free and bound components of water. Appendix D enlists the variation of these parameters with time as observed in the experiments of Potter *et al.*, 1998.

### 6.2.2 Model Formulation

#### 6.2.2.1 Outline

The HFBR set-up used for model development is described by Petersen *et al.*, 1997. The major findings of Potter *et al.*, 1998 on macroscopic tissue development are incorporated in the model. Cells were found organized into columns radiating from individual hollow fiber tubes. The transverse slices show bright central hollow fiber or capillary and cylindrical symmetry of tissue

growth. After week 2 of tissue formation, the extracapillary space is almost filled with tissue mass due to cell proliferation. The mean cell area is seen to increase with development time after 2 weeks. This is consistent with a period of rapid cell proliferation during the early culture time (first 2-3 weeks) followed by over-all tissue maturation (last 2-4 weeks). Following development, the wet tissue weight increased with time, whereas the tissue water content drops, consistent with an increase in tissue GAG and collagen content. Collagen content increased significantly for all the 4 weeks of culture whereas the GAG content increased till 3 weeks of culture and reached saturation. Water diffusion coefficient decreased from week 1 to week 4. However the drop is seen to be remarkable between weeks 3 and 4, in spite the fact that the overall tissue growth is almost over by week 3. The reduction is attributed to cartilage cell maturation (increase in dry weight) that occurs during later weeks of culture, and also to increase in collagen content over time (Potter *et al.*, 1998). These variations of the cell and NMR parameters as observed in the experiments are listed in Appendix D.

The modeling approach incorporates the idea of ‘unit cells’. A ‘unit cell’ comprises of a single chondrocyte cell and the niche it creates around itself. The niche is made up of the cell produced ECM mainly proteoglycan (GAG) and collagen and the void phase associated around it. These ‘unit cells’ propagate outwards from the surface of the hollow fiber as shown in Figure 6.1. The method of volume averaging is employed to derive effective diffusion and reaction rates of components in this cartilage tissue, a multiphase system (Wood *et al.*, 2000; Wood *et al.*, 2002; Whitaker, 1999). However, this method is not sufficient to account for the radial growth of cells in this reactor unit. Hence the moving boundary approach proposed by Galban and Locke, 1997 is incorporated with the volume averaging method to model the spatial growth patterns.

The developed model describes the following tissue and NMR parameters - cell mass production which includes cell proliferation (accounting for increase in number of cells) and cell growth (accounting for increase in area of cells during the maturation stage); cell metabolism (oxygen consumption by cells); cell ECM production (Proteoglycan (GAG) and Collagen); NMR parameters i.e.  $D_{eff}^w$  and T1 relaxation time. It must be noted here that the cell proliferation and cell growth are separated into two different distinct processes because experimental results clearly show that cells in these stages are different both metabolically and in their rates of ECM

production (Potter *et al.*, 1998). The concept used in our model development is unique and differs from previous modeling efforts of chondrocyte growth and ECM production for tissue engineered cartilage generation. The model couples all the cell physiological processes – the cell growth, cell metabolism, collagen and GAG synthesis in each ‘unit cell’, as well as accounts for the increase in number of ‘unit cells’ because of increase in cell number or proliferation using suitable kinetic functions.

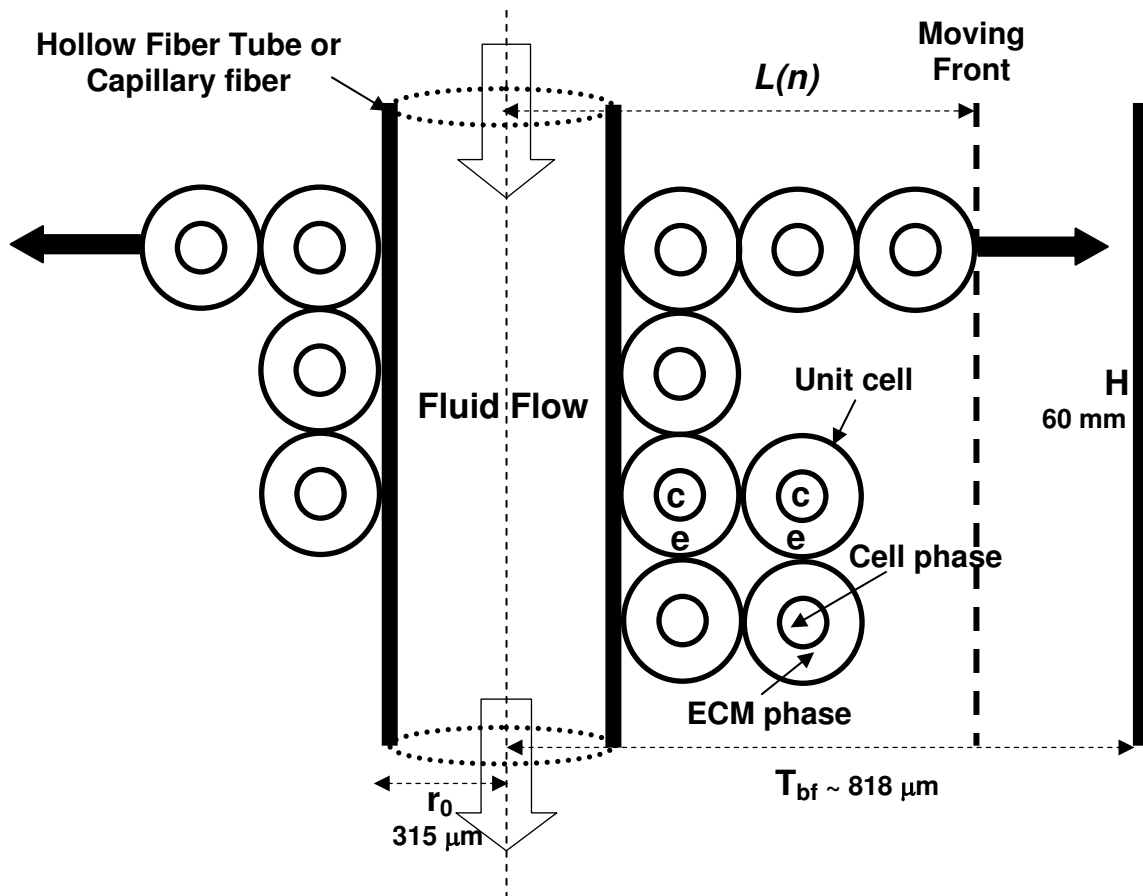


Figure 6. 1 Schematic of the reactor showing the idealized single hollow fiber with cells growing radially from the outer walls of the hollow fiber

### **6.2.2.2 Model Equations**

For the development of the model one hollow fiber tube is considered (Figure 6.1). It is assumed that tissue formation around each hollow fiber tube or capillary is identical. Each ‘unit cell’ is made up of two phases, the cell phase comprising of a single chondrocyte cell and the ECM phase. The ECM phase is made up of three phases, GAG or proteoglycans, collagen, and the void (or free) phase. Species continuity equations describing the local spatial and temporal variations of nutrient (oxygen) concentration are written for both the cell and ECM phases. The method of volume averaging is used to develop a single species continuity equation for this multi-phase system (Wood *et al.*, 2000; Wood *et al.*, 2002; Whitaker, 1999; Galban and Locke, 1999). Assuming that the processes of ECM synthesis and chondrocyte growth (maturation) in each ‘unit cell’ are identical; this material balance is then averaged in space along the available extracapillary space for tissue formation. Mass balances for ECM production are written in each ‘unit cell’ and then multiplied with the number of ‘unit cells’ to obtain the total GAG and collagen mass produced. Similarly cell growth mass balance is also written in each ‘unit cell’. Balance for increase in number of these ‘unit cells’ is written to account for the process of cell proliferation.

#### ***Nutrient (Oxygen) Balance***

Due to its low solubility, oxygen is expected to be one of the first nutrients to become limiting. Apart from being an essential nutrient, oxygen plays an important role in chondrocyte expansion and ECM production (Obradovic *et al.*, 2000; Zhou *et al.*, 2004, Malda *et al.*, 2004). Chondrocytes in hollow fiber reactor cultures need approximately 20% oxygen in the gas phase to produce ideal growth and GAG and collagen production (Ellis *et al.*, 2001). The current model assumes that the other much more soluble nutrients such as glucose are present in excess.

#### ***Method of Volume Averaging***

The method of volume averaging is used to formulate the material balances for this multiphase transport-reaction problem (Whitaker, 1967; Ochoa, 1988). In this method a small representative volume termed the averaging volume ( $V$ ) is selected. This corresponds to the ‘unit cell’ in our model. Figure 6.2 shows a schematic of the averaging volume. It is made up of two distinct

phases - the cell phase, indicated as ‘*c*’ and the ECM phase indicated as ‘*e*’. Cell growth is expressed in terms of the cell volume fraction ( $\varepsilon_c$ ), i.e., the volume occupied by cells in the averaging volume,  $V_c$ , relative to the total averaging volume  $V$ . The sum of the volume fractions of the cell phase and the ECM phase in the averaging volume is one,

$$1 = \varepsilon_c + \varepsilon_e \quad \text{where } \varepsilon_c = \frac{V_c}{V}, \varepsilon_e = \frac{V_e}{V} \tag{6.1}$$

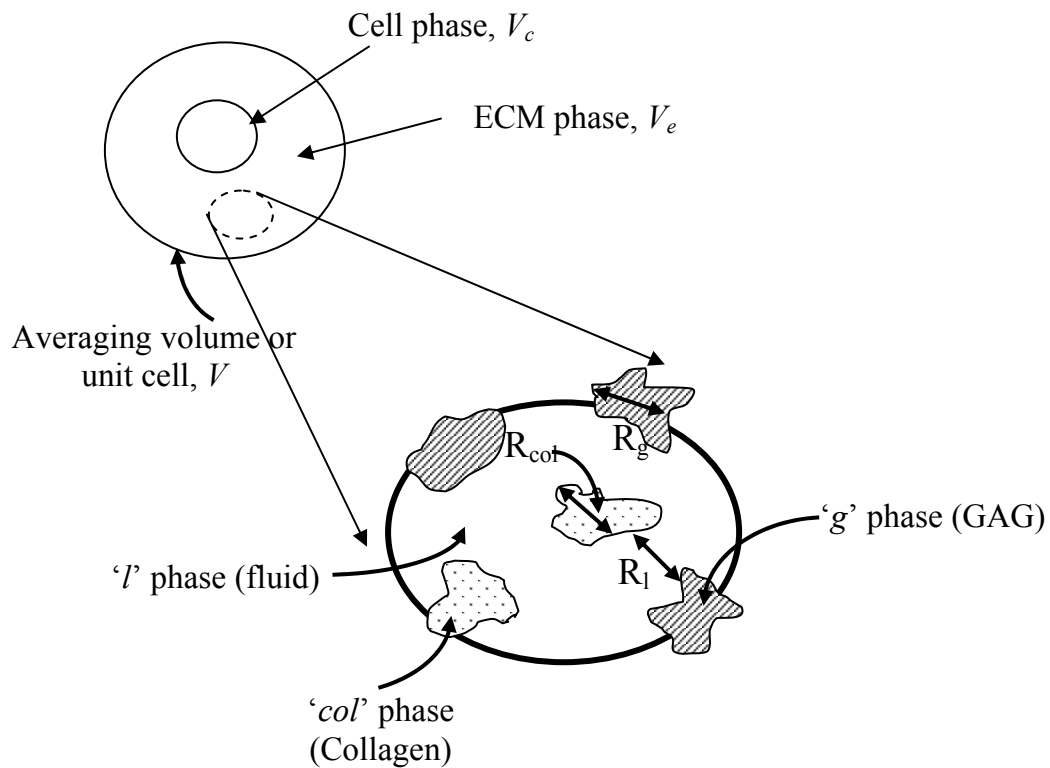


**Figure 6. 2 Schematic of the averaging volume showing the cell phase and details of the extracellular matrix**

The ECM phase is made up of three distinct phases – the fiber or GAG phase (*g*), collagen phase (*col*), and the void phase (*l*). As mentioned before the sum of the volume fractions of these phases is also one,

$$1 = \varepsilon_e^g + \varepsilon_e^{col} + \varepsilon_e^l \quad \text{where } \varepsilon_e^g = \frac{V_g}{V_e}, \varepsilon_e^{col} = \frac{V_{col}}{V_e}, \text{ and } \varepsilon_e^l = \frac{V_l}{V_e} \quad (6.2)$$

Species continuity balances of oxygen concentration in the particular phases are written and spatially smoothed to produce a single equation that is valid everywhere in the ‘unit cell’ (Whitaker, 1999).

### *Cell Phase*

This phase comprises of a single chondrocyte cell. The molar species continuity equations for oxygen in this phase incorporates oxygen diffusive transport, and also consumption of oxygen by the chondrocyte cell, and is written as,

$$\frac{\partial S_c}{\partial t} = \nabla D_c \nabla S_c - k_c S_c \quad \text{in } V_c \quad (6.3)$$

where  $S_c$  is the local oxygen concentration in the cell phase,  $D_c$  is the diffusion coefficient of oxygen through the cell phase, and  $k_c$  is the metabolic rate constant for oxygen consumption in the cell phase. The metabolic oxygen consumption reaction rate kinetic function is assumed to be first-order and independent of cell growth kinetics. This can be assumed by considering that the rate of oxygen consumption by metabolic reactions is much higher than the consumption for cell growth.

### *ECM Phase*

Oxygen in the ECM phase is not consumed by reaction. The molar balance describing the oxygen concentration variation in space and time by diffusive transport in the GAG, collagen and void phases are written as,

$$\frac{\partial S_l}{\partial t} = \nabla D_l \nabla S_l \quad \text{in } V_l$$

*GAG*

$$-n_g \cdot D_l \nabla S_l = \sigma_g^o (P_g^o S_l - S_g) \quad \text{at } A_{l_g}$$

*Collagen*

$$-n_{col} \cdot D_l \nabla S_l = \sigma_{col}^o (P_{col}^o S_l - S_{col}) \quad \text{at } A_{l_{col}}$$

(6.4)

where  $S_g$ ,  $S_{col}$  are the point oxygen concentrations on GAG and collagen surfaces, respectively and  $S_l$  is the point oxygen concentrations in the void phase;  $D_l$  is the diffusion coefficient of oxygen in the void phase;  $\sigma_g^o$ ,  $\sigma_{col}^o$  are detachment rate of oxygen on the surface of GAG fibers and collagen; and  $P_g^o$  and  $P_{col}^o$  are the binding coefficients of oxygen to GAG and collagen, respectively.

Equations 6.4 describe the oxygen concentration distribution throughout the various phases within the ECM of an averaging volume and are applicable at any spatial position in the appropriate phases. In order to develop a locally averaged equation to describe the concentration fields in the ECM phase of the ‘unit cell’, these equations are averaged spatially to obtain a single volume-averaged equations. Approach similar to that presented by Penke *et al.*, 1998 and Whitaker and coworkers (Carbonell and Whitaker, 1984; Ryan *et al.*, 1981; Nozad *et al.*, 1985; Kim *et al.*, 1987; Ochoa *et al.*, 1994) is used. The single averaged species continuity equation is written as,

$$\frac{\partial S_e}{\partial t} = \nabla \cdot D_{eff}^e \cdot \nabla S_e \quad \text{in } V_e$$

(6.5)



where  $S_e$  is the local oxygen concentration averaged over the entire ECM phase and  $D_{eff}^e$  is the effective diffusion coefficient of oxygen in the ECM phase. The effective diffusion coefficient is given as,

$$D_{eff}^e = \frac{D_l \cdot \varepsilon_e^l}{\left[ \varepsilon_e^l + \left( P_g^o \cdot \frac{A_g}{V} \right) + \left( P_{col}^o \cdot \frac{A_{col}}{V} \right) \right]} \cdot \left[ \frac{\varepsilon_e^l}{2 - \varepsilon_e^l} \right] \quad (6.6)$$

The area to volume ratio for GAG and collagen in equation 6.6 is given as,

$$\frac{A_g}{V} = \frac{4 \cdot \pi \cdot R^2}{V} \cdot \varepsilon_g^{2/3}, \quad \frac{A_{col}}{V} = \frac{4 \cdot \pi \cdot R^2}{V} \cdot \varepsilon_{col}^{2/3}$$

$$\varepsilon_g = \frac{V_g}{V}, \quad \varepsilon_{col} = \frac{V_{col}}{V} \quad (6.7)$$

### *Single Nutrient Balance*

The overall point equations in the cell phase and the ECM phase with appropriate boundary conditions can be summarized as,

$$\begin{aligned} \frac{\partial S_e}{\partial t} &= \nabla D_{eff}^e \nabla S_e \quad \text{in } V_e \\ BC1: \quad -n_{ce} \cdot D_c \nabla S_c &= P(S_c - Keq S_e) \quad \forall A_{ce} \\ BC2: \quad -n_{ec} \cdot D_{eff}^e \nabla S_c &= -n_{ce} \cdot D_c \nabla S_c \quad \forall A_{ec} \\ \frac{\partial S_c}{\partial t} &= \nabla D_c \nabla S_c - k_c S_c \quad \text{in } V_c \end{aligned} \quad (6.8)$$

where  $P$  represents the mass transfer coefficient at the cell membranes, i.e. at  $A_{ec}$  (*ECM-Cell interface*), and  $Keq$  is the equilibrium coefficient for oxygen between the 'c' and the 'e' phases

of the averaging volume. The method of volume averaging is used to obtain a single species nutrient balance by combining the local nutrient balances in the phases with appropriate boundary conditions (equation 6.8). The principle of local mass equilibrium is used to obtain a single averaged species continuity equation for the oxygen concentration (Whitaker, 1999; Ochoa, 1988; Galban and Locke, 1999). The single averaged species continuity equation is written as,

$$\frac{\partial \{S\}}{\partial t} = \nabla D_{eff} \nabla \{S\} - k_{eff} \{S\} \quad (6.9)$$

Equation 6.9 was obtained by assuming the following length scale constraints in the averaging volume (Ochoa, 1988),

$$\frac{R_c^{max}}{R} \gg \frac{R}{Tbf} \quad or \quad \frac{R_e^{max}}{R} \gg \frac{R}{Tbf} \quad (6.10)$$

where  $R_c^{max}$  and  $R_e^{max}$  are the maximum radius across the respective phase (cell and ECM, respectively) within the averaging volume ( $V$ ),  $R$  is the radius of the averaging volume, and  $Tbf$  is the available radius in the extracapillary space of the bioreactor for tissue production. One of the constraints needs to be valid for all changes in cell volume fraction over time. The initial length scale for the cell phase ( $R_c$ ) is nearly 3.34  $\mu\text{m}$  while the initial length scale for the ECM phase is approximately 0.6  $\mu\text{m}$ . With time in culture more ECM is produced by cells and the magnitude of  $R_e$  increases and so does the cell size, corresponding to increase in  $R_c$ . The ratio  $R/Tbf$  is a constant with an approximate value of 0.015, where  $R$  is 12.03  $\mu\text{m}$  and  $Tbf$  is 818  $\mu\text{m}$ . Although  $R_c$  and  $R_e$  may vary with time the condition in equation 6.8 will typically hold since the size of the reactor is much larger than the averaging volume. To be noted here while the individual volumes of the cell ( $V_c$ ) and ECM ( $V_e$ ) phase in the averaging volume ( $V$ ) vary with time, the volume of the averaging volume remains constant and is given as (Whitaker, 1985),

$$V = V_c(t) + V_e(t) \quad (6.11)$$

The effective diffusion coefficient and effective rate constant for oxygen consumptions are derived as functions of the cell and ECM volume fractions by using the solution of a closure problem posed over a well-defined ‘unit cell’ (Whitaker, 1999). However, for complex unit cell geometry numerical solutions are required, and a number of analytical solutions are available for isotropic media with simple geometry (see Locke, 2001 for review). In the present study an analytical expression for the effective diffusion coefficient of an isotropic two dimensional two phase medium defined by a square unit cell (Ochoa, 1988) containing circular particles is used. This relationship accounts for the diffusion in the non-cellular ‘e’ phase and the cellular ‘c’ phase as well as the mass transport across the two phases. This effective diffusion coefficient is written as,

$$D_{eff} = \frac{D_{eff}^e}{(\varepsilon_c \cdot K_{eq} + \varepsilon_e)} * \left[ \frac{2k - (k-1)\varepsilon_e + \varepsilon_e \varepsilon_c^{-1/2} \alpha}{2 + (k-1)\varepsilon_e + (2 - \varepsilon_e)\varepsilon_c^{-1/2} \alpha} \right] \quad (6.12)$$

where  $k = (K_{eq} D_c / D_{eff}^e)$  is the ratio of the diffusion coefficient in the cell phase over that in the ECM phase (here the non-cellular phase) and  $\alpha = (D_c / R P)$  is the ratio of the cell phase diffusion coefficient over the mass transfer coefficient at the cell-ECM interface in the averaging volume. The parameter  $K_{eq}$  is computed by dividing the solubility of oxygen in lipids to solubility of oxygen in water (Chow *et al.*, 2000). From our study of hematopoietic cells with much higher oxygen consumption rates we have seen that the model results are not highly sensitive to the functional form of the diffusion coefficient since diffusive restrictions of oxygen in the cellular region are not very large (Pathi *et al.*, 2005). For analysis of solutes that have larger restrictions to diffusion in the cellular phase further consideration of the local 3-dimensional geometry and solution of the closure problem would be needed. The effective oxygen consumption rate is found to be,

$$k_{eff} = \frac{\varepsilon_c \cdot Keq \cdot k_c}{(\varepsilon_c \cdot K_{eq} + \varepsilon_e)} \quad (6.13)$$

### *Moving Boundary Approach*

Experimentally, tissue growth along the long axis of the bioreactor was observed to be largely uniform (Potter *et al.*, 2000; Ellis *et al.*, 2001). Thus, it is reasonable to use a 1-D assumption for model development. The moving boundary approach as described in Galban and Locke, 1997 is used to account for the total nutrient concentration and total ECM production over the entire number of averaging volume units ('unit cells'). In contrast, if the cells were uniformly seeded in the space around the hollow fiber volume averaging could be used in that region and need not be coupled with the moving boundary approach.

$L(n)$  in Figure 6.1 is referred to as the moving front or the boundary and is a function of the number of averaging volumes or 'unit cells',  $n$ . It is the radius up to which cells are proliferating. The magnitude of  $L(n)$  can range from  $r_0$ , radius of a hollow fiber to  $Tbf$ , the maximum available radius for tissue mass production. For  $r_0 > L(n)$  the reaction terms (accounting for oxygen consumption by cells) in the balance in equation 6.9 would be zero since no cells are assumed present.

An analytical expression of nutrient (oxygen) concentration is obtained by simplifying equation 6.9 with the following assumptions,

- a) 1-D geometry
- b) quasi-steady state approximation (since the time scale for cell proliferation in the experiment is of the order of 4 weeks). This would mean,

$$\frac{Deff \cdot t}{Tbf^2} \gg 1 \quad (6.14 a)$$

- c) oxygen concentration can be spatially averaged from  $0 < r < \delta$  by assuming that the rate of nutrient consumption is small relative to the rates of diffusion provided,

$$\frac{k_{eff} \cdot Tbf^2}{Deff} \ll 1 \quad (6.14 \text{ b})$$

This assumption for small oxygen gradients is supported by experimental studies of Ellis *et al.*, 2001 using EPROM (EPR Oxygen Mapping). Although the spatial resolution was small this study showed that for chondrocyte cultures grown in HFBR for 4 weeks, small oxygen gradients occur in the cartilage tissue constructs. The constraints shown in equations 14 were found in the present study to hold for the entire culture time under consideration.

Using assumptions (a) [1-D geometry] and (b) [pseudo-steady state] equation 6.9 reduces to,

$$D_{eff} \cdot \frac{d^2}{dx^2} \{S\} = k_{eff} \cdot \{S\} \quad (6.15)$$

The flux of oxygen from the capillary to the tissue region at  $x = r_0$  occurs at both the cell boundary as well as ECM boundary (Galban and Locke, 1997). The oxygen flux at the moving front is set to zero. The macroscopic boundary condition is given as,

$$D_{eff} \cdot \frac{d}{dx} \{S\} = K_m \cdot \varepsilon_e (S_o - S_e) + K_m \cdot \varepsilon_c \left( S_o - \frac{S_c}{Keq} \right) \quad \forall x = r_0$$

$$\frac{d}{dx} \{S\} = 0 \quad \forall x = L(n) \quad (6.16)$$

where  $K_m$  is the external mass transfer coefficient at the interface between the cell and ECM phases,  $S_o$  is nutrient concentration in the hollow fiber. It is assumed that there is no significant drop in oxygen concentration in the axial and radial directions in the lumen of the hollow fiber or capillary.

The nutrient balance from equation 6.15 and the boundary conditions from equation 6.16 are non-dimensionalized to give,

$$\begin{aligned} \frac{d^2 \mu}{d\delta^2} &= \left( \frac{k_{eff} \cdot Tbf^2}{D_{eff}} \right) \cdot \mu = \phi^2 \cdot \mu \\ \frac{d\mu}{d\delta} &= Sh \cdot (\mu - 1) \quad \forall \delta = \frac{r_0}{Tbf} = u, Sh = \frac{Km \cdot Tbf}{D_{eff}} \\ \frac{d\mu}{d\delta} &= 0 \quad \forall \delta = \frac{L(n)}{Tbf} = v \end{aligned} \tag{6.17}$$

where the non-dimensional oxygen concentration,  $\mu = \{S\} / S_o$ , and non-dimensional distance,  $\delta = x / Tbf$ . Boundary condition in equation 6.16 is simplified to the above equation by utilizing the principle of local mass equilibrium and by assuming the local and macroscopic spatial deviations in nutrient concentrations to be negligible in the cell and ECM phases. Here one would appreciate the reason for choosing a first order kinetics for oxygen consumption vs. a Michaelis-Menten as has been extensively reported by Obradovic *et al.*, 2000 and others. The first order kinetics helps in obtaining a standard analytical solution as compared to any non-linear kinetic expressions. However, in the future once experimental data for the variation of nutrient concentration with time in the HFBR unit is available various kinetic expressions can be used to determine the effects of other kinetic forms if necessary. A spatially independent average nutrient concentration equation is obtained by deriving the analytical solution for the boundary-value problem in equation 6.17 and then averaging over  $r_0$  and  $L(n)$ . The average nutrient concentration is given as,

$$\langle \mu \rangle = \frac{A}{\phi \cdot [v - u]} \left[ \{ \text{Sinh}(\phi \cdot v) - \text{Sinh}(\phi \cdot u) \} - \tanh(\phi \cdot v) \cdot \{ \text{Cosh}(\phi \cdot v) - \text{Cosh}(\phi \cdot u) \} \right]$$

$$A = \frac{Sh}{Sh \cdot CTC - \phi \cdot STC}$$

$$STC = \text{Sinh}(\phi \cdot u) - \tanh(\phi \cdot v) \cdot \text{Cosh}(\phi \cdot u)$$

$$CTC = \text{Cosh}(\phi \cdot u) - \tanh(\phi \cdot v) \cdot \text{Sinh}(\phi \cdot u)$$
(6.18)

It must be noted here that  $\phi^2$  is not a constant with time since the effective rate coefficient for oxygen consumption,  $k_{eff}$  and effective rate of constant for oxygen diffusion through the cartilage tissue,  $D_{eff}$ , vary in time due to changes in the volume fractions of cells and ECM.

### ***Cell mass balance***

With tissue formation over time there is an increase in total cell mass due to the processes of cell proliferation and cell growth in the hollow fiber reactor. Experimentally it was observed around 3 weeks of culture that the cell number remained constant, however the average cell area (accounting for cell growth in a ‘unit cell’) increased significantly. Because these two processes occur at two different time frames and under different surrounding environmental conditions, they need to be accounted for by writing two distinct balances.

The increase in cell number is the process of cell proliferation and the total cell mass balance accounting for this process is given as,

$$\frac{dM(t)}{dt} = \frac{d}{dt} \int_{V_c^T(t)} \rho_c dV = \int_{V_c^T(t)} R_p dV$$
(6.19)

where  $M(t)$  is the total cell mass surrounding a hollow fiber in the reactor,  $\rho_c$  is the specific cell density,  $V_c^T$  the total volume occupied by the cells around a single fiber and  $R_p$  is the specific

total cell mass production rate. The total volume occupied by cells is a product of the volume of each chondrocyte cell,  $V_c$  and the number of ‘unit cells’ or averaging volumes,  $n_c$  ( $V_c^T = V_c \cdot n_c$ ). The above equation is based on the assumptions that the diffusivity and migration of cells are negligible, and that the specific cell density in the cell phase is uniform. Further expanding equation 6.19, dividing by the averaging volume  $V$  and rearranging we obtain,

$$\rho_c \frac{d}{dt}(n_c \cdot V_c) = R_p(n_c \cdot V_c)$$

*Expanding,*

$$n_c \frac{dV_c}{dt} + V_c \frac{dn_c}{dt} = \left( \frac{1}{\rho_c} \right) \cdot R_p \cdot (n_c \cdot V_c)$$

*Dividing by  $V$ ,*

$$n_c \frac{d\varepsilon_c}{dt} + \varepsilon_c \frac{dn_c}{dt} = \left( \frac{1}{\rho_c} \right) \cdot R_p \cdot (n_c \cdot \varepsilon_c)$$

*Rearranging,*

$$\frac{dn_c}{dt} = \frac{n_c}{\varepsilon_c} \left[ \left( \frac{R_p}{\rho_c} \right) \cdot \varepsilon_c - \frac{d\varepsilon_c}{dt} \right]$$

(6.20)

where  $dn_c/dt$  accounts for increase in cell number (or the number of averaging volumes) while  $d\varepsilon_c/dt$  signifies increase in cell area (cell growth) in each averaging volume or ‘unit cell’.

A modified Contois function (Galban and Locke, 1999) is used to describe overall increase in cell mass due to growth and proliferation and is given as,

$$R_p = \left[ \frac{k_p \cdot \{S\}}{K_{mf} \cdot n_c + \{S\}} - k_{pd} \right] \cdot \rho_c$$

(6.21)



where  $k_p$ ,  $K_{mf}$  and  $k_{pd}$  are the cell mass formation, cell saturation and cell death parameters. The overall cell proliferation balance is obtained by substituting equation 6.21 into 6.20 and non-dimensionalizing with respect to the maximum number of averaging volumes that can fill the available volume in the reactor ( $n_{max}$ ) and the nutrient concentration ( $S_o$ ).

$$\frac{dn}{dt} = \frac{n}{\varepsilon_c} \left[ \left( \frac{k_p \cdot \mu}{K_p \cdot n + \mu} - k_{pd} \right) \cdot \varepsilon_c - \frac{d\varepsilon_c}{dt} \right] \quad (6.22)$$

where non-dimensional number of cells is give as,  $n = n_c / n_{max}$  and  $K_p = (K_{mf} \cdot n_{max}) / S_o$ .

### **Cell growth balance**

Cell growth (denoted by a change in cell volume fraction,  $\varepsilon_c$ ) is obtained by writing a cell mass balance of a single chondrocyte cell in the averaging volume or ‘unit cell’. The conservation of cell mass is given by,

$$\frac{dm(t)}{dt} = \frac{d}{dt} \int_{V_c(t)} \rho_c dV = \int_{V_c(t)} R_c dV \quad (6.23)$$

where  $m(t)$  is the cell mass in a ‘unit cell’ or averaging volume,  $\rho_c$  is the specific cell density,  $V_c$  the averaging volume containing the cells and  $R_c$  is the specific cell growth rate. The above equation is based on the assumptions that the cell phase is made up of only chondrocyte cells, the diffusivity and migration of cell<sup>2</sup> in the cell phase are negligible, and the specific cell density in the cell phase is uniform. This balance signifies the stage of cell maturation, where increase in chondrocyte cell size takes place in each ‘unit cell’ or averaging volume, filling up the available extracapillary space.

---

<sup>2</sup> Mass transport of cells (by diffusion) is not included in the model, however it can be noted that future work may consider the effects of cell migration by diffusion or chemotaxis.

The integral in the above equation is evaluated over the cell volume  $V_c$  within the averaging volume  $V$  to give

$$\frac{d\varepsilon_c}{dt} = \frac{1}{\rho_c V} \int_{V_c} R_c dV \quad (6.24)$$

A Michaelis-Menten dependence of cell growth on nutrient (oxygen) concentration is proposed. Potter *et al.*, 1998 observed distinct cell growth only after cells stopped proliferating due to contact inhibition. Thus a marked decrease in cell proliferation favors cell maturation. To represent the experimental observations several kinetic functions were tested (see Results section) for the dependence of the cell growth rate on the number of cells; the second order dependence was found to fit best to the data. Therefore, the effects of nutrient concentration and number of cells (similar to number of averaging volumes or ‘unit cells’) on the growth of a single chondrocyte cell in a ‘unit cell’ is given as,

$$R_c = \left[ \left( \frac{1}{n_{max}^2} \right) \cdot \left( \frac{k_{growth} \cdot \{S\}}{(Kc \cdot \rho) + \{S\}} \right) \cdot n^2 - k_{cd} \right] \quad (6.25)$$

where  $k_{growth}$  is the homogeneous growth rate coefficient,  $Kc$  is the modified Contois saturation constant,  $\rho$  is the overall cell density ( $\rho_c \cdot \varepsilon_c$ ),  $k_{cd}$  cell death parameter; and  $n$  is the fractional number of cells [= number of cells at a particular time ( $n_c$ ) / maximum number of cells that can fit in the available volume ( $n_{max}$ ) ]. A modified Contois (Galban and Locke, 1999) is used to include effects of cell crowding and restricted volume of cell mass formation.

Substituting equation 6.25 in 6.24 and non-dimensionalizing with the nutrient concentration ( $S_o$ ), the material balance for cell growth can be rewritten as,

$$\frac{d\varepsilon_c}{dt} = \left[ \frac{k_g \cdot \mu \cdot n^2}{K_{cont} \cdot \varepsilon_c + \mu} - k_{cd} \right] \cdot \varepsilon_c \quad (6.26)$$

where the overall growth coefficient,  $k_g = k_{growth} \cdot n_{max}^2$  and overall Contois parameter

$$K_{cont} = K_c \cdot \rho_c / S_o.$$

### ***Extracellular Matrix (ECM) balance***

The material balance on the extracellular matrix, assuming negligible diffusion of ECM is given in terms of the local volume fraction of extracellular matrix,  $\varepsilon_e$ , as

$$\frac{d\varepsilon_e}{dt} = R_{ECM}(\mu, \varepsilon_c, \varepsilon_e) \quad (6.27)$$

where  $R_{ECM}$  denotes the rate function for extracellular matrix production. As mentioned before the cartilage ECM is primarily made up of GAG and collagen components. Specific balances for these components are written to quantify the amount of each ECM components present.

GAG and collagen molecules, when densely packed around a cell provide a mechanically competent native tissue-like housing, capable of changing pericellular osmolarity, permeability, and pH. These local physicochemical changes, which gradually occur with matrix molecule accumulation, may control cell metabolism by interfering with nutrient uptake and waste withdrawal, adjusting cell volume, or changing the ion channel activity (Wilkins *et al.*, 2000). Therefore, this model would help to understand the various factors controlling formation of these different ECM components. However, our current model does not account for the effects of osmolarity and pH change on cell growth, metabolism or ECM production and analysis of these factors is proposed as future work.

## GAG -

The conservation of GAG mass is given by,

$$\frac{dm_g(t)}{dt} = \frac{d}{dt} \int_{V_g(t)} \rho_g dV = \int_{A_g(t)} R_g dA \quad (6.28)$$

where  $m_g(t)$  is the total GAG mass in a unit averaging volume,  $\rho_g$  is the specific GAG density,  $V_g$  the total volume of GAG produced by a single chondrocyte cell in an averaging volume and  $R_g$  is the specific GAG production rate per unit area. The above equation is based on the assumptions that the diffusivity of GAG is negligible and that the specific GAG density in the ECM phase is uniform.

Obradovic *et al.*, 2000 have shown in engineered tissue constructs, GAG deposition begins at the construct periphery, where a high cell density promotes rapid GAG synthesis than catabolism. However, over the time of cultivation, a limiting steady state concentration ' $\varepsilon_{GAG}^{max}$ ' is approached at which there is a balance of production, degradation, and incorporation of GAG. Accordingly, they formulated a local GAG kinetics using product-inhibition kinetics, with ' $\varepsilon_{GAG}^{max}$ ' the maximum GAG concentration ( $\varepsilon_{GAG}$  at final time of experiment). The dependence upon oxygen concentration was modeled as first-order dependence. A similar kinetic form with respect to GAG and oxygen is used in our model as it best fits the experimental data as compared to the use of a Michaelis-Menten nutrient dependence and first order GAG dependences. Thus, the rate of GAG synthesis is formulated as,

$$R_g = k_G \cdot \left[ 1 - \frac{\varepsilon_g}{\varepsilon_{GAG}^{max}} \right] \cdot \{S\} \quad (6.29)$$

where  $k_G$ , and  $\varepsilon_{GAG}^{max}$  are the GAG production rate and maximum GAG volume fraction respectively. Non-dimensionalizing the nutrient concentration and substituting the specific GAG production rate in equation 6.28 the overall GAG balance is written as,

$$\frac{d\varepsilon_g}{dt} = q_{GAG} * \left\{ k_{GAG} \cdot \left[ 1 - \frac{\varepsilon_g}{\varepsilon_{GAG}^{\max}} \right] \cdot \mu \right\} * \varepsilon_c^{2/3} \quad \text{where } \varepsilon_g = V_g / V, q_{GAG} = \frac{3^{2/3}}{\rho_g} \cdot \left[ \frac{4\pi}{V} \right]^{1/3} \quad (6.30)$$

where overall GAG production coefficient,  $k_{GAG} = k_G \cdot S_o$ .

### **Collagen –**

The mass balance on collagen is given by,

$$\frac{dm_{col}(t)}{dt} = \frac{d}{dt} \int_{V_{col}(t)} \rho_{col} dV = \int_{A_{col}(t)} R_{col} dA \quad (6.31)$$

where  $m_{col}(t)$  is the total collagen mass in a unit averaging volume,  $\rho_{col}$  is the specific collagen density,  $V_{col}$  the total volume of collagen produced by a single chondrocyte cell in an averaging volume and  $R_{col}$  is the specific collagen production rate per unit area. The above equation is similarly based on the assumptions that the diffusivity of collagen is negligible and that the specific collagen density in the ECM phase is uniform.

The specific collagen formation rate is modeled with Michaelis-Menten dependence on oxygen concentration and is given as,

$$R_{col} = \frac{k_{em} \cdot \mu}{K_{col} + \mu} \quad (6.32)$$

where  $k_{em}$  and  $K_{col}$  are the Michaelis-Menten parameters. The overall collagen balance is written as,

$$\frac{d\varepsilon_{col}}{dt} = q_{col} * \left\{ \frac{k_{em} \cdot \mu}{K_{ec} + \mu} \right\} * \varepsilon_c^{2/3} \quad \text{where } \varepsilon_{col} = V_{col}/V, q_{col} = \frac{3^{2/3}}{\rho_{col}} \cdot \left[ \frac{4\pi}{V} \right]^{1/3} \quad (6.33)$$

where overall ECM saturation coefficient is given by,  $K_{ec} = K_{col}/S_o$ .

### ***NMR measurable parameters***

#### ***Effective water diffusion coefficient ( $D_{eff}^w$ ) and T1 relaxation time***

The proton magnetization  $M_l$ ,  $M_g$ ,  $M_{col}$ ,  $M_c$  within the bulk water volume, on the surface of the GAG fibers, on the surface of the collagen fibers, and within the cells, respectively, are described using Bloch equations (Penke *et al.*, 1997). Equations describing the proton magnetization in the void, collagen and the GAG phases, components in the ECM are written as,

$$\begin{aligned} \frac{\partial M_l}{\partial t} &= \nabla D_l \nabla M_l - \frac{M_l - M0_l^\infty}{T1_l} \quad \text{in } V_l \\ \frac{\partial M_{col}}{\partial t} &= \nabla D_{col} \nabla M_{col} - \frac{M_{col} - M0_{col}^\infty}{T1_{col}} + \sigma_{col} (P_{col}^w M_l - M_{col}) \quad \text{at } A_{l\_col} \\ -n_{col} \cdot D_l \nabla M_l &= \sigma_{col} (P_{col}^w M_l - M_{col}) \quad \text{at } A_{l\_col} \\ \frac{\partial M_g}{\partial t} &= \nabla D_g \nabla M_g - \frac{M_g - M0_g^\infty}{T1_g} + \sigma_g (P_g^w M_l - M_g) \quad \text{at } A_{l\_g} \\ -n_g \cdot D_l \nabla M_l &= \sigma_g (P_g^w M_l - M_g) \quad \text{at } A_{l\_g} \end{aligned} \quad (6.34)$$

where  $T1_l^{-1}(= k1_l)$ ,  $T1_{col}^{-1}(= k1_{col})$ ,  $T1_g^{-1}(= k1_g)$  are the bulk and surface (collagen and GAG) relaxation times;  $\sigma_g$ ,  $\sigma_{col}$  are detachment rate per proton of protons on the surface of GAG fibers and collagen;  $M0_l^\infty$ ,  $M0_g^\infty$ ,  $M0_{col}^\infty$  are the equilibrium magnetization values of the protons in the bulk water and on the surface of the GAG fiber and collagen;  $P_g^w$  and  $P_{col}^w$  are the binding coefficient of water to GAG and collagen respectively.

The volume averaging method was used to solve for the effective relaxation constant in the ECM phase and gives

$$\frac{\partial M^e}{\partial t} = \nabla \cdot D_{eff}^w \cdot \nabla M^e - k_{eff}^e \cdot M^e + M^\infty$$

where,

$$T1_{eff}^e = \frac{1}{k_{eff}^e} = \frac{(\varepsilon_l + P_{Ag}^w + P_{Acol}^w)}{\left(\frac{\varepsilon_l}{T1_l} + \frac{P_{Ag}}{T1_g} + \frac{P_{Acol}}{T1_{col}}\right)}; \quad D_{eff}^w = \left[ \frac{D_l \cdot \varepsilon_e^l}{\varepsilon_e^l + (P_{Ag}^w) + (P_{Acol}^w)} \right] \cdot \left[ \frac{\varepsilon_e^l}{2 - \varepsilon_e^l} \right]$$

$$P_{Acol}^w = \frac{P_{col}^w A_{col}}{V} = P_{col}^w \cdot \frac{4 \cdot \pi \cdot R^2}{V} \cdot \varepsilon_{col}^{2/3}; \quad P_{Ag}^w = \frac{P_g^w A_g}{V} = P_g^w \cdot \frac{4 \cdot \pi \cdot R^2}{V} \cdot \varepsilon_g^{2/3} \quad (6.35)$$

In order to obtain a one-equation model for the system, the above averaged equation 6.35 in the ECM phase has to be volume averaged with the magnetization equation in the cell phase given by

$$\frac{\partial M_c}{\partial t} = \nabla \cdot D_c^w \cdot \nabla M_c - \frac{(M_c + M0_c^\infty)}{T1_c} \quad \text{in } V_c$$

$$-n_{ce} \cdot D_c^w \nabla M_c = -n_{ec} \cdot D_{eff}^w \nabla M_c \quad \text{at } A_{ce}$$

$$-n_{ce} \cdot D_c^w \nabla M_c = B \cdot (M_c - K_{eq}^w M^e) \nabla M_c \quad \text{at } A_{ce}$$

$$\frac{\partial M^e}{\partial t} = \nabla \cdot D_{eff}^w \cdot \nabla M^e - k_{eff}^e \cdot M^e + M0^\infty$$

(6.36)

where  $D_c^w$  is the diffusion coefficient of water through the cells,  $M0_c^\infty$  is the equilibrium magnetization value of the protons on the cell surface,  $B$  is the rate coefficient for proton transfer into the  $c$  (cell) phase, and  $K_{eq}^w$  is the equilibrium coefficient into the  $c$  phase. Following the

similar averaging methodology the governing one-equation model for diffusion and relaxation constant in the reactor is,

$$\frac{\partial \{M\}}{\partial t} = \nabla \cdot D_{eff}^w \cdot \nabla \{M\} - k_{eff}^T \cdot (\{M\} - M0_{eff}^\infty)$$

where,

$$k_{eff}^T = \frac{1}{T1_{eff}} = \frac{1}{(\varepsilon_c + Keq^w \varepsilon_e)} \left[ \left( \frac{\varepsilon_l + \frac{P_{Ag}}{T1_l} + \frac{P_{Acol}}{T1_{col}}}{\varepsilon_l + P_{Ag} + P_{Acol}} \right) \cdot \varepsilon_e + Keq^w \cdot \left( \frac{1}{T1_c} \right) \cdot \varepsilon_c \right]$$

$$D_{eff}^w = \left( \frac{D_{eff}^e}{\varepsilon_c \cdot Keq^w + \varepsilon_e} \right) * \left[ \frac{2k^w - (k^w - 1)\varepsilon_e + \varepsilon_e \varepsilon_c^{-1/2} \alpha^w}{2 + (k^w - 1)\varepsilon_e + (2 - \varepsilon_e)\varepsilon_c^{-1/2} \alpha^w} \right]$$

(6.37)

where  $k^w = (K_{eq}^w D_c^w / D_{eff}^{ew})$  is the ratio of the diffusion coefficient of water in the cell phase over that in the ECM phase (here the non-cellular phase) and  $\alpha^w = (D_c^w / R P_w)$  is the ratio of the cell phase water diffusion coefficient over the mass transfer coefficient at the cell-liquid interphase in the averaging volume.  $P_w$  represents the mass transfer coefficient at the cell membranes, i.e. at  $A_{ec}$ , and  $Keq^w$  is the equilibrium coefficient for water between the ‘c’ and the ‘e’ phases of the averaging volume.

### 6.2.3 Note on Parameters

Reactor dimensions are taken from Peterson *et al.*, 1997. Data on diffusion coefficients of oxygen and water in the cell phase and the respective self-diffusion coefficients are obtained from the literature (Chow *et al.*, 2001; Horner *et al.*, 1998). The specific oxygen consumption rate for cell metabolism is obtained from Obradovic *et al.*, 2000. The first order rate constant ( $k_c$ ) is computed by calculating the ratio of  $Q_{max} / Km$ , the Michaelis-Menten parameters in the proposed Michaelis-Menten oxygen consumption rate in their model. Specific GAG and collagen densities are obtained from Baser *et al.*, 1998.



The remaining transport and reaction parameters are obtained by fitting the simulated model data of cell growth, cell proliferation, ECM (GAG and collagen) masses as functions of time to the experimental data of Potter *et al.*, 1998. Although the binding coefficients of water and oxygen to the GAG and collagen fibers are obtained by model experimental fitting, a fixed ratio of GAG to collagen binding to the components (water and oxygen) is maintained. It has been shown in the literature that 70% of the water in cartilage is bound to GAG and the remaining 30% to collagen (Nordin & Frankel, 1989). The parameters used in the model are listed with their references in Table 1.

#### 6.2.4 Sensitivity Analysis formulation

The sensitivity of model variables, including the collagen volume fraction ( $\varepsilon_{col}$ ), the GAG volume fraction ( $\varepsilon_g$ ), the cell volume fraction ( $\varepsilon_c$ ), the fractional number of cells, the effective diffusivities of oxygen and water, and the effective NMR relaxation constant, to changes in model parameters were evaluated as functions of time in terms of normalized sensitivities, i.e.  $Y(t, \phi_j)$  the model variable with respect to model parameters  $\phi_j$  and normalized sensitivity  $S(Y, \phi_j)$  given as,

$$S(Y, \phi_j) = \frac{\phi_j}{Y} \cdot s(Y, \phi_j)$$

$$\text{where } s(Y, \phi_j) = \frac{\partial Y(t, \phi_j)}{\partial \phi_j}$$
(6.38)

where  $s(Y, \phi_j)$  is the non-normalized sensitivity (Varma *et al.*, 1999).

#### 6.2.5 Solution Procedure

Kinetic expressions for cell metabolism, growth, proliferation, and ECM (GAG and collagen) production are proposed as functions of experimentally observed parameters that affect these

processes. The rate parameters of these cell processes along with the oxygen and water binding coefficient to ECM are varied to fit the model to experimental data (Potter *et al.*, 1998).

The equations describing cell growth [equation 6.26], cell proliferation [equation 6.22], and ECM (GAG [equation 6.30] and collagen [equation 6.33] production as functions of time are solved simultaneously using MATLAB (version 6.5, The Mathworks, Inc.). The model results are used in equations 6.18 and 6.12 to compute the nutrient concentration and effective diffusion coefficient variation of oxygen with time, due to changes in tissue mass, respectively. Similarly, the volume fractions of cell and ECM components are substituted in equation 6.37 to obtain the effective T1 relaxation time constant and effective diffusion coefficient of water in the tissue.

### **6.3 Results and Discussion**

The current model simulates the changes in cell mass, ECM mass, oxygen concentration, effective diffusion coefficient of oxygen, water diffusion coefficient and NMR relaxation coefficient as functions of time. Physiological kinetic functions describing cartilage tissue developmental processes are used. The effect of the microenvironment on the intrinsic tissue development characteristics in the 3-dimensional hollow fiber bioreactor system is studied. The model is used to determine the NMR measurable parameters to further establish their correlation with the chemical characteristics of the tissue.

The growth of a single chondrocyte cell inside an averaging volume with time is shown in Figure 6.3. Cell growth (maturation) is expressed in terms of volume fraction of cell and accounts for an increase in the average area of a chondrocyte cell in a ‘unit cell’ or averaging volume during the culture time. Since all ‘unit cells’ are identical this cell growth is representative of growth in all averaging volumes. The solid line represents the simulated results from the model whereas the solid dots denote the experimental data from Potter *et al.*, 1998 (Appendix D). Growth of cells is seen to be slow during early period in time, corresponding to the initial lag phase of cell growth. However, after week 3, the growth is exponential. The results shown here are for kinetic growth rate function with Michaelis-Menten nutrient dependence, second order cell

number dependence and first order cell volume fraction dependence, which gives the best fit to the experimental data among the various functions used. This kinetic function used in the model could not completely account for the higher cell growth during the later times in culture (Figure 3). Several other growth rate functions such as Contois, Modified Contois, Moser and heterogeneous functions (Galban and Locke, 1999a) were tested (results shown in Figure 6.13). However, these other functional forms did not fit the data as well. Probably there is a need to incorporate the effect of other environmental factors in future modeling efforts like lactate and glucose in order to better explain the growth pattern of chondrocytes as observed in the experiments. Moreover, in order to provide quantitative information of cell growth behavior there is need for further systematic experimental data on oxygen concentration for example, for the same reference system.

Cells synthesize ECM, which in our model system includes collagen and GAG, throughout the culture time. Figure 6.4 shows increase in collagen mass. The collagen mass is obtained by multiplying the volume fraction of collagen ( $\varepsilon_{col}$ ) in a ‘unit cell’ with the total of the sum of all the volume of the averaging volume ( $V$ ) and the density of the collagen fibers ( $Collagen\ Mass = \varepsilon_{col} \cdot (V \cdot n \cdot n_{max}) \cdot \rho_{col}$ ). Model simulations are in good accordance with the experimental results. Similarly, simulated GAG mass in the reactor is shown as a solid line as function of time in Figure 6.5. The GAG mass is also obtained by multiplying the simulated volume fraction of GAG in a ‘unit cell’ with the total volume of averaging volumes and density of GAG ( $GAG\ Mass = \varepsilon_g \cdot (V \cdot n \cdot n_{max}) \cdot \rho_g$ ). The GAG content increases during the early weeks in culture. However, once the maximum GAG concentration is reached at almost 2 weeks in culture a saturation level is reached. The model trend fits the experimental data very well.

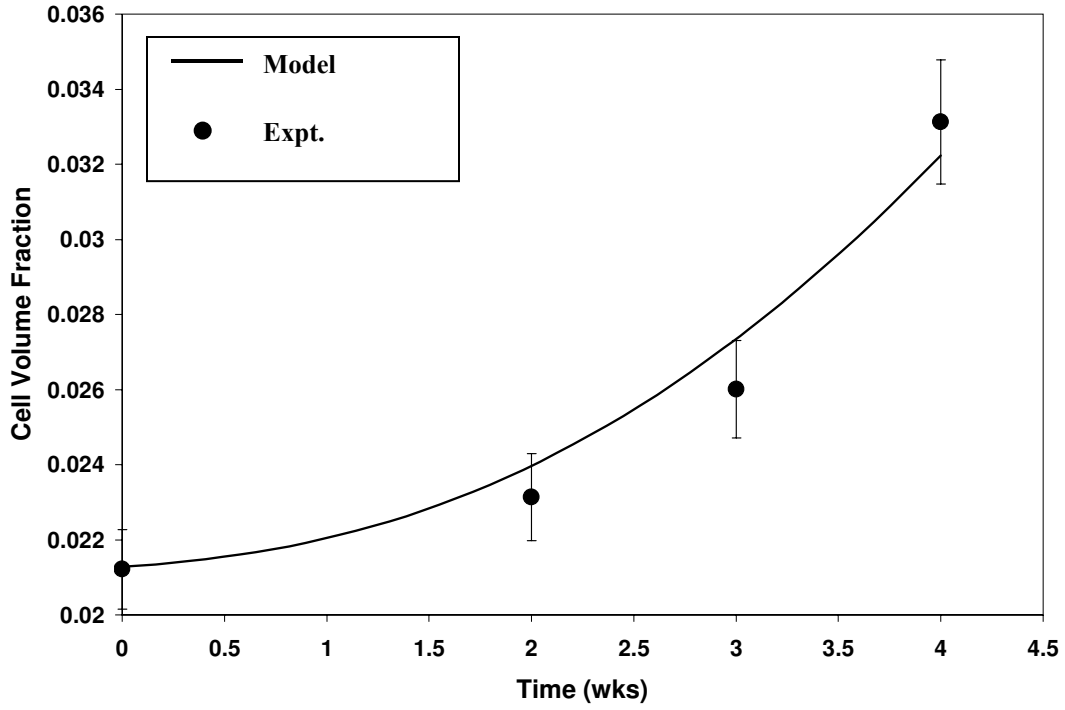


Figure 6. 3 Model-data comparison for the growth of cells ( $\epsilon_c=V_c/V$ ) with time (Experimental error bars obtained using error percentage of 5%)

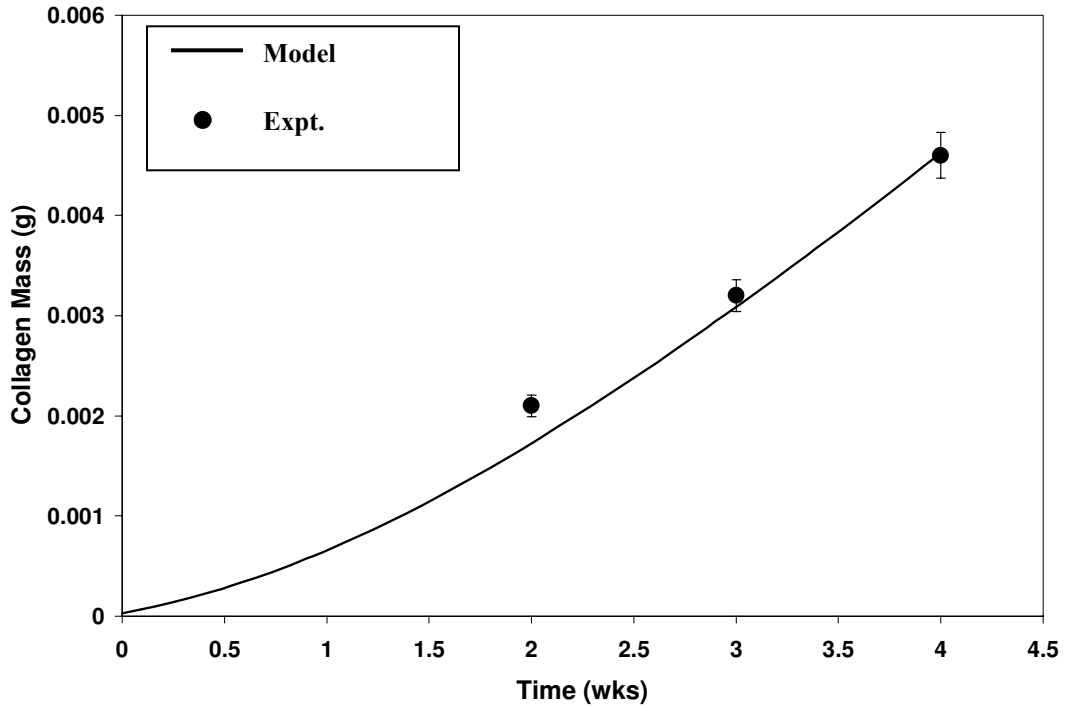


Figure 6. 4 Model-data comparison for total Collagen mass (g) in the reactor with time (Experimental error bars obtained using error percentage of 5%)

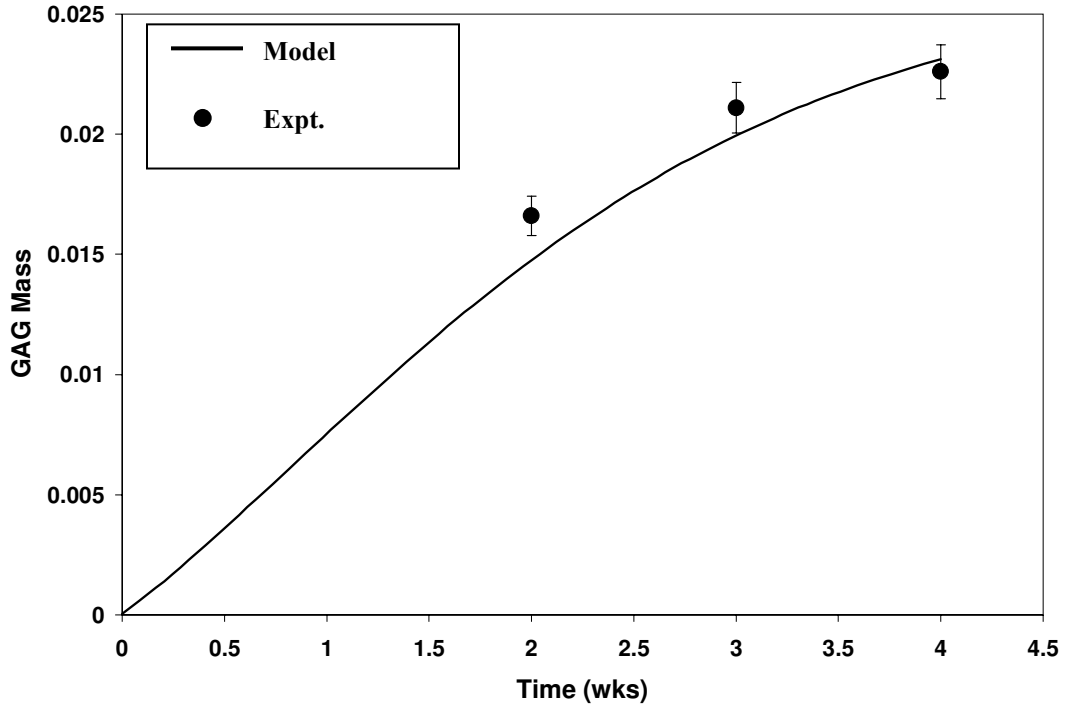


Figure 6. 5 Model-data comparison for total GAG mass (g) in the reactor variation with time (Experimental error bars obtained using error percentage of 5%)

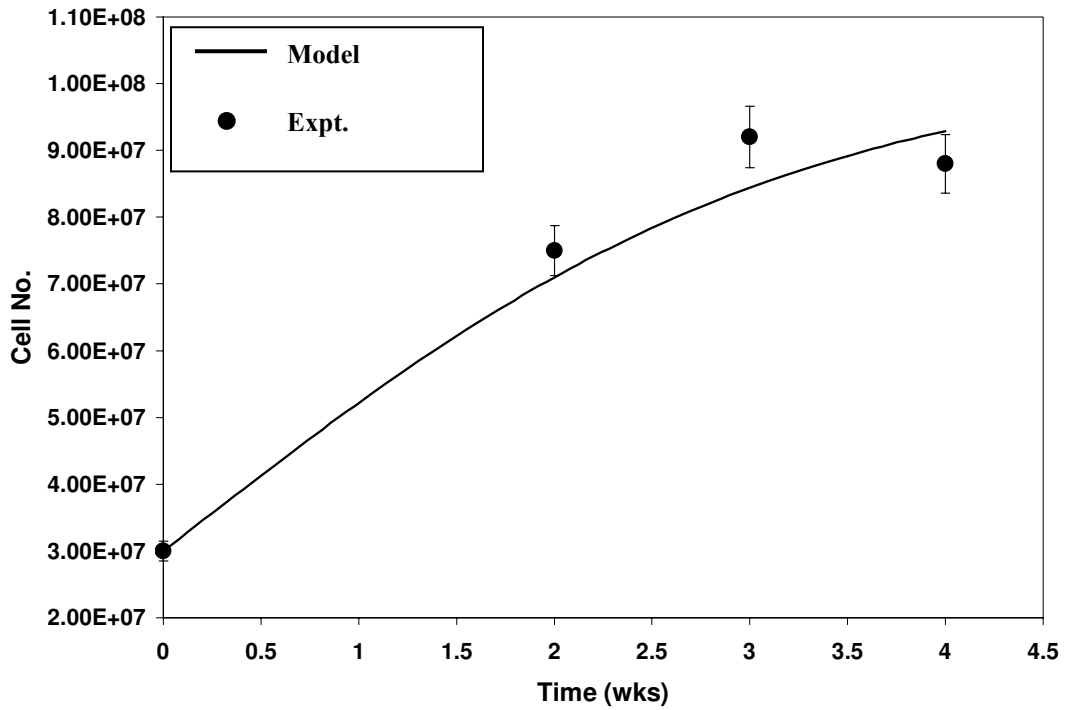
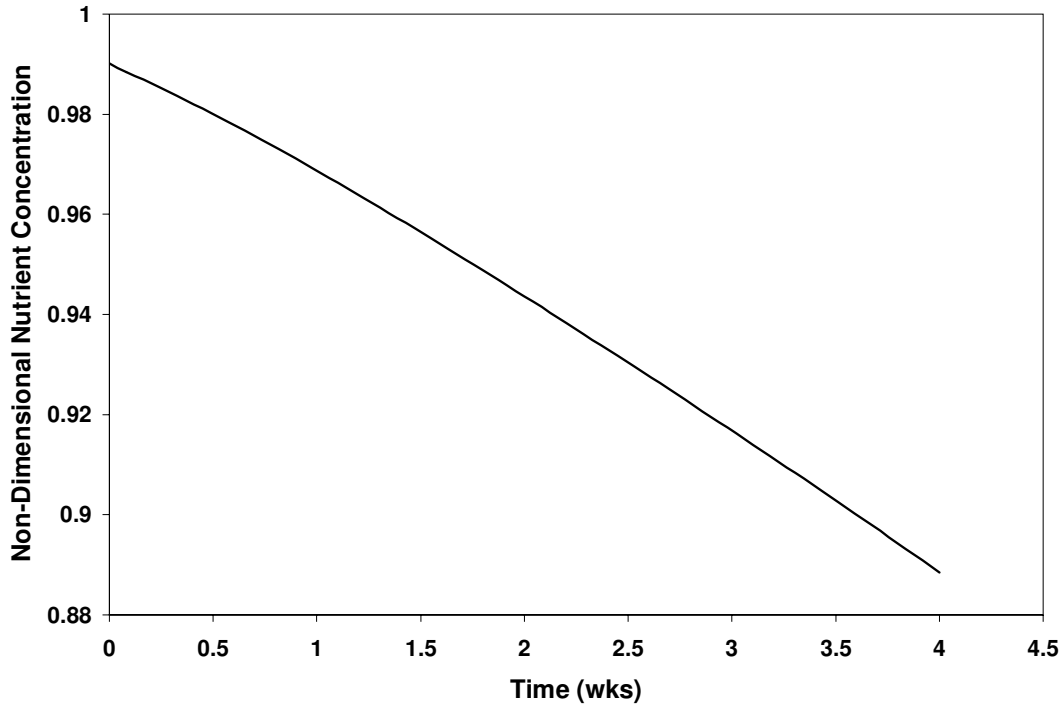


Figure 6. 6 Model-data comparison for total number of cells in the reactor (around all 6 fibers),  $[n_c]$  with time (Experimental error bars obtained using error percentage of 5%)



**Figure 6.7 Non-dimensional nutrient concentration ( $\mu$ ) variation with time**

Figure 6.6 denotes changes in cell number (or ‘unit cells’), i.e. cell proliferation during the culture time of 4 weeks. An increase in cell number occurs during the first 3 weeks of culture and then levels off with time. The model predicts saturation, i.e. no further increase in cell number, at later times in the culture, and this is primarily due to contact inhibition as reflected in the Contois form of the kinetic rate function. The model results seem to fit the experimental data very well. The experimental results of Potter *et al.*, 1998 have suggested that during cartilage tissue culture cell proliferation occurs during the early time period. Once the cells stop proliferating, cells start maturing by growing in size, corresponding to cell growth in our model. This developed mathematical model is able to explain the experimental data in this context very well.

Figure 6.7 shows the averaged non-dimensional nutrient concentration during the culture time. Due to the small hollow fiber or capillary diameter and high nutrient flow rate the variations in oxygen concentration in both the axial and radial directions inside the hollow fiber tube lumen are assumed to be negligible. The constant supply of oxygen at the surface of the hollow fiber or

capillary provides more oxygen for cell metabolism, even accounting for the presence of very high cell numbers. Hence, the drop of oxygen concentration is only to a non-dimensional value of nearly 0.885 (corresponding to a drop of nearly 12% of the feed concentration  $S_o$  in the hollow fiber tube). The simulated oxygen concentration results cannot be compared to experimental results because the rate of oxygen depletion over time in these types of reactors has not been reported in the literature, and it is recommended that such data need to be taken in future experiments.

An increase in cell mass (due to proliferation and cell growth) and ECM mass production over time increases the restrictions to diffusive transport of oxygen and water. Figure 6.8 (a) and 6.8 (b) show the decrease in effective diffusion coefficient of oxygen and water, respectively, in the reactor with time. The lower effective diffusion coefficient of oxygen due to larger restrictions and binding in the tissue construct, in turn, reduces the supply of oxygen for consumption by the cells for various physiological processes such as metabolism, growth, proliferation, and ECM synthesis. Figure 9 shows the simulated and experimental apparent diffusion coefficient of water as a function of time. The apparent diffusion coefficient is computed by normalizing the effective diffusion coefficient of water by dividing it by the self-diffusion coefficient of water. This is a measure of restricted transport of water due to increase in cell and ECM mass and is experimentally measured by NMR. Model results show a steady drop of this coefficient over the entire culture time of 4 weeks. However, experimental results (solid dots) show that the normalized diffusion coefficient does not drop until the 3<sup>rd</sup> week of the culture, after which it drops from a value of 0.8 to 0.43. Clearly the model is not able to capture that aspect of the experimental data.

One possible reason for the discrepancy between experimental and modeling results of the apparent diffusion coefficient of water is likely due to the NMR experimental diffusion measurement technique. Small NMR diffusion time ( $\Delta$ ) 10 ms considered in the experiments corresponds to a water diffusion distance of nearly 4.7  $\mu\text{m}$ . However, the roughly estimated average void phase radii at time = 1 wk and time = 4wk are 11.92  $\mu\text{m}$  and 11.79  $\mu\text{m}$ , respectively (Appendix F). These length scales were calculated based upon the free volume in the cellular domain (radius  $L(n)$ ) and assuming that the ECM components are clumped around the cells.

Since the length scale at the early times is higher than the NMR diffusion distance, probably the NMR measurement does not capture the restrictions due to spatial constraints and adsorption. The assumption that most of the ECM is clumped around the cell may be more appropriate at these earlier times when there is less ECM and more free void space around the cell/ECM complex. However, as the cells grow and produce ECM over time the fibrous nature of the matrix may be more pronounced and lead to more restrictions than are reflected in the computed length scale above. Therefore, the model can explain the data at four weeks and not at the earlier times.

It should also be stated that the decrease in diffusion coefficient shown in Figure 6.9 is dominated primarily by the binding of water to collagen and GAG fibers and not due to restrictions because of cell and ECM mass formation over time (model results shown in dotted line). This is further reflected by increase in magnetization transfer coefficient with time in the experimental results described by Potter *et al.*, 1998 as this denotes higher binding of water to the ECM components.

The effect of restricted transport because of tissue development can also be seen in Figure 6.10. The figure shows the variation of effective longitudinal relaxation coefficient ( $T1_{eff}$ ) with time. The relaxation constant decreases gradually between weeks 1 and 4, consistent with increases in collagen and GAG molecules, corresponding to not only increase in tissue mass but also larger binding of water to these ECM components. There appears to be a slightly larger drop between weeks 3 and 4 than in the earlier weeks, in partial agreement with the diffusion coefficient data. The significance of this drop is not known and more detailed analysis of the experimental error and the water binding process may help in further understanding the reason for the model-data comparison.

Figure 6.11 validates the basic model assumptions for derivation of analytical solution for nutrient (oxygen) concentration in the reactor. Figure 6.11 (a) shows the quasi-steady state assumption holds for the culture time of 4 weeks. Also, Figure 6.11 (b) shows that nutrient concentration can be spatially averaged in the reactor by assuming the nutrient consumption rate to be small compared to the rate of diffusion, again for the time of culture of 4 weeks. However,



upon running the program for a longer time of 8 weeks it is seen that similar trends in tissue growth persist. For this length of time the assumption  $(K_{eff} * T_{bf} * T_{bf}) / D_{eff} < 1$  does not hold anymore, which means that the nutrient concentration cannot be averaged due to large spatial variations (results not shown here). This is because over longer periods of time, there is larger tissue growth, due to increases in cell size and higher ECM (GAG and collagen) production by cells in culture.

The major kinetic parameters used in the model are obtained by model-experimental fit. A sensitivity analysis of the system would help in the identification of the most important parameters affecting tissue growth (collagen, GAG, and cell mass formation); metabolite (oxygen) concentration and its effective diffusion coefficient, as well as the NMR measurable parameters, from an appropriate selection of few shown in the Figures 6.12. The results of the analysis would thus suggest the key parameters that greatly affect each of these individual model variables, and thus suggest need for accurate estimation of these parameters through experimental studies.

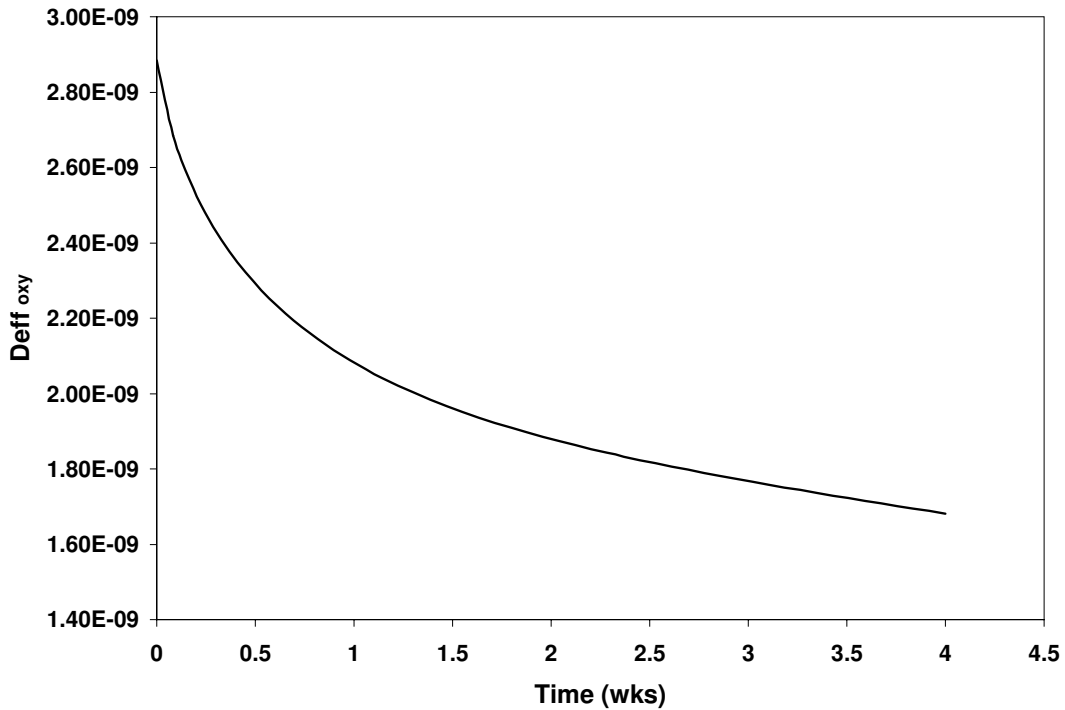


Figure 6.8 a Effective diffusion coefficient of oxygen ( $D_{eff}$ ) in the reactor

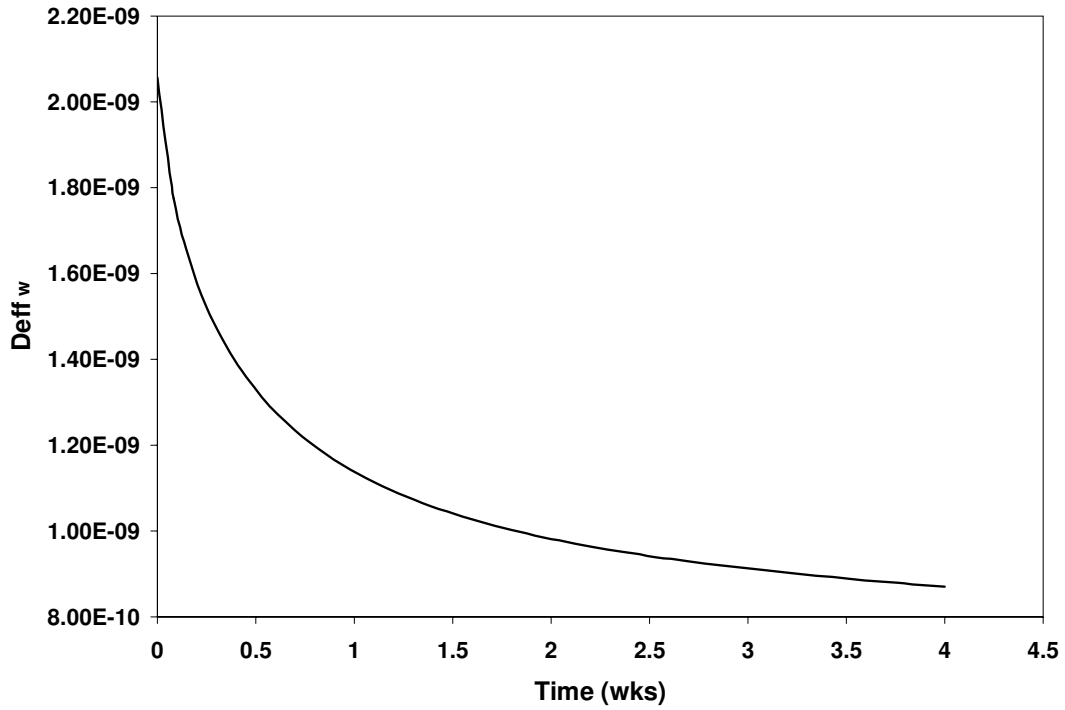


Figure 6. 8 b Effective diffusion coefficient of water ( $D_{eff}^w$ ) in the reactor

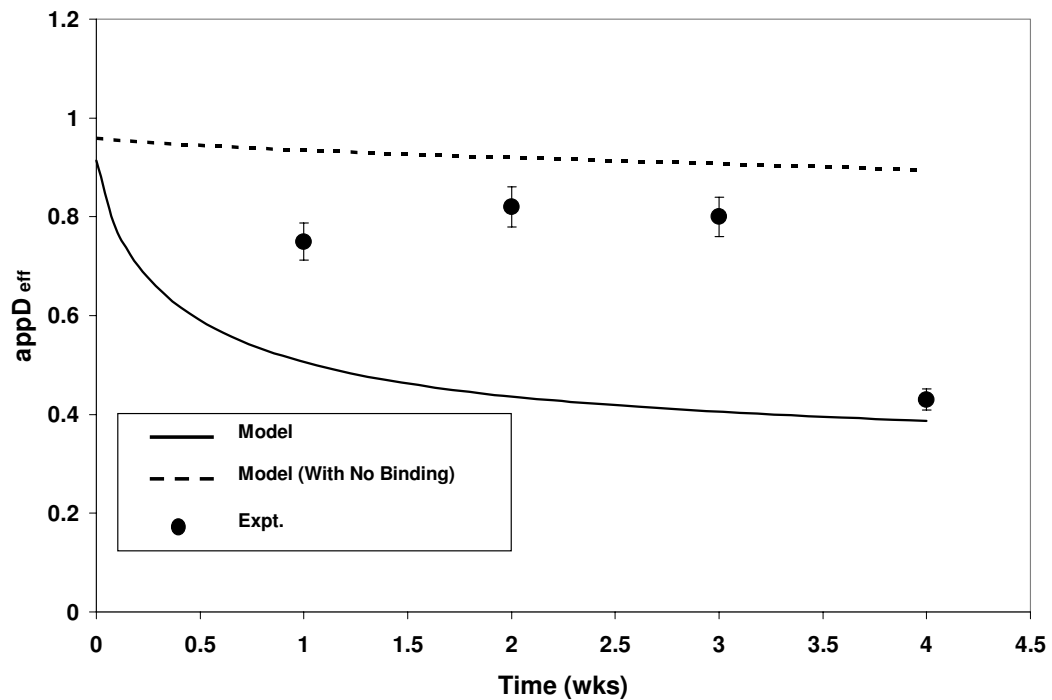


Figure 6. 9 Model-data comparison for normalized diffusion coefficient of water in cartilage construct in HFBR ( $appD_{eff} = D_{eff}^w/DI$ ) where  $D_{eff}^w$  is the effective diffusion coefficient of water in cartilage tissue,  $DI$  is the diffusion coefficient of water in cartilage free constructs (Experimental error bars obtained using error percentage of 5%)

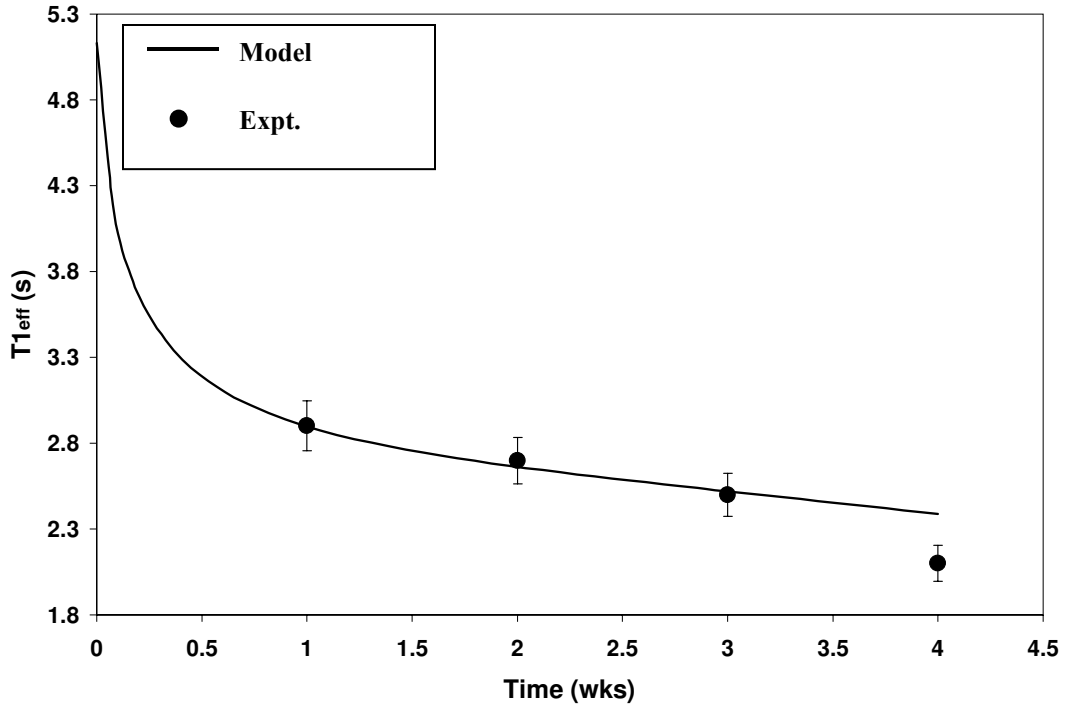


Figure 6. 10 Model-data comparison for effective relaxation constant  $[T1_{eff}]$  variation with time (Experimental error bars obtained using error percentage of 5%)

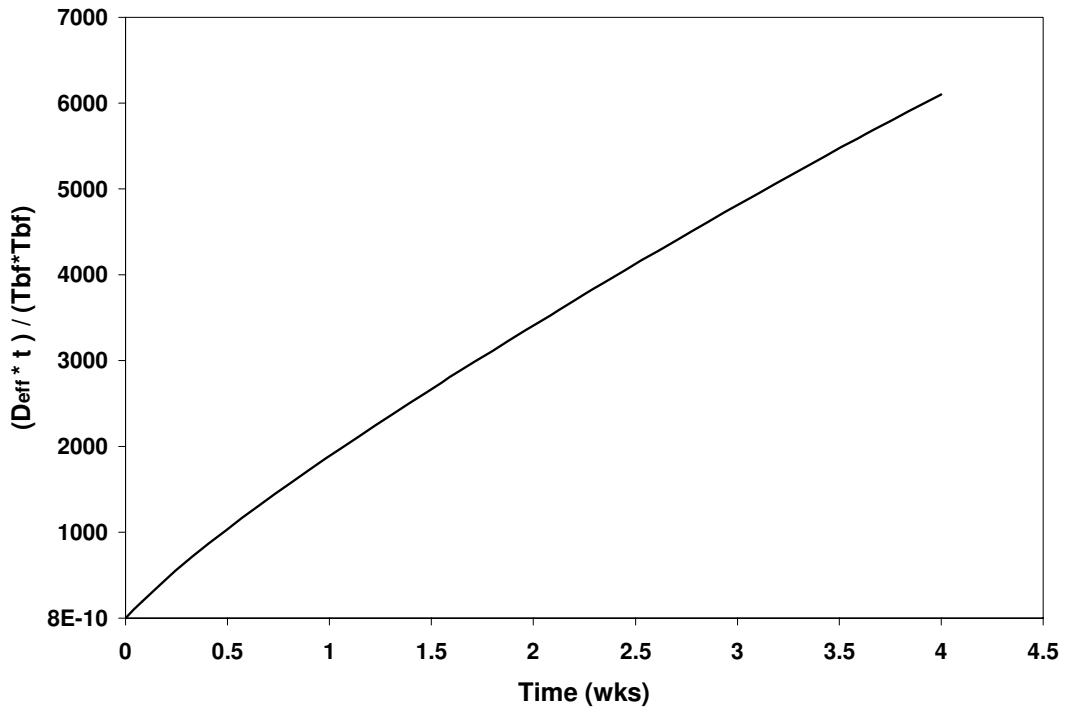
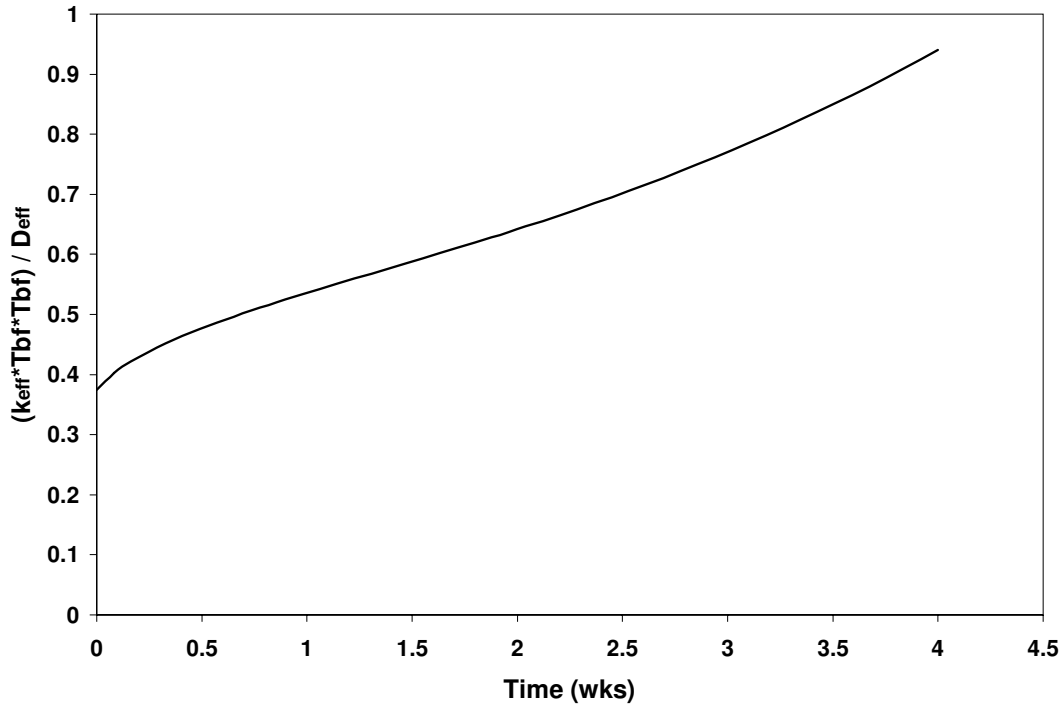


Figure 6.11 a Validity test for the quasi-steady state assumption (Equation 6.14 a)



**Figure 6. 11 b Validity test of Equation 6.14 b showing that the nutrient consumption rate is small relative to diffusion during the 4 weeks of culture**

Figure 6.12 (a) shows the normalized sensitivity of the collagen volume fraction inside an averaging volume. It is seen that this model variable is most sensitive to the collagen production rate ' $k_{em}$ ' and the saturation Michaelis-Menten parameter ' $K_{ec}$ '. Increasing ' $k_{em}$ ' or decreasing ' $K_{ec}$ ' is shown to increase the rate of collagen production over nearly 2 weeks. However, after week 2 the effects of the collagen production rate parameters level off. The normalized GAG production expressed as concentration is seen to be highly sensitive to its production rate ' $k_{GAG}$ ', and increases to 0.9 in the first 1-2 days and then drops gradually at later times to a value close to 0.1 (Figure 6.12 b). Positive sensitivity denotes that an increased ' $k_{GAG}$ ' would increase the GAG synthesis rate. The mass balance of GAG formation utilizes product-inhibition kinetics with ' $\epsilon_{GAG}^{max}$ ' the maximum GAG concentration. Hence, after the maximum limit of GAG volume fraction is reached the sensitivity of ' $k_{GAG}$ ' to a GAG volume fraction change decreases. Increases in the collagen and GAG volume fractions would lead to larger oxygen binding to these ECM components and thus decrease the diffusivity of oxygen (Figure 6.12 f).

The cell mass coefficient ' $k_p$ ', the modified-Contois saturation parameter ' $K_p$ ', the cell growth coefficient ' $k_g$ ' and the cell growth saturation coefficient ' $K_{cont}$ ' are the most important parameters affecting the chondrocyte cell mass. Figure 6.12 c shows that increasing ' $k_p$ ' or decreasing ' $K_p$ ', increases the cell number during the first 2 weeks of culture. However, later in time the sensitivity of cell number to changes in these parameters almost levels off. This is probably because of contact inhibition that restricts any further increase in cell number by proliferation. Figure 6.12 c also demonstrates the fact that the cell growth parameters ( $k_g$ ,  $K_{cont}$ ) have no effect at early times in culture, corresponding to the fact that this period corresponds to the cell proliferation stage. However, later during culture, increasing the cell growth rate by increasing ' $k_g$ ' and decreasing ' $K_{cont}$ ' the cell proliferation decreases (Figure 6.12 c). These results support the experimental observation that once the proliferation stops, the cells start growing in size filling up the space which is the stage of cell growth or maturation. Increased cell volume fraction (due to cell growth) within an averaging volume, increases the production of GAG and collagen associated with a 'unit cell' (Figures 6.12 a, 6.12 b). Larger cell and ECM mass decreases diffusion of the oxygen nutrient (Figure 6.12 f) and provides larger restrictions to water diffusion (Figure 6.12 g).

The nutrient concentration (Figure 6.12 e) is very sensitive to the cell mass coefficients ' $k_p$ ', and ' $K_p$ ' as well as the metabolic coefficient ' $k_c$ '. An increase in cell number by changing these parameters would lead to a larger consumption of oxygen, thus decreasing the oxygen concentration in the reactor. An increase in  $k_c$  also reduces the nutrient concentration, because of higher rates of oxygen consumption. Moreover, an increased binding of oxygen to GAG (by increasing ' $P_g^o$ ') also reduces the concentration of nutrient as expected.

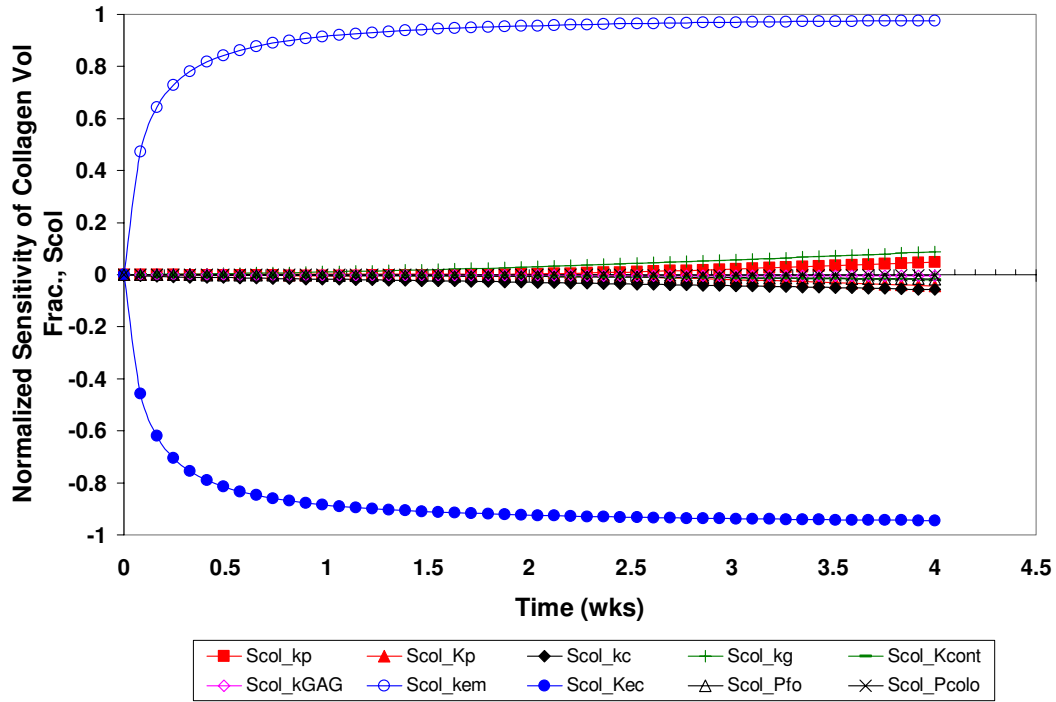


Figure 6.12 a Normalized Sensitivity of Collagen volume fraction with varying model parameters as a function of time; sensitivity highest to collagen production parameters

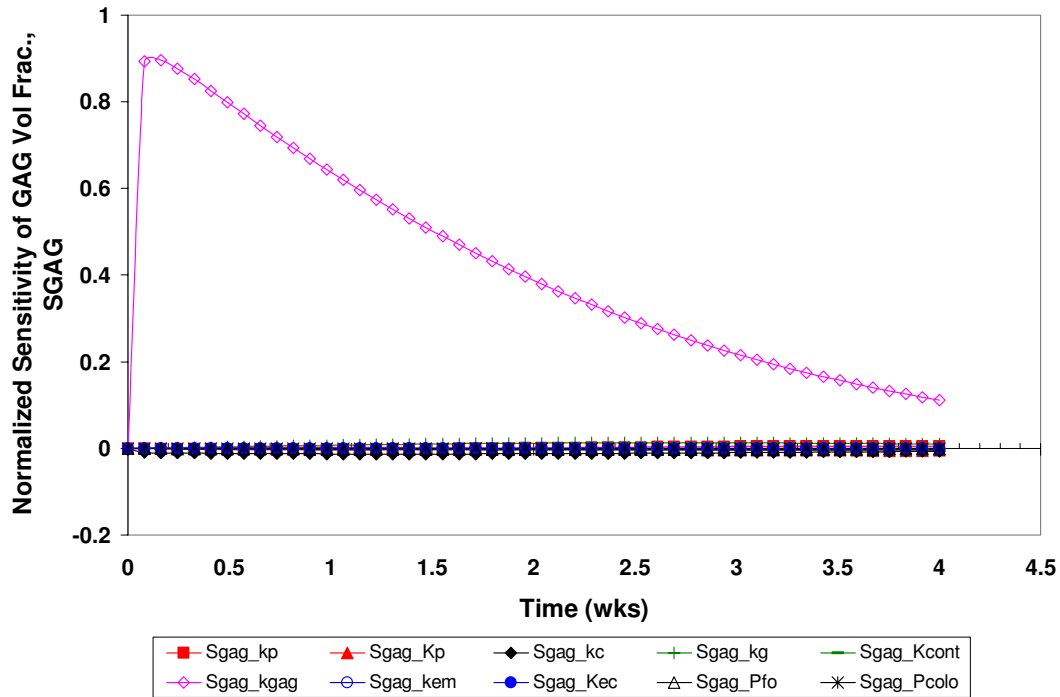


Figure 6.12 b Normalized Sensitivity of GAG volume fraction with varying model parameters as a function of time; sensitivity highest to GAG production parameter

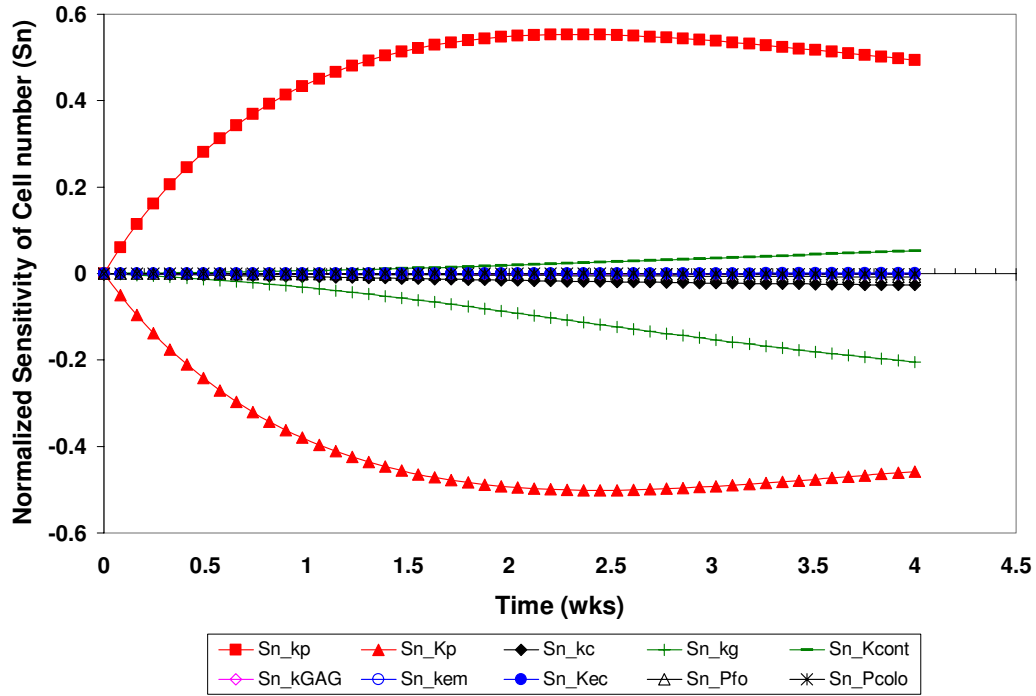


Figure 6.12 c Normalized Sensitivity of cell number with varying model parameters as a function of time; sensitivity highest to cell proliferation and cell growth parameters

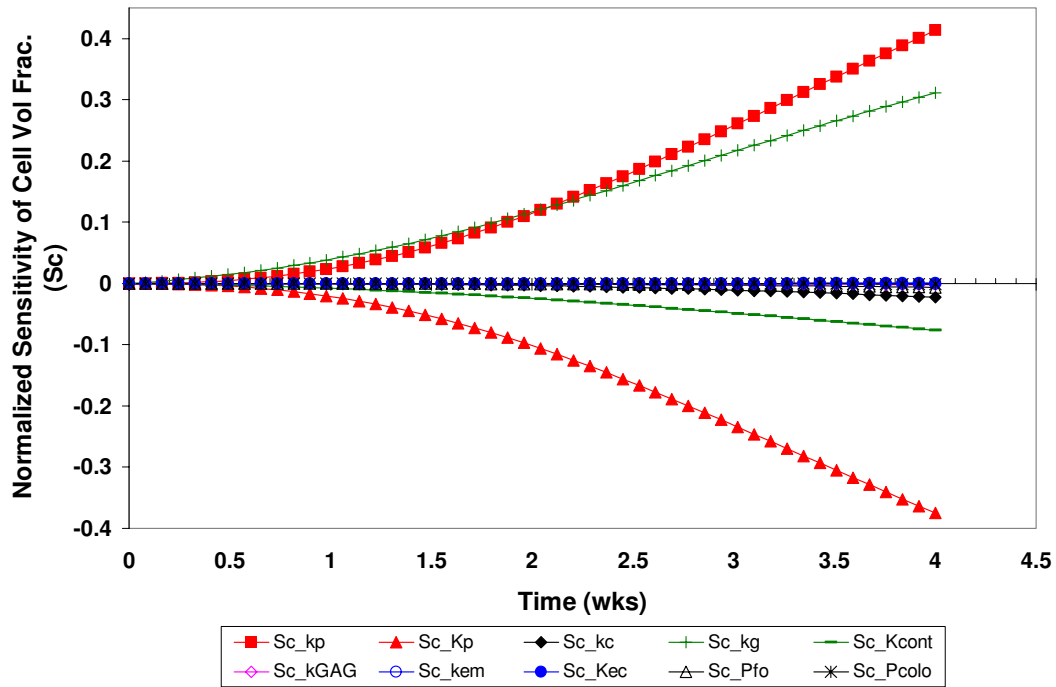


Figure 6.12 d Normalized Sensitivity of cell volume fraction with varying model parameters as a function of time; sensitivity highest to cell growth and proliferation parameters

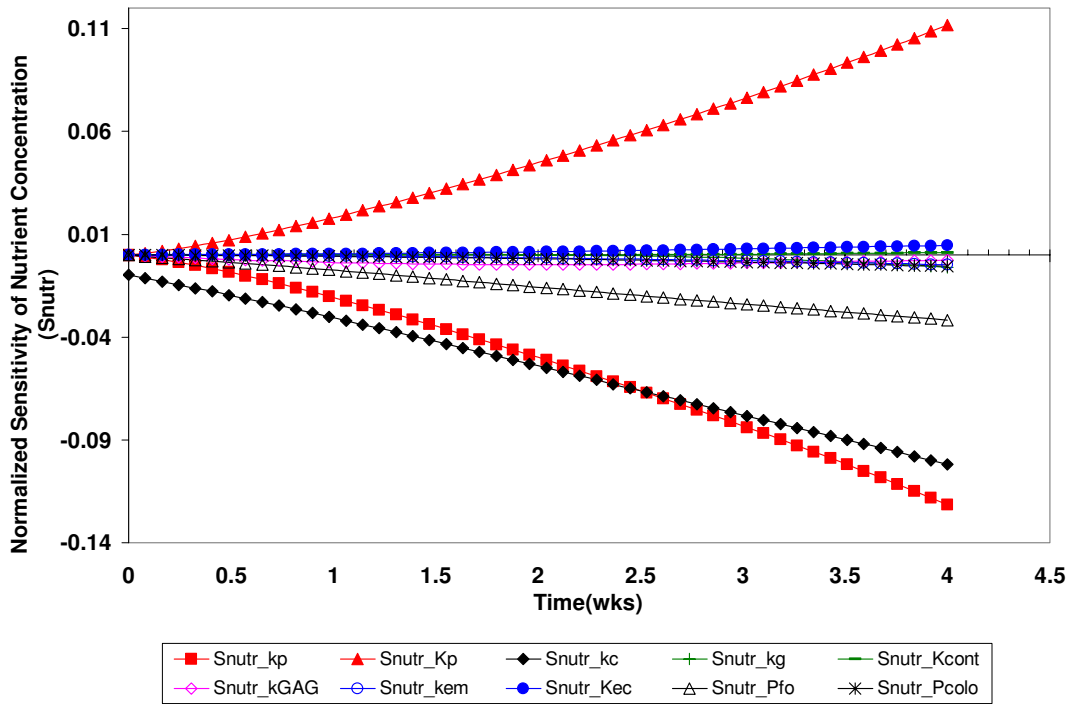


Figure 6.12 e Normalized Sensitivity of nutrient concentration with varying model parameters as a function of time; sensitivity highest to cell proliferation, first order oxygen consumption rate and oxygen binding parameters

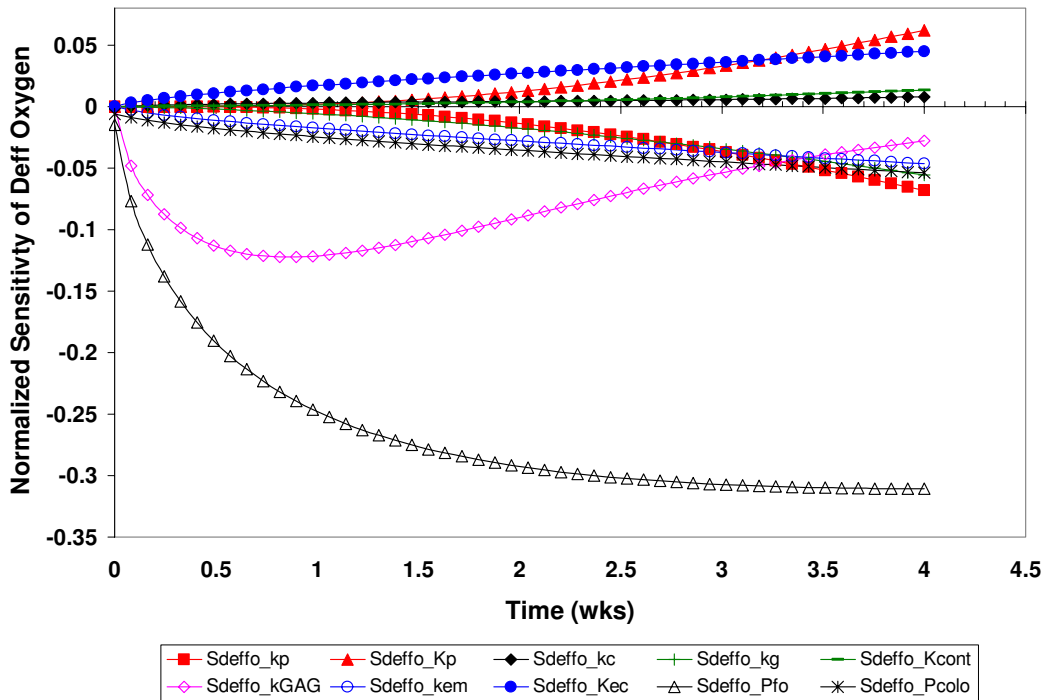


Figure 6.12 f Normalized Sensitivity of effective oxygen diffusion coefficient in the reactor with varying model parameters as a function of time; sensitivity highest to oxygen GAG binding coefficient and the GAG production rate



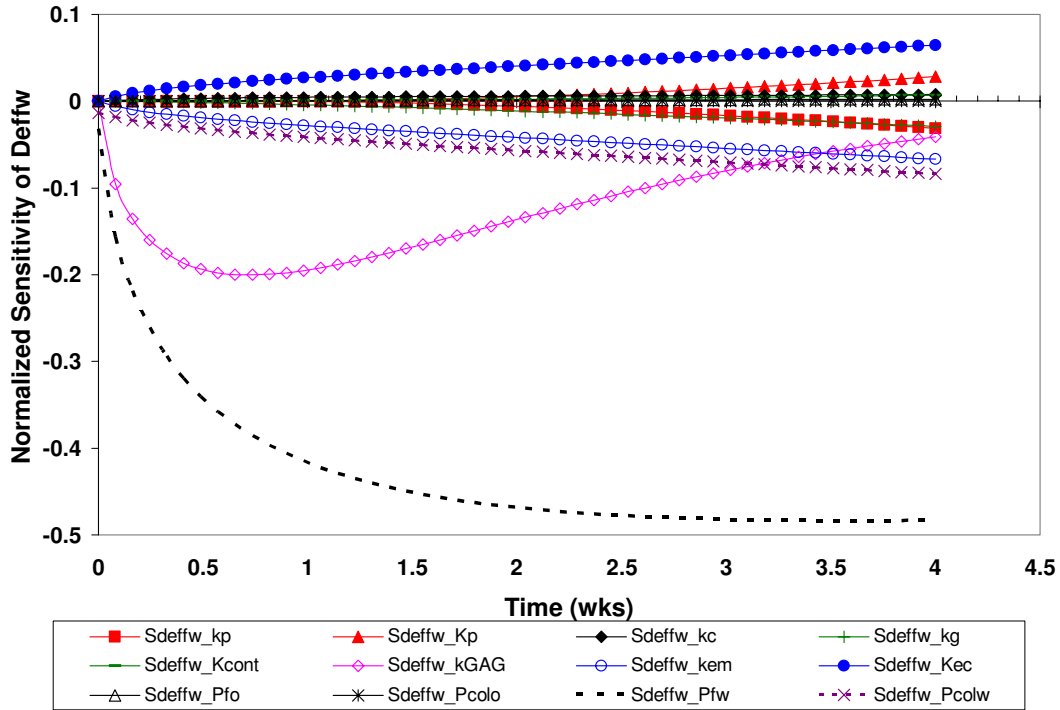


Figure 6.12 g Normalized Sensitivity of water diffusion coefficient in the reactor with varying model parameters as a function of time; sensitivity highest to water GAG binding coefficient and GAG production rate coefficient

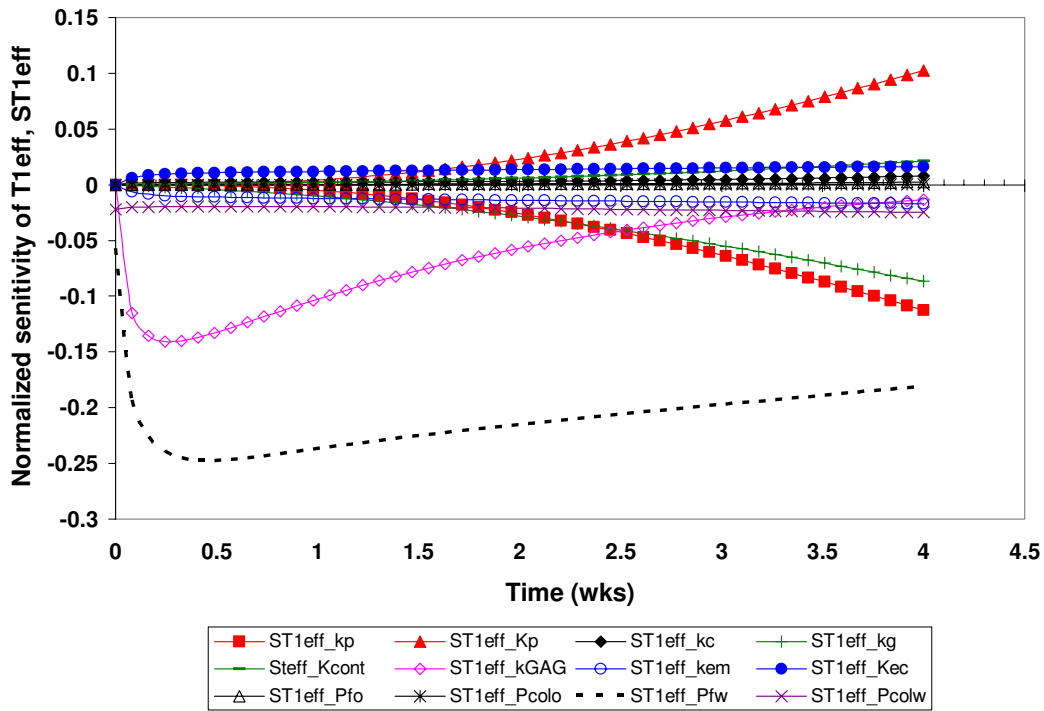


Figure 6.12 h Normalized Sensitivity of NMR effective relaxation coefficient in the reactor with varying model parameters as a function of time; sensitivity highest to water GAG binding coefficient, GAG production rate coefficient, cell growth and proliferation parameters

VARYING GROWTH RATE FUNCTIONS – [For the same set of parameters as used in model]

**Case 1:**

$$R_c = \left[ \left( \frac{k_g \cdot \mu}{K_{cont} \cdot \varepsilon_c + \mu} \right) \cdot n^0 - k_{cd} \right]$$

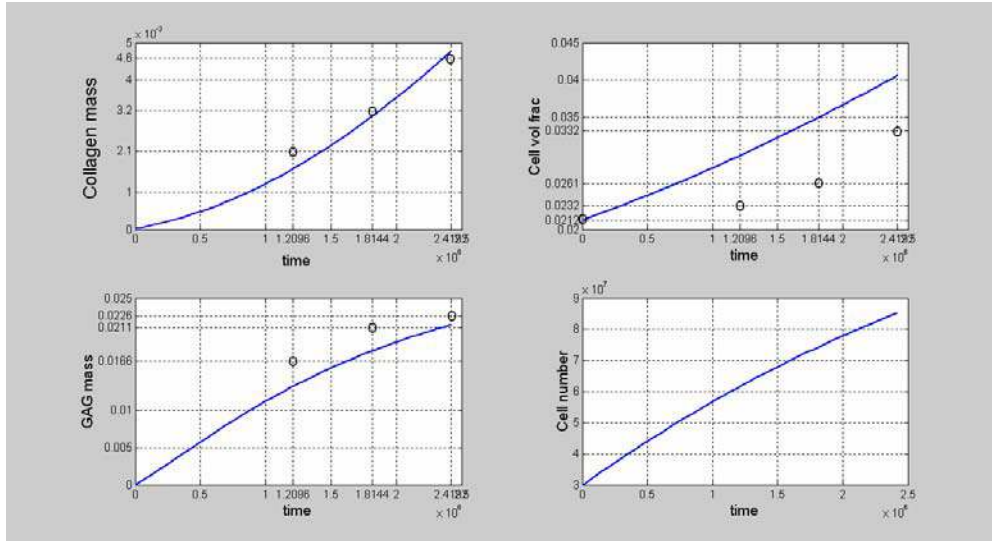


Figure 6.13 a Cartilage tissue growth over time obtained by the use of modified Contois function with respect to nutrient concentration and no dependence on cell number (as shown by the equation in case 1). Model results are shown by solid line and experimental results in dots.

**Case 2:**

$$R_c = \left[ \left( \frac{k_g \cdot \mu}{K_{cont} \cdot \varepsilon_c + \mu} \right) \cdot n^1 - k_{cd} \right]$$

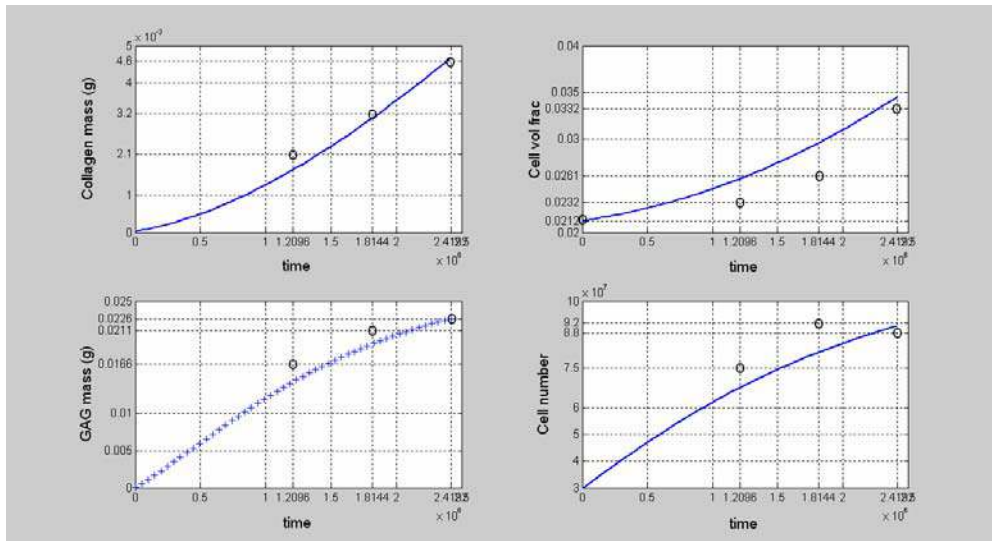


Figure 6.13 b Cartilage tissue growth over time obtained by the use of modified Contois function with respect to nutrient concentration and 1<sup>st</sup> order dependence on cell number (as shown by the equation in case 2).

**Case 3:**

$$R_c = \left[ \left( \frac{k_g \cdot \mu}{K_{cont} \cdot \varepsilon_c + \mu} \right) \cdot n^3 - k_{cd} \right]$$

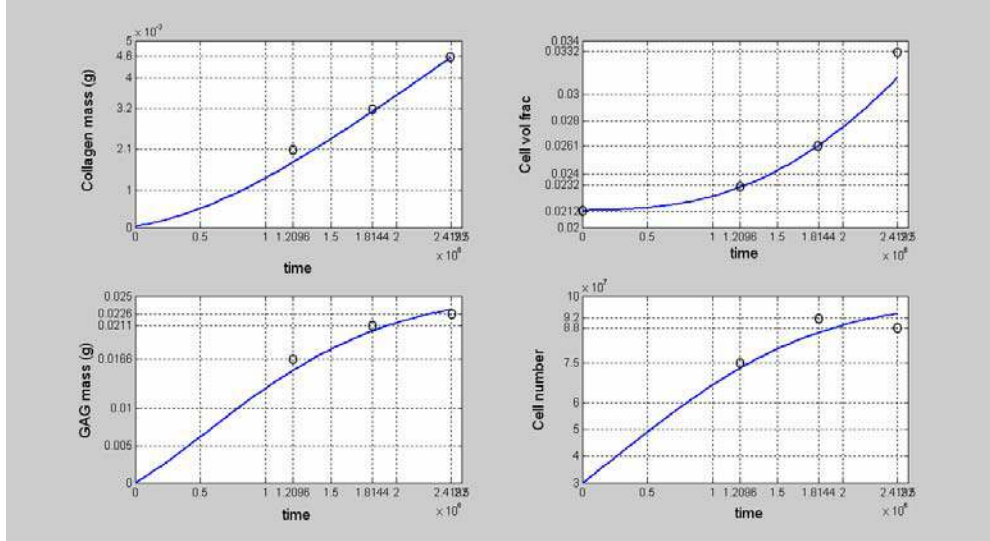


Figure 6.13 c Cartilage tissue growth over time obtained by the use of modified Contois function with respect to nutrient concentration and 3<sup>rd</sup> order dependence on cell number (as shown by the equation in case 3).

**Case 4:**

$$R_c = \left[ \left( \frac{k_g \cdot \mu}{K_{cont} \cdot \varepsilon_c + \mu} \right) \cdot n^{-1} - k_{cd} \right]$$

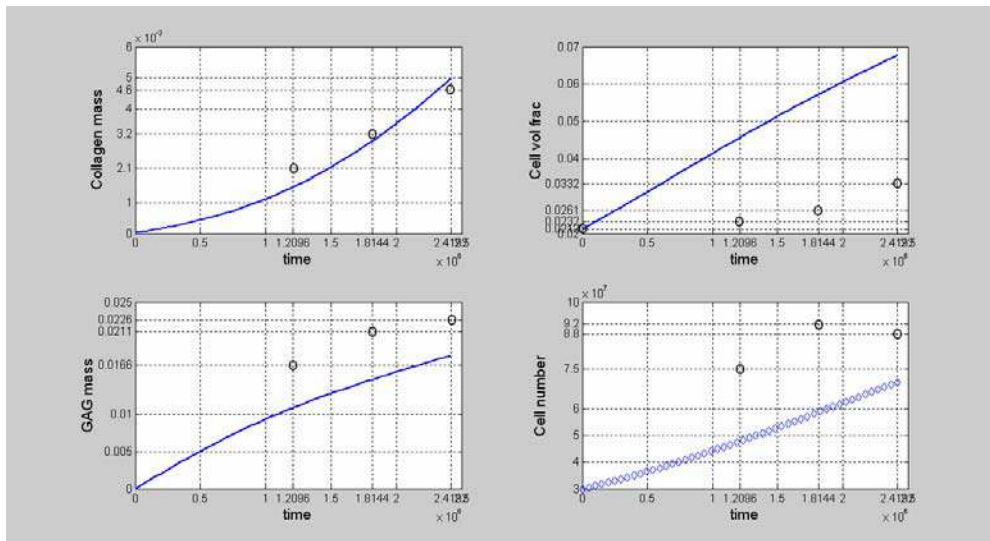


Figure 6.13 d Cartilage tissue growth over time obtained by the use of modified Contois function with respect to nutrient concentration and 1<sup>st</sup> order inverse (inhibitory) dependence on cell number (as shown by the equation in case 4).

**Case 5:**

$$R_c = \left[ \left( \frac{k_g \cdot \mu^2}{K_{cont} \cdot \varepsilon_c + \mu^2} \right) \cdot n^0 - k_{cd} \right]$$

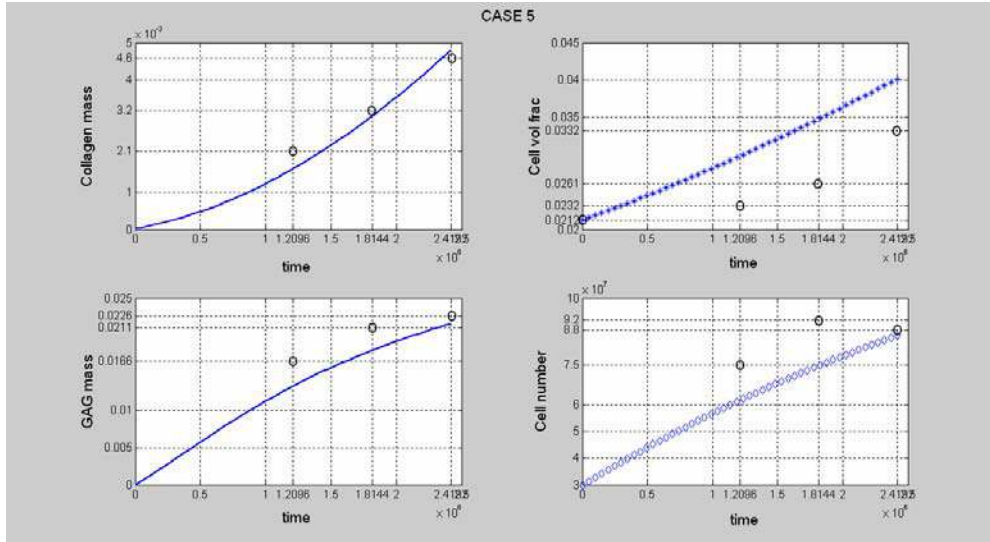


Figure 6.13 e Cartilage tissue growth over time obtained by the use of modified Contois function with respect to nutrient concentration and no dependence on cell number (as shown by the equation in case 5).

**Case 6:**

$$R_c = \left[ \left( \frac{k_g \cdot \mu^2}{K_{cont} \cdot \varepsilon_c + \mu^2} \right) \cdot n^1 - k_{cd} \right]$$

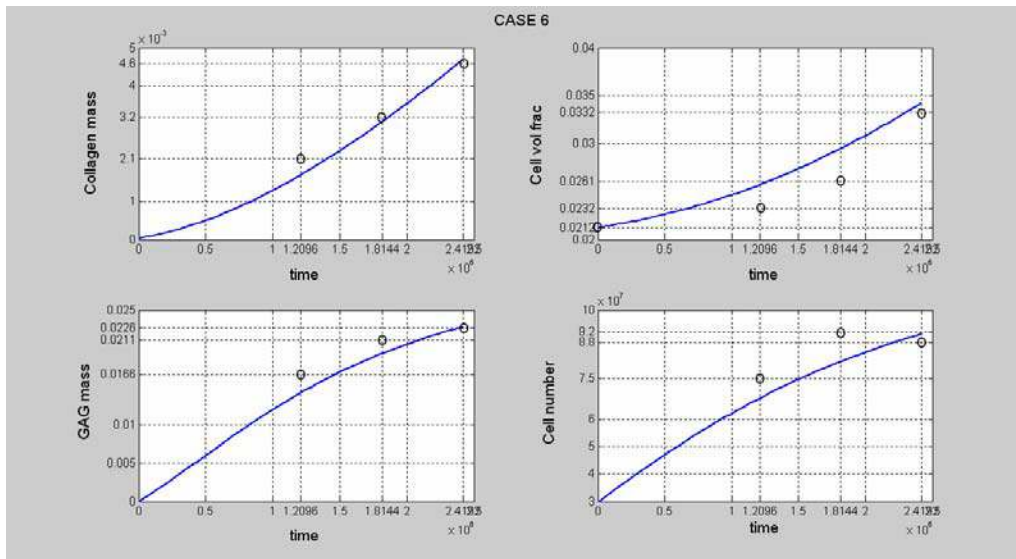
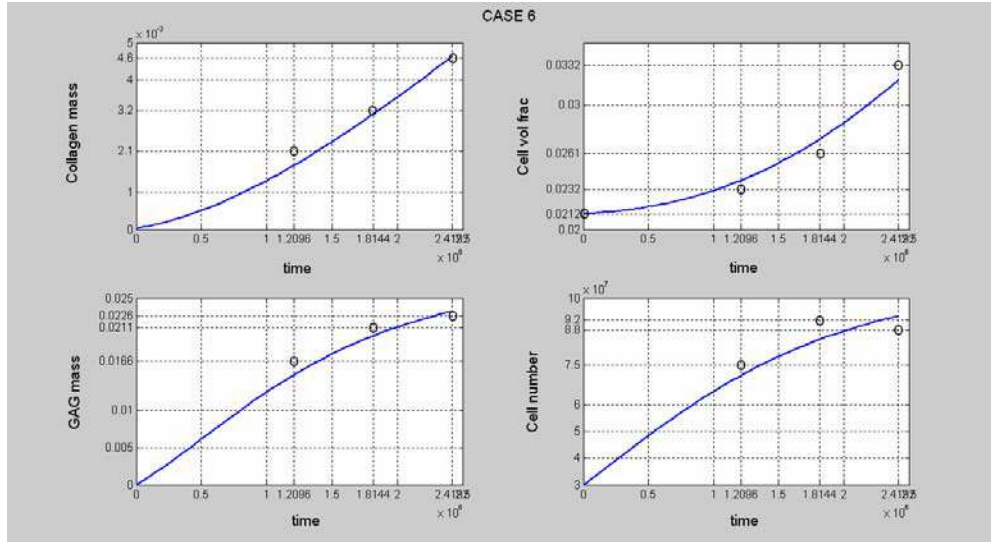


Figure 6.13 f Cartilage tissue growth over time obtained by the use of modified Contois function with respect to nutrient concentration and 1<sup>st</sup> order dependence on cell number (as shown by the equation in case 6).

**Case 7:**

$$R_c = \left[ \left( \frac{k_g \cdot \mu^2}{K_{cont} \cdot \epsilon_c + \mu^2} \right) \cdot n^2 - k_{cd} \right]$$



**Figure 6.13 g** Cartilage tissue growth over time obtained by the use of modified Contois function with respect to nutrient concentration and 2<sup>nd</sup> order dependence on cell number (as shown by the equation in case 7).

The most important factors that control the change in effective diffusion coefficient of oxygen are the binding coefficients of oxygen to GAG fibers, ' $P_g^o$ ' and collagen ' $P_{col}^o$ '. Increased ' $P_g^o$ ' and ' $P_{col}^o$ ' reduce the effective diffusion of oxygen (Figure 6.12 f) to the cells due to higher binding to the ECM fibers. Thus, larger GAG and collagen concentrations resulting from changes in their production parameters ' $k_{GAG}$ ', ' $k_{em}$ ' and ' $K_{ec}$ ', would lead to more binding of oxygen to available GAG and collagen decreasing the oxygen diffusivity as seen in Figure 6.12 f. Increased tissue mass due to increases in cell mass (changes in ' $k_p$ ' and ' $K_p$ ') and increase in ECM mass (changes in ' $k_{GAG}$ ', ' $k_{em}$ ', ' $K_{ec}$ ') would provide more restrictions to mass transport, further decreasing the oxygen diffusivity in the reactor. Similarly, the water diffusion coefficient and effective T1 relaxation coefficient in the reactor are highly sensitive to GAG-water binding coefficient (' $P_g^w$ ') and collagen-water binding coefficient (' $P_{col}^w$ ') and the kinetic parameters describing formation of tissue mass (cell and ECM) as seen in Figures 6.12 g and 6.12 h.

## 6.4 Conclusions

Summarizing, the developed mathematical model is able to quantify the bioreactor environment very well. The proposed modeling framework enables a study of restricted transport of important nutrients and its influence on cell behavior. The model supports the experimental evidence suggesting that construct growth in the reactor is not hindered by oxygen transport limitations (Williams *et al.*, 2002). NMR measurable parameters such as the effective water diffusion coefficient and T1 relaxation constant are also computed as functions of tissue mass. These model results are validated with available experimental data (Potter *et al.*, 1998) and show that restrictions to water diffusion are primarily due to binding of water to ECM components rather than due to increase in tissue mass. This work supports the use of NMR as a suitable monitoring tool for ECM production in *ex vivo* cartilage growth in hollow fiber bioreactors. The effective water diffusion coefficient predicted by the model did not correspond well with the experimental data during the earlier time periods and estimations of diffusion times in the experimental data suggest that the experimental measurements do not fully probe restrictions to transport due to binding of water to ECM components at these times. Additionally, the sensitivity analysis of tissue formation with various culture parameters provides information about the relative roles of cell mass production rates on ECM formation, and the change in microenvironment around the cell due to ECM formation on cell growth and proliferation.

The current model can be readily extended to include the effects of other environmental factors by incorporating mass balances of nutrients such as glucose and metabolic byproducts like lactate that might be important to be controlled in reactor culture units. Thus, modeling of transient events in the bioreactor - chondrocyte mass, matrix biosynthesis and nutrient transport provide additional insights into cartilage growth *in vitro* in bioreactors. This quantitative information could be used for proposing better reactor designs and suitable operational conditions for reactor scale-up. The model is also found to be suitable for suggesting improved experimental design and can be used to assess the important parameters to be measured experimentally.

## CHAPTER 7

### REACTION DIFFUSION MODEL OF MUSCLE METABOLISM

*(Based in part on work in press Kinsey et al., 2005, Journal of Experimental Biology)*

#### 7.1 Introduction

The complex processes involved in cell growth and metabolism require an input of energy. The human body extracts hydrocarbons from food and transforms the potential chemical energy in these nutrients to ATP, which ultimately fuels all physiological processes. The ‘production, transport, conversion and utilization of energy’ are facilitated via metabolic pathways involving a large number of tightly regulated enzyme-catalyzed reactions (Walliman *et al.*, 1992). The net rate of the metabolic processes in each pathway, in cells, depends on the competition between the reactivity of the system and the transport of nutrients to the reaction center (Weisz, 1973). The goal of the current work is to provide a quantitative framework of metabolic processes and their regulation and its relation to cellular design, in the light of reaction and diffusion.

It is well known that cells can metabolize and grow in culture, separate from the organism from which they are derived, and lead independent lives, yet exhibit the characteristics customarily associated with living things. This has been led to cell expansion *ex vivo* in reactors for the design of tissue-engineered substitutes. These engineered tissues can be easily manipulated to study various physiological cellular states and effects of metabolic parameters. The work reported in the previous chapters of this dissertation have focused on understanding the overall



macro-environmental changes to facilitate various cellular processes involved in cellular tissue substitute formations *in vitro* in bioreactors. The current study aims to develop an understanding of transport and reaction of these metabolites at the cellular level and to understand the role metabolite spatial distribution on cell structure and metabolic regulation. Such a structured framework, in future, would provide integration and coordination of detailed cellular metabolic pathways to overall inputs of the reactor system (or *in vivo* models), and in the long run with tissue, organ, and whole-body processes.

A complete quantitative analysis of metabolic regulation cannot be obtained just from *in vivo* or *in vitro* experimental studies even if all necessary measurements were possible. The complexity of interacting biochemical reactions distributed spatially, in the cellular metabolic pathways, and their integration to tissue/organ and eventually the whole organism level requires a formal theoretical framework for quantitative understanding (Saidel *et al.*, 2003). This framework is built by the development of physiological models based on the basic principles of conservation of mass, momentum, and energy, describing the metabolite production, transport and utilization through the various enzyme pathways. These model results can be analyzed using suitable analytical and numerical methods to understand the regulation pathways in metabolic reactions and its effect on cell structure.

Muscle cells are considered to be ideal models for this study. These cells are highly structured with very slight variations in organization from organism to organism. They can perform diverse mechanical functions and they display the largest changes in metabolic rates when undergoing transitions between rest and exercise (Suraz, 2003). Moreover, extensive literature on energy metabolism in muscle presents an excellent opportunity to develop quantitative, predictive, and testable models of cellular function across a wide range of spatial and temporal boundaries. Ultimately, the quantitative understanding of interaction between metabolism and cell structure would help in setting up a rationale for cellular design for attaining the desired functions.

The complexity of muscle metabolism is explored by developing suitable reaction-diffusion models of the transport and reaction dynamics of phosphorous metabolites involved in various metabolic pathways in the muscle. This descriptive mathematical model would account for the



spatial distribution of the various enzyme catalyzed reactions and provide quantitative understanding of the effects of diffusion on the chemical reaction processes under various physiological conditions. Understanding intracellular muscle energetics is a basic problem of optimizing ATP supply to meet ATP demands in these reaction processes. This metabolic study is designed to address the basic question ‘what are the rules that govern cell size, and in specific, muscle cell size in organisms?’. One of the possible factors governing cell size and organization is proposed to be the metabolic processes. Rationally, if the metabolic process is one of the reasons, then the model would help us quantitatively determine which one of the following is the controlling step –

- a) intracellular metabolite diffusion, and/or
- b) rates of ATP utilization corresponding to the contractile machinery of the cell, and/or
- c) rates of ATP production at the mitochondrial surface co-related directly to rate of oxygen delivery from the surrounding capillaries.

## **7.2 Current Modeling Objectives**

Muscle cells or fibers typically fall in the size range of 10-100  $\mu\text{m}$  along the shortest axis, usually the diameter (Johnson *et al.*, 2004). Fibers with dimension exceeding this range are believed to compromise aerobic metabolism, which relies upon oxygen flux across cell membranes, as well as ATP-equivalent flux from mitochondria to sites of ATP demand (Mainwood and Rakusan, 1982). This is because fiber diameters greater than 100  $\mu\text{m}$  would lead to a dramatic decrease in surface area to volume ratio (SA:V) and thus increase the time required for the metabolites to diffuse radially across the cell. Cell size maximum is thus believed to be modulated by the balance between aerobic ATP demand and oxygen supply to mitochondria. This can be justified by observations that aerobic muscle fibers have smaller diameter than anaerobic fibers in animal groups as diverse as mammals, fishes and crustaceans (Tse *et al.*, 1983).

Most work on aerobic energy metabolism in skeletal muscle in the literature has focused only on the catalytic aspects of cellular enzyme systems rather than the diffusive flux of metabolites from

the site of formation to its site of utilization and the other way around. This simplification has been based on the reasoning that cellular dimensions tend to be modest (muscle fibers ranging from 10-100  $\mu\text{m}$  in diameter; Russell *et al.*, 2000), and intracellular diffusion distances between mitochondria are typically very short in both aerobic and anaerobic skeletal muscle (e.g., Tyler and Sidell, 1984) fibers. Diffusion is assumed to be rapid, relative to the catalytic capacity of the mitochondria, leading to a global chemical equilibrium across the cell. This approach has been effectively employed to describe some of the major processes of energy metabolism in muscle, and a variety of kinetic models have been developed that closely match experimental data (e.g., Meyer, 1988; Jeneson *et al.*, 1995; Vicini and Kushmerick, 2000; Korzeniewski, 2003; Beard, 2005).

While the value of purely kinetic analysis of muscle energy metabolism is readily apparent, the conditions under which diffusive flux may be important in either limiting the net rate of aerobic process or influencing the evolution of metabolic pathways and further governing cellular designs to keep up with the muscle functions are unresolved (Suarez, 2003). The principal hurdle to understanding the role of diffusion and metabolic organization in muscle cells is that most metabolic measurements are weighted-averages over an entire cell or tissue, making it difficult to observe localized intracellular events or concentration gradients. However, several studies that have employed reaction-diffusion mathematical modeling of aerobic metabolism have found theoretical evidence for concentration gradients in high-energy phosphate molecules during steady-state contraction in muscle (Mainwood and Rakusan, 1982; Meyer *et al.* 1984; Hubley *et al.* 1997; Aliev and Saks, 1997; Kemp *et al.*, 1998; Vendelin *et al.*, 2000; Saks *et al.*, 2003).

In an effort to understand the role of diffusion and metabolic organization on the control of metabolism, we have been examining metabolic processes in an extremely anaerobic crustacean muscle model system. It is often difficult to test vertebrate models because the time scales of diffusive and catalytic processes seem to coincide (Meyer *et al.*, 1984). In contrast, the SA:V and diffusion challenges imposed by large muscle cells of crustaceans are dramatic and should result in easily discernible metabolic consequences and compensatory responses. Further, these

giant cells can be easily manipulated and this has made them a classic model system for metabolic physiologists.

The crustacean blue crab, *Callinectes Sapidus* have two distinct kinds of muscle fibers - small, dark region of aerobic fibers called 'dark fibers' that power sustainable swimming, surrounded by a large mass of anaerobic fibers called 'white fibers' used for burst swimming (Tse *et al.*, 1983). The white muscle fibers of large crustaceans like the blue crab have wide range of cell sizes during their life time. The juvenile blue crabs likely have muscle cells less than 60  $\mu\text{m}$  in diameter while the adult crustacean fiber diameters exceed 600  $\mu\text{m}$  (Boyle *et al.*, 2003). This means that during development these juvenile fibers cross and exceed the usual limit on cell dimensions while preserving muscle function (Boyle *et al.*, 2003). Moreover, the distribution of mitochondria in these white fibers has been also seen to change dramatically with increase in cell size during the life time of the crab. In small (juvenile) anaerobic white fibers mitochondria are uniformly distributed throughout the cell, whereas in large (adult) fibers the mitochondria are largely clustered at the sarcolemmal membrane forming an oxidative cylinder at the periphery of the cell (Boyle *et al.* 2003). Thus, the average distance between mitochondria in small fibers is several microns, while in large fibers there may be hundreds of microns between mitochondrial clusters. Aerobic dark fibers, however, have similar cell sizes as the small white fibers and uniformly distributed mitochondria throughout the cell. The average distance between two mitochondria in these fibers are also few microns.

In the muscle fibers of blue crabs the factors potentially limiting the rate of diffusive flux are not only the large metabolite diffusion distances but also the presence of various intracellular barriers. Experiments by various groups (Kinsey *et al.*, 1999; De Graaf *et al.*, 2001; Kinsey and Moerland, 2002) have shown that these barriers could lead to a time-dependent reduction in metabolite diffusion coefficients for substrate movements in the direction perpendicular to the fiber axis ( $D_{\perp}$ ). Over shorter diffusion distances characteristic of dark aerobic fibers and small anaerobic white fibers, the  $D_{\perp}$  is shown to be about 2-fold higher than  $D_{\perp}$  for the long diffusion distances that typify large white fibers. While the burst contraction functions of these muscles are not impacted by intracellular diffusion rates, the 'aerobic recovery' process may be compromised by the extreme fiber size in adult animals. This is again because of slower rate of

diffusion compared to the rate of metabolite demand. Furthermore, several size-dependent differences in the recovery of the anaerobic white fibers following burst contraction have been observed experimentally. Small anaerobic fibers are seen to accumulate lactate and modestly deplete glycogen during burst contractions, and both of these metabolites recover to resting levels relatively quickly following an exercise bout (Boyle *et al.*, 2003; Johnson *et al.*, 2004). The large anaerobic fibers similarly accumulate lactate and deplete glycogen during contraction, but following exercise they continue to accumulate large amounts of lactate and further deplete glycogen. Full aerobic recovery of metabolic species in these large white fibers of adult blue crabs requires several hours (Milligan *et al.*, 1989; Henry *et al.*, 1994; Boyle *et al.*, 2003; Johnson *et al.*, 2004).

The present study develops descriptive mathematical models to improve the quantitative understanding of the effects of diffusion on the chemical reaction processes occurring in this muscle model system. These models would include not only the appropriate chemical reactions, but also the specific spatial distribution of the reaction sites and other barriers or factors that affect mass transport. The proposed reaction-diffusion model would provide insight into the roles of cellular structure in the energy metabolism of muscle. This model could be easily extended to different muscle fiber types, with varying size, ATP demand and ATP supply, to study the metabolic consequences on cellular design.

Our general hypothesis is that increasing fiber size would induce in metabolic organization and dramatically impact the rates of metabolic processes. Experiments conducted in Dr S. T. Kinsey's laboratory (University of North Carolina, Wilmington) have aimed at detecting the effects of fiber size in blue crabs. Their focus is primarily the white anaerobic fibers because of the unique feature of these muscle fibers to grow during development by increasing their size and reorganizing the distribution of their mitochondria. In their previous work, Kinsey and coworkers have hypothesized that in large (adult) white fibers anaerobic metabolism is recruited following burst contractions in order to accelerate certain key phases of metabolite recovery that would otherwise be overly slow due to intracellular diffusion constraints (Kinsey and Moerland, 2002; Boyle *et al.*, 2003; Johnson *et al.*, 2004). In the present study we test this hypothesis by examining the fiber size-dependence of the rate of post-contraction arginine phosphate (AP)

resynthesis, by comparing the available experimental data to our mathematical model of aerobic metabolism in these fibers. The focus is to develop a suitable reaction-diffusion model of this model system (blue crab) that can be used to interpret the measured metabolic parameters in the light of cellular organization and diffusional constraints. From our study we propose probable model modifications to be able to explain the experimental results better.

## 7.3 Model Formulation

### 7.3.1 Model Schematic

The schematic of a muscle fiber cross-section is shown in Figure 7.1 (A). The myofibrils or the contractile units of muscles are packed within the muscle fiber. Few myofibrils are surrounded by a tubular system, the sarcoplasmic reticulum (SR), which stores the calcium ions that regulate muscle contraction. Rows of mitochondria are clustered near the SR and myofibrils, ready to supply ATP needed to fuel the contractile process. A plasma membrane, the sarcolemma, surrounds the muscle fiber.

As a first estimate for model development, it is reasonable to obtain a representative one dimensional radial profile of the fiber as shown in Figure 7.1 (B). The contraction of muscle requires consumption of ATP. ATP is formed in the mitochondria by oxidative phosphorylation. Once produced, ATP must diffuse across the cell cytoplasm to the myofibril, the functional unit of muscle contraction. The model developed for this study is a simplified 1-dimensional system that extends from the surface of a mitochondrion to a distance  $\lambda/2$ , equal to half of the mean free spacing between mitochondria or between clusters of mitochondria around a myofibril.

The proposed reaction-diffusion mathematical model is used to predict the concentration of five key muscle metabolites: Adenosine Triphosphate (ATP), Adenosine Diphosphate (ADP), Arginine Phosphate (AP), Arginine (Arg) and inorganic phosphate (Pi). These metabolic species participate in several reactions that take place in the myofibrillar region or in the mitochondria.

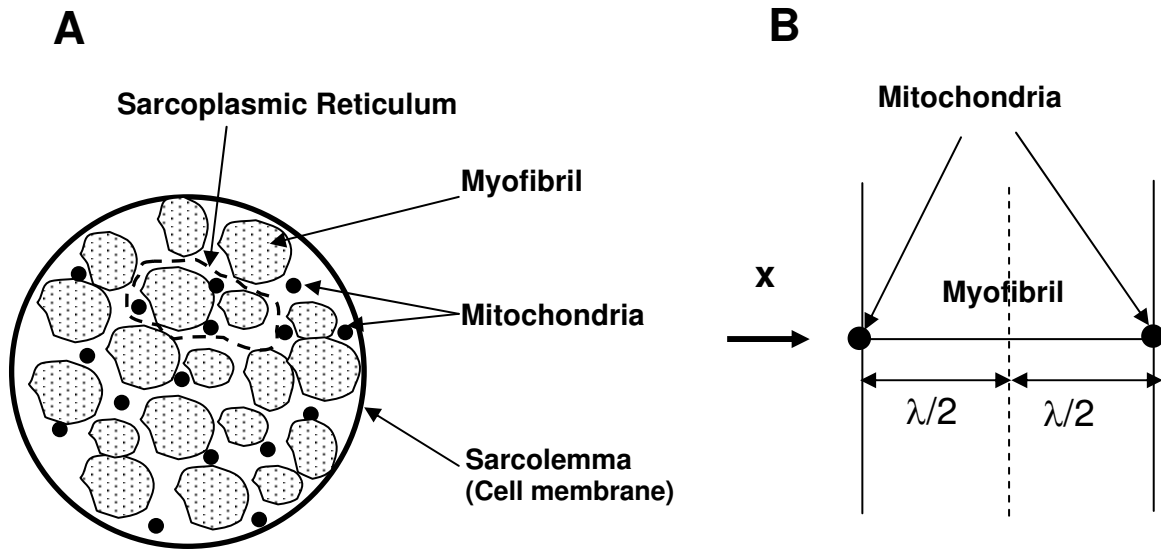


**Figure 7. 1 (A) Cross-sectional view of a muscle fiber cell. Packs of myofibrils, mitochondria, Sarcoplasmic Reticulum and the cell membrane or Sarcolemma also shown. (B) One-dimensional schematic of the intra-mitochondrial spacing as used for model development.**

*Muscle fiber types and Mitochondrial Distribution for model geometry determination -*

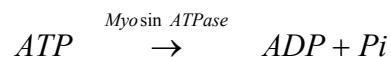
Crustacean muscle cells have been extensively used in membrane physiology experiments because of their large size which allows for its easy manipulation during experiments. The current model studies crustacean small white muscle fibers (100  $\mu\text{m}$  diameter), large white fibers (600  $\mu\text{m}$  in diameter) and dark aerobic muscle fibers (36  $\mu\text{m}$  in diameter). The mitochondria-rich dark levator fibers of the blue crab grow to similar sizes as the white large fibers. However, they maintain their aerobic function by subdividing into smaller functional units of diameter nearly 36  $\mu\text{m}$ . The mitochondria are distributed exclusively around the periphery of these aerobic fiber subdivisions. Neither size of subdivisions nor the mitochondrial fractional areas in each subdivision change during development of the animal from juvenile to adult crabs (Johnson *et al.*, 2004). So for our model for dark fibers we use dimensions of the functional subunits rather than the entire dark fiber with the mitochondrial separation of 36  $\mu\text{m}$ . The white levator anaerobic fibers grow in size and have two distinct size classes of fibers as mentioned before. The small white fibers are nearly 100  $\mu\text{m}$  in diameter with uniform mitochondrial distribution and modeled using mean mitochondrial spacing of 5.46  $\mu\text{m}$ . The large white fibers are nearly

600  $\mu\text{m}$  in diameter with mitochondria distributed at periphery of the fiber and thus the relative diffusion distance between mitochondria clusters is 600  $\mu\text{m}$ . This is discussed further in detail in the ‘Parameter Estimation’ section of the text.

### 7.3.2 Model Reactions

Reaction in this system occurs at two distinct sites – the myofibrils and is called the ‘bulk reaction’ and the mitochondria called the ‘surface reaction’. Reactions catalyzed by Arginine Kinase (AK), myosin ATPase (Myo) and basal ATPase (Basal) are assumed to occur homogenously throughout the domain  $0 \leq x \leq \lambda/2$ , where  $x$  is distance from the mitochondrial surface ( $x = 0$ ) to half of the mean free spacing between mitochondria ( $x = \lambda/2$ ), and are the ‘bulk reactions’ (Figure 7.2). As the mitochondria in the muscle fiber are small relative to the size of the myofibril and are present adjacent to SR, the surface jump boundary condition (Whitaker, 1992) at the boundary ( $x = 0$ ) includes the mitochondrial oxidative phosphorylation reaction as ‘surface reaction’ (Figure 7.2). All the bulk and surface reaction rates are written in the direction of ATP production. These reactions are described in detail below.

The energy source for muscle contraction utilized by the myofibrils is derived from the following reaction,



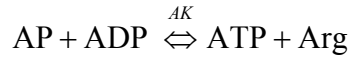
This myosin ATPase reaction is an irreversible ATP consuming process during muscle contraction. The reaction is modeled using Michaelis-Menten kinetics (Pate and Cooke, 1985; Hubley *et al.*, 1997). The rate of reaction is given as,

$$R_{ATP}^{myo} = -\frac{V_{mmyo} \cdot C_{ATP}}{K_{mmyo} + C_{ATP}} \tag{7.1}$$

where  $V_{mmyo}$  is the  $V_{max}$ ,  $K_{mmyo}$  is the apparent Michaelis constant. Determination of these parameters is discussed in the ‘*Parameter Estimation*’ section of the text. The rate of ADP and Pi formation in this step is given as,

$$R_{ATP}^{myo} = -R_{ADP}^{myo} = -R_{Pi}^{myo} \quad (7.2)$$

The enzyme, Arginine Kinase (AK), catalyzes the reversible transfer of a phosphate group from arginine phosphate to ADP to form ATP,



This reaction is called the Arginine Kinase reaction and is comparable to the Creatine Kinase reaction in vertebrates (Sweeny, 1994). During burst activities the AK reaction acts as a spatial and temporal buffer for ATP, by generating ATP by breaking down phosphagens, the high energy storage compounds of the muscle. Thus, intracellular AP serves as the initial fuel used during burst contraction in crustacean muscles. The model assumes AK to be uniformly distributed in the cytoplasm (Ellington, 2001) comprising of the space in between the mitochondria’s in our system. This reaction proceeds by a rapid equilibrium, random mechanism and is modeled according to the kinetic expression of Smith and Morrison (1969),

$$R_{ATP}^{AK} = \frac{V_{mAKrev} C_{ATP} C_{Arg} - V_{mAKfor} \frac{K_{iATP} K_{iArg}}{K_{mAP} K_{iADP}} C_{AP} C_{ADP}}{K_{iATP} K_{mArg} + K_{mATP} C_{Arg} + K_{mArg} C_{ATP} + C_{ATP} C_{Arg} + \frac{K_{iATP} K_{mArg} C_{AP}}{K_{iAP}} + \frac{K_{iATP} K_{mArg} C_{ADP}}{K_{iADP}} + \frac{K_{iATP} K_{mArg} C_{AP} C_{ADP}}{K_{iAP} K_{iADP}} + \frac{K_{iATP} K_{mArg} C_{ATP} C_{Arg}}{K_{iATP} K_{iAP}} + \frac{K_{iATP} K_{mArg} C_{Arg} C_{ADP}}{K_{iArg} K_{iADP}}} \quad (7.3)$$

where  $V_{mAKfor}$  and  $V_{mAKrev}$  are  $V_{max}$  values in the forward (ATP formation) and reverse direction, respectively,  $K_m$  values are Michaelis constants for ternary complex formation,  $K_i$  values are free



enzyme-substrate complex dissociation constants,  $K_I$  values are dissociation constants relevant to the formation of dead-end complexes. All rate constants are taken from study of Smith and Morrison (1969). Again the rates of AP consumption and ATP and Arg species formation are given as,

$$R_{ATP}^{AK} = -R_{ADP}^{AK} = -R_{AP}^{AK} = R_{Arg}^{AK}. \quad (7.4)$$

Even when the muscle is not exercising there exist a low rate of ATP consumption which is accounted for by incorporating the ‘basal ATPase reaction’. This rate in the bulk phase is modeled using a Michaelis-Menten equation and is given as,

$$R_{ATP}^{basal} = -\frac{V_{mbas} \cdot C_{ATP}}{K_{mbas} + C_{ATP}} \quad (7.5)$$

where  $V_{mbas}$  and  $K_{mbas}$  are the  $V_{max}$  and saturation constants of the basal reaction rate. This reaction is added as one of the bulk reactions occurring in the myofibrillar region in order to maintain the concentrations of metabolites ( $C_i$ ) constant over time in inactive fibers and to promote a return to the initial steady state following metabolic recovery. Details of the model parameter determination are discussed in the ‘*Parameter Estimation*’ section of the text. The reaction rate for species ADP and Pi involved in this reaction is written as,

$$R_{ATP}^{basal} = -R_{ADP}^{basal} = -R_{Pi}^{basal} \quad (7.6)$$

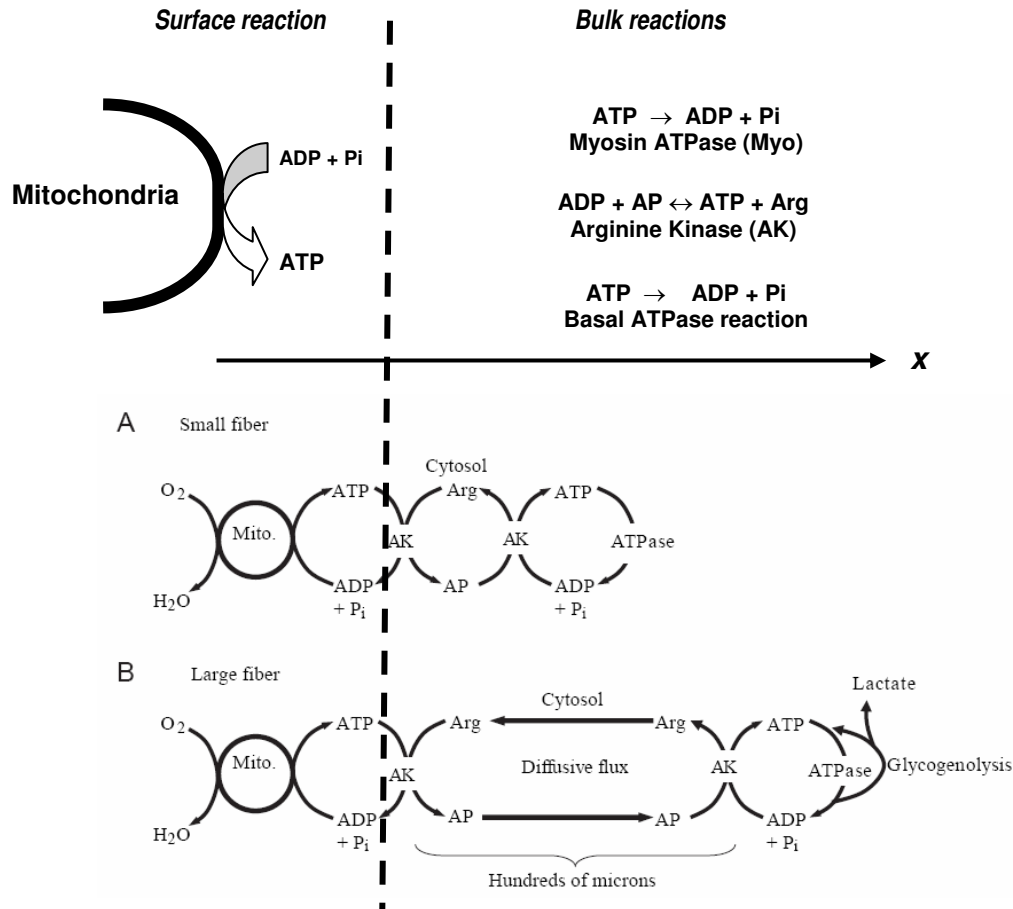
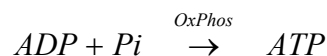


**Figure 7. 2 One-dimensional schematic of the intra-mitochondrial spacing as used for model development showing the various reactions occurring in the myofibrillar region (bulk) and in the mitochondria (surface). Arginine Kinase (AK) mediates ATP-equivalent flux in Crustacean muscle. (A) Reactions and diffusion distance in small white fibers of juvenile crabs (B) Reaction and diffusion distances over hundreds of microns in large white fibers of adult crab. Anaerobic glycogenolysis is believed to occur following contraction in large fibers, presumably to speed up phases of the recovery process. [Johnson *et al.*, 2004]**

The rate of ATP formation in the mitochondria is modeled as a first order activation by ADP, making a reasonable assumption that concentrations of oxidizable substrates (pyruvate derived from glycogen) are present at saturated levels in the muscle. The reaction is given as,



There are significant controversies in literature about the exact mechanism of activation of this mitochondrial oxidative phosphorylation (OxPhos) reaction and control is likely distributed

among several metabolites (Jeneson *et al.*, 1996) other than ADP. However, as a first step, a more established ADP activated reaction rate (Meyer, 1984; 1988) kinetics expression is used. More complex kinetics would be incorporated as the model progresses. The mitochondrial reaction follows Michaelis-Menten kinetics and is given as,

$$R_{ATP}^{OxPhos} = \frac{V_{mmito} \cdot C_{ADP}}{K_{mmito} + C_{ADP}} \quad (7.7)$$

where  $V_{mmito}$  is the maximal velocity ( $V_{max}$ ) of the boundary reaction, and  $K_{mmito}$  is the Michaelis constant for ADP for the boundary reaction. The simplified approach assumes this reaction to be functioning near  $V_{mmito}$  during most of recovery rate. This process assumes that oxygen is not limiting to oxidative phosphorylation, which we believe likely occurs *in vivo*, and is certainly valid using isolated muscle fibers and a high prevailing pO<sub>2</sub> (Crow and Kushmerick, 1982). The reaction rate of species ADP and Pi is given as,

$$R_{ATP}^{OxPhos} = -R_{ADP}^{OxPhos} = -R_{Pi}^{OxPhos} \quad (7.8)$$

During burst contractions, crustacean muscle metabolism is similar to that of vertebrates. Crustacean muscle initially relies on phosphagen (AP) hydrolysis and, once the AP pool is depleted, anaerobic glycogenolysis provides ATP for additional contractions. The glycogenolytically powered contractions are slower and less forceful than the initial phosphagen powered bursts (Baldwin *et al.*, 1999; Boyle *et al.*, 2003) which is consistent with the fact that in crustacean muscle glycolytic enzyme maximal activities are lower than that of myosin ATPase (Zammit and Newsholme, 1976). Lactate production, therefore, only occurs during prolonged series of burst contractions.

### 7.3.3 Model Equations

The diffusion and reaction of ATP, ADP, AP, arginine (Arg), and P<sub>i</sub> are modeled in the one-dimensional system. Again the geometry extends from the surface of a mitochondrion ( $x = 0$ ) to a distance ( $x = \lambda/2$ ) equal to half of the mean free spacing between mitochondria or between clusters of mitochondria. Reactions catalyzed by AK, myosin ATPase and basal ATPase are assumed to occur homogenously throughout the domain  $0 \leq x \leq \lambda/2$ . The species continuity equations for the metabolites ( $i$ ) is written as,

$$\frac{\partial C_i}{\partial t} = D_i \frac{\partial^2 C_i}{\partial X^2} + R_i \quad (7.9)$$

where  $C_i$  and  $D_i$  are the concentrations and diffusion coefficients of species  $i$  (ATP, ADP, AP, Arg, Pi) respectively and  $t$  is time.  $R_i$  denotes the sum of the reaction rates in the inter-mitochondrial bulk space (myofibril) in which species  $i$  participates and includes the basal ATP consumption, myosin ATPase and AK. The concentration terms in the continuity equation are non-dimensionalized using a fixed concentration of 1mM; and the spatial term using the value of half mean free spacing between mitochondria's. The time and space varying concentrations of each metabolite can be written as,

$$\begin{aligned} \frac{\partial u_{ATP}}{\partial t} &= \frac{D_{ATP}}{L^2} \cdot \frac{\partial^2 u_{ATP}}{\partial x^2} + \frac{1}{C_o} (R_{ATP}^{myo} + R_{ATP}^{AK} + R_{ATP}^{basal}) \\ \frac{\partial u_{ADP}}{\partial t} &= \frac{D_{ADP}}{L^2} \cdot \frac{\partial^2 u_{ADP}}{\partial x^2} + \frac{1}{C_o} (R_{ADP}^{myo} + R_{ADP}^{AK} + R_{ADP}^{basal}) \\ \frac{\partial u_{AP}}{\partial t} &= \frac{D_{AP}}{L^2} \cdot \frac{\partial^2 u_{AP}}{\partial x^2} + \frac{1}{C_o} (R_{AP}^{AK}) \\ \frac{\partial u_{Arg}}{\partial t} &= \frac{D_{Arg}}{L^2} \cdot \frac{\partial^2 u_{Arg}}{\partial x^2} + C_o (R_{Arg}^{AK}) \\ \frac{\partial u_{Pi}}{\partial t} &= \frac{D_{Pi}}{L^2} \cdot \frac{\partial^2 u_{Pi}}{\partial x^2} + \frac{1}{C_o} (R_{Pi}^{myo} + R_{Pi}^{basal}) \end{aligned} \quad (7.10)$$

where  $L$  is equal to  $\lambda/2$  and  $x$  ( $=X/L$ ) is the non-dimensionalized spatial co-ordinate.  $u_i$  ( $=C_i/C_o$ ) is the non-dimensionalized metabolite concentrations of species  $i$  and  $C_o$  of 1 mM (or  $1 \cdot 10^{-15}$  mmole/ $\mu\text{m}^3$ ) is used to non-dimensionalize the concentrations.

### *Frequency and Duty Cycle*

The myosin ATPase reaction is responsible for the consumption of ATP during muscle contractile activities. For each simulation, myosin ATPase was activated for 7 s at a frequency of 5 Hz and 50% duty to simulate burst contraction and was then deactivated during the post-contractile recovery period\*.

### *Boundary Conditions*

The boundary conditions at the mitochondrial surface at  $x = 0$  balances the fluxes of ATP, ADP and  $P_i$  into the bulk phase with the rates of formation and consumption at the mitochondria. No fluxes for metabolites AP, Arg and  $P_i$  into the bulk phase occur, as they do not participate in the mitochondrial reaction. The boundary conditions are written as,

$$\frac{D_{ATP}}{L^2} \frac{\partial u_{ATP}}{\partial x} = \frac{1}{L} \cdot \frac{1}{C_o} (R_{ATP}^{OxPhos})$$

$$\frac{D_{ADP}}{L^2} \frac{\partial u_{ADP}}{\partial x} = \frac{1}{L} \cdot \frac{1}{C_o} (R_{ADP}^{OxPhos})$$

$$\frac{\partial u_{AP}}{\partial x} = \frac{\partial u_{Arg}}{\partial x} = \frac{\partial u_{P_i}}{\partial x} = 0$$

(7.11)

Because of symmetry no-flux boundary conditions for all the species are written at  $x = \lambda/2$

---

\* Frequency is expressed in Hz (cycle/s) and is characterized by its on/off cycle. The frequency of activation can be varied through the duty cycle. Duty cycle is defined as the ratio of muscle contraction time to the total cycle time (work + rest time). The frequency, duty cycle, and time of contraction of the model were varied to fit the experimental data provided by Dr. S. T. Kinsey.

$$\frac{\partial u_{ATP}}{\partial x} = \frac{\partial u_{ADP}}{\partial x} = \frac{\partial u_{AP}}{\partial x} = \frac{\partial u_{Arg}}{\partial x} = \frac{\partial u_{Pi}}{\partial x} = 0 \quad (7.12)$$

### *Initial Conditions*

The initial conditions for the five metabolite species are written as,

$$u_i = u_i^0 \quad \forall 0 \leq x \leq \lambda/2 \quad t = 0 \quad (7.13)$$

where  $u_i^0$  is the non-dimensional concentration of species  $i$  at time  $t = 0$ , and is given as  $C_i/C_i^0$ , and  $C_i^0$  is the resting concentration of species  $i$  (see Appendix G).

### *Averaged Equations*

While the solution of the model generate concentrations of metabolites varying in time and space, the experimental measurements from Dr Kinsey's lab obtained concentration values that were spatially averaged across the fiber. In order to compare the model results to the experimental data, some of the model data was mathematically volume averaged over the domain from  $x = 0$  to  $x = \lambda/2$ :

$$\langle C_i(t) \rangle = \frac{\int_{x=0}^{x=\lambda/2} C_i(x,t) dx}{\lambda/2} \quad (7.14)$$

Since the time for the contraction phase is very small compared to the recovery phase, experimentally only the approximate averaged concentration to which AP is depleted can be obtained. The duration of myosin ATPase activation was adjusted so that the decrease in [AP] was comparable to that in the observed data. For the white small fibers and large fibers the duration of activation used in the model is 5.7s and 4s respectively.

### 7.3.4 Parameter Estimation

Model input parameters are detailed in Appendix G.

#### *Resting Metabolite Concentration -*

The resting metabolite concentrations for crustacean anaerobic locomotor fibers are obtained from a combination of the data in Head and Baldwin (1986), <sup>31</sup>P-NMR spectra collected by Kinsey and Ellington (1996), and calculations using the AK equilibrium constant (Teague and Dobson, 1999). The resting metabolite concentrations are same in the small and large fibers (Baldwin *et al.*, 1999).

#### *Diffusion coefficients -*

The diffusion coefficients,  $D_i$  values for each metabolite are based on direct measurements from crustacean anaerobic fibers and calculations from the relationship of molecular mass and diffusion coefficient in these fibers (Kinsey and Moerland, 2002). The  $D_i$  used for the short diffusion distances characteristic of small white fibers are higher than that for the long distances found in large white fibers due to the time dependence of radial diffusion in muscle (Kinsey *et al.* 1999; Kinsey and Moerland, 2002).

#### *Averaged Mitochondrial spacing -*

For white small anaerobic fibers the intracellular diffusion distance ( $\lambda/2$ ) is estimated from its correlation to the total mitochondrial fractional area and the mean area/mitochondrion.

$$\lambda/2 = \sqrt{\frac{\text{area}/\text{mito}}{\text{mito.area}/\text{cell.area}} \cdot \frac{1}{\pi}}$$

The total mitochondrial fractional area for small fibers is computed as 0.026 and for large fibers is 0.017 (recalculated from data collected by Boyle *et al.* 2003). The mean area/mitochondrion, is  $0.608 \mu\text{m}^2$  (Boyle *et al.*, 2003). For the white large fibers and dark fibers with peripherally distributed mitochondria,  $\lambda/2$  is half the fiber diameter.

### *Kinetic rate parameters -*

For white anaerobic fibers the  $V_{mmito}$  values were estimated from rates of aerobic post-contractile phosphagen resynthesis from white muscle fibers with a mitochondrial density comparable to blue crab light levator muscle<sup>♦</sup>. This approach was necessary due to an absence of suitable measurements of maximal oxygen consumption or ATP production rates from isolated crustacean anaerobic fibers, and because estimates of  $V_{mmito}$  derived from mammalian studies (corrected for differences in mitochondrial density) yielded AP recovery rates that were several-fold higher than observed in the literature or presented herein. This is consistent with the fact that PCr recovery rates in mammalian muscle (e.g., Vicini and Kushmerick, 2000) are >10-fold higher than rates in crustacean muscle (Thébault *et al.*, 1987). The rates of mitochondrial ATP production per cell volume were converted to rates of flux per mitochondrial surface area using a mitochondrial SA:V of 6.81 and the mitochondrial fractional area data for small and large levator fibers (Boyle *et al.* 2003). A  $K_{mmito}$  value for ADP of 20  $\mu\text{M}$  was used, which is within the range for fast skeletal muscle (Meyer *et al.*, 1984).

AK dissociation constants are obtained from Smith and Morrison (1969),  $V_{mAKrev}$  is taken from Zammitt and Newsholme (1976) and  $V_{mAKfor}$  is calculated from the AK Haldane relationship from Smith and Morrison (1969) using an equilibrium constant for AK of 39 (Teague and Dobson, 1999). Values for  $V_{mmyo}$  and  $K_{mmyo}$  for the Myosin ATPase reaction are the same as in Hubley *et al.* (1997) for white and red fibers corresponding to our white and dark fibers respectively. The basal reaction rate constants are computed by equating the basal rate of ATP consumption and the AK reaction rate of ATP production in the bulk with the oxidative phosphorylation reaction rate for ATP production in the mitochondrial surface.  $K_{mbas}$  is initially set to  $10^{-15}$  mol/ $\mu\text{m}^3$ , and  $V_{mbas}$  is determined so that the concentrations of the metabolites do not change over time.

---

<sup>♦</sup> Data from small prawn anaerobic tail muscle that would not be expected to have large fibers (Thébault *et al.*, 1987) and from isolated dogfish white muscle, which resynthesizes phosphocreatine (PCr) using only aerobic metabolism and has a mitochondrial fractional area of about 0.01 (Curtin *et al.* 1997) yielded very similar estimates for  $V_{mmito}$ .



### 7.3.5 Solution Procedure

The system of species continuity equations (equation 7.10) are solved by coupling with the boundary conditions (equation 7.11 and 7.12) and initial condition (equation 7.13) for the different fiber types – white small, white large, and dark fibers, using a commercially available finite element computer code FEMLAB (Comsol, Inc., Burlington, MA). The model calculations yield temporally and spatially resolved concentrations of AP, Arg, ATP, ADP, and Pi during a contraction-recovery cycle. The concentration of AP is spatially averaged as shown in equation 7.14 to compare with experimental data on white muscle fiber.

The solution of the partial differential equation using FEMLAB needed careful meshing and appropriate use of time steps. The number of mesh points used for the simulations was 120. Further mesh points close to the mitochondrial boundary were refined to prevent steep changes around this region. During the period of contraction, with a frequency of 5 Hz and 50 % duty, the muscle contracted every 0.1 s and contraction was turned off for the next 0.1 s, during the entire contractile phase of 7s. Time steps much smaller than 0.1s (e.g. 0.01s) had to be chosen to capture this effect. However, during muscle recovery period a larger time step was chosen. The mesh dimensions and time steps used in computations are mentioned below each of the result figures.

## 7.4 Results

Experimental results from Dr Kinsey's studies on white small (juvenile) and large (adult) anaerobic fibers and dark aerobic fibers of blue crab have shown that stimulation of these fibers gave rise to similar burst exercise responses. The frequency of swimming leg movement is seen to be higher in the juvenile animals, while the duration of swimming was greater in the adult animals. During exercise all these fibers had similar AP depletion (Figure 7.3; Kinsey *et al.*, 2005), glycogen depletion (Boyle *et al.*, 2003), and lactate accumulation (Johnson *et al.*, 2004) indicating that the metabolic effects of exercise on the muscle are independent of fiber size. To note here the experimental results reported are for only the white anaerobic fibers as these fibers are 'metabolically giant'.

The time course of relative changes in AP and Pi concentrations in the small and large white fibers are obtained using NMR (Figure 7.3, Dr Kinsey's laboratory). It can be seen that a rapid depletion of AP and corresponding increase in Pi is observed in the small and large fibers during contraction, and this is followed by a slow recovery that is complete in about 60 min. *Despite the large differences in body mass and fiber size between the small and large animals, the rate of recovery of AP (Figure 7.3) is seen to be essentially the same for both muscle fiber groups.*

In this study, the reaction-diffusion mathematical model is used to understand this size-independent post-contraction AP resynthesis in the white anaerobic fibers of blue crab. The similarity in the rate of recovery of AP is presumably due to anaerobic contributions to recovery in the large fibers (Boyle *et al.*, 2003; Johnson *et al.*, 2004). The mathematical model allows testing whether the need for this anaerobic recovery in the large fibers arises from diffusive constraints on the metabolites in these fibers. The space and time resolved concentrations of the high energy metabolites simulated in the aerobic model for the small and large white fibers are shown in Figure 7.4 and Figure 7.5, respectively. As can be seen from the model computations, the rate of recovery is somewhat faster in the small than in the large fibers, and there are no significant intracellular gradients in metabolite concentrations in the small fiber, as expected (Figure 7.4). However, in large fibers, there are mild gradients of metabolites, indicating that the diffusive flux is fast relative to the mitochondrial ATP production (Figure 7.5). This result seems to be inconsistent with the fact that intracellular diffusive flux is not limiting (no significant spatial gradients) aerobic metabolism in the large fibers during post-contraction recovery, even though metabolite diffusion in these fibers are modeled over a large diffusion distance of 300  $\mu\text{m}$ . Thus, it is believed that the *relatively small differences in gradients between the small and large fibers result most exclusively due to differences in mitochondrial density.*

The model results are volume-averaged over the spatial co-ordinate to obtain a comparison between the experimentally observed and simulated recovery rates of AP. The observed and modeled AP recovery data for the small white fibers are shown in Figure 7.6(A). The model seems to explain the experimental data very well. However, for large fibers, as seen in Figure 7.6 (B), the model simulated aerobic metabolism alone does not seem to account for the

relatively high observed rate of post-contraction AP recovery. Thus, anaerobic metabolism appears to be a necessity to account for AP recovery in these large fibers.

So now that we know that the recovery in the large fibers is not substantially constrained by diffusion, then how close are these fibers to being limited by intracellular diffusive flux? Figure 7.7 shows the effect of incremental increase in the rate of the mitochondrial boundary reaction. It can be seen that doubling the  $V_{\text{mito}}$  leads to the formation of only slightly steeper concentration gradients, which means that there is a minimally increased control of aerobic flux by intracellular diffusion. However, the concentration gradients grow more substantial as  $V_{\text{mito}}$  is increased further by 100 times.

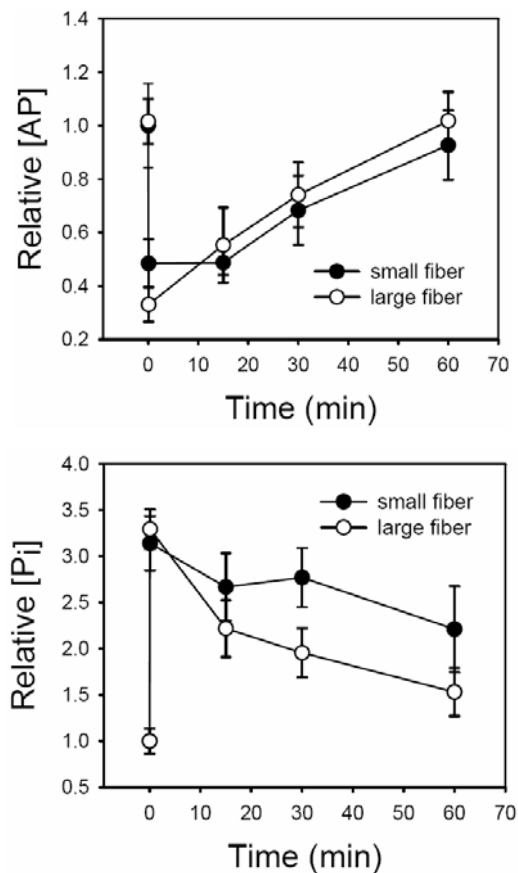


**Figure 7. 3** Relative changes in AP and  $P_i$  concentrations in small (filled symbols) and large (open symbols) light levator fibers during a contraction-recovery cycle. [ $N \geq 5$  for every point]. (Experimental results from Dr Kinsey's Laboratory, University of North Carolina, Wilmington)

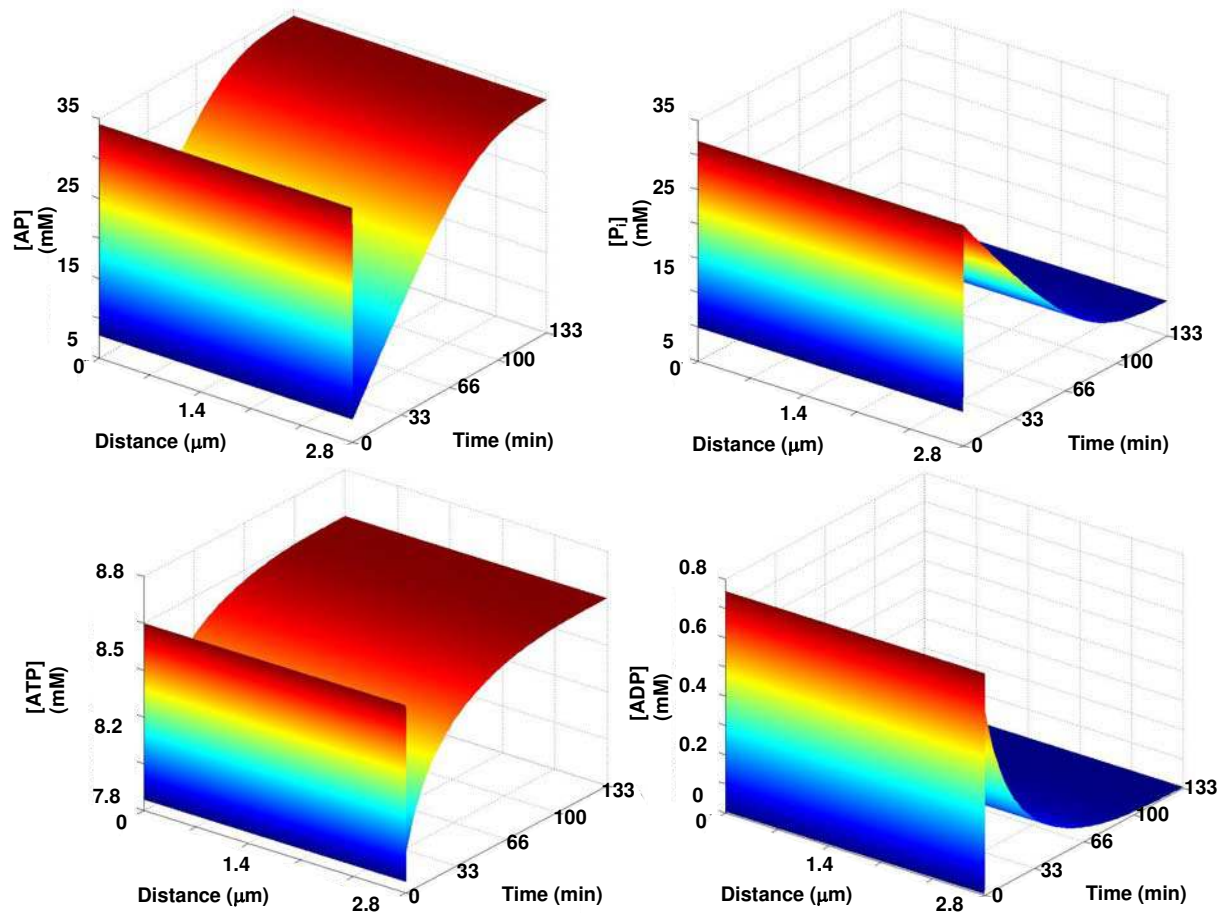


**Figure 7. 4 Model output for small light levator fibers using parameters in Appendix G assuming a uniform distribution of mitochondria. The temporally- and spatially-resolved concentrations of AP, P<sub>i</sub>, ATP and ADP during a contraction-recovery cycle are shown (Arg is not shown, but its concentration changes in reciprocal fashion to that of AP). [V<sub>mmtio</sub> = 1.9e-17 mmoles/micron<sup>2</sup>.s: 5 Hz frequency with 50% duty, 7s Stimulation, Mesh points: 120 pts, Time Step- 0:0.1:7, 8:1:99, 100:100:8000s]**

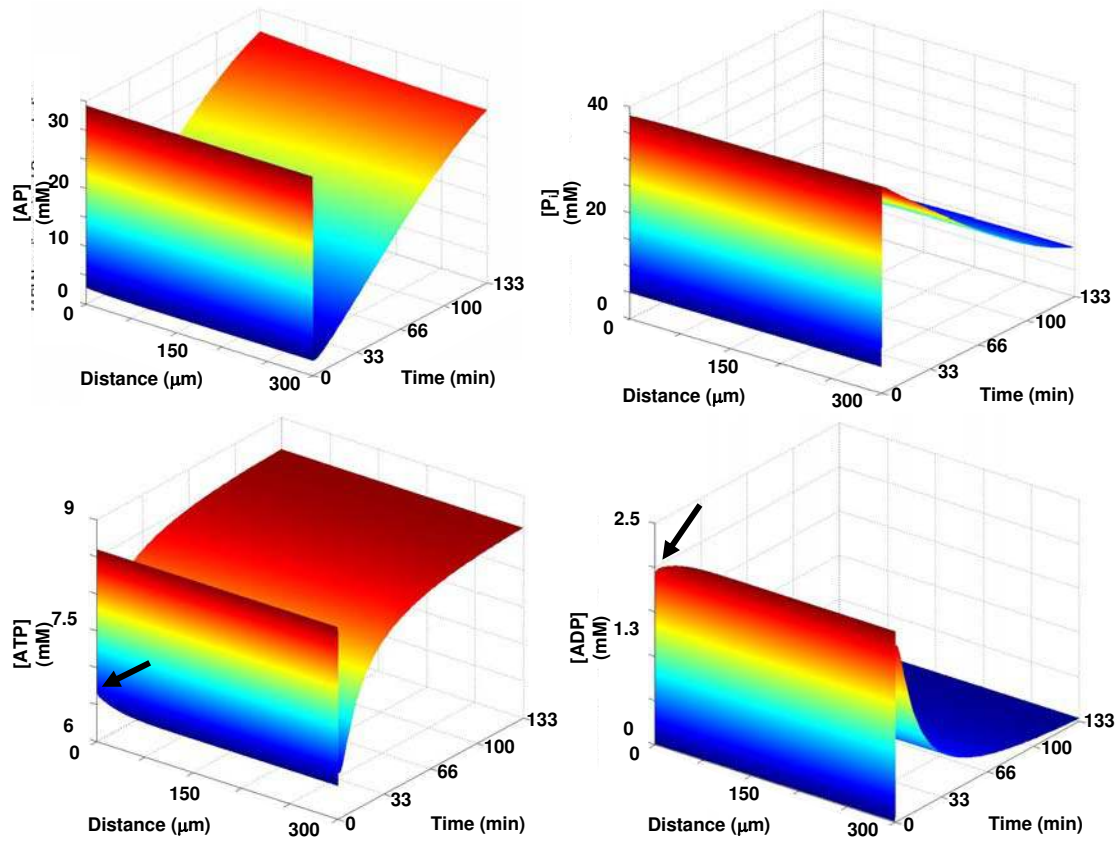
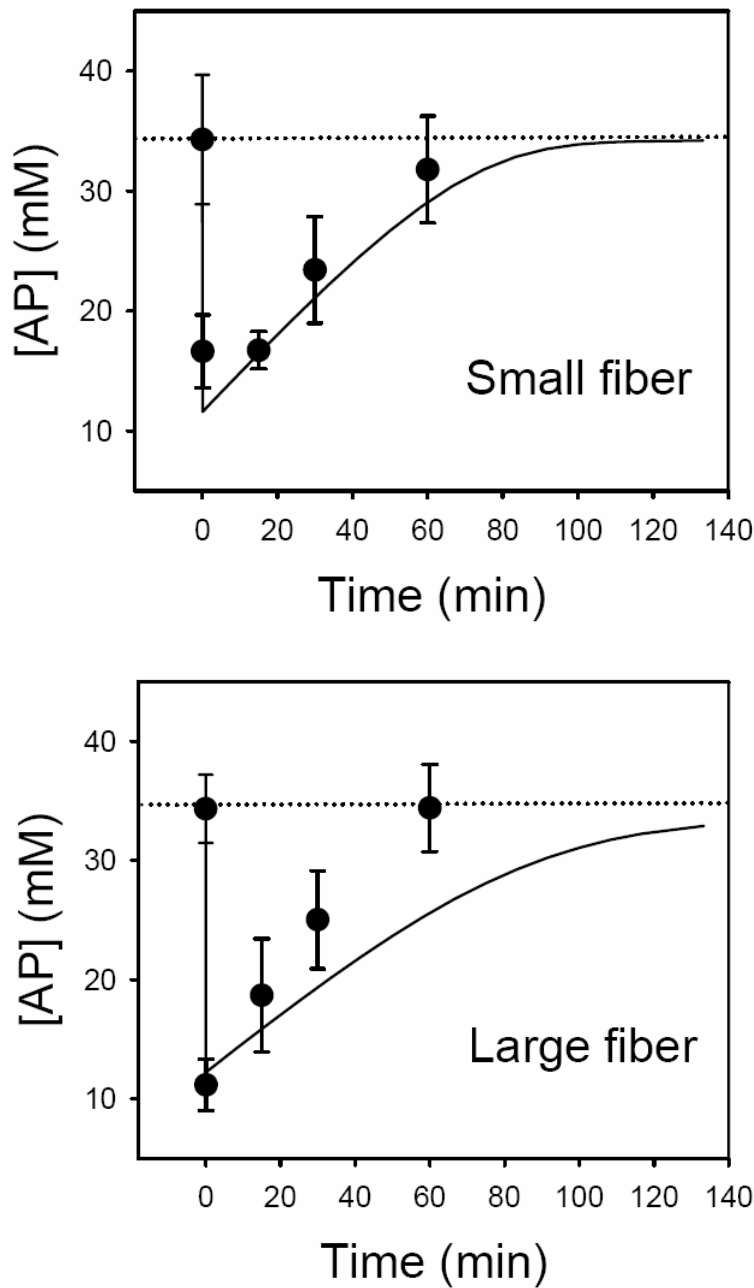


Figure 7.5 Model output for large light levator fibers using parameters in Appendix G assuming only subsarcolemmal mitochondria. The temporally- and spatially-resolved concentrations of AP, P<sub>i</sub>, ATP and ADP during a contraction-recovery cycle are shown (Arg is not shown, but its concentration changes in reciprocal fashion to that of AP). Arrows indicate the mild spatial gradients seen in the concentration 3-dimensional profiles. [ $V_{\text{mtio}} = 1.67e-15$  mmoles/micron<sup>2</sup>.s: 5 Hz frequency with 50% duty, 7s Stimulation, Mesh points: 120 pts, Time Step - 0:0.1:7, 8:1:99, 100:100:8000s]



**Figure 7. 6 Measured AP recovery (symbols) compared to the volume averaged model of AP recovery (solid line) in small (top) and large (bottom) fibers. The measured AP data has been normalized to a resting concentration of 34.3 mM to coincide with that of the model. In the model, the myosin ATPase was activated long enough to cause a decrease in AP that was comparable to the measured data. The dotted line indicates the resting concentration. [Small:  $V_{\text{mmtio}} = 1.9\text{e-}17$  mmol/micron<sup>2</sup>.s, 5 Hz frequency with 50% duty, 5.7s Stimulation; Large:  $V_{\text{mmtio}} = 1.67\text{e-}15$  mmol/micron<sup>2</sup>.s, 5 Hz frequency with 50% duty, 4s Stimulation]**

It is clear that the metabolic recovery rate is directly proportional to the  $V_{\text{mmito}}$ . It is also seen (Figure 7.7) that only when unrealistically high rates of  $V_{\text{mmito}}$  are used the steeper concentration gradients are observed, indicating that diffusion is limiting the rate of recovery in these muscle cells. As can be seen from the averaged plots the mitochondrial reaction rate used in the model fits the data well (Figure 7.6) and is considerably below the reaction rate which would lead to substantial diffusion limitations to aerobic flux in large fibers (Figure 7.7).

In the model computations for large white fibers the mitochondria were assumed to be distributed in the periphery of the fiber (subsarcolemmal). In order to assess the impact of this reorganization of mitochondria on muscle function as the animal grows from juvenile to adult, we also ran our model for uniform distribution of mitochondria in these fibers similar to that seen in small white fibers from juvenile crabs. The average  $\lambda/2$  value was computed by using a similar relationship between the mitochondrial fractional area and mean area/mitochondrion and obtained to be 3.4  $\mu\text{m}$ . This value is slightly higher from that obtained from small fibers (see Appendix G) but nearly two orders of magnitude less than that used for subsarcolemmal distribution used in the large fibers. Despite the large difference in diffusion distances of metabolites, the rate of metabolic recovery, assuming a uniform distribution of mitochondria in large fibers, was almost identical to that shown in Figure 7.5 (slightly higher), and no concentration gradients were observed (data not shown). So this result is consistent with the fact that there exists *very limited control of metabolic flux by intracellular diffusion*.

The model also computes the concentration profiles of metabolites in the dark aerobic fibers of the blue crab as shown in Figure 7.8. These fibers being aerobic rely on the supply of ATP by oxidative phosphorylation at the mitochondrial surface, and sustain long time burst exercise contractions. The model is run for a stimulation phase of 30s at 1 Hz frequency and 50% duty cycle. Mitochondrial clusters at the periphery of the segments of dark fibers seem to give rise to significant ATP production rates which are higher than the rates of diffusive flux. This can be observed as spatial gradients seen in the 3-dimensional concentration plots of ATP, ADP, and AP. After exercise burst, these dark fibers follow aerobic recovery. As can be seen from the recovery rates, the metabolites recover in less than 4 minutes, as compared to more than 100 minutes in the white anaerobic fibers.

Thus the principal finding of this study includes -

1. Model predicted rate of aerobic metabolism is insufficient to account for the relatively high rate of metabolite recovery in the large fibers, which is consistent with the hypothesis that anaerobic metabolism contributes to AP recovery to a greater extent.
2. Intracellular diffusive flux do not appear to limit metabolic recovery in large fibers, despite the fact that diffusion occurs over hundreds of microns. The fiber seems to have aerobic capacity that is considerably below the magnitude that would lead to substantial diffusion limitations (Figure 7.7).
3. Complete metabolite recovery in aerobic dark fibers occurs in a few minutes.

## **7.5 Discussion**

In the previous work by Kinsey and coworkers they have discussed the fiber size-dependence of post-exercise glycogen depletion (Boyle *et al.*, 2003) and lactate production (Johnson *et al.*, 2004) in crustacean muscle and have attributed this observed pattern to (a) long intracellular diffusion distances and/or (b) low SA:V of the large levator anaerobic fibers. While all these studies have shown that the post-contractile recovery is accelerated by anaerobic metabolism, the present study to our knowledge is the first quantitative demonstration in crustacean muscle of a metabolic recovery process (AP resynthesis) that is faster in large fibers as a result of anaerobic contributions. The model is used in light of experimental observations to explain the changes in metabolic capacity and organization associated with increasing cell size.



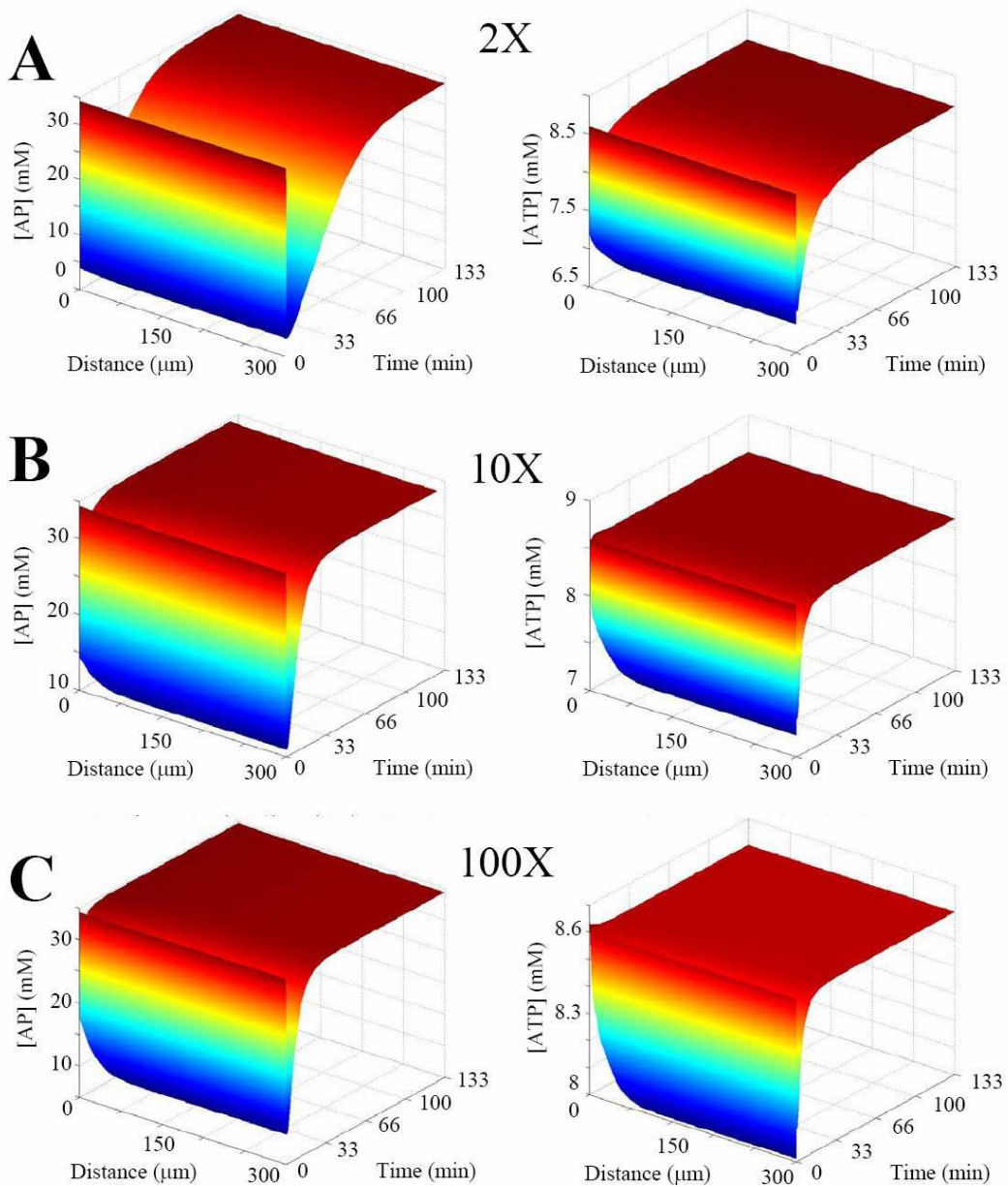


**Figure 7.7** The effect of increasing the rate of mitochondrial ATP production in large fibers on the temporal and spatial profiles of AP (left panels) and ATP (right panels) concentration. All parameters are the same as in Figure 7.5, except that the  $V_{mito}$  has been increased over the value used in Figure 7.5 by 2-fold (A), 10-fold and (B), and 100-fold (C).  $[V_{mito} = 1.67e-15 \text{ mmoles/micron}^2.s: 5 \text{ Hz frequency with } 50\% \text{ duty, } 7s \text{ Stimulation, Mesh points: } 120 \text{ pts, Time Step - } 0:0.1:7, 8:1:99, 100:100:8000s]$

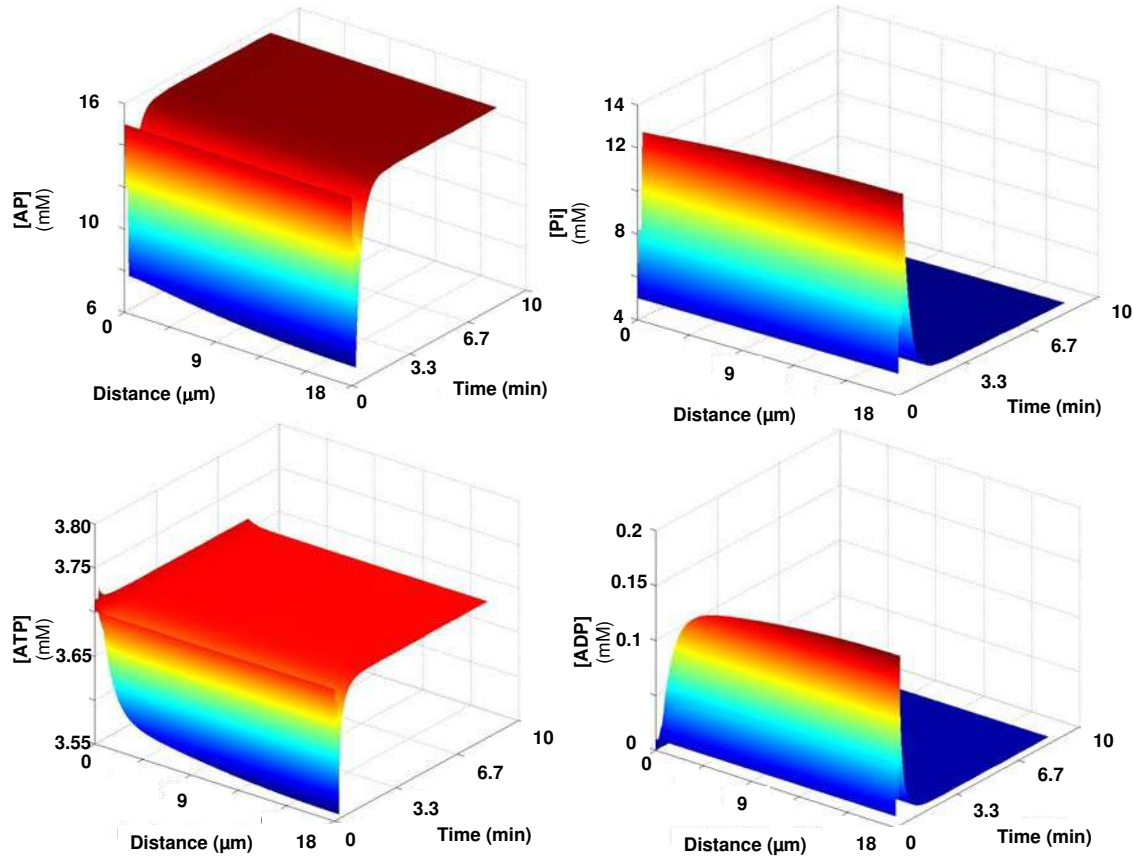


**Figure 7. 8 Model output for dark levator fibers using parameters in Appendix G. The temporally- and spatially-resolved concentrations of AP,  $P_i$ , ATP and ADP during a contraction-recovery cycle are shown (Arg is not shown, but its concentration changes in reciprocal fashion to that of AP). Mild spatial gradients are seen in the concentration 3-dimensional profiles. [ $V_{mmtio} = 4.315e-14$  mmoles/micron<sup>2</sup>.s: 1 Hz frequency with 50% duty, 30s Stimulation, Mesh points: 120 pts, Time Step - 0:0.01:30, 31:1:99, 100:50:600s]**

The patterns of metabolite recovery reported previously in the literature (Boyle *et al.*, 2003; Johnson *et al.*, 2004) and herein are clearly related to fiber size. Experimental studies have shown that AP and Arg, the key diffusing species (Ellington and Kinsey, 1998), can traverse the distance  $\lambda/2$  in small fibers in less than 30 ms, while needing 16,000 times longer (near 8 min) to cover the distance modeled for large fibers (Kinsey and Moerland, 2002). Therefore, it was surprising that our model results did not indicate a limitation of aerobic flux by intracellular metabolite diffusion. So from the model findings, it is apparent that kinetic expressions alone (no diffusion component) would have been nearly sufficient to simulate differences between the small and large fibers (Figures 7.4 and 7.5). This result of ours is in odds with the previous reaction-diffusion mathematical model studies in burst anaerobic muscle which have shown

substantial concentration gradients for high energy phosphate metabolites. Hubley *et al.*, 1997 have shown spatial gradients for PCr and free energy of ATP hydrolysis in fish white muscle during contraction. Mainwood and Rakusan, 1982 have likewise found dramatic concentration gradients for AP and free energy of ATP hydrolysis in blue crab light levator muscle. However, to be noted here, both these models assume high rates of steady state ATP demand and perfect buffering of high-energy phosphate concentrations at the mitochondrial membrane. This means that the rate of ATP supply at the mitochondria is always relatively high compared to the rates of diffusive flux. In contrast, the present model uses a simple kinetic expression for the mitochondrial boundary reaction producing ATP at reasonable rates (instead of constant supply at the mitochondrial surface). Furthermore, no additional ATP demand (as in previous models) was applied during the recovery beyond the thermodynamic drive to restore the resting steady-state metabolite concentrations (Basal ATPase rate).

However, it could also be argued here that we have underestimated the  $V_{mmito}$  and post-contractile ATP demand, and hence have eventually misjudged the effects of diffusion. It should be noted, however, that the model results for AP recovery paralleled our observations in the small fibers (Figure 7.6), which rely exclusively on aerobic metabolism for recovery (Boyle *et al.*, 2003; Johnson *et al.*, 2004), and the low  $V_{mmito}$  values were consistent with observations that complete aerobic recovery from exercise in blue crabs occurs over many hours (Booth and McMahon, 1985; Milligan *et al.*, 1989; Henry *et al.*, 1994; Boyle *et al.* 2003; Johnson *et al.*, 2004). Our results on varying  $V_{mmito}$  (Figure 7.7) are also consistent with the generalized analysis of diffusion limitation described by Weisz (1973), which relates the observed rate of the catalytic process to rates of diffusive flux. Applying this approach to the present case we can conclude that even if  $V_{mmito}$  and post-contractile ATPase rates were underestimated, the *observed rate of AP recovery is simply too slow to be limited by diffusive flux* (Weisz, 1973).

As can be seen the findings in the present study are somewhat paradoxical. If it is assumed that a relatively rapid post-contractile recovery in burst muscle is beneficial, which is apparently the case since large fibers use anaerobic metabolism to speed up recovery, and if intracellular diffusive flux does not limit recovery, then why do the large fibers not simply increase the mitochondrial density to accelerate recovery rather than relying on anaerobic processes that put

them further in oxygen debt? It is clear from our model study on varying the maximal reaction rate ( $V_{\text{mmtio}}$ ) of the mitochondria (Figure 7.7), that doubling the mitochondrial density would lead to a near doubling of recovery rate, with only mild limitations by diffusion. *So, we propose that in blue crabs the low SA:V associated with large fiber size is more important in limiting aerobic metabolism and/or driving metabolic design than is intracellular metabolite diffusion.* The most compelling evidence in support of this argument is the dramatic shift in the distribution of mitochondria towards the periphery of the fiber as the light levator muscle fibers grow (Boyle *et al.*, 2003) into large ones. This distributional change places more mitochondria at the sarcolemmal membrane near the source of  $O_2$  at the expense of increased intracellular diffusion distances. In our model analysis, there was a very slight advantage associated with a uniform, instead of subsarcolemmal, distribution of mitochondria in the large fibers (data not shown). However, *the fact that the developmental shift in mitochondria occurs anyway indicating that  $O_2$  flux (which was not included in the model) drives mitochondrial distribution more than intracellular diffusive flux.* This view has been suggested previously to explain mitochondrial clustering at the sarcolemma in non-giant mammalian (Mainwood and Rakusan, 1982) and crustacean muscle (Stokes and Josephson, 1992).

In addition to the above argument, the partial pressure of oxygen ( $PO_2$ ) in crustacean blood (including blue crabs) is low (Gannon and Wheatly, 1995; Forgue *et al.*, 2001) which leads to shallow  $PO_2$  gradients across the sarcolemma. *These shallow oxygen gradients when coupled to low SA:V of large fibers would lead to low rates of  $O_2$  flux into the muscle fiber.* Additionally, *the lack of myoglobin (Mb) in the light levator muscle amplifies this effect,* since Mb-less fibers require a higher extracellular  $PO_2$  to support a given rate of  $O_2$  consumption compared to muscles with Mb (Groebe and Thews, 1990). To add here, recent observations in isolated *Xenopus laevis* skeletal muscle fibers, which are also relatively large and lack Mb, that low intracellular  $PO_2$  limits the rate of NAD(P)H oxidation by the electron transport system during steady-state contraction (Hogan *et al.*, 2004). Further, the modeled differences between the recovery rate in small and large fibers are modest, due to the relatively small differences in their oxidative potentials (Figure 7.4 and 7.5; Appendix G note the  $V_{\text{mmito}}$ ), but the measured differences in post-contractile lactate production among these size classes are dramatic; far greater than would be necessary to accelerate AP resynthesis by the relatively small amount

indicated in Figure 7.6 (Johnson *et al.* 2004). If fiber SA:V limits aerobic metabolism then the size-dependence of aerobic recovery may be much more substantial than shown in Figures 7.4, 7.5 and 7.6, which would explain the strong size-dependence of post-contractile lactate production.

What then are the potential advantages associated with large muscle fibers? Rome and Lindsbelt, 1998 have proposed that burst contractile muscle composed of relatively few large fibers may yield a greater percentage of total muscle volume that is devoted to myofibrils, and therefore improve contractile force, compared to muscle with a much larger number of small fibers. Johnston *et al.* (2003; 2004) have also proposed that in certain cold-water fish groups white muscle fibers attain a size that is just below that which would be diffusion-limited in order to minimize sarcolemmal surface area over which ionic gradients must be maintained, thus lowering metabolic rates. A similar argument could be made for blue crab anaerobic fibers, with the additional consideration that *a low mitochondrial content may also constitute an energy saving strategy to avoid the costs of mitochondrial biogenesis and the maintenance of electrochemical gradients across the inner membrane.* Forgue *et al.* (2001) have made complimentary arguments that the low blood PO<sub>2</sub> in crustaceans limits resting metabolic rate to reduce costs during periods of inactivity. These proposed energy saving measures are linked; *if the capacity to produce ATP is strategically lowered, then there is no negative consequence to the low SA:V associated with large fibers. Similarly, if SA:V is lowered, then there is no further consequence to lowering aerobic capacity, since O<sub>2</sub> flux would limit mitochondrial respiration in large fibers anyways.* It should be noted that even the small fibers in the present study are relatively large and have a low mitochondrial content compared to anaerobic fibers from most animals, thus benefiting from this putative energy saving strategy.

The implication of the above is that the benefits of a rapid aerobic recovery following a burst contraction are outweighed by long-term energetic savings. Blue crabs have large chelipeds and highly effective defensive behavior, and they also have the capacity to rapidly bury themselves to avoid predators. These characteristics may obviate the need for additional high-force contractions following an initial bout of burst swimming, and may explain why the juvenile crabs do not also employ anaerobic metabolism to accelerate recovery. Large fibers might be

particularly important in reducing metabolic costs in cases where anaerobic muscle constitutes a large fraction of the total body mass and is used infrequently, but must maintain a polarized sarcolemma at all times. Examples may include lobster abdominal muscle that is used for tail-flip escape maneuvers, or fish white muscle in species that infrequently undergo burst swimming. At present, however, the benefits of large fiber size, if any, in crustaceans and other groups are not known.

## 7.6 Future Recommendations

This present work primarily deals with improving on the previous work by Hubley *et al.*, 1997, utilizing a simple geometrical arrangement of the region surrounding a single mitochondrion, and incorporating the detailed description of reactions at the mitochondrial surface and in the sarcoplasmic region near the mitochondrion (the myofibril). This model is used to explain the possible reasons for recruitment of anaerobic recovery processes in large adult white fibers of blue crab. The most important conclusion is that intracellular diffusive flux of metabolites even over the modeled large diffusion distances does not seem to restrict high energy phosphate recovery during post-exercise period. This is because of the low ATP demand-ATP supply region this muscle fiber is in. So we propose the possible reason for anaerobic recovery in these large fibers is attributed to the mitochondrial distribution and low SA:V of the muscle fiber limiting oxygen flux into the fiber, and consequently ATP production by oxidative phosphorylation.

Therefore, in order to quantify the experimental results for the large white fibers the simple mitochondria ADP dependent ATP production needs to be modified. We think this can be done by incorporating the effects of extracellular O<sub>2</sub> concentration along with the ADP dependence on mitochondrial ATP production reaction. An oxygen flux balance accounting for its diffusion and consumption by various enzyme catalyzed processes in the Tri-carboxylic acid (TCA) cycle and Electron Transport Chain (ETC) in the mitochondria, as proposed actively in the works of Korzeniewski, 2003 and Beard, 2005 needs to be obtained.

The subsequent models would utilize the reaction kinetics from these developed models, but should incorporate the entire muscle fiber (with a one-dimensional radial coordinate system) including a multi-domain (myofibril) system with sarcoplasmic reticulum (SR) barriers. This SR has been believed to impose considerable restrictions to metabolite transport (Kinsey and Moerland, 2002). This could be further extended to a 2-dimensional system (axial and radial) to account for anisotropic diffusion, mitochondrial distribution, and variation of SR barrier properties.

While in the current study with anaerobic blue crab giant muscle fibers, intracellular diffusive fluxes of high-energy phosphate metabolites did not appear to exert substantial control over the rate of aerobic metabolism, there may be several other cell types where diffusion is limiting. These cell types likely include systems with relatively high rates of ATP production and distant sites of ATP utilization, such as in some muscle fibers with a higher aerobic capacity than examined here (Meyer *et al.* 1984; Stokes and Josephson, 1992; Vendelin *et al.*, 2000; Saks *et al.*, 2003; Suarez, 2003) or in the flagellum of spermatozoa, which has been the subject of many reaction-diffusion analyses (e.g., Nevo and Rikmenspoel, 1969; Tombes and Shapiro, 1985; Van Dorsten *et al.*, 1997; Ellington and Kinsey, 1998). Even in cases where neither intracellular metabolite diffusion nor sarcolemmal O<sub>2</sub> flux limit aerobic metabolism *per se*, the interaction between the two, i.e. the diffusive processes and ATP demand, has certainly shaped the evolution of cellular design. The model developed in this study can be extended for these cell types. Moreover, it is believed that in certain muscle types the presence of myoglobin, a small intracellular oxygen-binding heme protein, accelerates oxygen delivery to the mitochondria. The current model could be extended for these muscle types to incorporate measurements of myoglobin and oxygen consumption rate in the muscle fibers. This can be done by using the facilitated diffusion mechanism and using suitable boundary conditions and reaction kinetics proposed before for CK in skeletal muscle systems (Meyer *et al.*, 1984).

Summarizing, the complete reaction-diffusion analysis provides insight into the role of cellular structure in energy metabolism of muscle. Practical motivations of this project come from the interest in utilizing the model for quantitative evaluation of metabolic pathways and regulatory mechanisms under normal and abnormal condition of the muscle, and in turn, offer a logical

basis for assessing the progress of disease processes, thus evaluating possible treatments. To be also noted here, the model approach developed has broader impact and significance, as it provides a general applicable framework that could be extended for the analysis of complex spatial and temporal process in other cells and tissues.



## CHAPTER 8

### SUMMARY

*Ex vivo* engineering of living tissue is a rapidly developing area with vast potential to impact significantly a wide-range of biomedical applications (Martin *et al.*, 2004). Bioreactor cultures have been shown to be essential for improving the functional properties of these tissue engineered constructs. However, the major obstacles to the generation of functional tissues in these reactors for wide-spread clinical use is the limited understanding of the regulatory role of specific physicochemical culture parameters on tissue development. Not only is the cellular environment within and around the constructs ill defined, in addition, the complex cellular responses to this environment are not fully understood. In this context, computational methods can serve as a valuable tool to facilitate better understanding of the micro and macro environmental changes of biochemical factors as well as reveal the fundamental mechanisms of cell function in a 3-dimensional environment in culture units. This study has the potential to improve tissue engineered functional constructs.

In this context, in the present work, a general modeling framework for hematopoietic cell tissue engineering, human mesenchymal stem cell tissue engineering and cartilage tissue engineering was proposed and subsequently elaborated. The aim of this approach was to provide an integration of interactions between the biochemical factors and the cell behavior, which are believed to affect each other in a mutual iterative way. This chapter summarizes the findings of all the previous chapters of the work presented in this dissertation.

Chapters 2, 3 and 4 of this dissertation focused on the study of hematopoietic cell expansion in bioreactors. Chapter 2 provided a detailed biological background towards the understanding of hematopoiesis process, discussed the various culture systems currently being used for expansion of these types of cells, and also the various environmental factors that have been found to be important for these cell types in different culture systems. In the model study developed in this work *ex vivo* cell expansion in perfusion reactor systems are considered. The later part of Chapter 2 summarized the various mathematical models that have been developed in literature to describe hematopoietic process *in vivo* in the bone marrow and *ex vivo* in bioreactors. The mathematical approach used for the study of cell growth characteristics and environmental changes in this dissertation, is the *method of volume averaging*. This approach has been carefully outlined with a simple example at the end of Chapter 2.

Chapter 3 discusses the dynamic mathematical model developed in the present study to understand the expansion of granulocyte progenitors in the hematopoietic process in a 3-dimensional perfusion bioreactor system. Molar balances describing oxygen consumption and cell growth were written to describe the physiological process in the reactor. The method of volume averaging (Whitaker, 1999) was used to compute the effective reaction and transport terms accounting for the effects of the local 3-dimensional geometry. All the model parameters were obtained from literature. Spatial and temporal variations of oxygen concentration and granulocyte progenitor cell density are obtained in the bioreactor. The maximum cell volume fraction reached when oxygen is depleted in the cell layer at 15 days is nearly 0.63, corresponding to a cell density of  $2.25 \times 10^8$  cells/ml. The model results illustrate the effects of oxygen mass transfer restrictions in the matrix to the growth of these cells. Moreover, the substrate inhibition kinetics used for cell growth has been shown to lead to complex effects with respect to the roles of oxygen concentration and its supply by convection and diffusion on cell growth.

Additionally, the model provides quantitative estimates of the oxygen consumption for growth and for metabolism, and this information on oxygen consumption and cell growth was further used to estimate the roles of key bioreactor design parameters, including flow rates and liquid depth, and to optimize the reactor performance. Variation in the height of the liquid layer above

the cell matrix where nutrient supply is introduced affected the relative and absolute amounts of oxygen supply by hydrodynamic flow and by diffusion across a gas permeable FEP membrane. However, due to high mass transfer restrictions of the FEP membrane, the delivery of oxygen by hydrodynamic flow always exceeded that by membrane transport, thus leading to larger growth rates at higher liquid layer heights. A maximum growth rate occurs at a specific flow rate. Lower residence times, i.e. higher flow rates, supplied larger amounts of oxygen to the cell layer of the bioreactor. Larger amounts of the oxygen were then available for cell growth and metabolic consumption, which produced a larger number of progenitor cells. However, an optimal growth rate at a specific flow rate was found whereby at lower flows the growth was transport limited by oxygen supply and at higher flows the growth was limited by kinetic inhibition. The spatial pattern of delivery by convection was also found to play a significant role increasing the rate of cell growth. The model results clearly indicate that variation of the oxygen concentration in the inlet feed with time may lead to enhanced cell growth.

In order to rationally optimize *ex vivo* expansion of hematopoietic cells, there was a need to improve our understanding of the complex dynamics of hematopoiesis by incorporating other important reactor input biochemical factors such as glucose and lactate. Additionally, as mentioned these culture systems are different from other culture systems in terms of multiple cells coexisting in the culture at the same time which makes it essential to go beyond modeling a single cell type. The model incorporates the effects of local 3-dimensional geometry by deriving the effective diffusivities and effective rate expressions used for solving the effect of oxygen delivery to the cells. However, the volume averaged expressions do not include the effect of the local 3-dimensional cell-cell interactions and ECM environment, an important factor in the 3-dimensional structure that affects cell proliferation.

The model in Chapter 3 was improved in Chapter 4 by addition of glucose and lactate to the material balances along with oxygen. The idea of co-existence of more than one cell type in culture was studied by the use of a simple two cell-group model. The cell types were separated on the basis of large differences in their metabolic lactate production rates. The dynamic model was developed for a well-mixed system. This was done by spatially averaging the concentrations of the various reacting species in the reactor components of the perfusion

bioreactor. The model showed that reactor systems can sustain larger cell growth rates, while maintaining the glucose and oxygen concentration high enough and also facilitate efficient removal of lactate.

As a first step towards model improvement, the dynamic model developed in Chapter 4 should be extended to study growth and metabolism in the perfusion reactor (Chapter 3) by incorporating the effects of mass transport due to diffusion and flow and computing the spatial distribution of the nutrients and products. The model also needs to be improved to account for the existence of a complete lineage of hematopoietic cells or multi-lineages in cultures. The major obstacle to this model extension is the limited availability of experimental data on metabolic and growth kinetics for cells in this hematopoietic process. Moreover, in future for the determination of improved delivery of nutrients and better mass transfer conditions in the perfusion bioreactor system, the model needs to be analyzed for different matrix geometries to study the formers effect on cell growth. Finally, in order to completely model a 3-dimensional system, analyzing the variation in diffusion coefficient of metabolites due to restrictions and/or consumption due to cell growth is not enough. It is essential to account for the local 3-dimensional cell-cell and cell-ECM interactions. In order to address the effects of cell-ECM interactions a systematic model describing ECM production by the cells and change in the cell microenvironment due to presence of ECM needs to be developed. To do so the current model hints at the necessity of systematic quantitative information of ECM formation by various cell types in culture. The information obtained from experiments, used suitably in these models would help to improve our understanding of hematopoietic cell growth in *ex vivo* culture systems.

In a broader sense, the developed transport-reaction model framework is very general, and could be easily applied for any cell type, by using suitable kinetic parameters, to describe cell growth, nutrient depletion and product formation in 2-dimensional or 3-dimensional *ex vivo* culture systems. This was illustrated in the study in Chapter 5. In this study, experimental results on hMSC metabolism and growth were available for cell cultures in 3-dimensional PET matrices placed in two different culture units – the perfusion bioreactor system and the static culture system. Mathematical models describing the transport and consumption of oxygen for

experimentally determined cell growth were written for the two culture systems. The model simulations on spatial and temporal oxygen distribution were used to address the role of oxygen distribution on cell growth and metabolic processes. Thus, this combination of model and experimental result analysis in our study demonstrates the effects of perfusion conditions on intrinsic cellular events and the significant role of perfusion culture environment to sustain the development of engineered tissue constructs.

The next major application of mathematical modeling in tissue engineering was illustrated by studying the development of cartilage constructs in reactors described in Chapter 6 of this dissertation. The limited repair capacity of the articular cartilage along with its simple tissue structure, and available experimental data enabled the development of a detailed structured computational model for this tissue engineering application. The study developed a dynamic mathematical model of cartilage tissue formation in a hollow fiber bioreactor unit and compared the model results with available experimental data obtained by *in situ* NMR experiments (reported in the work of Potter *et al.*, 1998). In this approach, the volume averaging method was combined with elements of a moving boundary approach in order to account for the radial growth of cells from the surface of the hollow fibers. Model simulations of cell and extracellular matrix formation as well as changes in the NMR spin-lattice relaxation time constant and water diffusion coefficient with time were compared to experimental results in hollow fiber bioreactor over four weeks of culture. Although several of the model parameters were fit to the experimental data, the model trends showed good agreement with the data. A model sensitivity analysis was performed to indicate the important key parameters effecting cell behavior in the reactor. The model was successfully utilized to establish relationships between the environmental factors, such as nutrients, within and around the constructs to the processes occurring at the cellular level, such as chondrocyte cell maturation, proliferation and ECM synthesis.

These tissue engineering model development applications have considered the cellular metabolic and growth processes in terms of net kinetic expressions linked to changes in macroscopic environmental parameters. In order to understand and incorporate a complete model framework understanding of processes at the cellular level is necessary. To do so, muscle cell was chosen to

study metabolic processes in terms of production, transport, conversion and utilization of metabolite species. It is known that in a muscle cell many cellular compartments, chemical species, enzymes, biochemical reactions, metabolic pathways, and control mechanisms interact with each other simultaneously to maintain homeostasis of the most important energy delivering metabolite, ATP. The proposed reaction-diffusion model of phosphorous metabolites involved in various metabolic pathways in the muscle described in Chapter 7 was shown to provide a suitable framework for the study of diffusion, reaction and metabolic organization on the control of muscle metabolism. In this study of crustacean blue crabs the model results suggest that in the interaction between mitochondrial ATP production rates, ATP consumption rates and diffusion distances yield a system that is not particularly close to being limited by intracellular metabolite diffusion. We concluded that the fiber SA:V and oxygen flux exert more control than intracellular diffusive flux over the developmental changes in metabolic organization and metabolic fluxes that characterize these muscles. This metabolic study is intended to answer the basic questions on the role of metabolite spatial and temporal distribution due to transport and reaction on cell structure, and vice versa, and the current model is a first step towards this overall goal.

## APPENDIX A: LIST OF PARAMETERS USED IN CHAPTER 3

### Cellular parameters

Cell diameter = 10  $\mu\text{m}$  (Chow et. al., 2001)  
Specific cell volume,  $V_g = 2.8 \cdot 10^{-9} \text{ cm}^3/\text{cell}$   
[Chow et al., 2001]

#### *Metabolic parameters:*

Specific oxygen uptake rate,  $Q_{mm} = 4.5 \cdot 10^{-14} \text{ mol/cell/hr} = 1.25 \cdot 10^{-17} \text{ mol/cell/s}$   
Dimensionless oxygen consumption rate,  $Q_m = Q_m/(V_g \cdot C_o) = 0.021158 \text{ 1/s}$   
 $K_m = 1.055 \cdot 10^{-8} \text{ mol/cm}^3$   
[Chow et al., 2001]

#### *Growth parameters:*

$kk = 1.264 \cdot 10^{-11} \text{ mol/cm}^3 \cdot \text{s}$   
 $KI = 2.78 \cdot 10^{-15} (\text{mol/cm}^3)^2$   
 $K_I = 5.1 \cdot 10^5 \text{ cm}^3/\text{mol}$   
 $p = kk/C_o = 5.9905 \cdot 10^{-5}$   
 $q = KI/C_o^2 = 0.062442$   
 $r = 1/(K_I \cdot C_o) = 9.2928$  (Heaven et. al. 2000)  
Yield coefficient,  $Y = \text{mass of cells produced/ mass of oxygen consumed} = 0.45$   
[Bailey et al. 1986]

Initial cell seeding density,  $d_o = 2 \cdot 10^4 \text{ cells/ml}$

### Substrate parameters

Effective oxygen permeability =  $3.20 \cdot 10^{-14} \text{ mol/cm/s/mm Hg}$   
Henry's coefficient for oxygen,  $k_h = 0.95 \text{ atm.L/mmol}$   
Oxygen diffusion coefficient in medium (liquid layer),  $D_\beta = 3.29 \cdot 10^{-5} \text{ cm}^2/\text{s}$   
Oxygen diffusion coefficient in the matrix (cell layer),  $D_\gamma = 1.59 \cdot 10^{-5} \text{ cm}^2/\text{s}$   
[Chow et al., 2001]

*Averaging volume parameters*

Radius of the averaging volume,  $R = 50 \mu\text{m}$

Mass transfer coefficient at the interface of the cell and liquid region in the averaging volume,  $P = 0.004 \text{ cm/s}$

$$\alpha = (D_\gamma/L P) = 3.18$$

Equilibrium coefficient,  $K_{eq} = 1$

$$k = (K_{eq} D_\gamma/D_\beta) = 0.48328$$

[Galban *et al.* 1999]

**Reactor Parameters**

Matrix thickness,  $2l = 0.12 \text{ cm}$

Liquid layer thickness,  $T = 0.6 \text{ cm}$

Reactor Length,  $L = 10 \text{ cm}$

Reactor Width,  $w = 2.5 \text{ cm}$

**Membrane characteristics**

FEP membrane

Thickness =  $25 \mu\text{m}$

Length =  $10 \text{ cm}$

Membrane permeability ( $Perm$ ) =  $1.343 * 10^{-5} \text{ cm/s}$



## APPENDIX B: LIST OF PARAMETERS USED IN CHAPTER 4

### Reactor Parameters

#### *Tissue Culture Flask System –*

Number of tissue culture system =  $N = 24$

Volume of liquid layer in one tissue flask,  $V_{cl} = 2 \text{ cm}^3$

Total Volume of liquid layer,  $V_l = N * 2 \text{ cm}^3 = 48 \text{ cm}^3$

Matrix Diameter, *dia* = 1.4 cm

Matrix thickness,  $l = 0.1 \text{ cm}$

Total Cross-sectional Area of cell layer,  $A = N * (22/7) * (\text{dia}/2)^2$

Liquid layer thickness,  $T = V_l / A = 1.299 \text{ cm}$

Volume of cell layer,  $V_c = l * A$

Flow Rate,  $F = 0$

Average velocity,  $v_{avg} = 0$

#### *Well-mixed Reactor -*

Matrix thickness,  $2l = 0.12 \text{ cm}$

Liquid layer thickness,  $T = 0.6 \text{ cm}$

Reactor Length,  $L = 10 \text{ cm}$

Reactor Width,  $w = 2.5 \text{ cm}$

Cross-sectional Area of flow,  $A = L * w$

Volume of cell layer,  $V_c = l * L * w$

Volume of other containers used in experiments =  $V_{reservoir} + V_{cell-collector}$   
 $= 100/2 + 350/2 \text{ cm}^3$

Volume of liquid layer,  $V_l = T * L * w + V_{reservoir} + V_{cell-collector}$

Residence time of flow,  $t = 3600 \text{ s}$

Flow Rate,  $F = V_l / t$

Average velocity,  $v_{avg} = F/A$

## Mass Transfer Coefficients for transport of oxygen, glucose and lactate across the liquid layer to the cell layer

Oxygen diffusivity in the liquid layer,  $Dl_o = 3.29 \times 10^{-5} \text{ cm}^2/\text{s}$   
Glucose diffusivity in the liquid layer,  $Dl_{glu} = 0.6 \times 10^{-5} \text{ cm}^2/\text{s}$   
Lactate diffusivity in the liquid layer,  $Dl_{lac} = 1.45 \times 10^{-5} \text{ cm}^2/\text{s}$

### *Tissue Culture Flask System –*

Oxygen,  $km_o = Dl_o/T$   
Glucose,  $km_{glu} = Dl_{glu}/T$   
Lactate,  $km_{lac} = Dl_{lac}/T$

### *Well-mixed Reactor -*

Oxygen,  $km_o = 1.165 \cdot (Dl_o^{(2/3)}) \cdot (v_{avg}/(L \cdot T))^{(1/3)}$   
Glucose,  $km_{glu} = Dl_{glu}/T$   
Lactate,  $km_{lac} = Dl_{lac}/T$

## Membrane characteristics

FEP membrane  
Thickness = 25  $\mu\text{m}$   
Length = 10 cm  
Membrane permeability ( $k_{mem}$ ) =  $1.343 \cdot 10^{-5} \text{ cm/s}$

## Initial Concentrations

Oxygen concentration used for non-dimensionalizing,  $C_o = 2.10 \cdot 10^{-7} \text{ mmol/cm}^3$   
[Oxygen concentration in equilibrium with 20% gas phase oxygen]

### *Tissue Culture Flask System –*

Initial lactate concentration,  $C_{lac}^o = 2.36 \cdot 10^{-8} \text{ mol/cm}^3$   
[Equivalent to 2.125 mg/l; MW = 90]  
Initial glucose concentration,  $C_{glu}^o = 2.822 \cdot 10^{-6} \text{ mol/cm}^3$   
[Equivalent to 0.95 g/l; MW = 180]  
Initial oxygen concentration,  $C_{o_2}^o = 0.25$   
[Dissolved oxygen concentration in equilibrium with 5% gas phase oxygen]

### *Well-mixed Reactor -*

Initial glucose concentration,  $C_{glu}^o = 5.07 \cdot 10^{-6} \text{ mol/cm}^3$   
[Equivalent to 0.913 g/l; MW = 90]  
Initial oxygen concentration,  $C_{o_2}^o = 0.25$   
[Dissolved oxygen concentration in equilibrium with 5% gas phase oxygen]  
Initial lactate concentration,  $C_{lac}^o = 2.822 \cdot 10^{-6} \text{ mol/cm}^3$   
[Equivalent to 0.0254 g/l; MW = 180]

These numbers (glucose and lactate) are also used to non-dimensionalized the respective concentrations in the reactor cell and liquid layers.

Non-dimensional dissolved oxygen concentration supplied by the media by flow,  $C_{o_2}^{in} = 1$   
[Dissolved oxygen concentration in equilibrium with 20% gas phase oxygen]

Non-dimensional dissolved oxygen concentration in the gas phase,  $C_{o_2}^g = 1$   
[Dissolved oxygen concentration in equilibrium with 20% gas phase oxygen]

## Cellular parameters

Cell diameter = 10  $\mu\text{m}$  (Chow et. al., 2001)  
Specific cell volume,  $V_g = 2.8 \cdot 10^{-9} \text{ cm}^3/\text{cell}$   
(Chow et al., 2001)

### Metabolic parameters -

#### **Aerobic Metabolism**

Specific oxygen uptake rate,  $Q_{mm} = 4.5 \cdot 10^{-14} \text{ mol/cell/hr} = 1.25 \cdot 10^{-17} \text{ mol/cell/s}$   
Dimensionless oxygen consumption rate,  $Q_m = Q_m/(V_g \cdot C_o) = 0.021158 \text{ 1/s}$   
 $K_m = 1.055 \cdot 10^{-8} \text{ mol/cm}^3$   
(Chow et al., 2001)

#### **Anaerobic Metabolism**

$k_{glu} = 0.022 \text{ 1/h}$   
 $K_{glu} = 0.028 \cdot 10^{-6} \text{ mol/cm}^3$

Metabolic rate of progenitor cells (group 1),  $\alpha = 8.06 \cdot 10^2 \text{ 1/s}$

Metabolic rate of post-progenitor cells (group 2),  $\beta = 7.52 \cdot 10^{-3} \text{ 1/s}$

[Computed by linear fit to experimental data shown in Table 4.2 from Yan et al., 2001]

### Growth parameters for cell group 1

#### **Oxygen -**

$kk = 1.264 \cdot 10^{-11} \text{ mol/cm}^3 \cdot \text{s}$

$KI = 2.78 \cdot 10^{-15} \text{ (mol/cm}^3)^2$

$K_I = 5.1 \cdot 10^5 \text{ cm}^3/\text{mol}$

$p = kk/C_o = 5.9905 \cdot 10^{-5} \text{ 1/s}$

$q = KI/C_o^2 = 0.062442$

$r = 1/(K_I \cdot C_o) = 9.2928$

[Heaven et. al. 2000]

#### **Glucose -**

$K_s = 0.89 \cdot 10^{-6} \text{ mol/cm}^3$

$\mu_m = 1.3$

$K_p = 0.779 \cdot 10^{-6} \text{ mol/cm}^3$

Initial cell seeding number,  $d_o = 0.35 \cdot 10^5 \text{ cells}$

Initial cell volume fraction,  $\epsilon_{\gamma 1} = 3.27 \cdot 10^{-5}$

### *Growth parameters for cell group 2*

Differentiation rate coefficient of cell group 1 to cell group 2,  $\phi_d^2 = 4 \cdot 10^{-6}$  1/s

Initial cell number,  $d_o = 0.15 \cdot 10^5$  cells

Initial cell volume fraction,  $\epsilon_{\gamma 2} = 1.44 \cdot 10^{-5}$

### **Yield Coefficients**

$Y_{cell/o_2}$  = mol of cells produced/ mol of oxygen consumed = 0.45

[Bailey *et al.* 1986]

$Y_{lac/o_2}$  = mol of lactate produced/mol of oxygen consumed = 1

[Collins *et al.*, 1998]

[At earlier stages of culture maximum number of progenitors present]

$Y_{lac/glu}$  = mol of lactate produced/mol of glucose consumed = 1.4

[Heidemann *et al.*, 1998]

$Y_{glu/o_2}$  = mol of glucose consumed/mol of oxygen =  $Y_{glu/lac} * Y_{lac/o_2} * (C_{o_2}^o / C_{glu}^o)$

$Y_{lac/cell} = (0.65 * 100) * 4.4 * 10^{-12}$  mol/cell

Computed yield =  $[Y_{lac/cell} / (V_g * C_{lac}^o)] = 7.08 * 10^2$  mol/mol / cell vol fraction

$Y_{cell/glu} = 10 * 0.062 * 10^{12}$  cell/ $\mu$ mol

Computed Yield =  $[(Y_{cell/glu} * V_g * C_{glu}^o)]$

[RPMI 8226 cell, Truskey *et al.*, 1990]

## APPENDIX C: LIST OF PARAMETERS USED IN CHAPTER 5

### Cellular parameters

Specific cell volume,  $V_g = 2.8 \cdot 10^{-9}$  cm<sup>3</sup>/cell  
[Chow et al., 2001]

#### *Metabolic parameters*

##### *Static*

Dimensionless specific oxygen consumption rate,  $Q_m = 0.002588$  1/s

[From experimental data reported in this paper]

Saturation constant,  $K_m = 1.105265 \cdot 10^{-8}$  mol/cm<sup>3</sup> (= 0.05\*Co)

[Peng and Palsson, 1996; Chow et al., 2001a]

##### *Perfusion*

Dimensionless specific oxygen consumption rate,  $Q_m$  (1/s)

=  $-3.6198E-16 \cdot t^2 + 6.6040E-10 \cdot t + 2.3413E-03$

[From experimental data reported in this paper]

Saturation constant,  $K_m = 1.105265 \cdot 10^{-8}$  mol/cm<sup>3</sup> (= 0.05\*Co)

[Peng and Palsson, 1996; Chow et al., 2001a]

#### *Growth parameters*

##### *Static*

Cell growth rate,  $m = 3.87454 \cdot 10^{-7}$  1/s

Initial cell volume fraction,  $\epsilon_{y0} = 9.65 \cdot 10^{-3}$

[From experimental data reported in this paper]

##### *Perfusion*

Cell growth rate,  $m = 1.18 \cdot 10^{-6}$  1/s

Initial cell volume fraction,  $\epsilon_{y0} = 1.53 \cdot 10^{-3}$

[From experimental data reported in this paper]

### Substrate parameters

Henry's coefficient for oxygen,  $k_h = 0.95$  atm.L/mmol

$C_o = 2.10 \cdot 10^{-7}$  mmol/cm<sup>3</sup>

[Oxygen concentration in equilibrium with 20% gas phase oxygen]  
Oxygen diffusion coefficient in medium (liquid layer),  $D_{\beta} = 3.29 \cdot 10^{-5} \text{ cm}^2/\text{s}$   
Oxygen diffusion coefficient through cells in the matrix (in cell layer),  $D_{\gamma} = 1.59 \cdot 10^{-5} \text{ cm}^2/\text{s}$   
[Chow et. al., 2001]

#### *Averaging volume parameters*

Radius of the averaging volume,  $R = 50 \text{ }\mu\text{m}$   
Mass transfer coefficient at the interface of the cell and liquid region in the averaging volume,  $P = 0.004 \text{ cm/s}$   
 $\alpha = (D_{\gamma}/L P) = 3.18$   
Equilibrium coefficient,  $K_{eq} = 1$   
 $k = (K_{eq} D_{\gamma}/D_{\beta}) = 0.48328$   
[Pathi et. al., 2005]

## **Reactor Parameters**

### *Static*

Matrix thickness,  $2l = 0.12 \text{ cm}$   
Liquid layer thickness,  $T = 0.6 \text{ cm}$   
Reactor Length,  $L = 10 \text{ cm}$   
Reactor Width,  $w = 2.5 \text{ cm}$

### *Perfusion*

Matrix thickness,  $2l = 0.12 \text{ cm}$   
Liquid layer thickness,  $T = 0.6 \text{ cm}$   
Reactor Length,  $L = 10 \text{ cm}$   
Reactor Width,  $w = 2.5 \text{ cm}$   
Flow rate/ chamber =  $0.1 \text{ ml/min} = 1.67 \cdot 10^{-3} \text{ cm}^3/\text{s}$   
Average velocity,  $v_{avg} = 1.11 \cdot 10^{-3} \text{ cm/s}$

### *Membrane characteristics*

FEP membrane  
Thickness =  $130 \text{ }\mu\text{m}$   
Length =  $10 \text{ cm}$   
Membrane permeability ( $Perm$ ) =  $1.343 \cdot 10^{-5} \text{ cm/s}$

**APPENDIX D: EXPERIMENTAL DATA [POTTER *ET AL.*, 1998]  
USED FOR MODEL VALIDATION IN CHAPTER 6**

<b>Week</b>	<b>0</b>	<b>1</b>	<b>2</b>	<b>3</b>	<b>4</b>
<b>Wet Wt (mg)</b>			241+/-6	311+/-7	328+/-3
<b>Dry Wt (mg)</b>			37+/-2	62+/-5	70+/-4
<b>Water Content (%)</b>			85+/-1	80+/-1	79+/-1
<b>Total Cell No. (10<sup>6</sup>)</b>	30		75+/-4	92+/-5	88+/-7
<b>Cell Area (μm<sup>2</sup>) 4πR<sub>c</sub><sup>2</sup></b>	139.68		148	160	188
<b>Cell Radius (μm) R<sub>c</sub></b>	3.335		3.43	3.57	3.87
<b>Cell Volume (μm<sup>3</sup>) V<sub>c</sub>=(4/3)πR<sub>c</sub><sup>3</sup></b>	155.3		169	190.5	242.66
<b>Cell Volume Fraction (ε<sub>c</sub>=V<sub>c</sub>/V)</b>	0.02123		0.0232154	0.0260953	0.0332368
<b>Total GAG (mg)</b>			16.6+/-1.8	21.1+/-2.1	22.6+/-1.8
<b>Total Collagen (mg)</b>			2.1+/-0.3	3.2+/-0.3	4.6+/-0.4
<b>Avg. MT</b>		0.45+/-1	0.60+/-0.01	0.62+/-0.002	0.71+/-0.01
<b>Avg. T1 (s)</b>		2.9+/-0.3	2.7+/-1	2.5+/-0.1	2.1+/-0.1
<b>Avg. T2 (ms)</b>		60+/-4	48+/-2	38+/-2	35+/-5
<b>Avg. D</b>		0.75	0.82	0.80	0.43

## APPENDIX E: LIST OF PARAMETERS USED FOR MODEL DEVELOPMENT IN CHAPTER 6

### Reactor Parameters

Flow rate = ~5ml/min – 14 ml/min (increased gradually in 10 days)

#### *Bioreactor Dimensions:*

Inner diameter,  $T = 4 \cdot 10^{-3}$  m

Height,  $H = 60 \cdot 10^{-3}$  m

Total Bioreactor Volume,  $BV = \pi \cdot (T/2)^2 \cdot H = 7.54 \cdot 10^{-7}$  m<sup>3</sup>

#### *Capillary Dimensions:*

Number of hollow/capillary fibers,  $fnum = 6$

Capillary Inner diameter,  $d0 = 330 \cdot 10^{-6}$  m

Capillary fiber wall thickness,  $wt0 = 150 \cdot 10^{-6}$  m

Capillary fiber radius,  $r0 = d0/2 + wt0 = 3.15 \cdot 10^{-4}$  m

Capillary fiber volume,  $fV = \pi \cdot (r0)^2 \cdot H = 1.87 \cdot 10^{-8}$  m<sup>3</sup>

Volume around a single fiber,  $BVf = BV/fnum = 1.26 \cdot 10^{-7}$  m<sup>3</sup>

Radius of the volume around single fiber,  $Tbf = (BVf/\pi H)^{1/2} = 8.18 \cdot 10^{-4}$  m

Volume available for tissue formation,  $BVtf = BVf - fV = 1.073 \cdot 10^{-7}$  m<sup>3</sup>

Radius of the available volume for cell growth,  $Tb = Tbf - r0 = 6.53 \cdot 10^{-4}$  m

### Transport Parameters

Water self diffusion coefficient,  $Dl = 2.25 \cdot 10^{-9}$  m<sup>2</sup>/s

Water diffusion coefficient in cellular phase,  $Dcw = Dl = 2.25 \cdot 10^{-9}$  m<sup>2</sup>/s

Oxygen diffusion coefficient in aqueous medium,  $Dl_{oxy} = 3.29 \cdot 10^{-9}$  m<sup>2</sup>/s

[Horner et al., 1998; Chow et al, 2000]

Oxygen diffusion coefficient through cells,  $Dcoxy = 1.50 \cdot 10^{-9}$  m<sup>2</sup>/s

[Chow et al, 2000; Obradovic, 2000]

Equilibrium coefficient of water between the cell 'c' and the ECM 'e' phases of the averaging volume,  $Keq^w = 1$

Equilibrium coefficient of oxygen between the cell 'c' and the ECM 'e' phases of the averaging volume,  $Keq = \text{oxygen solubility in lipids or membranes} / \text{oxygen solubility in water}$

= 4.387 [Chow et. al., 2001]



### *Averaging volume parameters*

Volume of averaging volume or unit cell,  $V$   
= (BVtf\*fnum)/Maximum cell number at 4 weeks)  
=  $7.316 * 10^{-15} \text{ m}^3$

Radius of the averaging volume,  $R = 1.203 * 10^{-5} \text{ m}$

Mass transfer coefficient at the interface of the cell and ECM phases in the averaging volume,  $P = 1 * 10^{-5} \text{ m/s}$

[Galban and Locke, 1999]

## **Cellular parameters**

### *Cell Metabolic parameters:*

Specific oxygen uptake rate,  $k_c = 1.86 * 10^{-2} \text{ 1/s}$

[Obradovic et. al., 2000; ratio of  $Q_{max}/K_m$ , the Michaelis-Menten parameters]

Mass transfer coefficient,  $K_m = 1 * 10^{-3} \text{ 1/s}$

### *Cell Growth parameters:*

Overall cell Contois parameter,  $K_{cont} = 1.13 * 10^1$

Overall cell growth coefficient,  $k_g = 3.78 * 10^{-7} \text{ 1/s}$

Cell death coefficient,  $k_{cd} = 1 * 10^{-8} \text{ 1/s}$

Initial cell seeding number,  $d_o = 3 * 10^7 \text{ cells}$

### *Cell proliferation parameters:*

Estimated cell mass at week 4,  $EstCellmass^{4wk}$

= Dry Wt. - (ECM+GAG) value at 4th week

=  $0.07 - (0.0226 + 0.0046) \text{ g}$

Maximum Available volume for cell growth, around a single fiber

=  $\pi \cdot (Tbf^2 - r0^2) \cdot H$

Maximum available volume for cell growth / Volume of an averaging volume

=  $n_{max} \text{ (single fiber)}$

=  $\frac{3 \cdot H \cdot (Tbf^2 - r0^2)}{4 \cdot R^3}$

Total number of averaging volumes,  $Total\_n = n_{max} * fnum$

Total cell volume at week 4,  $Totalcellvol^{4wk} = [\epsilon_c^{4wk}] * (V * Total\_n)$

Cell density,  $\rho_c = EstCellmass^{4wk} / Totalcellvol^{4wk}$

### *Total Cell Mass production coefficients*

Overall Contois parameter,  $K_p = 3.045 * 10^7 / rhoc$

Cell mass formation coefficient,  $k_p = 7.97143 * 10^{-6} \text{ 1/s}$

Total cell death coefficient,  $k_{pd} = 1.2 * 10^{-8} \text{ 1/s}$

### *Cell ECM parameters:*

GAG –

Specific fiber density =  $0.54 \text{ cm}^3/\text{g}$

[Baser et. al., 1998]

Density of GAG fibers,  $\rho_f = 1.85185 \cdot 10^6 \text{ g/m}^3$

GAG production coefficient,  $k_{GAG} = 2.52 \cdot 10^{-6} \text{ 1/s}$

GAG saturation coefficient,  $\epsilon_{GAG}^{max}$

$$= \frac{\text{GAGmass}^{4\text{wk}}}{\rho_f \cdot \text{Total\_n} \cdot V} = 0.019016$$

Binding coefficient of water to GAG,  $P_g^w = (7/10) \cdot 9 \cdot 10^{-5}$

Binding coefficient of oxygen to GAG,  $P_g^o = (7/10) \cdot 4 \cdot 10^{-5}$

[Penke et. al., 1998; Letnam, 1951]

*COLLAGEN* –

Specific collagen density =  $0.695 \text{ cm}^3/\text{g}$

[Baser et. al., 1998]

Density of collagen,  $\rho_{col} = 1.43885 \cdot 10^6 \text{ g/m}^3$

Overall ECM Collagen Saturation Constant,  $K_{ec} = 4 \cdot 10^7 / \rho_{col}$

ECM Collagen Production Coefficient,  $k_{em} = 3.975 \cdot 10^{-6} \text{ 1/s}$

Binding coefficient of water to collagen,  $P_{col}^w = (3/10) \cdot 9 \cdot 10^{-5}$

Binding coefficient of oxygen to collagen,  $P_{col}^o = (3/10) \cdot 4 \cdot 10^{-5}$

[Penke et. al., 1998; Letnam, 1951]

## APPENDIX F: COMPUTAION OF AVERAGE RADII OF FREE SPACE FOR WATER DIFFUSION IN *EX VIVO* CARTILAGE CULTURE IN HFBR

$$t = 10 \text{ ms}$$

$$Dl = 2.25 * 10^{-9} \text{ m}^2/\text{s}$$

$$\text{Water diffusion distance, } x = \sqrt{Dl \cdot t} = 4.74 * 10^{-6} \text{ m} = 4.74 \text{ } \mu\text{m}$$

**Time: 0 s**

Cell volume per fiber –

$$\text{Initial cell area} = 139.68 * 10^{-12} \text{ m}^2 = 4\pi R_c^2$$

$$\text{Radius of chondrocyte cell, } R_c = 3.33 * 10^{-6} \text{ m}$$

$$\text{Volume of a single chondrocyte cell, } V_c = (4/3)\pi R_c^3 = 154.74 * 10^{-18} \text{ m}^3$$

$$\text{No. of cells} = 30 * 10^6$$

$$\text{Total volume occupied by cells, } V_c^T = V_c * \text{No. of cells} = 4.64 * 10^{-9} \text{ m}^3$$

Collagen volume per fiber –

$$\text{Initial collagen volume fraction, } \epsilon_{col} = 0.0001 = V_{col}/V$$

$$V_{col} = 0.0001 * (7.316 * 10^{-15} \text{ m}^3) = 7.316 * 10^{-19} \text{ m}^3$$

$$\text{Total volume occupied by collagen} = V_{col}^T = V_{col} * \text{No. of cells} = 2.195 * 10^{-11} \text{ m}^3$$

GAG volume per fiber –

$$\text{Initial GAG volume fraction, } \epsilon_{GAG} = 0.0001 = V_{GAG}/V$$

$$V_{GAG} = 0.0001 * (7.316 * 10^{-15} \text{ m}^3) = 7.316 * 10^{-19} \text{ m}^3$$

$$\text{Total volume occupied by GAG} = V_{GAG}^T = V_{GAG} * \text{No. of cells} = 2.195 * 10^{-11} \text{ m}^3$$

Total available volume for tissue formation around a single fiber,  $V^T$

$$= (\text{BVf} - fV) * \text{fnum} = 1.073 * 10^{-7} * 6 \text{ m}^3$$

Volume of void phase,  $V_I = V^T - (V_c^T + V_{col}^T + V_{GAG}^T)$

$$= (1.073 * 10^{-7} * 6) - (4.64 * 10^{-9} + 2.915 * 10^{-11} + 2.915 * 10^{-11}) \sim 6.3912 * 10^{-7} \text{ m}^3$$

Representative volume of void phase,  $V_1^{rep} = (V_1 / \text{No. of cells}) \sim = 2.13 * 10^{-14} \text{ m}^3$

Assuming spherical geometry, radii of free space available for water diffusion,  $R_{free-space}$   
 $\sim = 1.719 * 10^{-5} \text{ m} = \mathbf{17.19 \mu m} \gg x (= 4.74 \mu m)$

Similarly calculations are done for free space radii from weeks 1 to 4 as shown below.

Time (wk)	No. of averaging volumes (N)	Volume occupied by the tissue $V_{tissue} = N * \text{Volume of a single unit cell (V)}$
1	$5.24 * 10^7$	$3.834 * 10^{-7}$
2	$7.10 * 10^7$	$5.194 * 10^{-7}$
3	$8.45 * 10^7$	$6.182 * 10^{-7}$
4	$9.29 * 10^7$	$6.797 * 10^{-7}$

Time (wk)	Cell volume fraction $\epsilon_c$	Total Volume of cells ( $V_c^T = \epsilon_c * N * V$ ) ( $\text{m}^3$ )
1	$5.24 * 10^7$	$8.4531 * 10^{-9}$
2	$7.10 * 10^7$	$1.2451 * 10^{-8}$
3	$8.45 * 10^7$	$1.6908 * 10^{-8}$
4	$9.29 * 10^7$	$2.1919 * 10^{-8}$

Time (wk)	Cell volume fraction $\epsilon_{col}$	Total Volume of Collagen ( $V_{col}^T = \epsilon_{col} * N * V$ ) ( $\text{m}^3$ )
1	$5.24 * 10^7$	$2.5187 * 10^{-10}$
2	$7.10 * 10^7$	$8.9343 * 10^{-10}$
3	$8.45 * 10^7$	$1.9072 * 10^{-10}$
4	$9.29 * 10^7$	$3.1400 * 10^{-10}$

Time (wk)	GAG volume fraction $\epsilon_{GAG}$	Total Volume of GAG ( $V_{GAG}^T = \epsilon_{GAG} * N * V$ ) ( $\text{m}^3$ )
1	$5.24 * 10^7$	$2.9135 * 10^{-9}$
2	$7.10 * 10^7$	$7.6877 * 10^{-9}$
3	$8.45 * 10^7$	$1.2302 * 10^{-8}$
4	$9.29 * 10^7$	$1.5700 * 10^{-8}$

Time (wk)	Volume of Void Phase $V_1 = V_{tissue} - (V_c^T + V_{col}^T + V_{GAG}^T)$ ( $\text{m}^3$ )	Representative volume of void phase, $V_1^{rep} = V_1 / N$ ( $\text{m}^3$ )	Radii of free space available for water diffusion [ $R_{free-space}$ ] ( $\mu\text{m}$ )
1	$3.71782 * 10^{-7}$	$7.09508 * 10^{-15}$	<b>11.919</b>
2	$4.98368 * 10^{-7}$	$7.01927 * 10^{-15}$	<b>11.876</b>
3	$5.87083 * 10^{-7}$	$6.94773 * 10^{-15}$	<b>11.836</b>
4	$6.38941 * 10^{-7}$	$6.87773 * 10^{-15}$	<b>11.796</b>

## APPENDIX G: LIST OF PARAMETERS USED IN CHAPTER 7

Parameter type	Parameter	White Small Fiber	White Large Fiber	Dark Fiber	Units
<b>Initial concentrations</b>	AP	34.3	34.3	15	mmoles/L
	Arginine	0.47	0.47	1.58	mmoles/L
	P <sub>i</sub>	4.88	4.88	5	mmoles/L
	ATP	8.6	8.6	3.7	mmoles/L
	ADP	0.003	0.003	0.01	mmoles/L
<b>Diffusion</b>	$D_{AP}$	$2.20 \times 10^{-6}$	$1.00 \times 10^{-6}$	$1.00 \times 10^{-6}$	cm <sup>2</sup> /s
	$D_{Arg}$	$2.79 \times 10^{-6}$	$1.27 \times 10^{-6}$	$1.27 \times 10^{-6}$	cm <sup>2</sup> /s
	$D_{P_i}$	$3.56 \times 10^{-6}$	$1.62 \times 10^{-6}$	$1.62 \times 10^{-6}$	cm <sup>2</sup> /s
	$D_{ATP}$	$1.54 \times 10^{-6}$	$0.70 \times 10^{-6}$	$0.70 \times 10^{-6}$	cm <sup>2</sup> /s
	$D_{ADP}$	$1.75 \times 10^{-6}$	$0.79 \times 10^{-6}$	$0.79 \times 10^{-6}$	cm <sup>2</sup> /s
	$\lambda/2$	2.73	300	18	μm
<b>Mitochondrial boundary reaction</b>	$V_{mmito}$	$1.9 \times 10^{-17}$	$1.67 \times 10^{-15}$	$4.315 \times 10^{-14}$	mmoles/μm <sup>2</sup> /s
	$K_{mmito}$	20	20	20	μmoles/L
<b>Basal ATPase</b>	$V_{mbas}$	11.75	11.75	182.7	μmoles/L/s
	$K_{mbas}$	100	100	10	mmoles/L
<b>Arginine kinase reaction</b>	$V_{mAKfor}$	611	611	331.8	mmoles/L/s
	$V_{mAKrev}$	39	39	21.15	mmoles/L/s
	$K_{ATP}$	0.32	0.32	0.32	mmoles/L
	$K_{Arg}$	0.75	0.75	0.75	mmoles/L
	$K_{AP}$	3.82	3.82	3.82	mmoles/L
	$K_{ADP}$	0.40	0.40	0.40	mmoles/L
	$K_{iATP}$	0.34	0.34	0.34	mmoles/L
	$K_{iArg}$	0.81	0.81	0.81	mmoles/L
	$K_{iAP}$	0.26	0.26	0.26	mmoles/L

Parameter type	Parameter	White Small Fiber	White Large Fiber	Dark Fiber	Units
Arginine kinase reaction	$K_{iADP}$	0.024	0.024	0.024	mmoles/L
	$K_{IATP}$	2.43	2.43	2.43	mmoles/L
	$K_{IArg}$	3.45	3.45	3.45	mmoles/L
Myosin ATPase	$V_{mmyo}$	6.92	6.92	3.81	mmoles/L/s
	$K_{mmyo}$	0.15	0.15	0.15	mmoles/L

## APPENDIX H: PERMISSION FROM JOHN WILEY & SONS, INC.

John Wiley & Sons, Inc.

Publishers Since 1807  
Dear Pragyanshi Pathi:



SCIENTIFIC, TECHNICAL,  
AND MEDICAL PUBLISHING  
111 River Street  
Hoboken, NJ 07030  
www.wiley.com  
TEL 201.748.6000  
FAX 201.746.8800


Thank you for your recent request. We grant you the following rights in your Contribution to **Biotechnology & Bioengineering 2005, Volume 89, Issue 7 and Pages 743-758**.

1. The right to share with colleagues print or electronic "preprints" of the unpublished Contribution, in form and content as accepted by Wiley for publication in the Journal. Such preprints may be posted as electronic files on your own website for personal or professional use, or on your internal university or corporate networks/intranet, or secure external website at your institution, but not for commercial sale or for any systematic external distribution by a third party (e.g., a listserve or database connected to a public access server). Prior to publication, you must include the following notice on the preprint: "This is a preprint of an article accepted for publication in **Biotechnology & Bioengineering** © copyright 2005 Wiley Periodicals, Inc., A Wiley Company)". After publication of the Contribution by Wiley, the preprint notice should be amended to read as follows: "This is a preprint of an article published in **Biotechnology & Bioengineering 2005, Volume 89, Issue 7 and Pages 743-758**", and should provide an electronic link to the Journal's WWW site, located at the following Wiley URL: <http://www.interscience.Wiley.com/>. You agree not to update the preprint or replace it with the published version of the Contribution.
2. The right, without charge, to photocopy or to transmit online or to download, print out and distribute to a colleague a copy of the published Contribution in whole or in part, for your personal or professional use, for the advancement of scholarly or scientific research or study, or for corporate informational purposes.
3. The right to republish, without charge, in print format, all or part of the material from the published Contribution in a book written or edited by you.
4. The right to use selected figures and tables, and selected text (up to 250 words, exclusive of the abstract) from the Contribution, for your own teaching purposes, or for incorporation within another work by you that is made part of an edited work published (in print or electronic format) by a third party, or for presentation in electronic format on an internal computer network or external website of yours or your employer.
5. The right to include the Contribution in a compilation for classroom use (course packs) to be distributed to students at your institution free of charge or to be stored in electronic format in datarooms for access by students at your institution as part of their course work (sometimes called "electronic reserve rooms") and for in-house training programs at your employer.

Please include the following notice: **Biotechnology & Bioengineering** © copyright 2005 Wiley Periodicals, Inc., A Wiley Company.

Please retain this letter for any future uses you may wish to make of your Contribution that are covered by the above grant of rights and for which no additional correspondence is needed.

Sincerely,

  
Rachel Smaltz  
Electronic Permissions

## REFERENCES

- Abkowitz, J. L., Golinelli, D., Harrison, D. E., and Gutter, P., "In vivo kinetics of murine hematopoietic stem cells", *Blood*, Vol. 96(10), 3399 (2000)
- Aliev, M. K. and Saks, V., "Compartmentalized energy transfer in cardiomyocytes: use of mathematical modeling for analysis of in vivo regulation of respiration", *Biophys. J.*, Vol. 73, 428 (1997)
- Annabi, B., Lee, Y. T, Turcotte, S., Naud, E., Desrosiers, R. R., Champagne, M., Eliopoulos, N., Galipeau, J., and Beliveau, R., "Hypoxia promotes murine bone-marrow-derived stromal cell migration and tube formation", *Stem Cells*, Vol. 21, 337 (2003)
- Baldwin, J., Gupta, A. and Iglesias, X., "Scaling of anaerobic energy metabolism during tail flipping behavior in the freshwater crayfish", *Cherax destructor. Mar. Freshwater Res.*, Vol. 50, 183 (1999)
- Baser P. J., R. Schneiderman, R. A. Bank, E. Wachtel, and A. Maroudas, "Mechanical Properties of the Collagen Network in Human Articular Cartilage as Measured by Osmotic Stress Techniques", *Archives of Biochemistry*, Vol. 351 (2), 207 (1998)
- Bailey, J. E., Ollis D. F., "Biochemical engineering fundamentals", Second edition, 1986, McGraw-Hill Book Company
- Bailey, J., "Mathematical modeling and analysis in biochemical engineering: past accomplishments and future opportunities", *Biotechnology Progress*, Vol. 14, 8 (1998)
- Beard, D. A., "Biophysical Model of Oxidative Phosphorylation", *PLOS Computational Biology*, *In Review* (2005)
- Bhatia, M., Bonnet, D., Kapp, U., Wang J. C. Y., Murdoch, B., and Dick, J. E., "Quantitative analysis reveals expansion of human hematopoietic repopulation cells after short-term ex vivo culture", *J. Exp. Med.*, Vol. 186(4), 619 (1997)
- Booth, C. E. and McMahon, B. R., "Lactate dynamics during locomotor activity in the blue crab, *Callinectes sapidus*", *J. Exp. Biol.*, Vol. 118, 461 (1985)



- Boyle, K. L., Dillaman, R. M. and Kinsey, S. T., "Mitochondrial distribution and glycogen dynamics suggest diffusion constraints in muscle fibers of the blue crab, *Callinectes sapidus*", *J. Exp. Zool.*, Vol. 297A, 1 (2003)
- Buckwalter, J.A., and Mankin, H.J., "Articular Cartilage. Part I: tissue design and chondrocyte-matrix interactions", *J. Bone Joint Surgery*, Vol. 79-A, 600 (1997)
- Bursac, P.M., L.E. Freed, R.J.Biron and G. Vunjak-Novakovic, "Mass Transfer Studies of Tissue Engineered Cartilage", *Tissue Engineering*, Vol. 2, 141 (1996)
- Cabrita, G. J. M., Ferreira, B. S., Silva, C. L., Goncalves, R., Porada, G. A., and Cabral, J. M. S., "Hematopoietic stem cells: from the bone to the bioreactor", *TRENDS in Biotechnology*, Vol. 21(5), 233 (2003)
- Carbonell, R. G., Whitaker, S., "Heat and mass transport in porous media", In: Bear J, Corapcioglu M Y, editors. *Mechanics of Fluids in porous media*. Brussels:Martinus Nijhoff. (1984)
- Chen, C. P., and Aplin, J. D., "Placental extracellular matrix: Gene expression, deposition by placental fibroblasts and the effect of oxygen", *Placenta*, Vol. 24, 316 (2003)
- Chen, J. L., Li, Y., Zhang, R. L., Katakowski, M., Gautam, S. C., Xu, Y. X., Lu, M., Zhang, Z. G., Chopp, M., "Combination therapy of stroke in rats with a nitric oxide donor and human bone marrow stromal cells enhances angiogenesis and neurogenesis", *Brain Res*, Vol. 1005, 21-28 (2004)
- Chen, J. L., Zhang, Z. G., Li, Y., Wang, L., Xu, Y. X., Gautam, S. C., Lu, M., Zhu, Z., Chopp, M., "Intravenous administration of human bone marrow stromal cells induces angiogenesis in the ischemic boundary zone after stroke in rats", *Circ Res*, Vol. 92, 692-699 (2003)
- Chow, D. C., Wenning, L. A., Miller, W. M., and Papoutsakis, E. T., "Modeling pO<sub>2</sub> distributions in the bone marrow hematopoietic compartment I. Krogh's Model", *Biophysical Journal*, Vol. 81(2), 675 (2001 a)
- Chow, D. C., Wenning, L. A., Miller, W. M., and Papoutsakis, E. T., "Modeling pO<sub>2</sub> distributions in the bone marrow hematopoietic compartment II. Modified Krogh's Models", *Biophysical Journal*, Vol. 81(2), 685 (2001 b)
- Cipolleschi, M. G., Sbarba, P. D., and Olivotto, M., "The role of hypoxia in the maintenance of hematopoietic stem cells", *Blood*, Vol. 7, 2031 (1993)
- Collins, P. C., Nielsen, L. K., Wong, C. K., Papoutsakis, E. T., and Miller, W. M., "Real-time method for determining the colony-forming cell content of human hematopoietic cell cultures", *Biotechnology and Bioengineering*, Vol. 55(4), 693 (1997)

- Collins, P. C., Nielsen, L. K., Patel, S. D., Papoutsakis, E. T., and Miller, W. M., "Characterization of hematopoietic cell expansion, oxygen uptake, and glycolysis in a controlled, stirred tank bioreactor system", *Biotechnol. Prog.*, Vol. 14, 466 (1998)
- Contois, D. E., "Kinetics of Bacterial Growth: Relationship between Population Density and Specific Growth Rate of Continuous Cultures. *J. Gen. Microbiol.*, 21:40-50 (1959)
- Crow, M. T., and Kushmerick, M. J., "Chemical energetics of slow- and fast-twitch muscles of the mouse", *J. Gen. Physiol.*, Vol. 79, 147 (1982)
- Damas, N. M., Rodriguez, J. M., Carmona, M., Gonzalez, M., and Prieto, J., "Ex-vivo expansion and maturation of CD34-positive hematopoietic progenitors optimization of culture conditions", *Leukemia Research*, Vol. 23, 1035 (1999)
- Danckwerts, P. V., "Continuous flow systems", *Chemical Engineering Science*, Vol. 2, 1 (1953)
- de Graaf, R. A., van Kranenburg, A. and Nicolay, K., "In vivo <sup>31</sup>P-NMR diffusion spectroscopy of ATP and phosphocreatine in rat skeletal muscle", *Biophys. J.*, Vol. 78, 1657 (2000)
- Dimicco MA, Sah RL., "Dependence of Cartilage Matrix Composition on Biosynthesis, Diffusion, and Reaction", *Transport in Porous Media*, Vol. 50, 57 (2003)
- Duggan, O., Hyland, P., Annett, K., Freeburn, R., Barnett, C., Pawelec, G., and Barnett, Y., "Effects of a reduced oxygen tension culture system on human T cell clones as a function of in vitro age", *Exp Gerontol*, Vol. 39, 525 (2004)
- Ellington, W.R. and Kinsey, S.T., "Functional and evolutionary implications of the distribution of phosphagens in primitive-type spermatozoa", *Biol. Bull.*, Vol. 195, 264 (1998)
- Ellington, W.R., "Evolution and physiological roles of phosphagen systems", *Ann. Rev. Physiol.*, Vol. 63, 289 (2001)
- Ellis, S. J., M. Velayutham, S. Sendhil Velan, E. F. Peterson, J. L. Zweier, P. Kuppusamy, and R. G. Spencer, "EPR Oxygen Mapping (EPROM) of Engineered Cartilage Growth in a Hollow-Fiber Bioreactor", *Magnetic Resonance in Medicine*, Vol. 46, 819 (2001)
- Forgue, J., Legeay, A. and Massabuau, J. C., "Is the resting rate of oxygen consumption of locomotor muscles in crustaceans limited by the low blood oxygenation strategy?", *J. Exp. Biol.*, Vol. 204, 933 (2001)
- Freed, L. E., J. C. Marquis, G. Vunjak-Novakovic, J. Emmanuel, A. G. Mikos, and R. Langer, "Composition of Cell-Polymer Cartilage Implants," *Biotechnology and Bioengineering*, Vol. 43, 605 (1994a)
- Freed, L. E., G. Vunjak-Novakovic, J. C. Marquis, and R. Langer, "Kinetics of Chondrocyte Growth in Cell-Polymer Implants," *Biotechnology and Bioengineering*, Vol. 43, 597 (1994b)

- Freed, L.E., G. Vunjak-Novakovic, "Tissue Culture Bioreactors," Principles of Tissue Engineering, R.P.Lanza, R.Langer, and W.Chick, eds., 2<sup>nd</sup> ed., Academic Press, San Diego, CA, 143 (2000b)
- Galban, C.J., Locke, B. R., "Analysis of Cell Growth in a Polymer Scaffold Using a Moving Boundary Approach", Biotechnology and Bioengineering, Vol. 56 (4), 422 (1997)
- Galban, C.J., Locke, B. R., "Effects of spatial variation of cells and nutrient and product concentrations coupled with product inhibition on cell growth in a polymer scaffold", Biotechnology and Bioengineering, Vol. 64(6), 633 (1999 a)
- Galban, C.J., Locke, B. R., "Analysis of cell growth kinetics and substrate diffusion in a polymer scaffold", Biotechnology and Bioengineering, Vol. 65(2), 121 (1999 b)
- Gannon, A. T. and Wheatly, M. G., "Physiological effects of a gill barnacle on host blue crabs during short-term exercise and recovery", Mar. Behav. Physiol., Vol. 24, 215 (1995)
- Gebb, S. A.. and Jones, P. L., "Hypoxia and lung branching morphogenesis", Adv Exp Med Biol, Vol. 543, 117-125 (2003)
- Green, J. E. F., Byrne, H. M., Walters, S. L., and Shakesheff, K. M., "Mathematical modeling in tissue engineering", European Cells and Materials, Vol. 6, Suppl. 2, 38 (2003)
- Grayson, W. L., Ma, T., and Bunnell, B., "Human mesenchymal stem cells tissue development in 3D PET matrices", Biotechnol Prog, Vol. 20, 905 (2004)
- Grimshaw, M.J., R.M.Mason, "Bovine articular chondrocyte function in vitro depends upon oxygen tension", Osteoarthritis and Cartilage, Vol. 8, 386 (2000)
- Groebe, K. and Thews, G., "Calculated intra- and extracellular gradients in heavily working red muscle", Am. J. Physiol. Heart Circ. Physiol., Vol. 259, H84 (1990)
- Hascall, V.C., J.D.Sandy, and C.J.Handley, "Regulation of Proteoglycan Metabolism in Articular Cartilage", Biology of the Synovial Joint, C.W.Archer, ed., Ch 7, Harwood Academic Publishers, Amsterdam (1999)
- Heidemann, R., Lutkeymeyer, D., Lehmann, J., "Effects of dissolved oxygen levels and role of extra- and intracellular amino acid concentrations upon metabolism of mammalian cell lines during batch and continuous cultures", Cytotechnol., Vol. 26, 185 (1998)
- Head, G., and Baldwin, J., "Energy metabolism and the fate of lactate during recovery from exercise in the Australian freshwater crayfish, *Cherax destructor*." Aust. J. Mar. Freshw. Res., Vol. 37, 641 (1986)

- Henry, R. P., Booth, C. E., Lallier, F. H. and Walsh, P. J., "Post-exercise lactate production and metabolism in three species of aquatic and terrestrial decapod crustaceans". *J. Exp. Biol.*, Vol. 186, 215 (1994)
- Hevehan, D. L., Papoutsakis, E. T., and Miller, W. M., "Physiologically significant effects of pH and oxygen tension on granulopoiesis", *Experimental Hematology*, Vol. 28, 267 (2000)
- Hevehan, D. L., Wenning, L. A., Miller, W. M., and Papoutsakis, E. T., "Dynamic model of ex vivo granulocytic kinetics to examine the effects of oxygen tension, pH, and interleukin-3", *Experimental Hematology*, Vol. 28, 1016 (2000)
- Hogan, M. C., Stary, C. M., Balaban, R. S. and Combs, C. A., "NAD(P)H fluorescence imaging of mitochondrial metabolism in contracting *Xenopus* skeletal muscle fibers: effect of oxygen availability", *J. Appl. Physiol.* (2004) [e-pub ahead of print].
- Horner, M., Miller, W. M., Ottino, J. M., and Papoutsakis E. T., "Transport in a grooved perfusion flat-bed bioreactor for cell therapy applications", *Biotechnol. Prog.* Vol. 14, 689 (1998)
- Horwitz, E. M., Prockop, D. J., Fitzpartick, L. A., Koo, W. W., Gordonm, P. L., Neel, M., Sussman, M., Orchard, P., Marx, J. C., Pyeritz, R. E., and Brenner, M. K., "Transplantability and therapeutic effects of bone marrow-derived mesenchymal cells in children with osteogenesis imperfecta", *Nature Med*, Vol. 5, 309-313 (1999)
- Hubleby, M. J., Locke, B. R., and Moerland, T. S., "Reaction-diffusion analysis of effects of temperature on high-energy phosphate dynamics in goldfish skeletal muscle", *J. Exp. Biol.*, Vol. 200, 975 (1997)
- Ishikawa, Y., and Ito, T., "Kinetics of hematopoietic stem cells in a hypoxic culture". *Eur J Haematol*, Vol. 40, 126 (1998)
- Jeneson, J. A. L., Westerhoff, H. V., Brown, T. R., van Echteld, C. J. A. and Berger, R., "Quasi-linear relationship between Gibbs free energy of ATP hydrolysis and power output in human forearm muscle", *Am. J. Physiol. Cell Physiol.*, Vol. 268, C1474 (1995)
- Jeneson, J. A. L., Wiseman, R. W., Westerhoff, H. V., and Kushmerick, M. J., "The signal transduction function for oxidative phosphorylation is at least second order in ADP", *J. Biol. Chem.*, Vol. 271(45), 27995 (1996)
- Jiang, B., Semenza, G. L., Bauer, C., Marti, H. H., "Hypoxia Inducible Factor 1 levels vary exponentially over a physiologically relevant range of O<sub>2</sub> Tension", *Am J Phys.*, Vol. 271, C1172 – C 1180 (1996)
- Johnson, L. K., Dillaman, R. M., Gay, D. M., Blum, J. E. and Kinsey, S. T., "Metabolic influences of fiber size in aerobic and anaerobic muscles of the blue crab, *Callinectes sapidus*", *J. Exp. Biol.*, Vol. 207, 4045 (2004)

Johnston, I. A., Fernández, D. A., Calvo, J., Vieira, V. L. A., North, A. W., Abercromby, M. and Garland, T., Jr., “Reduction in muscle fiber number during the adaptive radiation of notothenioid fishes: a phylogenetic perspective”, *J. Exp. Biol.*, Vol. 206, 2595 (2003)

Johnston, I. A., Abercromby, M., Vieira, V. L. A., Sigursteindóttir, R. J., Kristjánsson, B. K., Sibthorpe, D. and Skúlason, S., “Rapid evolution of muscle fiber number in post-glacial populations of charr *Salvelinus alpinus*”, *J. Exp. Biol.*, Vol. 207, 4343 (2004)

Kemp, G. J., Manners, D. N., Clark, J. F., Bastin, M. E. and Radda, G. K., “Theoretical modeling of some spatial and temporal aspects of the mitochondrion/creatine kinase/myofibril system in muscle”, *Mol. Cell. Biochem.*, Vol. 184, 249 (1998)

Kim JH, Ochoa JA, Whitaker S. 1987, “Diffusion in Anisotropic Porous Media”, *Transport in porous Media*, Vol. 2, 327 (1987)

Kinsey, S. T. and Ellington, W. R., “<sup>1</sup>H- and <sup>31</sup>P-Nuclear magnetic resonance studies of L-lactate transport in isolated muscle fibers from the spiny lobster, *Panulirus argus*”, *J. Exp. Biol.*, Vol. 199, 2225 (1996)

Kinsey, S. T., Penke, B., Locke, B. R. and Moerland, T. S., “Diffusional anisotropy is induced by subcellular barriers in skeletal muscle”, *NMR Biomed.*, Vol. 11, 1 (1999)

Kinsey, S.T. and Moerland, T.S., “Metabolite diffusion in giant muscle fibers of the spiny lobster”, *Panulirus argus*. *J. Exp. Biol.*, Vol. 205, 3377 (2002)

Kinsey, S. T., Pathi, P., Hardy, K. M., Jordan, A., and Locke, B. R., “Does Intracellular metabolite Diffusion Limit Post-Contractile Recovery in Burst Locomotor Muscle”, *Journal of Experimental Biology*, In Press (2005)

Koller, M. R., Bender, J. G., Miller, W. M., and Papoutsakis, E. T., “Reduced oxygen tension increases hematopoiesis in long-term culture of human stem and progenitor cells from cord blood and bone marrow”, *Exp. Hematol*, Vol. 20, 264 (1992)

Koller, M. R., Bender, J. G., Miller, W. M., and Papoutsakis, E. T., “Expansion of primitive human hematopoietic progenitors in a perfusion bioreactor system with IL-3, IL-6, and stem cell factor”, *Bio/Technology*, Vol. 11, 358 (1993a)

Koller, M. R., Emerson, S. G., and Palsson, B., “Large-scale expansion of human stem and progenitor cells from bone marrow mononuclear cells in continuous perfusion cultures”, *Blood*, Vol. 82(2), 378-384 (1993b)

Koller, M. R., and Palsson B., “Tissue engineering: Reconstitution of human hematopoiesis ex vivo”, *Biotechnology and Bioengineering*, Vol. 42, 909 (1993c)

Koller, M. R., Manchel, I., Palsson, M. A., Maher, R. J., and Palsson, B., "Different measures of human hematopoietic cell culture performance are optimized under vastly different conditions", *Biotechnology and Bioengineering*, Vol. 50, 505 (1996)

Korzeniewski, B., "Regulation of oxidative phosphorylation in different muscles and various experimental conditions", *Biochem. J.*, Vol. 375, 799 (2003)

Laluppa, J. A., Papoutsakis, E. T., and Miller, W. M., "Oxygen tension alters the effects of cytokines on the megakaryocyte, erythrocyte, and granulocyte lineages", *Experimental Hematology*, Vol. 26, 835 (1998)

Langer, R., Vacanti, J. P., "Tissue Engineering", *Science*, 920-926 (1993)

Lee, R. B., Urban, J. P. G., "Evidence for a negative Pasteur effect in articular cartilage", *Biochemical J.*, Vol. 321, 95 (1997)

Letnam, M. C. 1951. Adsorption. McGraw-Hill, New York

Li, Y., Ma, T., Kniss, D. A., Yang, S. T., and Lasky, L. C. "Human cord cell hematopoiesis in three-dimensional nonwoven fibrous matrices: In vitro simulation of the marrow microenvironment", *Journal of Hematotherapy & Stem Cell Research*, Vol. 10, 355 (2001)

Li, Y. J., Batra, N. N., You, L., Meier, S. C., Coe, I. A., Yellowley, C. E., Jacobs, C. R., "Oscillatory fluid flow affects human marrow stromal cell proliferation and differentiation", *J Orthop Res*, Vol. 22, 1283 (2004)

Locke, B. R., "Electro-transport in hydrophilic nanostructured materials", Chapter 15, 527, *Nano-Surface Chemistry*, Marcel Dekker, Inc., New York

Mahaffy, J. M., Belair, J., and Mackey, M. C., "Hematopoietic model with moving boundary conditions and state dependent delay: Applications in erythropoiesis", *J. Theor. Biol.*, Vol. 190, 135 (1998)

Mainwood, G.W., and Raukusan, K., "A model for intracellular energy transport", *Can. J. Physiol. Pharmacol.*, Vol. 60, 98 (1982)

Malda, J., Rouwkema, J., Martens, D. E., Comte, E. P. Le, Kooy, F. K., Tramper, J., Blitterswijk, C. A. van, Riesle, J., "Oxygen Gradients in Tissue-Engineered PEGT/PBT Cartilaginous Constructs: Measurement and Modeling", *Biotechnology and Bioengineering*, Vol. 86 (1), 9 (2004)

Mantalaris, A., Keng, P., Bourne, P., Chang, A. Y. C., and Wu, J. H. D., "Engineering a human bone marrow model: A case study on ex vivo erythropoiesis", *Biotechnol. Prog.*, Vol. 14, 126 (1998)

- Martin, I., B. Obradovic, L. E. Freed, G. Vunjak-Novakovic, "Method for Quantitative Analysis of Glycosaminoglycan Distribution in Cultured Natural and Engineering Cartilage," *Annals of Biomedical Engineering*, Vol. 27, 656 (1999)
- Martin, I. B., Wendt, D., and Heberer, M., "The Role of Bioreactors in Tissue Engineering", *Trends in Biotechnology*, Vol. 22 (2), 80 (2004)
- McAdams, T., A. Miller, W., M., and Papoutsakis, E. T., "Hematopoietic cell culture therapies (Part I): cell culture considerations", *TIBTECH*, 14 (1996)
- MacArthur, B. D., and Oreffo, R. O. C., "Concept Bridging the gap", *Nature*, Vol. 433, 19 (2005)
- Meinel, L., Karageorgiou, V., Fajardo, R., Snyder, B., Shinde-Patil, V., Zichner, L., Kaplan, D., Langer, R., Vunjak-Novakovic, G., "Bone tissue engineering using human mesenchymal stem cells: Effects of scaffold material and medium flow", *Ann Biomed. Eng.*, Vol. 32, 112 (2004)
- Meyer, R. A., Sweeney, H. L. and Kushmerick, M. J., "A simple analysis of the 'phosphocreatine shuttle'", *Am. J. Physiol.*, Vol. 246, C365 (1984)
- Meyer, R.A., "A linear model of muscle respiration explains monoexponential phosphocreatine changes", *Am. J. Physiol.*, Vol. 254, C548 (1988)
- Middleman, S., "An Introduction to mass and heat transfer: Principal of analysis and design", John Wiley & Sons, Inc., (1998)
- Milligan C. L., Walsh P. J., Booth C. E. and McDonald D. L. (1989), "Intracellular acid-base regulation during recovery from locomotor activity in the blue crab, *Callinectes sapidus*", *Physiol. Zool.*, Vol. 62, 621 (1989)
- Mitchell, S. A., Poulsson, A. H. C., Davidson, M. R., Emmison, N., Shard, A. G., and Bradley, R. H., "Cellular attachment and spatial control of cells using micro-patterned ultra-violet/ozone treatment in serum enriched media", *Biomaterials*, Vol. 25, 4079-4086 (2004)
- Mostafa, S. S., Miller, W. M., and Papoutsakis, E. T., "Oxygen tension influences the differentiation, maturation and apoptosis of human megakaryocytes", *British Journal of Haematology*, Vol. 111, 879 (2000)
- Mow, V.C., W.C.Hayes (Eds.), "Basic Orthopaedic Biomechanics", 2<sup>nd</sup> ed., Lippincott-Raven Publishers, PA, 113-117 (1997)
- Nevo, A. C. and Rikmenspoel, R., "Diffusion of ATP in sperm flagella", *J. Theor. Biol.* 26, 11 (1970)
- Nielsen, L. K., "Bioreactors for hematopoietic cell culture", *Annu. Rev. Biomed. Eng.*, Vol. 1, 129 (1999)

Nielsen, L. K., Papoutsakis, E. T., and Miller, W. M., "Modeling ex vivo hematopoiesis using chemical engineering metaphors", *Chemical Engineering Science*, Vol. 53(10), 1913 (1988)

NIST/SEMATECH e-Handbook of Statistical Methods,  
[<http://www.itl.nist.gov/div898/handbook/>, section 4.1.4.1]

Nordin M, Frankel VH., "Basic Biomechanics of the Musculoskeletal System", 2<sup>nd</sup> ed. Lee & Febiger, PA, USA. 36 (1989)

Obradovic, B., Carrier, R. L., G.Vunjak-Novakovic, and Freed, L. E., "Gas Exchange is Essential for Bioreactor Cultivation of Tissue Engineered Cartilage," *Biotechnology and Bioengineering*, Vol. 63 (2), 197 (1999)

Obradovic, B., Meldon, J. H., Freed, L. E., and G.Vunjak-Novakovic, "Glycosaminoglycan Deposition in Engineered Cartilage: Experiments and Mathematical Model," *AIChE. J.*, Vol. 46(9), 1860 (2000)

Ochoa, J., "Diffusion and reaction in heterogeneous media", Ph.D. Dissertation, University California Davis, (1988)

Oh, D. J., Koller, M. R., and Palsson, B. O., "Frequent harvesting from perfused bone marrow cultures results in increased overall cell and progenitor expansion", *Biotechnology and Bioengineering*, Vol. 44, 609 (1994)

Orlic, D., Kajstura, J., Chimenti, S., Jakoniuk, I., Anderson; S. M., Li, B. S., Pickel, J., McKay, R., Nadal-Ginard, B., Bodine, D. M., Leri, A., and Anversa, P., "Bone marrow cells regenerate infarcted myocardium", *Nature*, Vol. 410, 701 (2001)

Palsson, B. O., Paek, S. H., Schwartz, R. M., Palsson, M., Lee, G. M., Silver, S., and Emerson, S. G., "Expansion of human bone marrow progenitor cells in a high cell density continuous perfusion system", *Bio/Technology*, Vol. 11, 368 (1993)

Park, J. S., Chu, J. S. F., Cheng, C., Chen, F., Chen, D., Li, S., "Differential effects of equiaxial and uniaxial strain on mesenchymal stem cells", *Biotechnol Bioeng*, Vol. 88, 359 (2004)

Pate, E. and Cooke, R., "The inhibition of muscle contraction by adenosine 5' ( $\beta$ ,  $\gamma$ -imido) triphosphate and by pyrophosphate", *Biophys. J.*, Vol. 47, 773 (1985)

Patel, S. D., Miller, W. M., Winter, J. N., and Papoutsakis, E. T., "Cell density-dependent proliferation in frequently-fed peripheral blood mononuclear cell cultures", *Cytotherapy*, Vol. 2(4), 267 (2000)

Patel, S. D., Papoutsakis, E. T., Winter, J. N., and Miller, W. M., "The Lactate issue revisited: Novel feeding protocols to examine inhibition of cell proliferation and glucose metabolism in hematopoietic cell cultures", *Biotechnol. Prog.*, Vol. 16, 885 (2000)



- Pathi, P., Ma, T., and Locke, B. R., "Role of nutrient supply on cell growth in bioreactor design for tissue engineering of hematopoietic cells", *Biotechnology and Bioengineering*, Vol. 89, 743 (2005 a)
- Pathi, P., Galban, C. J., Spencer, R. G., Locke, B. R., "Analysis of Tissue Growth and Extracellular Matrix Formation in a Hollow Fiber Bioreactor", submitted *Biotechnology and Bioengineering* (June 2005 b)
- Peng, C. A., and Palsson, B. O., "Determination of specific oxygen uptake rates in human hematopoietic cultures and implications for bioreactor designs", *Annals of Biomedical Engineering*, Vol. 24, 373 (1996 a)
- Peng, C. A., Koller, M. R., and Palsson, B., "Unilineage model of hematopoiesis predicts self-renewal of stem and progenitor cells based on ex vivo growth data", *Biotechnology and Bioengineering*, Vol. 52, 24 (1996 b)
- Penke, B., S. Kinsey, S. J. Gibbs, T. S. Moerland, and B. R. Locke, "Proton Diffusion and T<sub>1</sub> relaxation in Polyacrylamide Gels: A Unified Approach Using Volume Averaging", *Journal of Magnetic Resonance*, Vol. 132, 240 (1998)
- Petersen, E., Potter, K., Butler, J. J., Fishbein, K. W., Horton, W. E., Spencer, R. G., and McFarland, E. W., "Bioreactor and Probe System for Magnetic resonance Microimaging and Spectroscopy of Chondrocytes and Neocarilage", *Int. J. Imag. Sys. and Tech.*, Vol. 8, 285 (1997)
- Pisu, M., Lai, N., Coincotti, A., Delogu, F., and Cao, G., "A Simulation Model for the Growth of Engineered Cartilage on Polymeric Scaffolds", *International Journal of Chemical reactor Engineering*, Vol. 1, Article A. 38 (2003)
- Potter, K., Butler, J. J., Adams, C., Fishbein, K. W., Mcfarland, E. W., Horton, W. E. and Spencer, R. G., "Cartilage formation in a Hollow Fiber Bioreactor Studied by Proton Magnetic Resonance Microscopy", *Matrix Biology*, Vol. 17, 513 (1998)
- Potter, K., Butler, J. J., Horton, W. E., and Spencer, R. G., "Response of Engineered Cartilage Tissue to Biochemical Agents as Studied by Proton Magnetic Resonance Microscopy", *Arthritis & Rheumatism*, Vol. 43 (7), 1580 (2000)
- Prockop, D. J., "Marrow stromal cells as stem cells for nonhematopoietic tissues", *Science*, Vol. 276, 71 (1997)
- Raimondi, M. T., Boschetti, F., Falcone, L., Fiore, G., B., Remuzzi, A., Marinoni, E., Marazzi, M., and Pietrabissa, R., "Mechanobiology of Engineered Cartilage Cultured under a Quantified Fluid Dynamic Environment", *Biomechan Model Mechanobiol*, 69 (2002)
- Rome, L. C. and Lindstedt, S. L., "The quest for speed: muscles built for high-frequency contractions". *NIPS.*, Vol. 13, 261 (1998)

Rotem, A., Toner, M., Bhatia, S., Foy, B. D., Tompkins, R. G., and Yarmush, M. L., "Oxygen is a factor determining in vitro tissue assembly: Effect on attachment and spreading of hepatocytes", *Biotechnol Bioeng*, Vol. 43, 654-660 (1994)

Russel, B., Motlagh, D., and Ashley, W. W., "Form follows function: how muscle shape is regulated by work", *J. Appl. Physiol.*, Vol. 88, 1127 (2000)

Ryan DJ, Carbonell RG, Whitaker S., "A Theory of Diffusion and Reaction in Porous Media", *AIChE Symposium Series*, Vol. 71, 46 (1981)

Saks, V., Kuznetsov, A., Andrienko, T., Usson, Y., Appaix, F., Guerrero, K., Kaambre, T., Sikk, P., Lemba, M. and Vendelin, M., "Heterogeneity of ADP diffusion and regulation of respiration in cardiac cells", *Biophys. J.* 84, 3436 (2003)

Saidel, G. M., DiBella II, J. A., Cabrera, M. E., "Metabolic system dynamics: lumped and distributed models", *Simulations in Biomedicine V*, Transaction: Biomedicine and Health volume 6 (2003)

Schwartz, R. M., Palsson, B. O., and Emerson, S. G., "Rapid medium perfusion rate significantly increases the productivity and longevity of human bone marrow cultures", *Proc. Natl. Acad. Sci. USA*, Vol. 88, 6760 (1991)

Sengers, B. G., Oomens, Cees W. J., and Baaijens, Frank P. T., "An Integrated Finite-Element Approach to Mechanics, Transport and Biosynthesis in Tissue Engineering", *Transactions of the ASME*, Vol. 126, 82 (2004)

Silva, C. L., Goncalves, R., Lemos, F., Lemos, M. A. N. D. A., Zanjani, E. D., Porada, G. A., and Gabral, J. M. S., "Modeling of ex vivo expansion/maintenance of hematopoietic stem cells", *Bioprocess and Biosystems engineering*, Vol. 25, 365 (2003)

Skalak, R., Fox, C. F., "Tissue engineering", *Ann Biomed Eng.*, Vol. 19, 529 (1991)

Smith, C., "Hematopoietic stem cells and hematopoiesis", *Cancer Control*, Vol. 10, 9 (2003)

Smith, E. and Morrison J. F., "Kinetic studies on the arginine kinase reaction", *J. Biol. Chem.*, Vol. 244(15), 4224 (1969)

Stokes, D. R. and Josephson, R. K., "Structural organization of two fast, rhythmically active crustacean muscles", *Cell Tiss. Res.*, Vol. 267, 571 (1992)

Suarez, R.K., "Shaken and stirred: muscle structure and metabolism", *J. Exp. Biol.*, Vol. 206, 2021 (2003)

Sweeney, H. L., "The importance of the creatine kinase reaction: the concept of metabolic capacitance", *Medicine and Science in Sports and Exercise*, Vol. 26 (1), 30 (1994)

Teague, W. E. and Dobson, G. P., "Thermodynamics of the arginine kinase reaction", *J. Biol. Chem.*, 274(32), 22459 (1999)

Temenoff, J. S., Mikos, A. G., "Review: Tissue Engineering for Regeneration of Articular Cartilage", *Biomaterials*, Vol. 21, 431 (2000)

Terai, H., Hannouche, D., Ochoa, E., Yamano, Y., and Vacanti, J. P., "In vitro engineering of bone using a rotational oxygen-permeable bioreactor system", *Mat Sci Eng C-Bio*, S 20, 3-8 Sp. Iss. SI (2002)

Thébault, M. T., Raffin, J. P., and LeGall, J. Y., "In vivo  $^{31}\text{P}$  NMR in crustacean muscles: fatigue and recovery in the tail musculature from the prawn, *Palaemon elegans*. *Biochem". Biophys. Res. Comm*, Vol. 145, 453 (1987)

Tombes, R. M. and Shapiro, B. M., "Metabolite channeling: a phosphocreatine shuttle to mediate high energy phosphate transport between sperm mitochondrion and tail", *Cell*, Vol. 41, 325 (1985)

Trinh, S. H., Arce, P., Locke, B. R., "Effective diffusivities of point-like molecules in isotropic porous media by Monte Carlo Simulation", *Transport in Porous Media*, Vol. 38, 241-259 (2000)

Truskey, G. A., Nicolakis, D.P., DiMasi, D., Haberman, A., "Kinetic studies and unstructured models of lymphocyte metabolism in fed-batch culture", *Biotechnology and Bioengineering*, Vol. 36, 797 (1990)

Tse, F. W., Govind, C. K., and Atwood, H. L., "Diverse fiber composition of swimming muscles in the blue crab, *Callinectes sapidus*", *Can. J. Zool.*, Vol. 61, 52 (1983)

Tyler, S., and Sidell, B. D., "Changes in mitochondrial distribution and diffusion distances in muscle of goldfish upon acclimation to cold temperatures", *J. Exp. Biol.*, Vol. 232, 1 (1984)

Van Dorsten, F. A., Wyss, M., Walliman, T. and Nicolay, K., "Activation of sea urchin sperm motility is accompanied by an increase in the creatine kinase flux", *Biochem. J.*, Vol. 325, 411 (1997)

Varma, A., Morbidelli, M., and Wu, H., "Parametric Sensitivity in Chemical Systems". Oxford University Press, New York, NY (1999)

Vendelin, M., Kongas, O. and Saks, V., "Regulation of mitochondrial respiration in heart cells analyzed by reaction-diffusion model of energy transfer", *Am. J. Physiol. Cell Physiol.*, Vol. 278, C747 (2000)

Vicini, P. and Kushmerick, M., "Cellular energetics analysis by a mathematical model of energy balance: estimation of parameters in human skeletal muscle", *Am. J. Physiol. Cell Physiol.*, Vol. 279, C213 (2000)

Vunjak-Novakovic, G., Freed, L. E., Biron, R. J., and Langer, R., "Effects of Mixing on the Composition and Morphology of Tissue-Engineered Cartilage", *AIChE J.*, Vol. 42, 860 (1996)

Vunjak-Novakovic, G., Martin, G. I., Obradovic, B., Treppo, S., Grodzinsky, A. J., and Freed, L. E., "Bioreactor Cultivation Conditions Modulate the Composition and Mechanical Properties of Tissue-Engineered Cartilage", *J. Orthop. Res.*, Vol. 17, 130 (1999)

Vunjak-Novakovic, G., Obradovic, B., Martin, G. I., and Freed, L. E., "Bioreactor Studies of Native and Tissue-Engineered Cartilage", *Biorheology*, Vol. 39, 259 (2002)

Walliman, T., Wyss, M., Brdiczka, D., Nicolay, K. and Eppenberger, H.M., "Intracellular compartmentation, structure and function of creatine kinase isoenzymes in tissues with high and fluctuating energy demands: the 'phosphocreatine circuit' for cellular energy homeostasis", *Biochem. J.*, Vol. 281, 21 (1992)

Weisz, P.B., "Diffusion and chemical transformation", *Science*, Vol. 179, 433 (1973)

Wang, T. Y., and Wu, J. H. D., "A continuous perfusion bioreactor for long-term bone marrow culture", *Annals New York Academy of Sciences*, Vol. 665, 274 (1992)

Wang, T. Y., Brennan, J., and Wu, J. H. D., "Multilineal hematopoiesis in a three-dimensional long-term bone marrow culture", *Experimental Hematology*, Vol. 23, 26 (1995)

Wastney, M. E., Yang, D. C., Andretta, D. F., Blumenthal, J., Hylton, J., Canolty, N., Collins, J. C., and Boston, R. C., "Distributing working versions of published mathematical models for biological systems via the Internet", *Adv Exp Med Biol.*, Vol. 445, 131 (1998)

Whitaker S., "Diffusion and Dispersion in porous Media", *AIChE J*, Vol.13, 420 (1967)

Whitaker, S., "The method of volume averaging - Theory and applications of transport in porous media", *Kluwer Academic Publishers* (1999)

Wilkins, R. J., Browning, J. A., and Ellory, J. C., "Surviving in a Matrix: Membrane Transport in Articular Chondrocytes", *Journal of Membrane Biology*, Vol. 177, 95 (2000)

Williams, K. A., Saini, S., and Wick, T. M., "Computational Fluid Dynamics Modeling of Steady-State Momentum and Mass Transport in a Bioreactor for Cartilage Tissue Engineering", *Biotechnology Progress*, Vol. 18, 951 (2002)

Wilson, C. G., Bonssar, L. G., and Kohles, S. S., "Modeling the dynamic composition of engineered cartilage", *Archives of Biochemistry and Biophysics*, Vol. 408, 246 (2002)

Wood, B.D., Whitaker, S., "Diffusion and reaction in biofilms", *Chemical Engineering Science*, Vol. 53, 397 (1994)

Wood, B. D., Whitaker, S., “Multi-species Diffusion and reaction in biofilms and cellular media”, *Chemical Engineering Science*, Vol. 55, 3397 (2000)

Wood, B. D., Quintard, M., Whitaker, S., “Calculation of effective diffusivities for biofilms and tissues”, *Biotechnology and Bioengineering*, Vol. 77(5), 495 (2002)

Yang H., Papoutsakis, E. T., Miller, W. M., “Model-based estimation of myeloid hematopoietic progenitor cells in ex vivo cultures for cell and gene therapies”. *Biotechnology and Bioengineering*, Vol. 72 (2), 144 (2000)

Zammitt, V. A., and Newsholme, E. A., “The maximum activities of hexokinase, phosphorylase, phosphofructokinase, glycerol phosphate dehydrogenases, lactate dehydrogenase, octopine dehydrogenase, phosphoenolpyruvate carboxykinase, nucleoside diphosphatekinase, glutamate-oxaloacetate transaminase, and arginine kinase in relation to carbohydrate utilization in muscles from marine invertebrates”, *Biochem. J.*, Vol. 160, 447 (1976)

Zhao, F., and Ma, T., “Perfusion bioreactor system for human mesenchymal stem cell tissue engineering: dynamic cell seeding and constructs development”, *Biotechnol Bioeng.*, *In early review* (2005 a)

Zhao, F., Pathi, P., Grayson, W., Xing, Q., Locke, B., R., Ma, T., “Effects of oxygen transport on 3-dimensional human mesenchymal stem cell metabolic activity in perfusion and static cultures: experiments and mathematical model”, *Biotechnology Progress*, *In print* (2005 b)

Zhou S, Cui Z, Urban JPG, “Factors Influencing the Oxygen Concentration Gradient from the Synovial Surface of Articular Cartilage to the Cartilage-Bone Interface”, *Arthritis & Rheumatism*, Vol. 50 (12) 3915 (2004)

## **BIBLIOGRAPHICAL SKETCH**

Pragyansri Pathi was born November 29<sup>th</sup>, 1979 in Cuttack a small town in Orissa, India. She completed her undergraduate study in Chemical Engineering at the Birla Institute of Technology & Science (BITS), Pilani, Rajasthan, India in 2001. Upon graduation, she joined Dr Bruce R Locke for her doctoral degree program at Florida State University. During her tenure she presented her work in annual regional meetings including the American Chemical Society (March 2003) and Tissue Engineering Society International (Dec 2003). She participated in summer school programs organized by Mathematical Biosciences Institute, Columbus, Ohio (July-Aug 2004). She also won the Graduate Student Seminar Presentation Contest (Spring 2004). She is looking forward to join Intel Corporation to work as a Senior Process Engineer after the completion of her doctorate degree. If you have any questions you can contact the author at [pragyan\\_pathi@yahoo.com](mailto:pragyan_pathi@yahoo.com).